Moisture-induced stress and distortion of wood

*A numerical and experimental study of wood's drying
and long-term behaviour*

MOISTURE-INDUCED STRESS AND DISTORTION OF WOOD

A numerical and experimental study of wood's drying and long-term behaviour

SARA FLORISSON

Abstract

With Europe's ambition to create a carbon-neutral building industry, wood is an excellent choice of construction material due to its low carbon footprint, its renewable character and high strength to weight ratio. Since the nineties, with the introduction of cross-laminated timber, the use of wood as a construction material has excelled, now finding not only purpose in residential buildings and halls, but also in multi-storey housing. In contrast to other construction materials, wood continuously interacts with its surrounding climate, which affects the mechanical behaviour and shape stability of the product. This creates challenges in each stage of the manufacture and building process: from felling the tree, to drying the timber and to its actual performance as a structural element. There are several available techniques to monitor moisture content and deformations experienced by wood in real time. Nevertheless, most of these techniques only provide an average value or data in specific locations, which paint a fragmented picture. In addition, these measurements do not give insight into the mechanisms that affect stress and deformation. Now, with the current advances made in three-dimensional modelling, it is possible to predict the moisture flow, the moisture-induced deformations and the stress fields of a complete wood element and validate the results based on the outcomes of the previously mentioned experimental techniques.

The main aim of the doctoral thesis is to investigate the possibilities of the developed numerical model to predict the behaviour of wood when simultaneously exposed to mechanical load and a particular climate. The numerical model was used in three different applications: 1) the study of the effect of the green-state moisture content in different configurations of timber boards on the stress development in the tangential material direction experienced during drying at a constant temperature of 60℃ and 59% relative humidity (RH), 2) the calibration of the numerical model based on a self-performed four-point bending test on small clear-wood beams ($30 \times 15 \times 595$ mm) that were subjected to a constant temperature (60℃) and systematic changes in RH (40-80%), and 3) the validation of the numerical model by means of a self-performed four-point bending test on solid timber beams ($195 \times 45 \times 3100$ mm) exposed to natural Northern European climate. With respect to the first application, moisture content profiles obtained with computed tomography scanning and a so-called slicing technique were taken from literature to calibrate the moisture flow model. As part of the second application, an experimental methodology and an analytical method were created.

In this doctoral thesis, a three-dimensional numerical model is presented that is able to simulate the transient nonlinear moisture flow in wood, and the stress and deformations experienced by wood when subjected to a particular climate. The model is developed in finite element (FE) software Abaqus FEA® and includes several so-called user-subroutines that cover the material orientation of wood (annual ring pattern, conical shape and spiral grain), and the selected constitutive

behaviour and required boundary conditions to simulate wood. To describe the moisture flow, a nonlinear single-Fickian approach was combined with a nonlinear Neumann boundary condition, which describes the flux normal to the exchange surface based on a moisture and temperature dependent surface emission coefficient. A strain relation was used that accounts for hygro-expansion, and the elastic, creep and mechano-sorptive behaviour. The developed analytical method as part of the second application describes the elastic and creep deflection in the constant moment area of the four-point bending setup, and contributed to the isolation and assessment of the mechano-sorption deflection in the constant moment area of the long-term four-point bending test.

The results showed that the three-dimensional character of the numerical model contributed to the analysis and visualisation of the moisture content change, and the different stress and deformation states, each affected by material properties that vary (i.e. from pith to bark, between heartwood and sapwood, and due to temperature and moisture content), material orientation and climate. The analysis of timber boards as part of the first application clarified phenomena, such as stress reversal and casehardening associated with wood drying, and showed that the green-state moisture content affected the time, size and frequency with which extremes in tangential tensile stress developed inside the timber during drying. The results of the calibrations and validation indicated that the numerical model is able to describe moisture change and gradients in the considered temperature and RH ranges (between $-2°C$ and $60°C$ and 40% and 80% RH), as well as the deflection. The small clear-wood beams analysed as part of the second application showed the strong effect of spiral grain and climate on deflection, calibrated material parameters and normative stress states. The results from the third application showed that the larger beam exposed to mechanical load and natural climate experienced a slower change in moisture, smaller moisture gradients, more seasonal fluctuation in longitudinal stress, tangential stress and longitudinal-tangential shear stress, and higher drying stress in tension compared to the smaller beam. The experimental methodology and analytical method designed as part of the second application led to a successful identification of each deflection component and isolation of the mechano-sorptive deflection curves of small timber beams that were subjected to low-level bending (stress level/ultimate bending strength < 34%) and a controlled climate generated inside a climate chamber. The experimental methodology benefitted the calibration of the numerical model, and a mentionable fit was found between numerical and experimental results. A similar conclusion could be drawn for the validation of the numerical model performed in the third application. However, the process would have benefitted from continuous recordings of mass change as part of the experiment.

For all three applications, in the areas where the tangential material direction aligned with the exchange surface of the timber boards and beams, high tensile stress developed in the same direction during drying. Adjacent to the tension area, in the inner section of the wood elements, this stress field was always compensated by a compression field. For the first application, these tension areas showed prone

to stress-reversal and casehardening, which caused the stress field to change from tension to compression during drying at the same time as the compression state in the inner section of the beam changed to tension. For the beams tested in the second and third application, the tangential tension fields below the exchange surface continuously changed between tension and compression due to desorption and adsorption, respectively. The results showed that these particular type of stress fields were strongly affected by changes in climate and material orientation, and resulted in values that can make the material prone to cracking (0.68-1.7 MPa). Since the beams studied in the second and third application were exposed to both mechanical load and fluctuating climate, the changes in moisture content also led to a mentionable increase in stress related to the longitudinal material direction (3.2 - 33.4%) and longitudinal-tangential shear plane (2.4-14.7%).

In conclusion, the three-dimensional numerical model contributed to the understanding of phenomena associated with wood drying and long-term behaviour of wood. A powerful numerical tool for scientists and timber engineers is created, which is compatible with the commercially available FE-program Abaqus FEA® and can be used to study the combined effect of load and climate on stress and deformation state of various timber products in a wide field of applications.

Sammanfattning

Med Europas ambition att skapa en koldioxidneutral byggnadsindustri är trä ett utmärkt val av byggmaterial på grund av dess låga koldioxidavtryck, dess förnybara karaktär och dess höga styrka i förhållande till sin vikt. Sedan nittiotalet har användningen av trä som byggmaterial ökat, och nu används det inte enbart för enklare byggnader och hallar utan också i flervånings bostadshus. Till skillnad från många andra byggmaterial interagerar trä med det omgivande klimatet vilket påverkar dess mekaniska beteende och formstabilitet. Detta skapar utmaningar i hela kedjan från avverkning av trädet i skogen till torkning av virket och dess egenskaper som konstruktionselement. Det finns flera tillgängliga tekniker för att övervaka fuktinnehåll och deformationer i träprodukter i realtid. De flesta av dessa tekniker ger enbart ett genomsnittligt värde eller data i specifika punkter vilket ger en fragmenterad bild. Dessutom ger dessa mätningar inte insikt i de mekanismer som påverkar spänningar och deformationer. Med de framsteg som gjorts i tredimensionell numerisk modellering är det möjligt att förutsäga fuktflöde och beräkna de fuktinducerade deformationer och spänningsfält för ett helt konstruktionselement i trä. Modellerna valideras med hjälp av resultat från experimentella försök.

Huvudsyfte i denna doktorsavhandling har varit att undersöka möjligheterna att med hjälp av numeriska modeller förutsäga träets beteende vid samtidig exponering för mekanisk belastning och ett känt varierande klimat. Den numeriska modellen användes i tre olika applikationer: 1) för att studera effekten av höga initiala fuktkvoter (grönt tillstånd) i träbrädor på hur spänningstillståndet utvecklas i den tangentiella materialriktningen under torkning vid en konstant temperatur på 60 ℃ och 59% relativ luftfuktighet, 2) kalibrering av den numeriska modellen baserat på fyrpunkts balkböjning av små balkar av kvistfritt trä (30 × 15 × 595 mm) under konstant temperatur (60 ℃) och vid förbestämda förändringar i relativ luftfuktighet (40-80%), och 3) validering av den numeriska modellen med hjälp av fyrpunkts balkböjning av konstruktionsvirke (195 × 45 × 3100 mm) utsatt för naturligt varierande nordeuropeiskt klimat. I den första applikationen användes initiala fuktprofiler, erhållna med datortomografisk scanning för att kalibrera fuktflödesmodellen. Som en del av den andra applikationen skapades en experimentell metodik och en analytisk beräkningsmetod.

I denna doktorsavhandling presenteras en tredimensionell numerisk modell som kan simulera det transienta icke-linjära fuktflödet i trä och de spänningar och deformationer som uppstår när träprodukter utsätts för ett visst givet klimat under en bestämd tidsperiod. Modellen är utvecklad i programvaran Abaqus FEA® och innehåller flera så kallade 'user-subroutines' som tar hänsyn till träets materialorientering (årsringmönster, stammens koniska form och fiberorienteringen på grund av spiralväxt beaktas liksom), det valda konstitutivt beteende och aktuella randvillkor. För att beskriva fuktflödet kombinerades en olinjär Fickian-modell med

ett olinjärt Neumann-randvillkor, som beskriver flödet vinkelrätt mot träts yta baserat på en fukt- och temperaturberoende 'surface emission coefficient'. En töjningsmodell användes som kan delas upp i en krympning/svällning komponent, en elastisk, en kryp och en mekanosorptiv komponent. Den analytiska metoden som ingår i den andra applikationen kan användas vid beräkning av elastisk deformation och deformation orsakad av krypning i området med konstant moment vid fyrpunktsböjning och gör det möjligt att urskilja deformationer orsakade av mekanosorption.

Erhållna resultat visar att den tredimensionella modellen bidrar till korrekt analys och visualisering av fuktinnehåll och olika spännings- och deformationstillstånd när de påverkas av materialegenskaper som varierar (dvs. från märg till bark, mellan kärnved och splintved, och på grund av temperatur och fuktinnehåll), materialorientering och klimat. Analysen av träbrädor, se applikation ett, visade att det höga initiala fuktinnehållet påverkade tidpunkt, storlek och hur ofta extrema tangentiella dragspänningar utvecklades inuti virket under torkning. Resultaten av kalibreringarna och valideringen visade att den numeriska modellen kan beskriva fuktändring och gradienter för temperatur- och relativa luftfuktighetsintervall (-10 till $60\ ^{\circ}\text{C}$ och 40 till 80% relativ luftfuktighet), samt balkens utböjning. De små kvistfria träbalkarna som analyserades som en del av den andra applikationen visade en stark inverkan av spiralväxt och klimat på utböjning och spänningar. Resultaten från den tredje applikationen visade att större balkar utsatta för mekanisk belastning och naturligt varierande klimat utsattes för långsam förändring i fuktkvot, lägre fuktgradienter, säsongsmässiga variationer i longitudinella spänningar, tangentiella spänningar och longitudinella-tangentiell skjuvspänning, och högre torkspänningar. Den experimentella och den analytiska metoden utvecklade som en del av den andra applikationen bidrog till att respektive delar av den totala utböjningen kunde särskiljas och utböjningen orsakad av mekanosorption kunde isoleras. Detta gjordes för små träbalkar som utsattes för böjning (spänningsnivå / böjhållfasthet $<$ 34%) och ett kontrollerat klimat genererat inuti en klimatkammare. Den experimentella metoden var fördelaktig vid kalibreringen av den numeriska modellen och resultat från den numeriska modellen överensstämde väl med de experimentella resultaten. En liknande slutsats kan dras för valideringen av den numeriska modellen som utfördes i den tredje applikationen. Utvärderingen skulle dock ha gynnats av kontinuerlig datainsamling av massförändringar som en del av experimentet.

För alla tre applikationer utvecklades hög tangentiell dragspänning under torkning i de områden där den tangentiella materialriktningen sammanföll med brädans yta. I anslutning till områden med sådan dragspänning kompenserades detta spänningsfält alltid av tryckspänning inuti träelementet. För den första applikationen uppvisade dessa spänningsområden benägenhet för spänningsomvandling och 'casehardening', vilket fick spänningsfältet att ändras från drag till tryck under torkning samtidigt som tryckspänningar i balkens inre del ändrades till dragspänningar. För balkarna som testades i den andra och tredje applikationen ändrades de tangentiella spänningsfälten under träytan kontinuerligt

mellan dragspänning och tryckspänning på grund av desorption och adsorption. Resultaten visade att denna speciella typ av spänningsfält påverkades starkt av klimatvariationen och materialorientering och kunde resultera i så höga värden att materialet riskerade att spricka (0.68-1.7 MPa). Eftersom balkarna som studerades i den andra och tredje applikationen utsattes för både mekanisk belastning och varierande klimat ledde fuktändringen också till en nämnbar ökning av spänning i materialets longitudinella riktning (3.2-33.4%) och skjuvning i det longitudinella-tangentiella planet (2.4-14.7%).
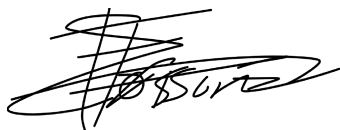
Sammanfattningsvis bidrog den tredimensionella numeriska modellen till förståelsen av fenomen associerade med virkestorkning och trämaterialets långtidsbeteende. Ett kraftfullt numeriskt verktyg för forskare och ingenjörer, kompatibelt med det kommersiellt tillgängliga finita elementprogrammet Abaqus FEA®, har tagits fram och kan användas för att studera den kombinerade effekten av mekanisk belastning och klimatbelastning på spännings- och deformationstillstånd hos olika träprodukter i ett brett tillämpningsområde.

Nyckelord: analysmetod, kalibrering, kontrollerat klimat, krypning, formförändring, experimentell metodik, FEM, fiberorientering, mekano-sorption, fukttransport, naturligt klimat, gran, numerisk modell, tredimensionell, träbalk, validering, trä

Preface

Hovmantorp, January 2021

Sara Florisson

Contents

Appended papers

List of appended papers

Paper I

Sara Florisson (SF), Sigurdur Ormarsson (SO), Johan Vessby (JV). A numerical study of the effect of green-state moisture content on stress development in timber boards during drying. *Wood and Fiber Science*, **2019**, 51(1):41–57. https://doi.org/10.22382/wfs-2019-005

Paper II

Sara Florisson, Johan Vessby, Winston Mmari (WM), Sigurdur Ormarsson. Three-dimensional orthotropic nonlinear transient moisture simulation for wood: analysis on the effect of scanning curves and nonlinearity. *Wood Science and Technology*, **2020**, 52:1197–1222. https://doi.org/10.1007/s00226-020-01210-4

Paper III

Sara Florisson, Lech Muszyński (LM), Johan Vessby. Analysis of hygro-mechanical behaviour of wood in bending. *Wood and Fiber Science,* **2021**, 53(1):27-47. https://doi.org/10.22382/wfs-2021-04

Paper IV

Sara Florisson, Johan Vessby, Sigurdur Ormarsson. A three-dimensional numerical analysis of moisture flow in wood and of the wood's hygro-mechanical and visco-elastic behaviour. *Wood Science and Technology,* submitted December 2020.

Other publications related to the thesis work

Abstract I

Sara Florisson, Sigurdur Ormarsson. The effect of initial green state moisture gradients on stresses in timber boards during drying. In Proceedings of ECCOMAS Congress 2016, Crete, Greece, 5–6 June 2016

Abstract II

Sara Florisson, Sigurdur Ormarsson. The effect of surface emission, diffusion and initial moisture profiles on stress development in timber boards. In Proceedings of CompWood 2017, Vienna, Austria, 7–9 June 2017

Abstract III

Johan Vessby, Sara Florisson, Tadios Habite. Numerical simulation of moisture driven fracture in mechanical timber connection using XFEM. In Proceedings of CompWood 2017, Vienna, Austria, 7–9 June 2017

Conference proceeding I

Sara Florisson, Sigurdur Ormarsson, Johan Vessby. Modelling of mechano-sorption in clear wood by using an orthotropic non-linear moisture flow and stress model. In Proceedings of the World Conference on Timber Engineering, Seoul, Republic of Korea, 20–23 August 2018

Conference proceeding II

Tadios Habite, Sara Florisson, Johan Vessby. Numerical simulation of moisture driven crack propagation in mechanical timber connection using XFEM. In Proceedings of the World Conference on Timber Engineering, Seoul, Republic of Korea, 20–23 August 2018

Paper V

Joran van Blokland, Sara Florisson, Michael Schweigler, Thomas K Bader, Stergios Adamopoulos. Evaluation of test methods to determine embedment properties of dowel-type joints used in thermally modified timber. *Manuscript*

Author contributions[1]

Paper I

Conceptualisation: SF, JV, SO; Methodology: SF, SO; Software: SF; Validation: SF; Formal analysis: SF; Investigation: SF; Resources: SO; Data curation: SF; Writing – original draft: SF; Writing – review & editing: SF, JV, SO; Visualisation: SF; Supervision: SO, JV; Project administration: SF

Paper II

Conceptualisation: SF, SO, JV; Methodology: SF, SO; Software: SF; Validation: SF; Formal analysis: SF; Investigation: SF; Data curation: SF; Writing – original draft: SF; Writing – review & editing: SF, JV, WM, SO; Visualisation: SF; Supervision: SO, JV; Project administration: SF

---

[1] In accordance with the Contributor Roles Taxonomy (CRediT)

Paper III

Conceptualisation: SF, LM; Methodology: SF, JV, LM; Software: SF; Validation: SF; Formal analysis: SF; Investigation: SF; Resources: LM; Data curation: SF; Writing – original draft: SF; Writing – review & editing: SF, JV, LM; Visualisation: SF; Supervision: LM; Project administration: SF

Paper IV

Conceptualisation: SF, JV, SO; Methodology: SF, JV, SO; Software: SF; Validation: SF; Formal analysis: SF; Investigation: SF; Resources: SO; Data curation: SF; Writing – original draft: SF; Writing – review & editing: SF, JV, SO; Visualisation: SF; Supervision: SO, JV; Project administration: SF

Notations

List of symbols

Roman upper case letters

$\boldsymbol{C}$	Compliance matrix
$\boldsymbol{C}_{C_k}$	Creep compliance matrix
$\boldsymbol{C}_w$	Damping matrix
$\widetilde{\boldsymbol{C}}_w$	Nonlinear damping matrix
$\boldsymbol{D}$	Diffusion matrix
$\boldsymbol{D}_b$	Bound water diffusion matrix
D_l, D_r, D_t	Diffusion coefficient in orthotropic directions l, r and t
$\boldsymbol{D}_v$	Vapour diffusion matrix
E	Elastic modulus analytical method
E_l, E_r, E_t	Elastic modulus in orthotropic directions l, r and t
E_{ms}	Parameter of mechano-sorptive model analytical method
E_0	Reference value to describe E
F	Force
$\widetilde{\boldsymbol{F}}_b$	Nonlinear boundary matrix
G_{lr}, G_{lt}, G_{rt}	Shear modulus in the orthotropic plane l-r, l-t and r-t
K, K_1, K_2	Temperature dependent parameter Simpson's formula
$\boldsymbol{K}^*$	Tangent diffusion matrix (Jacobian) Newton Raphson method
$\boldsymbol{K}$	Stiffness matrix
$\widetilde{\boldsymbol{K}}$	Nonlinear stiffness matrix
$\boldsymbol{K}_c$	Complementary stiffness matrix
$\widetilde{\boldsymbol{K}}_c$	Nonlinear complementary stiffness matrix
$\boldsymbol{N}$	Shape function vector
T	Temperature
W	Temperature dependent parameter Simpson's formula
Y_{w0}	Term to indicate relation of E to moisture

Roman lower case letters

a	Distance between load and support
$\boldsymbol{a}$	Nodal point vector containing the moisture content
b	Width of specimen
c	Sorption
c_b	Bound water concentration
c_v	Water vapour concentration
c_w	Moisture capacity
f_b	Ultimate bending strength
$\boldsymbol{f}^*$	Out-of-balance force Newton Raphson method

h	Depth of specimen
l_l	Gauge length
$\boldsymbol{m}$	Matrix containing mechano-sorption parameters
m_l, m_r, m_t	Mechano-sorption moduli in orthotropic directions l, r and t
m_{lr}, m_{lt}, m_{rt}	Mechano-sorption moduli in orthotropic plane l-r, l-t and r-t
$\boldsymbol{n}$	Retardation matrix
n_l, n_r, n_t	Retardation properties in orthotropic directions l, r and t
n_{lr}, n_{lt}, n_{rt}	Retardation properties in orthotropic plane l-r, l-t and r-t
q_n	Flux normal to the boundary
$\boldsymbol{q}$	Flux vector
r	Distance between pith and point of evaluation
s	Surface emission coefficient
t	Time
t'	Time correspondent to a recent stress change $\Delta\boldsymbol{\sigma}$
u	Total deflection
u_c	Creep deflection
u_e	Elastic deflection
u_e^*	Instantaneous elastic deflection
u_{ms}	Mechano-sorptive deflection
v	Cumulative moisture content change
w	Moisture content
w_a	Moisture content below fibre saturation point
w_{eq}	Equilibrium moisture content
w_{gs}	Green-state moisture content
w_f	Fibre saturation point
w_v	Average volumetric moisture content
w_∞	Moisture content of ambient air

Greek upper case letters

Δt	Time increment
$\Delta\boldsymbol{\sigma}$	Stress increment

Greek lower case letters

α_1, α_2	Parameter of mechano-sorptive model analytical method
$\boldsymbol{\alpha}$	Matrix containing hygro-expansion coefficients
$\alpha_l, \alpha_r, \alpha_t$	Hygro-expansion coefficients in orthotropic directions l, r and t
δ	Conical angle
$\boldsymbol{\varepsilon}$	Total strain
$\boldsymbol{\varepsilon}_c$	Creep strain
$\boldsymbol{\varepsilon}_e$	Elastic strain
$\boldsymbol{\varepsilon}_h$	Strain caused by hygro-expansion
$\boldsymbol{\varepsilon}_{ms}$	Mechano-sorptive strain
θ	Spiral grain angle

μ	Mean
ρ	Density of liquid moisture
ρ_0	Oven-dry density
$\boldsymbol{\sigma}$	Stress vector
$\sigma_l, \sigma_r, \sigma_t$	Normal stress in orthotropic directions l, r and t
τ_k	Retardation time
$\tau_{lr}, \tau_{lt}, \tau_{rt}$	Shear stress in the orthotropic plane $l\text{-}r$, $l\text{-}t$ and $r\text{-}t$
ϕ	Relative humidity
ϕ_σ	Initial deformation rate in Kelvin creep model analytical method
$\phi_{\sigma 0}$	Reference term to describe ϕ_σ
$\phi_{\sigma_l}, \phi_{\sigma_r}, \phi_{\sigma_t}$	Creep property in orthotropic directions l, r and t
$\phi_{\tau_{lr}}, \phi_{\tau_{lt}}, \phi_{\tau_{rt}}$	Creep property in the orthotropic plane $l\text{-}r$, $l\text{-}t$ and $r\text{-}t$
χ_{w0}	Term to indicate relation of ϕ_σ to moisture
$\boldsymbol{\psi}$	Residual vector
ψ_{fT}	Term to describe relation of w_f to temperature

List of mathematical notations

$\nabla \cdot \boldsymbol{q}$	Divergence flux vector
$\nabla(\bullet)$	Spatial gradient
$(\bar{\bullet})$	Local coordinate system
$(\dot{\bullet})$	Time differentiation
$\lvert \bullet \rvert$	Absolute value
$(\bullet)^T$	Transpose of a matrix
$(\bullet)^{-1}$	Inverse of a matrix
$\sum(\bullet)$	Summation
$\int_A (\bullet)\, \mathrm{d}A$	Integration over the surface
$\int_V (\bullet)\, \mathrm{d}V$	Integration over the volume
$\int_0^t (\bullet)\, \mathrm{d}t$	Integration over time
i	Relates to the iteration number of the Newton Raphson method
k	Relates to the number of the Kelvin model modules
l, r, t	Primary orthotropic material directions
lr, lt, rt	Orthotropic material planes
m	Relates to the number of the ϕ-cycles
n	Relates to the time increment's number
x, y, z	Primary directions Cartesian coordinate system

Abbreviations

|	
CLT	Cross-laminated timber
EMC	Equilibrium moisture content
EWP	Engineered wood products
FEM	Finite element method
FSP	Fibre saturation point
RH	Relative humidity
XFEM	Extended finite element method

1 Introduction

The building and construction sector, together, account for a large percentage of the total carbon dioxide emission and global energy consumption (IEA 2021; RON 2015). To achieve an energy neutral construction industry a more efficient use of energy and a wider use of renewable energy sources is needed (Swedisch Wood 2021). In this context, the term renewable sources refers to non-fossil resources. From the perspective of the structural engineer, this requires the use of construction materials that have a low carbon footprint and a renewable character, such as wood (Dodoo 2011).

At the beginning of the twentieth century, timber was primarily used in timber-frame housing (Brandner et al. 2016); see **Fig. 1-1**. Around the same time, the first glue-laminated timber (glulam) was introduced to the building market (Thelandersson et al. 2003). This engineered wood product (EWP) resulted in higher capacity beams and columns, which allowed for longer floor and roof spans. Since the nineties, another EWP named cross-laminated timber (CLT) entered the European market (Brandner et al. 2016), allowing for the production of long-span diaphragms that can be used as floor, wall and roof elements. This development exhilarated the use of timber in structures, since the construction speed with CLT is high, and wood could compete with materials such as steel and concrete for the construction of multi-story buildings.

Nowadays, there are multiple EWPs available on the construction market that are suitable for use in structures, such as parallel strand lumber (PSL), laminated veneer lumber (LVL), I-joist, glulam, CLT, brettstapel panels, stress-laminated panels, and nail-laminated panels (Ramage et al. 2017). Popular examples, where wood is part of the load-bearing structure, are the six storey Limologen building constructed in Växjö, a city located in South Sweden (CLT and timber-frame), the sixteen storey Treet building situated in Bergen in Norway (glulam and CLT) (Malo et al. 2016), and the seven storey student residence in Norwich in the United Kingdom (CLT). A most recent development is the prefabricated volumetric element, see **Fig. 1-1**. This element is ideal for low-rise residential buildings, and just like CLT, allows for a speedy construction process (Ormarsson et al. 2019).
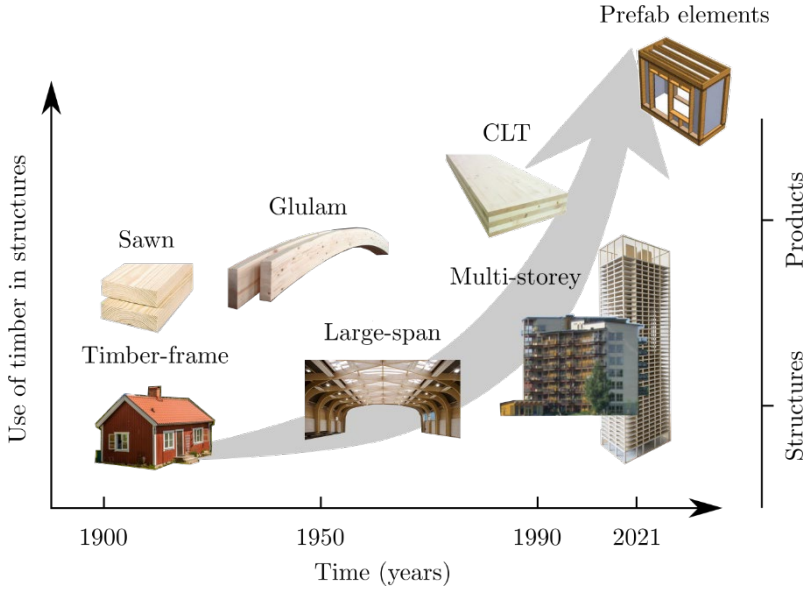
Fig. 1-1: *Events contributing to the increased use of timber in structures since the beginning of the twentieth century*

The higher the timber structures become, also the more complex. With this increasing complexity, more knowledge is needed to understand the mechanical performance of wood as a construction material. Especially since, unlike other construction materials, wood continuously interacts with its surrounding environment due to its hygroscopic nature. This behaviour affects the shape stability of timber products and its mechanical performance both in the short-term and long-term, which creates challenges during production, construction and service life (Mårtensson et al. 1997; Olsson 2019; Ormarsson et al. 2010; Ormarsson et al. 2016; Ormarsson et al. 2014; Serrano et al. 2014; Svensson et al. 2002a).

1.1 Background

The mechanical performance of wood is complex. It does not only dependent on the variation of material properties from pith to bark within the log (i.e. radial variation), or the moisture and temperature dependency of material properties, but also on local imperfections such as knots, cracks and reaction wood. In addition, the type of load, the climate conditions of the surrounding air, and the moisture induced distortion (cup, bow, twist and crook) affected by fibre orientation (annual rings, spiral grain and conical shape) also have an effect on the performance (Ormarsson 1999; Persson 2000).

During the interaction between wood and the ambient air, the wood will try to establish an equilibrium moisture content (EMC). EMC refers to a state in which wood can occur, when no moisture is gained nor lost by the material. When wood

is subjected to a combined interaction of mechanical load and a continuous change in moisture content, also a continuous change in stress and distortion can be experienced (Angst et al. 2012; Fortino et al. 2019a; Fortino et al. 2019b; Ormarsson et al. 1999; Pang 2007). There are several experimental techniques available to monitor changes of moisture content inside wood, and deformations experienced by the wood when tested inside a climate chamber or in situ (Gowda et al. 1998; Gustafsson et al. 1998; Ranta-Maunus et al. 1998). However, these techniques often only provide average values or values in specific locations in or around the wood, and do not give insight into the mechanisms that play a role in the behaviour of wood or how stress fields inside the wood change. Here, numerical models can play an important role.

Many numerical models based on the FE-method have been developed in the past fifty years that can account for moisture flow and moisture-induced deformations in wood. However, these models vary in the spatial dimensions they cover (one, two or three), the theories that are used to describe the moisture dependent behaviour of wood, and what additional features they account for (hysteresis, fibre orientation, description of material properties). The advantages with three-dimensional modelling are that a complete prediction can be made of moisture flow, moisture-induced deformations and stress development in the entire wood or timber element, while also accounting for fibre orientation and potential variation in material properties (radial, moisture and temperature). It also allows for the simultaneous analysis of the effect of climate and mechanical load, might they occur in different dimensional planes, such as with beams loaded in bending. When such a numerical model is implemented in commercial software, it benefits from the strong computational abilities, graphical interface and pre- and post-processing abilities that comes with such software. In addition, there is a possibility to reach a much wider audience, such as the industry, then when implemented in general computational software. Most recently, progression has been made in the three-dimensional modelling of the moisture dependent behaviour of wood using the FE - method (Fortino et al. 2019b; Huč 2019). These numerical models are characterised by advanced moisture models that closely resemble the moisture flow in wood from a physics standpoint. However, these models require a vast amount of experimentally verified material parameters, something that is already a challenge with three-dimensional modelling. Therefore, the analysis of the hygro-mechanical behaviour of wood could benefit from a three-dimensional numerical model that uses simpler theories to describe moisture flow to be able to analyse engineering problems; theory that is based on material parameters that are easier to substantiate with experimental data.

1.2 Focus and scope

The focus of the present doctoral thesis is on the development of a three-dimensional numerical model based on the FE-method. The model will be used to

observe the behaviour of wood elements that are simultaneously exposed to load, such as a moisture-induced constraint or externally applied mechanical loads, and climate, either controlled or natural. The model, at the same time, also accounts for material orientation and, where appropriate, the variation in material properties (radial, moisture and temperature). Here, 'controlled climate' is defined as the programmed set of temperature and RH conditions experienced inside an environmental chamber, and 'natural climate' refers to the same type of conditions, but in accordance to the weather, without the direct influence of rain, sun and wind. The model is developed in FE and engineering software Abaqus FEA® and suits the description of wood's behaviour associated with the macroscopic level, i.e. on the scale of annual rings.

The numerical model will be used in three different applications to proof the validity of the model to describe moisture flow and moisture-induced stress and deformation of wood based on experimental data gathered from literature and self-performed tests. These applications cover the areas of wood drying and long-term behaviour of wood. The first application involves the analysis of the drying behaviour of timber boards when dried from green-state to an EMC below the fibre saturation point (FSP). The second application focusses on the calibration of the numerical model based on experimental data obtained on small-clear wood beams subjected to four-point bending and controlled climate. The third application involves the validation of the numerical model using the experimental data from a four-point bending test performed on solid timber beams subjected to natural climate in the North of Europe. In this context, 'calibration' is the iterative process of adjusting material parameters and comparing the model to experimental data until good agreement is found. Whereas, 'validation' is the process where a set of preselected material parameters is used to see how well the numerical model is able to describe the material's behaviour under natural circumstance.

1.3   Relevance and importance

At this moment in time, there is a need for a three-dimensional FE-model to simulate nonlinear transient moisture flow and moisture-induced distortion in wood that: • Describes material behaviour on macroscopic level • Has the necessary theory available inside user-subroutines compatible with a commercially available software to create more flexibility, but also to benefit from the programs pre- and post-processing features • Can more easily be substantiated by experimentally verified material parameters, and • Includes the material orientation of wood and the variation of material parameters between pith and bark, and with respect to moisture and temperature. Such a model is suitable to solve engineering problems, and has the advantage that numerous variations of certain problems can be analysed without the costs and workload of experiments. A simpler version of such a model was previously discussed by Fortino et al. (2010). However, it is suggested that the therein applied theory is not able to sufficiently describe the drying speed and

moisture content gradients when quick RH-changes are experienced (Konopka et al. (2018). This model uses a constant surface emission coefficient in the description of the flux normal to the exchange surface. The correct description of speed and gradients is extremely important when describing the moisture-dependent behaviour of wood.

Although, much research has already been conducted in the field of simulating wood drying (Pang 2007; Salin 2010), much can still be done to improve kiln-operation schedules to reduce energy consumption, costs, and loss of material (Salin et al. 2008). Usually, when simulations of wood drying are made, a constant moisture content is taken as the initial state. In this thesis, the effect of the actual initial state, *i.e.* the green-state moisture content, on the size, time of occurrence and location of the tangential stress within the cross-section of different configurations of timber boards is studied. With respect to simulating the long-term behaviour of wood in bending, for a long time the emphasis has been on one- and two-dimensional models, and their calibration and validation (Mohager et al. 1993; Ranta-Maunus 1975; Toratti 1992). Morlier (1994), Hunt (1999). Muszyński et al. (2005) pointed out that the experimental programs used to observe the behaviour of wood subjected to long-term load under changing climate conditions show a lot of variation and are often superficial in the analysis of results. The experimental methodology and analytical method, proposed in this thesis, need to improve these aspects and the calibration of numerical models based on experimental data. In addition, results from a long-term bending test exposed to Northern European climate contributes to the validation of the numerical model. The outcomes of both the calibration and the validation from the numerical model allow for a thorough analysis of the different stress states of small-clear wood beams and solid timber beams in the three-dimensional plane, and see the impact of moisture, material orientation, mechanical load, climate and beam size on its behaviour. In general, the doctoral thesis contributes to the better understanding of moisture flow, creep and mechano-sorption in boards and beams, and the selection procedure of methods and mathematical models that are essential in such a process.

1.4   Aim, research questions and objectives

The aim of the thesis is to investigate the possibilities of the numerical model to predict the behaviour of wood/timber elements subjected to load and climate. To contribute to the understanding of moisture-induced mechanical behaviour both during drying and long-term use; the following six research questions (RQs) were formulated:

1.   Which theories and heuristic approaches are suitable to describe the nonlinear transient moisture flow of wood and corresponding boundary conditions on macroscopic level?

2. Which material models are suitable to describe the hygro-expansion, and the elastic, creep and mechano-sorptive behaviour of wood on macroscopic level?
3. How does the green-state moisture content influence the stress development of timber boards that contain both sapwood and heartwood and are dried to an EMC below FSP?
4. How does the nonlinearity of the transient moisture flow analysis and the sorption hysteresis with associated scanning behaviour affect moisture change in wood?
5. How to improve the calibration of numerical models that are used to study the long-term behaviour of beams exposed to controlled climate, and the analytical analysis of the deflection results obtained with such an experiment?
6. What is the influence of spiral grain on the calibration of small beams of clear wood subjected to load and controlled climate, and how does beam size affect moisture change and stress/strain development of beams subjected to load and natural climate?

RQs 1 and 2 refer to the development of the numerical model. RQs 3, 4 and 6 involve the implementation of the numerical model, and RQ 5 refers to the calibration of the numerical model. The research objectives (ROs) related to the RQs are:

1. To implement the selected theory into user-subroutines, which are used to describe nonlinear transient moisture flow (Paper II) and moisture-induced stress and distortion (Paper IV) of wood.
2. To collect necessary experimental data from the literature or by means of self-performed tests, which facilitate input parameters for the numerical model that can be moisture- and/or temperature-dependent (Paper I, II and IV).
3. To develop an experimental program to improve the calibration of numerical models used to simulate beams subjected to load and controlled climate (Paper III).
4. To develop an analytical method based on the material models used for the numerical model that allows to isolate and assess the mechano-sorptive deflection part of the total deflection obtained from the constant moment area of a four-point bending test (Paper III).
5. To assess the performance of the numerical model to simulate moisture flow (Paper I and II) by means of experiments from literature (Paper I and II) or self-performed experiments (Paper II).
6. To assess the performance of the numerical model to simulate the hygro-mechanical and visco-elastic behaviour of wood by means of self-performed four-point bending tests (calibration or validation), which were conducted in either controlled or natural climate (Paper IV).

7. To study the stress development of different configurations of timber boards, which contain both sapwood and heartwood, when dried from green-state to an EMC below FSP (Paper I).
8. To study the effect of sorption hysteresis with associated scanning behaviour, and the moisture- and temperature-dependency of flow parameters, on the moisture content change in wood (Paper II).
9. To study the effect of spiral grain on the calibration (deflection, material parameters and normative stress states) made on small-clear wood beams subjected to load and controlled climate, and to study the effect of beam size on the moisture change and stress/strain development of beams subjected to load and natural climate.

1.5 Overview of appended papers

Paper I (RQ 1, 3 – RO 2, 5, 7): A first version of the three-dimensional numerical model is used to simulate the stress development related to the tangential material direction of different configurations (annual ring pattern) of timber boards that are dried from green-state to an EMC below FSP. The model is able to simulate the transient nonlinear moisture flow (standard module in the FE-software) and moisture-induced stress by accounting for elastic, hygro-expansion and mechano-sorptive response (user-subroutine) of wood. The stress state affected during drying by the uneven formation of moisture gradients along the surface due to the green-state moisture content and the difference between hygro-expansion parameters related to the sapwood and heartwood areas is compared to a situation where the initial moisture content is constant and close to FSP.

Paper II (RQ 1, 4 – RO 1, 2, 5, 8)**:** A set of user-subroutines is developed to create more flexibility with regard to the nonlinear transient moisture flow model, while benefitting from the computational power and graphic capacity provided by the FE-software. The routines cover the necessary theory for a nonlinear transient flow analysis combined with a Neumann boundary condition that describe the flux perpendicular to the exchange surface using a moisture and temperature dependent surface emission coefficient. A heuristic technique is developed, which is part of the boundary condition, to account for sorption hysteresis and its associated scanning behaviour. Moisture content profiles of a wood cube dried from green-state to EMC obtained from literature, and the volumetric average moisture content of a small wood beam subjected to systematic RH-changes obtained from a self-performed test, are used to validate the moisture flow model.

Paper III (RQ 5 – RO 3, 4)**:** An experimental program and analytical method are presented that are aimed at improving the validation of numerical models, which are used to simulate the behaviour of small-clear wood specimens subjected to a combination of four-point bending and systematic changes in RH. Both sapwood

and heartwood specimens are used that correspond to a specific cardinal or inter-cardinal wind direction. The experimental program consist of 1) static four-point bending tests performed on end-matched specimens to indicate the potential variation in testing material between wind directions, 2) additional creep tests to study the effect of moisture on creep parameters, and 3) long-term four-point bending tests performed under constant temperature and continuous variation between two RH-phases. The analytical method is used to efficiently isolate and assess the mechano-sorption deflection, by separating the total deflection curve obtained from the constant moment area into an elastic, hygro-expansion and creep component using similar material models as used for the numerical model.

Paper IV (RQ 1, 2, 5, 6 – RO 1, 2, 6, 9)**:** The most recent version of the three-dimensional numerical model is calibrated and validated based on self-performed four-point-bending tests made on clear-wood specimens and solid timber beams subjected to controlled climate and natural Northern European climate, respectively. Simpson's formula is added to the user-subroutine, which describes the boundary conditions of the moisture flow analysis, to account for the moisture content of the ambient air. Exponential equations are composed based on a collection of experimental data from literature to describe the moisture and temperature dependency of the diffusion and surface emission coefficient used to describe moisture flow within the wood within the necessary climate ranges. The hygro-mechanical behaviour is described on the notion that wood experiences elastic, creep, hygro-expansion and mechano-sorptive behaviour. The combined effect of moisture and spiral grain on material parameters, deflection and stress is studied based on the experiment performed on clear-wood specimens subjected to constant temperature and systematic changes in RH. The deflection results obtained with the bending experiment exposed to natural climate is used to validate the numerical model and analyse the moisture content, stress and strain development in time for two different sizes of beams.

1.6 Thesis outline

The introduction given in *Chapter 1* provides relevant background information, together with a description of the scope and the aim of the research, the relevance of the doctoral thesis, the research questions and the research objectives. The literature review presented in *Chapter 2* focusses on the state-of-the-art knowledge concerning the moisture transport in wood and the moisture-induced mechanical behaviour of wood. Besides a general description of these topics and their related phenomena, such as green-state moisture content, sorption hysteresis, material orientation, and elastic, hygro-expansion, creep and mechano-sorptive behaviour, also an overview of important models is given. The research methodology adopted in this doctoral thesis is discussed in *Chapter 3*, which gives a description of the different methods (numerical, analytical and experimental) and how they relate to

each paper. *Chapter 4* is focussed on the primary findings from each of the appended papers and, finally, *Chapter 5* provides the main conclusions and recommendations for future studies. At the end of the thesis, a list of references can be found, which the appended papers follow.

2   Literature review

2.1   Introduction

The most common softwoods in Sweden are Norway spruce (*Picea abies*) and Scots pine (*Pinus sylvestris*), where Norway spruce is the most important softwood when it comes to the production of structural timber. A thorough description of the softwood's macroscopic and microscopic structure can be found in Bodig et al. (1982), Kollmann et al. (1968), Dinwoodie (1981), Skaar (1988) and Rowell (2012). In the current section, only the most important aspects concerning this doctoral thesis will be highlighted.

In softwood, the outer growth rings relate to sapwood, and are important in the transportation of moisture; see **Fig. 2-1b**. One growth ring relates to around one year of cell production, and consists of early and late wood. The remaining part of the cross-section is made up of heartwood, which are transitioned sapwood cells. Heartwood cells have a distinct dark colour, and experience a lower green-state moisture content, lower permeability and less porosity than sapwood (Rowell 2012). Between the pith and bark, a linear increase and linear decrease in elastic stiffness and longitudinal hygro-expansion, respectively, in radial direction (between pith and bark) can be found (Dahlblom et al. 1999; Ormarsson 1999), which is the point of departure used in the modelling work presented in this thesis. However, the first 15 to 20 growth rings centred around the pith relate to juvenile wood, which is characterised by a lower stiffness, an increased longitudinal hygro-expansion, a lower tangential hygro-expansion and a lower density then mature wood (Persson 2000).

The cells of softwood, or tracheid, have long stretched bodies, with tapered ends. The transport of moisture takes place through the lumen, the cell wall and the pits located on the cell wall of the tracheid. During drying, these pits may aspirate, which is an irreversible process. The tracheid have a specific orientation; see **Fig. 2-1c**. To describe the material orientation of wood, often a local coordinate system is adopted, which consists of a longitudinal (l), radial (r) and tangential (t) direction, see **Fig. 2-1a** and **c**. The material orientation is important when it comes to the

definition of material parameters related to the moisture transport, and the hygro-mechanical and visco-elastic behaviour of wood. It also effects the stress development in the wood and the deformations experienced by the wood.
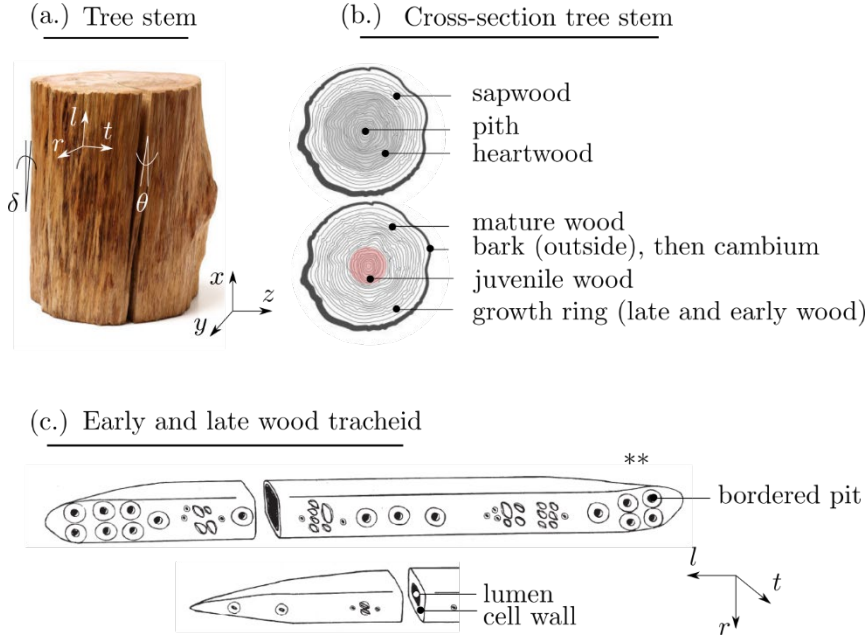
*Fig. 2-1: (a.) Tree stem with an indication of the local (l,r,t) and global (x,y,z) coordinate system, spiral grain θ, and conical shape δ, (b.) the cross-section of the tree stem with an indication of general aspects concerning wood on macroscopic level, and (c.) the softwood tracheid in early or late wood with important aspect that concern moisture transport in wood **Fragment of an illustration from Krabbenhøft (2003)*

The material orientation of wood is affected by the conical shape of the three stem, the annual ring curvature in the cross-section of the stem, and the spiral grain related to the spiralling wood fibre around the pith; see **Fig. 2-1a**. The magnitude of the conical shape and spiral grain at each point in the material can be expressed by an angle δ and an angle θ in the longitudinal-radial and longitudinal-tangential plane, respectively. Based on 7023 observations made on 390 logs of Norway spruce, Säll (2002) indicated that the θ can deviate from +8 to $-5°$ over a distance of 200 mm from pith to bark, see **Fig. 2-2**. For one specific log of Norway spruce, Dahlblom et al. (1999) found a variation between +5 and $-1°$ over a distance of 130 mm. Close to the pith, the wood fibres in Norway spruce generally experience a positive angle (left-handed), while close to the bark the spiral can turn into a negative angle (right-handed).
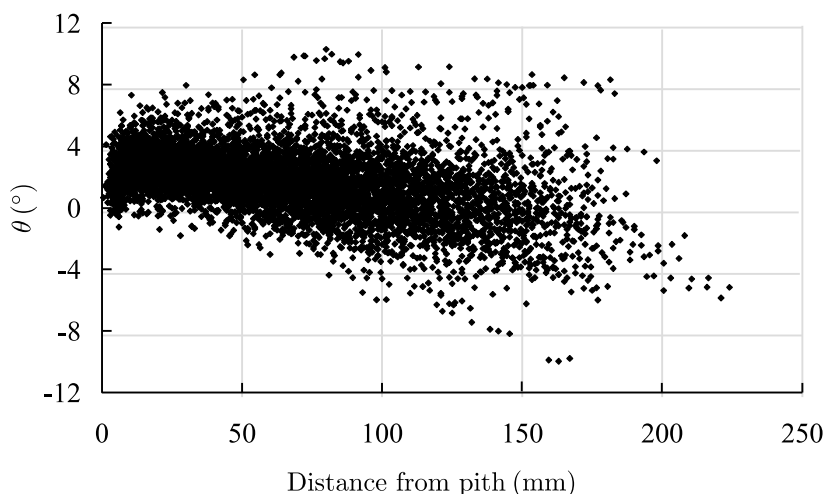
Fig. 2-2: *Experimentally obtained variation in spiral grain angle θ from pith to bark for Norway spruce (Säll 2002)*

2.2 Moisture transport

2.2.1 Moisture phases

Within material science, the EMC related to the RH-range between 0 and about 95 - 98% is considered the hygroscopic-range, while between 98 and 100% it is seen as the over-hygroscopic range (Fredriksson 2019). Here, the term hygroscopic refers to wood being a material that takes in (wetting; adsorption) or releases moisture (drying; desorption) into the ambient air to establish a balance with its surroundings, *i.e.* the EMC.

In the over-hygroscopic range, the moisture content increases rapidly, since the lumen are capable of holding large volumes of water. The moisture content of wood is a quantity that relates the amount of moisture present inside the material to the dry-mass of wood (EN 13183-1 2003). In this range, the transport of moisture is governed by capillary pressure and can be divided into two phases: the constant drying rate period and the pseudo-constant drying rate period (Rémond et al. 2005). The first phase is characterised by a gradient free moisture content change in the inner section of wood, and a formation of a thin dry-shell just below the exchange surface (Wiberg 1996; Wiberg 1998). The end of the constant drying rate period, and the initiation of the pseudo-constant drying rate period is indicated by the point of irreducible saturation, which can be expected around 70% moisture content (Salin 2010). Below this point, the liquid flow is interrupted, and the moisture collects at the end of the tapered tracheid (Krabbenhøft 2003). Transport takes place

through bordered pits and formation of films between water-filled clusters (Krabbenhøft 2003; Salin 2008; Salin 2010).

The transition between the hygroscopic and over-hygroscopic range is characterised by the FSP. Below this point, the strength, stiffness and deformations of wood are strongly affected by moisture content (Gerhards 1982). For Norway spruce, this points lies between 26% and 28% moisture content when a temperature of 20℃ is experienced (Bratasz et al. 2012; Wiberg et al. 1999).

In the hygroscopic range, the transport of moisture is mainly observed through water vapour diffusion in the lumen, bound water diffusion in the cell walls and as sorption processes between the two phases (Frandsen 2007; Krabbenhøft 2003). Where sorption refers to either the process of adsorption, where moisture is taken up by the cell wall, or desorption, where moisture is released by the cell wall. The hygroscopic range is associated with the decreasing drying rate period, where the moisture transport slows down significantly, and the formation of moisture content gradients at the exchange surface exceeds the dry-shell seen in the over-hygroscopic range (Wiberg 1998). In both the over-hygroscopic and hygroscopic range, moisture leaves the wood by surface emission during drying. In the hygroscopic range, moisture can re-enter the wood by surface absorption during wetting.

2.2.2   Green-state moisture content

The green-state moisture content is the moisture content of the tree right after felling (Skaar 1988). For softwood species, such as Norway spruce, this state is characterised by a radial variation in moisture content in the cross-section of the tree. Typically in green-state, the heartwood region experiences values between 30% and 80% moisture content, whereas the sapwood region has much higher values between 80% to 200% (Absetz 1999; Larsen 2013; Samuelsson et al. 1994).

2.2.3   Sorption hysteresis

The sorption isotherm, *i.e.* the relation between the ambient RH and the EMC in the hygroscopic range, is characterised by an envelope formed by the desorption and adsorption isotherms, which are obtained at first complete drying and wetting, respectively (Frandsen 2007; Time 1998). The sorption isotherm is affected by temperature and mechanical load (Skaar 1988). Where, an increase in temperature or a mechanical compressive stress reduces sorption (lowers the EMC), and a tensile stress increases it. The difference in EMC seen between the desorption and adsorption isotherms for equal ambient conditions is known as sorption hysteresis (Engelund et al. 2013; Fredriksson et al. 2018). This phenomenon indicates that the equilibrium state is not only dependent on the RH, but also on the moisture history. What exactly causes hysteresis is still open for discussion (Engelund et al. 2013). Sorption hysteresis decreases with increasing temperature and disappears at temperatures above 75℃ (Engelund et al. 2013; Skaar 1988).

In the hygroscopic range, a water molecule is absorbed in cell walls and mainly interacts with hydroxyl groups (entity with formula OH) of the chemical compounds cellulose, hemicellulos and lignin, and directly binds to one or two sorption sites (Engelund et al. 2013; Fredriksson 2019). Where, sorption sites are the hydroxyl groups that are able to create hydrogen bonds (symbol H) with water molecules (Simpson 1980). Hemicellulos contains most sorption sites, followed by cellulose and lignin (Engelund et al. 2013). The sigmoidal curves describing ad- and desorption in the hygroscopic range can be divided into three sections, which give an indication in which manner the moisture resides in the microstructure of wood. Assuming a wetting process, the first section represents monolayer adsorption into the cell wall, followed by multilayer adsorption in the second section. Here, monolayer indicates that the absorbed molecules are in direct contact with the wood constituent, and multilayer indicates the formation of more than one layer of molecules, which are not all in direct contact with the wood constituent. Traditionally, the third section is assigned to the condensation of capillary water, which should be completed at RH-levels between 60 and 70% (Bratasz et al. 2012; Kollmann and Côté 1968). However, Thygesen et al. (2010) and Engelund et al. (2010) indicate that below 99.5% RH no capillary water is present in the lumen of softwoods, and that the upward bend of the boundary curves characterising the third section is caused by softening of hemicellulose, which creates more room for water molecules to enter the cell wall.

Upon cyclic ambient climatic conditions, the EMC follows a unique path between the border isotherms characterising the sorption isotherm that is dependent on the previously experienced moisture content change. This creates so-called intermediate or scanning curves (Frandsen 2007; Time 2002b). The curves develop with a unique path in desorption and adsorption. The sorption isotherm is affected by mechanical stress, where compression stress reduces sorption (lowers EMC) and tensile stress increases sorption (heightens EMC) (Skaar 1988).

2.2.4 Moisture transport models

The most traditional way to simulate moisture transport is with a single-Fickian model (Fick 1995), see Eq. (1), which can be used to describe moisture transport both above and below FSP on macroscopic scale. Fick's law assumes an instantaneous equilibrium between RH in the lumen and the bound water in the cell wall.

$$c_w \rho \frac{\partial w}{\partial t} + \nabla \cdot \boldsymbol{q} = 0 \qquad (1)$$

$$\overline{\boldsymbol{q}} = -\overline{\boldsymbol{D}}(w,T)\overline{\nabla}w \qquad (2)$$

In Eq. (1), c_w is the moisture capacity, ρ is the density of liquid moisture, w is the moisture content, t is time, and ∇ is the divergence. The dot ($\cdot$) denotes the operation where the components of ∇ are applied to $\boldsymbol{q}$ and summated. Fick's first law describes the moisture flux $\overline{\boldsymbol{q}}$ according to Eq. (2), where T is the temperature,

D is a w and T dependent diffusion matrix (Avramidis et al. 1987), and ($\bullet$) indicates the orthotropic material direction.

More accurate from a physics standpoint are the multi-Fickian models (Autengruber et al. 2020; Eitelberger et al. 2011; Eriksson et al. 2007; Fortino et al. 2021; Frandsen et al. 2007; Johannesson et al. 2009; Konopka and Kaliske 2018; Svensson et al. 2011) and the multi-phase moisture transport models (Alexandersson et al. 2016; Di Blasi 1997; Fortino et al. 2013; Janssen et al. 2007; Krabbenhøft et al. 2004; Mmari et al. 2020; Pang et al. 1995; Perré et al. 1999; Younsi et al. 2007). The multi-Fickian models use separate equations to describe each moisture phase and a coupling term to describe the sorption rate between phases. In its most simplest and popular form, the moisture transport below FSP is described according to Eq. (3)

$$
\begin{aligned}
\frac{\partial c_b}{\partial t} + \boldsymbol{\nabla} \cdot (-\boldsymbol{D}_b(w,T)\boldsymbol{\nabla}c_b) &= \dot{c} \\
\frac{\partial c_v}{\partial t} + \boldsymbol{\nabla} \cdot (-\boldsymbol{D}_v(w,T)\boldsymbol{\nabla}c_v) &= -\dot{c}
\end{aligned}
\tag{3}
$$

where, c_b is the bound water concentration, c_v is the concentration of water vapour, $\dot{c}$ is the sorption rate, $\boldsymbol{D}_b$ is the w and T dependent bound water diffusion matrix, and $\boldsymbol{D}_v$ is the w and T dependent vapour diffusion matrix. To describe the flux normal to the boundary surface q_n, the single and multi-Fickian models are often combined with the Neumann boundary condition presented by Eq. (4)

$$
q_n = s(w,T)(w - w_\infty)
\tag{4}
$$

where, s is a w and T dependent surface emission coefficient (Yeo et al. 2002) and w_∞ the moisture content of the ambient air.

Compared to the multi-Fickian model, the single-Fickian model is simpler to implement and only requires the definition of one diffusion matrix and a surface emission coefficient, of which w and T dependent experimental data are available (Avramidis and Siau 1987; Rosenkilde 2002; Siau et al. 1996; Yeo et al. 2002). However, it is not uncommon to use this model in conjunction with constant values of D and s, or only with D dependent on w and T (Angst-Nicollier 2012; Konopka and Kaliske 2018). Based on sorption curves (fractional weight increase versus $\sqrt{\text{time}}$) obtained for different volumes of specific wood species at 23℃, Wadsö (1993) concludes that the linear form (without w dependent D) of Fick's law of diffusion can only be applied for situations below 75% RH. Above this level of RH, non-Fickian processes become prominent, which are not only governed by Fick's law of diffusion, but possibly also by thickness of specimens, surface (boundary layer) resistance and sorption processes.

In Frandsen et al. (2007), the sorption curves from Wadsö (1993) are used to produce moisture content profiles using a multi-Fickian model. A good agreement

is seen between simulation data and experimental data. However, the sorption curves do not provide a validation of the moisture gradients ∇w experienced just below the exchange surface. Since the hygro-mechanical behaviour of wood is dependent on these gradients, it is recommended to validate these moisture content profiles with experimentally obtained moisture profiles, such as presented in Samuelsson and Arfvidsson (1994) and Rosenkilde (2002).

In Konopka and Kaliske (2018), a comparison is made between results obtained with a hygro-mechanical analysis using a single-Fickian and a multi-Fickian analysis as input data. The moisture transport models are validated using the simulated moisture content profiles generated by Frandsen et al. (2007) with the previously describes procedure based on sorption curves. The results obtained with the single-Fickian model, which uses a w dependent D and a constant s, show an accurate drying speed between 54 and 75% RH, but a medium fit to the surface moisture gradients. The study concludes that s has a strong effect on ∇w, and that the overestimation of ∇w leads to an overestimation of certain stress components. Therefore, Konopka and Kaliske (2018) recommend their version of the single-Fickian model to be used only on thin bodies, small or slow RH-changes, low RH spectra below 65% and high ratios between s and D, which should help minimize moisture gradients.

It is not uncommon to describe sorption in wood by using the average sorption isotherm and neglect the effect of hysteresis (Salin 2011). Unfortunately, this approach affects the expected moisture gradients and rate of moisture change, which are important in the description of hygro-mechanical behaviour (Frandsen et al. 2007; Time 2002b). The independent domain model (Everett et al. 1952) is the most traditional model to describe hysteresis and the associated scanning behaviour, and was first applied to wood by Peralta (1995). Unfortunately, this model is not user friendly due to the double integral that needs to be solved to obtain EMC (Frandsen 2007; Shi et al. 2017b). The most popular hysteresis model in the field of hygroscopic computational research is the one by Frandsen et al. (2007). The model can be used in conjunction with the multi-Fickian model in the location of the coupling term $\dot{c}$, which expresses the sorption rate.

2.2.5   Surface and diffusion coefficient

Both the diffusion coefficient D and surface emission coefficient s have a dependency on w and T (Avramidis and Siau 1987; Kollmann and Côté 1968; Yeo et al. 2008), which makes the moisture transport analysis nonlinear. The diffusion coefficient increases with w and T, where the surface emission coefficient increases with T and decreases with w (Avramidis and Siau 1987). One anomaly is D related to the longitudinal material direction l, which is constant with changing moisture content (Rosenkilde 2002). In **Fig. 2-3** a collection is given of the experimental data available in literature that covers the w and T dependent D_l, D_r, D_t and s. The data is a mixture of sapwood and heartwood specimens, and a combination of wood species Eastern white pine (Yeo et al. 2008), Scots pine (Rosenkilde 2002) and

Western white pine (Avramidis and Siau 1987). To the authors knowledge there is no complete set of w and T dependent D and s available for Norway spruce or any other species for that matter.
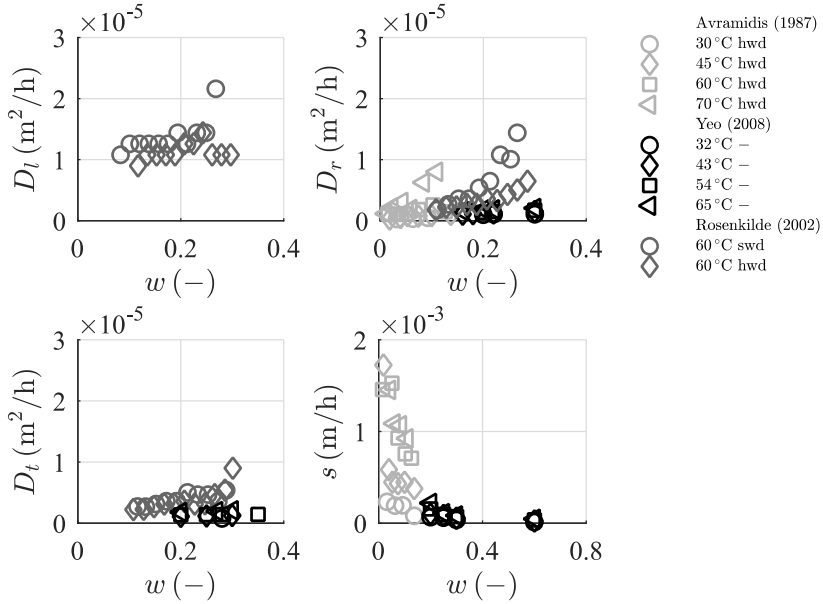
Fig. 2-3: *Moisture- w and temperature- T dependent longitudinal l, radial r, and tangential t diffusion coefficient D and surface emission coefficient s from different literary sources, where* hwd *refers to heartwood and* swd *refers to sapwood*

2.3 Hygro-mechanical behaviour

2.3.1 Background

The hygro-mechanical and visco-elastic behaviour of wood is a complex phenomenon and generally considered as a combined effort of the elastic, hygro-expansion, creep and mechano-sorptive behaviour. In absence of knots and other irregularities, the total behaviour in the three-dimensional plane is mostly affected by the time, the moisture gradients, the material orientation, and the variation in material properties due to the radial position with the cross-section of a log or climate.

2.3.1.1 Creep

Rheology is the study of time-dependent behaviour of materials (Bodig and Jayne 1982). In wood, such time-dependent behaviour is observed as creep, which can be analysed under constant mechanical load, moisture content and temperature by

subtracting the initial elastic deformation or strain. The magnitude of creep depends on the alignment of the orthotropic axes, the magnitude and type of stress, the rate and/or duration of load, moisture content and temperature (Bodig and Jayne 1982). The phenomenon is particularly interesting in the analysis of long-term behaviour of beams, and can experience three different phases characterised by the rate of deflection: 1) the decreasing deflection rate phase, 2) the constant deflection rate phase, and 3) the increasing deflection rate phase (Bodig and Jayne 1982). Creep develops faster at higher moisture content and higher temperature (Engelund et al. 2012; Holzer et al. 1988; Wu et al. 1994).

2.3.1.2   Hygro-expansion

Hygro-expansion refers to the hygroscopic shrinkage and swelling of the material, when water leaves or enters the cell wall, respectively. In case of swelling, the water will take up space between the so-called cellulose micro fibrils (a component that makes up certain cell wall layers), and will therewith push the entities apart (Engelund et al. 2013). The amount of hygro-expansion that will be experienced is dependent on the amount of water gained or lost, the material orientation (longitudinal, radial or tangential), the wood species and the drying stress caused by moisture gradients (Skaar 1988). In Hunt et al. (1988), it is mentioned that the hygro-expansion coefficient related to the longitudinal material direction α_l is less with tensile strain and more with compressive strain, then when unloaded.

2.3.1.3   Mechano-sorption

Mechano-sorption is the additional deformation observed when wood is exposed to both stress and moisture content change below the FSP, which cannot be explained by a simple superposition of elastic behaviour, hygro-expansion and creep (Muszyński et al. 2005). The stress can either be generated by a mechanical load or by internal constraints caused by differences in hygro-expansion or moisture gradients. The magnitude of mechano-sorption depends on the alignment of the orthotropic axes, the magnitude and type of stress, temperature and moisture content change (Ranta-Maunus 1975; Rybarczyk 1973). Analogue to what is observed for creep, the deformations may experience three phases when subjected to high load-levels (load divided by ultimate strength) and numerous moisture cycles: 1) a decreasing deflection rate phase, 2) a constant deflection rate phase, and 3) an increasing deflection rate phase that potentially can lead to failure (Armstrong et al. 1961; Hearmon et al. 1964; Hunt 1989; Hunt 1999). Mechano-sorption is said to be non-symmetrical in tension and compression, although the final magnitude appears to be similar (Morlier 1994).

2.3.2   Hygro-mechanical models

For wood in bending and exposed to varying climate, it was found that 50% of the ultimate stress in green-state is an approximate limit of the hygro-mechanical and visco-elastic behaviour to enter the increasing deflection rate phase (Hunt 1989).

Under normal service conditions (Porteous et al. 2007), the stress level rarely exceeds this 50% (Dinwoodie 1981), and only a decreasing and constant deflection rate phase is experienced. In this range, the most common method to describe the total strain rate $\dot{\bar{\varepsilon}}$ ($-$) of wood is by the sum of four components

$$\dot{\bar{\varepsilon}} = \dot{\bar{\varepsilon}}_e + \dot{\bar{\varepsilon}}_h + \dot{\bar{\varepsilon}}_c + \dot{\bar{\varepsilon}}_{ms} \qquad (5)$$

where, $\dot{\bar{\varepsilon}}_e$ is the elastic strain rate, $\dot{\bar{\varepsilon}}_h$ is the strain rate caused by hygro-expansion, $\dot{\bar{\varepsilon}}_c$ is the creep strain rate, $\dot{\bar{\varepsilon}}_{ms}$ is the mechano-sorption strain rate, ($\dot{\cdot}$) relates to the rate of change, and ($\bar{\cdot}$) indicates the orthotropic material direction. Each strain component is described with a unique equation, which will be discussed in the next subsections.

2.3.2.1 Elastic

The elastic response of wood relates to the recoverable part of deformation after unloading and can be modelled by Hooke's law

$$\dot{\bar{\varepsilon}}_e = \dot{\bar{\varepsilon}}_{e,1} + \dot{\bar{\varepsilon}}_{e,2} = \overline{C}(w,T)\dot{\bar{\sigma}} + \dot{\overline{C}}(w,T)\bar{\sigma} \qquad (6)$$

where, C is the compliance matrix and holds the reciprocal of the elastic and shear moduli in three-dimensional plane, and σ is stress. The size of the elastic and shear moduli depends on w and T (Gerhards 1982).

2.3.2.2 Hygro-expansion

The most commonly used expression to describe hygro-expansion is a linear relation between the hygro-expansion coefficient and the moisture content rate

$$\dot{\bar{\varepsilon}}_h = \boldsymbol{\alpha}\dot{w}_a \qquad (7)$$

where, $\boldsymbol{\alpha}$ is a matrix that contains the hygro-expansion coefficients in the main orthotropic directions l, r and t, and $\dot{w}_a$ is the moisture content rate below FSP.

2.3.2.3 Creep

The available creep models can be divided into 1) the equation of state formulation and 2) the hereditary, or integral-type formulation (Holzer et al. 1988). In the field of wood science, the hereditary is most popular, which relates the response of the material to the entire stress history (Dahlblom 1987; Ormarsson 1999; Schniewind et al. 1972; Toratti 1992). The response of the material to different loading histories is solved by means of the Boltzmann superposition principle (Ottosen et al. 2005). An example of a hereditary model that can describe the increasing and constant deflection rate phases is

$$\dot{\bar{\boldsymbol{\varepsilon}}}_c = \sum_{k=1}^{K} \frac{1}{\tau_k} e^{-\frac{t}{\tau_k}} \int_0^t e^{\frac{t'}{\tau_k}} \, \overline{\boldsymbol{C}}_{c_k}(w,T) \frac{\mathrm{d}\overline{\boldsymbol{\sigma}}(t')}{\mathrm{d}t'} \, \mathrm{d}t' \qquad (8)$$

where τ_k is the so-called retardation time, t is the total time, t' is the time corresponding to a recent stress change $\Delta\boldsymbol{\sigma}$, and $\boldsymbol{C}_{c_k}$ is the creep compliance matrix (Dahlblom 1987; Ormarsson et al. 2010). $\boldsymbol{C}_{c_k}$ holds $\boldsymbol{C}$, which is scaled with a creep parameter ϕ_σ^k. The equation results in a series-coupled Kelvin model with K-amount of modules that can be studied in more detail in, e.g. Dahlblom (1987) or Ottosen and Ristinmaa (2005).

2.3.2.4   Mechano-sorption

A summary of available mechano-sorption models can be found in Toratti (1992) and Hanhijärvi (2000). The earliest and most conventional model, suitable to be used in conjunction with FEM, is the so-called constant slope model (Ranta-Maunus 1975; Rybarczyk 1973). This model can adequately describe the effects due to continuous drying. The model was extended by Salin (1992) and Yahiaoui (1991), to be able to describe the decreasing and constant deflection rate phases seen under moderate stress-levels and changing climate. In the three-dimensional plane, this model describe the mechano-sorption strain rate as

$$\dot{\bar{\boldsymbol{\varepsilon}}}_{ms} = \bar{\boldsymbol{m}}(T)(\overline{\boldsymbol{\sigma}} - \overline{\boldsymbol{n}}\bar{\boldsymbol{\varepsilon}}_{ms})|\dot{w}_a| \qquad (9)$$

where, $\boldsymbol{m}$ is the mechano-sorption property matrix and $\boldsymbol{n}$ is the retardation matrix (Ormarsson et al. 1998). The mechano-sorption moduli of wood are temperature dependent (Carlsson et al. 1975; Castera 1989).

3 Methodology

3.1 General approach

To fulfil the main aim in this doctoral thesis, four different methods are used: 1) FEM, 2) an analytical method, 3) a long-term four-point bending test performed on small-clear wood specimens subjected to a constant temperature of 60℃ and a RH between 40% and 80%, and 4) an additional long-term four-point bending test for timber beams exposed to Northern European climate (between -2℃ and 20℃, and between 50% and 90% RH).
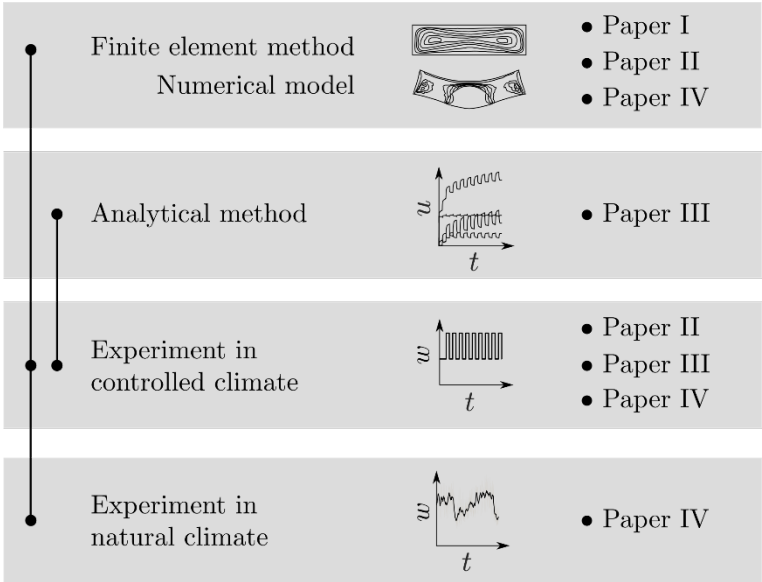

Fig. 3-1: *Relationship between different methods and papers used in this doctoral thesis*

In **Fig. 3-1**, the relationship between the different methods is illustrated and their connection to each individual paper. The main method adopted in this thesis is FEM, which is used to create the numerical model. The four-point bending test subjected to controlled climate and natural climate are used to calibrate and validate, subsequently, the numerical model. The analytical method is developed to assess the deflection data obtained in the constant moment area of the four-point bending tests conducted in controlled climate before the calibration of the numerical model. In the following paragraph each method will be elaborated on.

3.2   Finite Element Method

The developed three-dimensional numerical model consists of a transient nonlinear moisture flow analysis and a moisture-induced distortion or stress analysis based on FEM; see **Fig. 3-2**. Both models use the same geometry and orthotropic material orientation. The system of equations is solved with a sequential solution scheme, where the nodal based moisture content output from the moisture flow model is used as input to the distortion model. This paragraph covers the discussion of theory, input parameters, and boundary conditions for both models with respect to different applications. In addition, the function of user-subroutines UMATHT, UMAT and ORIENT are presented, together with their position in the numerical solution.
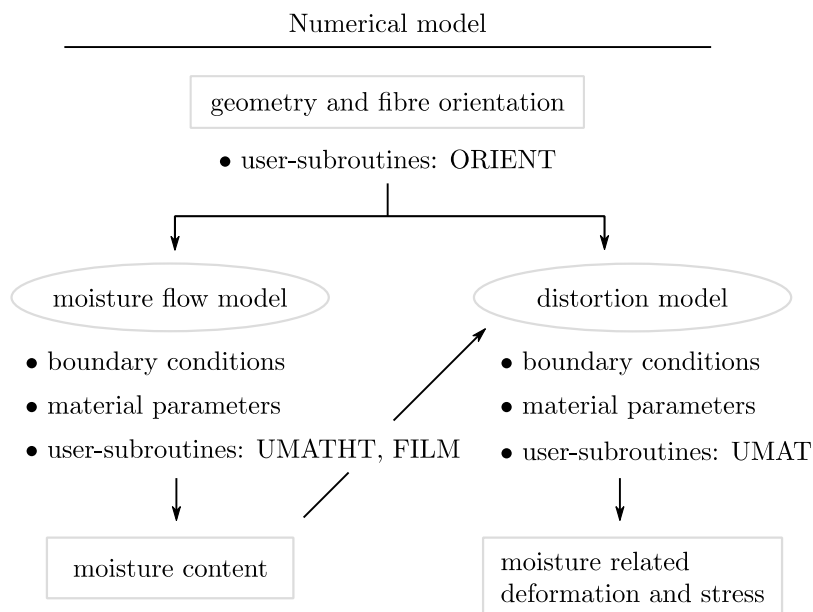
Fig. 3-2: *The principle components of the numerical model (Paper IV)*

3.2.1 Moisture flow model

The orthotropic nonlinear transient moisture flow in wood is analysed with a single-Fickian approach as presented by Eq. (1) and (2) combined with the Neumann boundary condition presented by Eq. (4). The procedure to derive the FE-formulation can be found in Ottosen et al. (1992) and Johannesson (2019). The derived form can be found in Paper I.

3.2.1.1 Numerical solution

To iteratively solve the nonlinear system of equations within a given increment Δt, the FE-program uses the Newton-Raphson method (Dassault Systèmes 2017b); see **Fig. 3-3**.
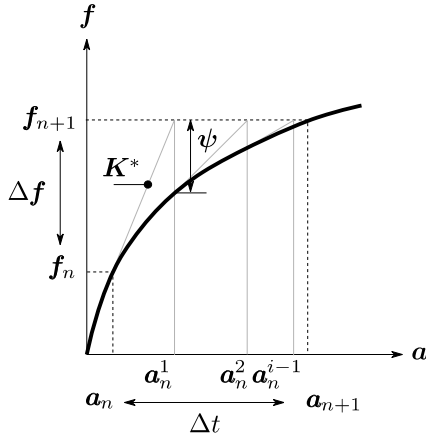

Fig. 3-3: Schematisation of the Newton Raphson iteration procedure

For each iteration, the state at $i-1$ is known, and the method updates the Jacobian (or tangent diffusion matrix) $\boldsymbol{K}^*$ and the out-of-balance force $\boldsymbol{f}^*$ to determine the state at i as

$$\boldsymbol{K}^* \boldsymbol{a}_{n+1}^i = \boldsymbol{f}^* \tag{10}$$

$$\boldsymbol{K}^* = \left(\frac{\partial \boldsymbol{\psi}^{i-1}}{\partial \boldsymbol{a}_{n+1}^{i-1}}\right) = \frac{\boldsymbol{C}_w^{i-1}}{\Delta t} + \widetilde{\boldsymbol{C}}_w^{i-1} + \boldsymbol{K}^{i-1} + \widetilde{\boldsymbol{K}}^{i-1} + \boldsymbol{K}_c^{i-1} \\ + \widetilde{\boldsymbol{K}}_c^{i-1} - \widetilde{\boldsymbol{F}}_b^{i-1} \tag{11}$$

$$\boldsymbol{f}^* = -\boldsymbol{\psi}^{i-1} + \boldsymbol{K}^* \boldsymbol{a}_{n+1}^{i-1} \tag{12}$$

where, $\boldsymbol{\psi}$ is the residual vector for each element, $\boldsymbol{a}$ is a nodal point vector containing the moisture content, $(\bullet)_{n+1}$ denotes the value of the quantity at the current time step, and $(\bullet)_n$ the value at the previous known time step at equilibrium. The different components that make up $\boldsymbol{K}^*$ can be described as

$$C_w^{i-1} = \int_V N^T c_w \rho N \, \mathrm{d}V \tag{13}$$

$$\widetilde{C}_w^{i-1} = \int_V N^\mathrm{T} \frac{\partial c_w}{\partial w} \rho N(a_{n+1}^{i-1} - a_n) N \, \mathrm{d}V \tag{14}$$

$$K^{i-1} = \int_V B^T D B \mathrm{d}V \tag{15}$$

$$\widetilde{K}^{i-1} = \int_V B^\mathrm{T} \frac{\partial D}{\partial w} B a_{n+1}^{i-1} N \mathrm{d}V \tag{16}$$

$$K_c^{i-1} = \int_A N^\mathrm{T} s N \mathrm{d}A \tag{17}$$

$$\widetilde{K}_c^{i-1} = \int_A N^\mathrm{T} \frac{\partial s}{\partial w} N a_{n+1}^{i-1} N \mathrm{d}A \tag{18}$$

$$\widetilde{F}_b^{i-1} = \int_A N^\mathrm{T} \frac{\partial s}{\partial w} w_\infty N \mathrm{d}A \tag{19}$$

where, V and A indicate volume and surface, respectively, N is the shape function vector and $B = \nabla N$. A more detailed introduction of the residual vector ψ can be found in Paper II. More information on how to derive the residual and the Newton Raphson method can be read in Ottosen and Ristinmaa (2005) and Johannesson (2019).

3.2.1.2   Material parameters

Between the different papers, a variety of sets containing w and T dependent D and s are obtained. Values related to a temperature of 60℃ are collected in **Fig. 3-4**. The material parameters related to Paper I and II are obtained with a fit made to moisture content profiles created by Rosenkilde (2002) using the standard moisture flow analysis provided by the FE-program (Paper I-I and Paper I-II) and the user-subroutines (Paper II-I), respectively. In Paper II, and referred to as Paper II-II in **Fig. 3-4**, an additional set of parameters were determined with a fit made to the volumetric average moisture content from a matched unloaded specimen that is part of the four-point bending test performed in controlled climate. In Paper IV, to widen the application field of the numerical model, exponential equations were established that can describe the w and T dependency of s and D in a temperature range of −10 and 70℃ and a moisture content range of 0 to 30% based on data from the literature; see **Fig. 2-3** and see Eq. (20) to (22). An exception is D related to the longitudinal material direction l, which has no dependency on w (Rosenkilde 2002), but does exponentially depend on T, see Eq. (20).
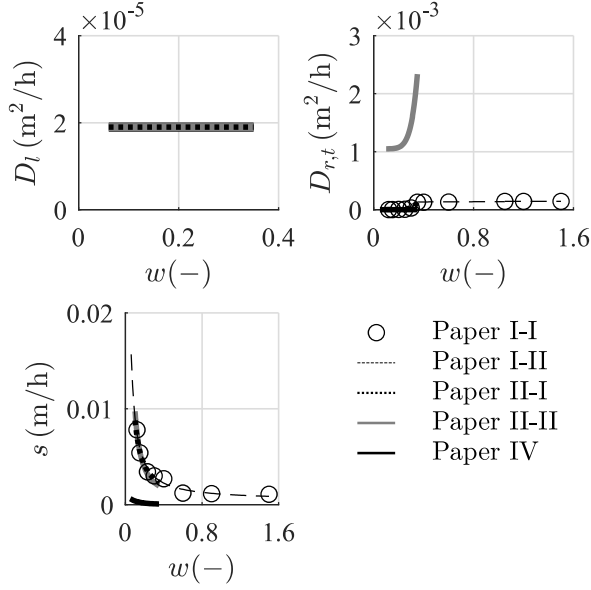
Fig. 3-4: Longitudinal l, radial r and tangential t diffusion coefficient D and surface emission coefficient s collected from the different papers that are part of this doctoral thesis. The curves show the variation the coefficients experience with respect to moisture, and are related to a constant temperature of $60°C$

In Eq. (20) to (22), the parameters indicated by w_1 to w_3 describe the relation of D and s to w, and by T_1 and T_2 describe the relation of D and s to T. The values found with a fit made to experimental data provided by Avramidis and Siau (1987), Rosenkilde (2002) and Yeo et al. (2008) are collected in **Table 3-1**.

$$D_l(w,T) = D_{w1} \cdot (D_{T1}e^{D_{T2}T}) \tag{20}$$
$$D_{r,t}(w,T) = (D_{w1}e^{-D_{w2}w} + D_{w3}) \cdot (D_{T1}e^{D_{T2}T}) \tag{21}$$
$$s(w,T) = (s_{w1}e^{-s_{w2}w} + s_{w3}) \cdot (s_{T1}e^{s_{T2}T}) \tag{22}$$

Table 3-1: Variables used to describe the moisture- w and temperature- T dependency of the surface emission s and diffusion D coefficient below FSP in combination with Eq. (20) to (22) (Paper II)

	Moisture			**Temperature**	
	$(\bullet)_{w1}$	$(\bullet)_{w2}$	$(\bullet)_{w3}$	$(\bullet)_{T1}$	$(\bullet)_{T2}$
$D_{r,t}$	1.7×10^{-9}	11	9.3×10^{-13}	8	0.07
D_l	2.7×10^{-8}			8	0.07
s	2.1×10^{-4}	13	4.5×10^{-6}	0.9	0.04

3.2.1.3   Initial moisture content

In Paper I, a polynomial expression, see Eq. (23), is used to add the green-state moisture content w_{gs} as an initial state to the analysis. This expression, visualised in **Fig. 3-5a**, is obtained with a fit made to experimental data (Larsen 2013). Four timber boards, each obtained with a different saw cut, are analysed, see **Fig. 3-5b** to **e**, which experience a moisture content of 28.4% at the pith and a moisture content between 105% and 190% just below the exchange surface. The details of the fit, and how the expression is incorporated into the FE-analysis, can be found in Paper I.

$$
\begin{aligned}
w_{gs}(x,y) = {} & 0.434 - 5.3e^{-3}x - 3.87e^{-16}y + 69.56x^2 - 1.29e^{-14}xy \\
& + 69.55y^2 + 0.119x^3 + 3.5e^{-16}x^2y + 9.89e^{-2}xy^2 \\
& - 2.78e^{-17}y^3 - 748.1x^4 + 2.86e^{-13}x^3y - 1496x^2y^2 \\
& + 2.7e^{13}xy^3 - 747.9y^4
\end{aligned}
\tag{23}
$$

In Paper II and IV, a uniform initial moisture content of 7.35% and 16%, respectively, is assigned to the geometries.

3.2.1.4   Neumann boundary condition

In each application, the Neumann boundary condition presented by Eq. (4) is used. In Paper I, a constant moisture content of 10% is used for w_∞. In Paper II and IV, a heuristic approach is developed to describe w_∞. In Paper II, w_∞ in ad- (ad) and desorption (de) for each RH-phase are described by Eq. (24) and (25) (Johannesson 2019), where ϕ is the RH, w_f is the FSP, and the values for a and b obtained in Paper II are collected in **Table 3-2**. The expressions describe both sorption hysteresis and associated scanning behaviour.

$$
w_\infty^{ad} = \frac{a \cdot \phi^{0.4} + b \cdot \phi^5}{5} \cdot w_f
\tag{24}
$$

$$
w_\infty^{de} = \left(\frac{a \cdot \phi^{0.4} + b \cdot \phi^5}{6} + 0.08 \cdot \sin(\pi \cdot \phi) \right) \cdot w_f
\tag{25}
$$

Table 3-2: *Variables used to describe the scanning curves in adsorption (ad) and desorption (de) with Eq. (24) and (25) related to an FSP w_f of 0.27 (−) (Paper II)*

cycle		1	2	3	4	5	6	7	8	9
ad	a	2.033	2.063	2.062	2.058	2.056	2.047	2.047	2.040	2.020
	b	1.530	1.255	1.073	1.000	1.015	0.995	0.991	0.945	0.945
de	a	1.797	1.798	1.794	1.793	1.782	1.783	1.775	1.747	
	b	2.774	2.535	2.325	2.225	2.270	2.215	2.225	2.228	
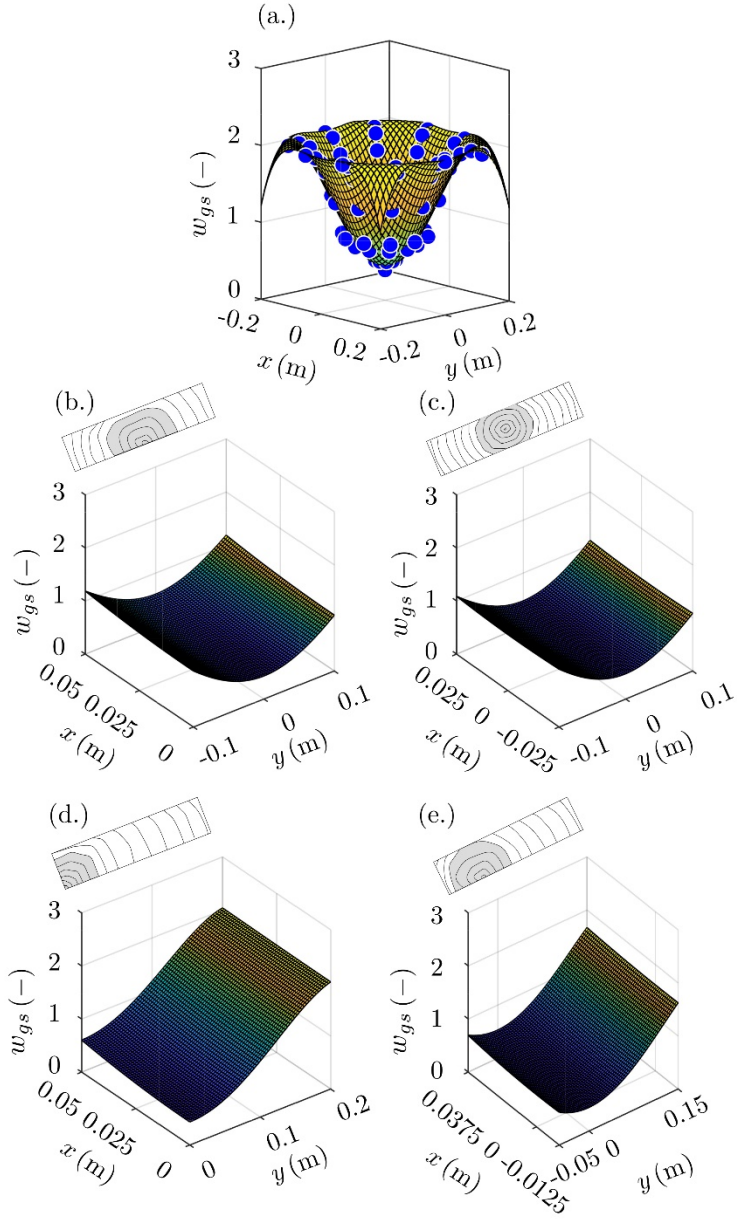
Fig. 3-5: *Green-state moisture content w_{gs} for (a.) a cross section of a log based on a fit made to experimental data (blue scatter) (Larsen 2013) to obtain Eq. (23), and (b. to e.) different configurations of timber boards, B_1 to B_4 (Paper I)*

27

In Paper IV, Simpson's formula (Simpson 1971) is used to describe w_∞ based on T and ϕ recorded in a testing facility in Asa Research Park; see Eq. (26) to (30). Here, W, K, K_1 and K_2 are parameters that depend on temperature.

$$w_\infty = \frac{1800}{W}\left[\frac{K\phi}{1 - K\phi} + \frac{K_1 K\phi + 2K_1 K_2 K^2 \phi^2}{1 + K_1 K\phi + K_1 K_2 K^2 \phi^2}\right] \tag{26}$$

$$W = 349 + 1.29T + 0.0135T^2 \tag{27}$$

$$K = 0.805 + 0.000736T - 0.00000273T^2 \tag{28}$$

$$K_1 = 6.27 - 0.00938T - 0.000303T^2 \tag{29}$$

$$K_2 = 1.91 + 0.0407T - 0.000293T^2 \tag{30}$$

3.2.2   Moisture induced distortion model

3.2.2.1   Theory

The moisture-induced stress and distortion is described according to Eq. (5) to (9). The time integral that is part of the creep strain rate described by Eq. (9) is solved with the Trapezoidal rule (Ottosen and Ristinmaa 2005). A detailed description of each material model and the FE-formulation can be found in Ormarsson (1999).

3.2.2.2   Material parameters

Each application uses a unique set of material parameters to run the distortion analysis. The set of hygro-mechanical material parameters used in Paper I come directly from Ormarsson (1999). In Paper IV, a collection of different sources is used to create a set of material parameters that cover hygro-expansion, and the elastic, creep and mechano-sorption behaviour in the primary material directions r and t, and the shear planes lr, lt and rt. The parameters in the l-direction are obtained with the calibration (with and without θ) that is part of the second application; see **Fig. 3-7**. The same set is used in Paper IV to validate the solid timber beams subjected to natural climate, with small adjustments made to the elastic and mechano-sorption material parameters related to the l-direction.
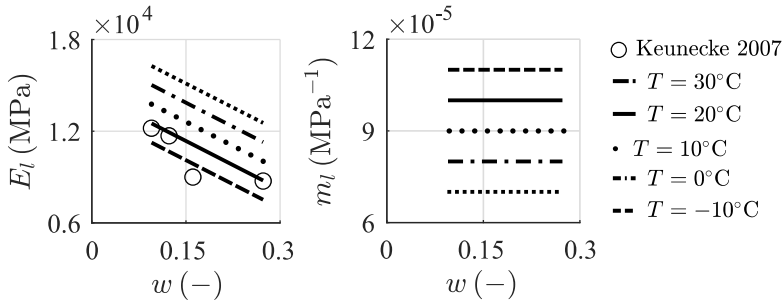

Fig. 3-6: *Description of the longitudinal elastic modulus E_l and longitudinal mechano-sorptive parameter m_l with respect to moisture w and/or temperature T (Paper IV)*

To incorporate the moisture and temperature dependency of material parameters in Paper I and IV, linear expressions are used (Ormarsson et al. 1998). In **Fig. 3-6**, the expressions used to describe the elastic and mechano-sorption moduli are plotted in the temperature range $-10°C$ to $30°C$ and moisture content range 10% to 27% relevant for the timber beams in Paper IV. Here, the w dependency of E_l is calibrated based on experimental data by Keunecke et al. (2007).
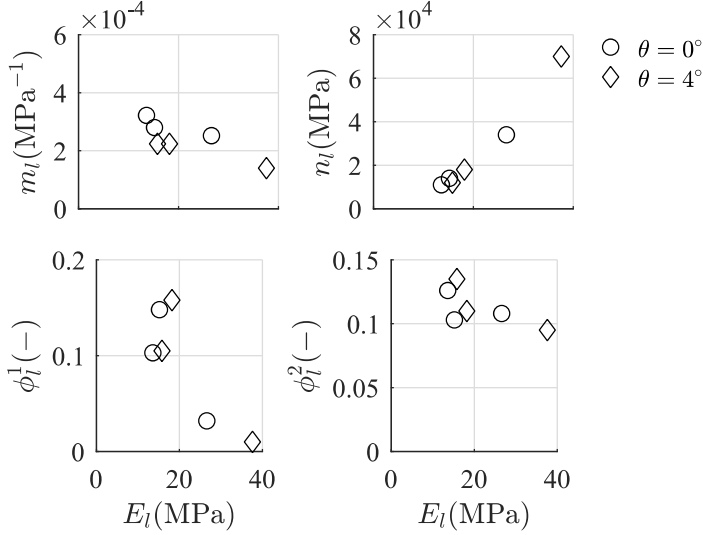
Fig. 3-7: *Longitudinal elastic modulus E_l, mechano-sorptive parameter m_l and creep parameters ϕ_l^k obtained with the calibration that is part of the second application (Paper IV)*

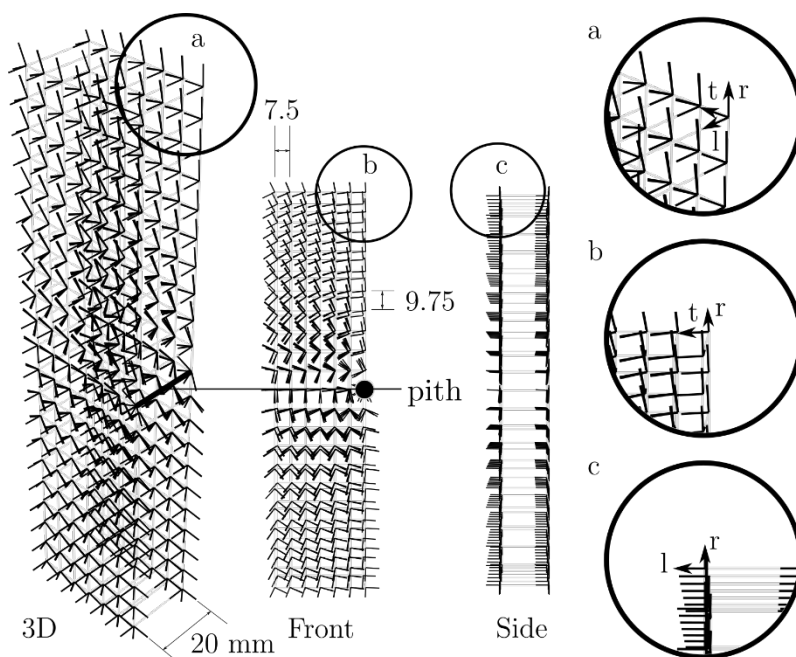### 3.2.3   Material orientation

The fibre orientation of wood is incorporated into the numerical analysis by defining the location of the pith, the conical angle and spiral grain angle inside the user- subroutine that is used to describe the material orientation. In Paper I, the pith of the four timber boards is uniquely defined within the cross-section to create a specific annual ring pattern for each board. In Paper II and IV, the centre of the clear-wood beam's cross-section is located 137.5 mm from pith, which leads to a slight annual ring curvature in the cross-section of the beam. Each beam also has a positive spiral grain angle θ of 4°. The solid timber beams treated in Paper IV have the pith located within the cross- section as indicated in **Fig. 3-8**. The variation over the cross-section in θ is assumed to follow $4 - 40r$, where r is the distance from pith to the point in the cross-section where θ is analysed (Ormarsson 1999). The conical angle of the tree is assumed to be $-0.5°$.

3.2.4 User-subroutines in Abaqus FEA®

3.2.4.1 Background

FE-software Abaqus FAE® provides a large number of user-subroutines with unique frameworks that can manage external databases, initial conditions (pore pressure, moisture content), constitutive relations or boundary conditions to a model, or allow reading data from restricted databases (Dassault Systèmes 2017a). Some examples of such routines are available (Dassault Systèmes 2007), and written in programming language FORTRAN® (The Fortran Company, Colorado, USA), but most need to be built from scratch.

The numerical model presented in this doctoral thesis consists of four different user-subroutines: FILM, ORIENT, UMAT and UMATHT. The boundary condition subroutine FILM can be used to describe s and w_∞ as part of the Neumann boundary condition presented by Eq. (4). The material orientation routine ORIENT allows for a unique description of fibre orientation (spiral grain, conical shape and annual ring curvature) (Ormarsson et al. 1998); see **Fig. 3-8**. Material routines UMAT and UMATHT are used to describe the constitutive behaviour related to the distortion and moisture flow model, respectively. For more details on the user-subroutines, Paper II and IV can be considered.

Fig. 3-8: *Three-dimensional local material orientation of a fragment of a solid timber beam, where details a, b and c highlight the principle material axes l, r and t (Paper IV)*

3.2.4.2   Numerical implementation

The Newton Raphson method is used by the FE-program as the default numerical technique to solve the set of equilibrium equations of both the moisture transport and moisture-induced distortion analysis (Dassault Systèmes 2017b). **Fig. 3-9** gives an overview of the followed numerical procedure, and the position of the user-subroutines within this procedure. In the current context, the step mentioned in **Fig. 3-9** refers to either the moisture flow analysis or the moisture-induced distortion analysis. User-subroutine ORIENT is called at the start of the analysis at each material point that makes up the wood's geometry. The subroutines UMAT, UMATHT and FILM provide results at the beginning and at the end of each time increment Δt. Nevertheless, the FE-program enters these routines with each iteration i. When assigned to the entire domain, *i.e.* wood geometry, the material routines UMAT and UMATHT are called for each Gauss integration point for each mesh element. By assigning subroutine FILM to the necessary surfaces, it is able to find the mesh elements that correspond to the boundary condition.
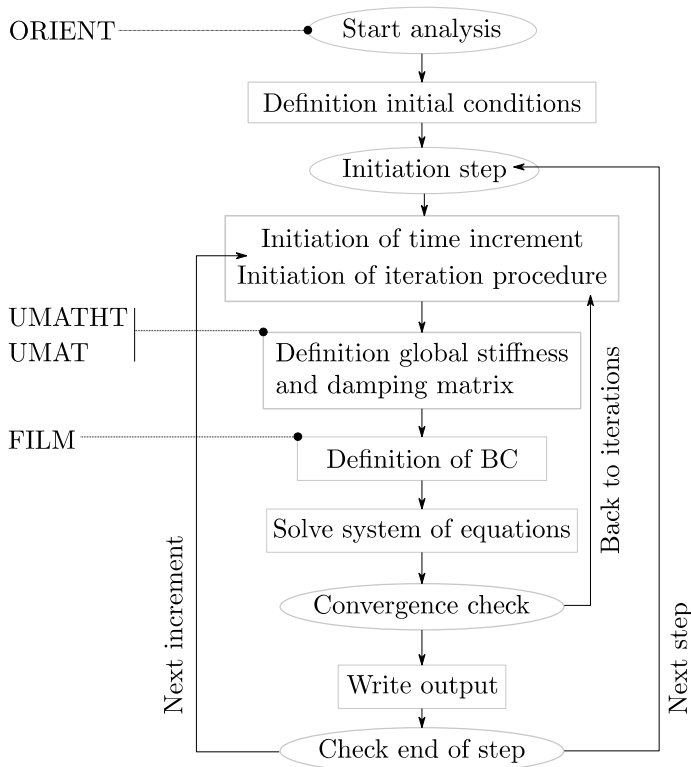
Fig. 3-9: *General overview Newton-Raphson procedure FE-program*

Fig. 3-10 gives a more detailed description of the iteration process for the uncoupled moisture flow and moisture induced distortion analysis. The figure describes which variables are estimated by the user-subroutines and which need to be defined by the user inside the user-subroutines. A general difference between subroutines FILM, UMATHT and UMAT is the definition of the Jacobian. Inside UMATHT and FILM, the user defines a specific set of expressions (see **Fig. 3-10** and compare with section 3.2.1.1), which are then taken by the FE-program to determine $\boldsymbol{\psi}$ and $\boldsymbol{K}^*$. On the contrary, inside routine UMAT the user is specifically requested to define the entire Jacobian (see $\partial\Delta\bar{\boldsymbol{\sigma}}/\partial\Delta\bar{\boldsymbol{\varepsilon}}$ in **Fig. 3-10**). More details on the numerical implementation of the moisture flow analysis can be found in Paper II. More about the numerical implementation of the distortion analysis can be found in Santaoja et al. (1991) and Ormarsson (1999).
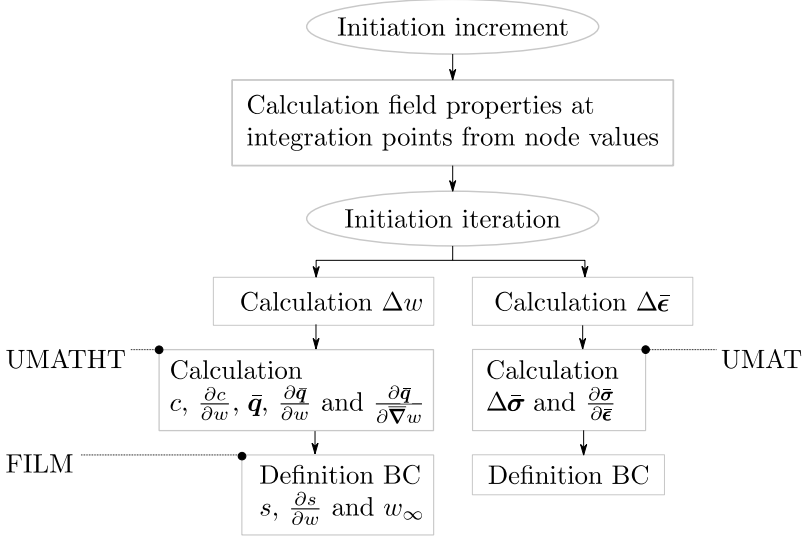
Fig. 3-10: Newton-Raphson iteration procedure for the sequential moisture and distortion analysis

3.3 Analytical method

An analytical method developed in computer program MATLAB® (The MathWorks Inc., Natick, Massachusetts, United States) was used to separate the total deflection curve obtained in constant-moment area of the four-point bending test in the second application and assess the isolated mechano-sorption deflection in the cumulative moisture content change domain. In this paragraph, the selected theory and material parameters are discussed.

3.3.1 Total deflection curve

To be able to isolate the mechano-sorption deflection u_{ms} from the total deflection curve u, the expressions presented by Eq. (31) to (33) are used, where u_e is the elastic and u_c is the creep deflection.

$$u = u_e + u_c + u_{ms} \qquad (31)$$

$$u_e = \frac{3Fal_l^2}{4E(w)b(w)h^3(w)} \qquad (32)$$

$$u_c = u_e^* \sum_{k=1}^{2} \phi_\sigma^k(w)(1 - e^{-t/\tau_k}) \qquad (33)$$

In the formulation of u_e, F is the total load, a is the distance between load and support, l_l is the gauge length, E is the elastic modulus, w is moisture content and in this context indicates moisture dependency, h is the depth of the specimen, and b is the width of the specimen (NEN-EN 408 2012). The effect of hygro-expansion is included by adding u_h, which is the hygro-expansion experienced over the depth of the specimen, to the measured h at 40% RH and 60°C, and $0.33u_h$ to the measured b at 40% RH and 60°C (Bengtsson 2001). A 2-module Kelvin model is used to describe u_c; see Eq. (33). The model is modified, such that the elastic deflection right after loading u_e^* is used to scale u_c, which is analogue to the description of ε_c by Eq. (8).
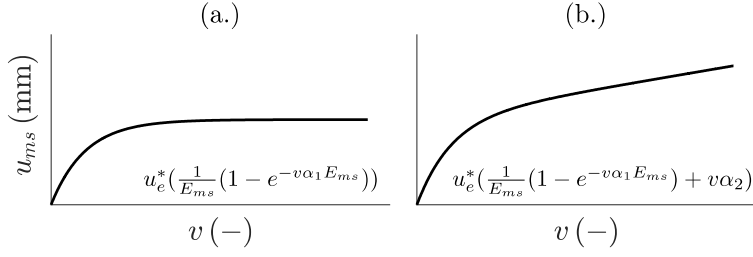
3.3.2 Mechano-sorption deflection curve

The isolated u_{ms} is analysed in the cumulative moisture change or v-domain (rather than in the time domain); see Eq. (34). Here, E_{ms} is the mechano-sorption modulus equivalent to $\boldsymbol{n}$ in Eq. (9) and α_1 and α_2 are mechano-sorption parameters, of which α_1 is equivalent to $\boldsymbol{m}$ in Eq. (9).

$$u_{ms}(v) = u_e^* \left(\frac{1}{E_{ms}}(1 - e^{-v\,\alpha_1 E_{ms}}) + v\,\alpha_2 \right) \qquad (34)$$

$$v = \int_0^t |\dot{w}|\,dt \qquad (35)$$

Equation (34) originates from the model presented by Salin (1992), but is extended with a linear expression (see **Fig. 3-11a** and **b**). The deflection is scaled using the same elastic deflection right after loading u_e^* as used for u_c.

Fig. 3-11: Mechano-sorptive deflection in the cumulative moisture change v domain, where (a.) is the exponential part of Eq. (34), and (b.) is a complete plot of Eq. (34) (Paper III)

3.3.3 Material parameters

The linear expressions (36), (37) and (38) were used to describe the shift in the FSP w_f at elevated temperature and the effect of moisture content w below FSP w_a on the visco-elastic parameters. In Eq. (36), the term ψ_{fT} describes the change in w_f due to a unit increment in temperature, and holds a value of $0.0033\,°C^{-1}$ (Dinwoodie 1981). T_0 is a reference temperature of 20°C and T the temperature of 60°C at which is tested. In Eq. (37), the reference value E_0 is unique for each specimen and can be determined from u_e^*. The term Y_{w0} indicates the change of E_0 due to unit moisture content increment, and hold a value of 21000 MPa (Keunecke et al. 2007). In Eq. (38), the reference value $\phi_{\sigma0}^n$ is also unique for each specimen and obtained with a fit made to u_c recorded in the first 5 days of testing. The term χ_{w0} is determined with additional creep tests, and indicates the change of ϕ_σ due to unit moisture content increment.

$$w_f = 0.26\,(1 + \psi_{fT}(T_0 - T)) \tag{36}$$

$$E = E_0 + Y_{w0}(w_f - w_a) \tag{37}$$

$$\phi_\sigma^k = \phi_{\sigma0}^k + \chi_{w0}^k(w_f - w_a) \tag{38}$$

3.3.4 Creep under controlled climate

The moisture content influences the deflection rate du_c/dt during either of the two RH-phases of the climate cycle (Engelund and Salmen 2012; Hering et al. 2012). The procedure adopted by the analytical method to analyse the effect of moisture on u_c for each specimen is visualised in **Fig. 3-12**. Here, a simplified but conservative assumption is made that the creep rate changes according to the EMC corresponding to a RH-phase at either 40% or 80%. The u_c affected by systematic RH-cycles is estimated by a summation of deflection increments Δu_c at 40% and 80% RH for each 9 cycles (M) analysed in the LT-experiment, indicated by m.
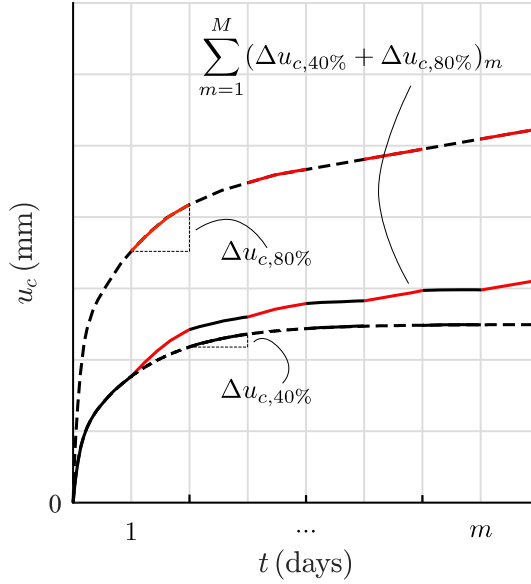
Fig. 3-12: *Procedure used to analyse the increase in creep deflection u_c due to systematic changes in RH between 40% and 80%, where Δu_c is the increase in deflection after each RH-phase and m indicates the number of regarded RH-cycles (Paper III)*

3.4 Experiment under controlled climate

The experimental program used to calibrate the numerical model assumes that the total deflection curve originating from the constant-moment area of the four-point bending test is conceptually separable into an elastic, creep and mechano-sorption component. **Table 3-3** provides an outline of the experimental program. The main part of the program consists of a long-term (LT) four-point bending test subjected to controlled climate. To help isolate the mechano-sorption deflection, additional creep tests in constant climate (high and moderate RH), short-term (ST) static tests, and recordings of mass and hygro-expansion were made. Three logs of Norway spruce (T1-2, T1-3 and T2-4) were used to obtain paired specimens (reference and control) by end matching. This process resulted in 2 sample sets that contained both 24 sapwood and 24 heartwood specimens ($30 \times 15 \times 640$ mm) related to the cardinal and intercardinal wind directions (SS, NN, EE, WW, NW, SE, NE, and SW). In **Table 3-3**, f_b (MPa) refers to the ultimate bending strength. A complete description of the experimental program, methodology and design can be found in Paper III.

Table 3-3: Outline experimental program (Paper III)

Test	Data type	Load-level	Specimen label	Number of sap- and heartwood specimens	u_e	u_c	u_h	u_{ms}	E	ϕ_σ^k	τ	f_b
Main (LT) (40-80% 60°C)			T1-2									
	Deflection	34%	NN/SS/EE	3/3	×	×		×	×	×	×	×
	Hygro-expansion	0%	WW	1/1			×					
	Mass change	0%										
Reference (LT) (40-80% 60°C)			T1-3									
ST (98% 21°C)		—	T1-3, T1-3, T2-4	24/24					×			×
Creep (40% 60°C)			T1-3									
	Deflection	34%	NN/SS/EE	3/3	×	×		×	×	×	×	×
	Mass	0%	WW	1/1								
Creep (80% 60°C)												
	Deflection	34%	NW/SE/NE	3/3	×	×			×	×	×	×
	Mass	0%	SW	1/1								

Header group (spanning): Deflection components = u_e, u_c, u_h, u_{ms}; Material parameters = E, ϕ_σ^k, τ, f_b.

* Percentage of the mean (μ) MOR at 30% moisture content

36

3.4.1 Long-term and creep tests

A custom-made loading frame positioned inside a climate chamber of type Vötsch VCR 4033/S (Vötsch Industrietechnik GmbH, Balingen, Germany) (see **Fig. 3-13**) was used to test a selection of reference specimens in bending and in a particular climate. During testing, the total deflection u from the constant-moment area, the mass of the total beam and the hygro-expansion over the depth of the beam u_h were recorded.
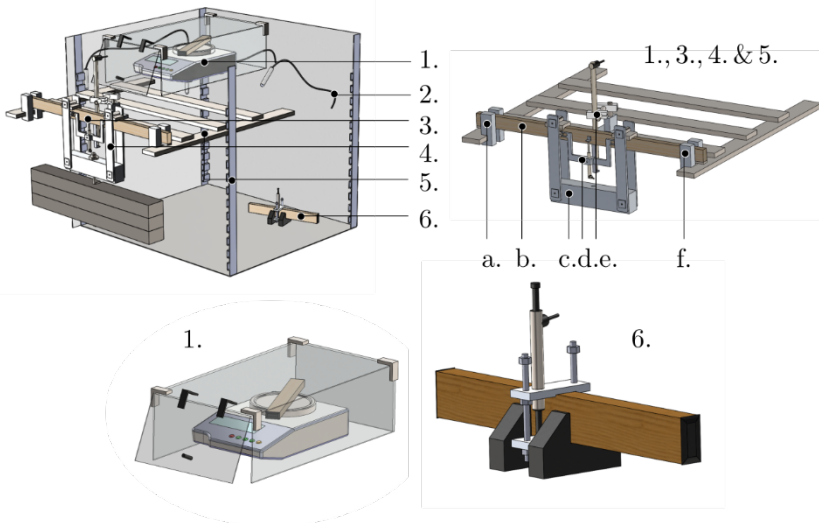
Fig. 3-13: Render climate chamber with equipment: (1.) scale, (2.) pin-type temperature and humidity sensors, (3.) displacement transducers, (4.) aluminium loading rig, (5.) steel supporting frame and supporting struts, and (6.) fixture to measure hygro-expansion, (a.) lateral and pin supports, (b.) specimen, (c.) loading rig, (d.) small displacement transduced, (e.) large displacement transducer, and (f.) lateral and roll supports (Paper III, IV)

In the LT-experiment, a load and climate schedule are used that first initial a period of pure elastic and creep behaviour, before systematic RH-cycles (two RH-phases) initiate mechano-sorption over a period of 90 days; see **Fig. 3-14**. The specimens were subjected to low-level bending ($< 34\%$), a constant temperature of $60°C$ and RH-phases at 40% and 80%. The additional creep tests covered a 10-day period at constant temperature of $60°C$ and constant RH at either 40% or 80%. For sapwood specimens a total load of 413 kN is used, and for heartwood specimens 313 kN. The data obtained with the LT-experiment is used to calibrate the numerical model and assess u_{ms} with the analytical method. The creep tests are used to estimate χ_{w0}.
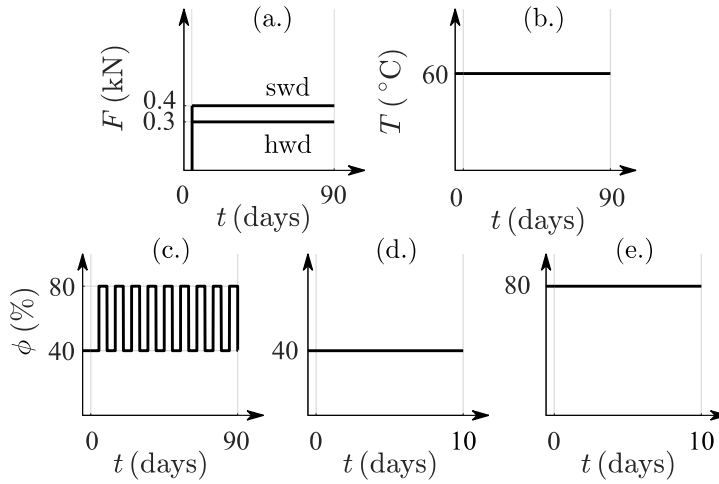
Fig. 3-14: Climate and load schedules for the long-term experiment and additional creep tests (a.) load F schedule, (b) temperature T schedule, (c.) RH ϕ schedule long-term experiment, and (d.) & (e.) ϕ-schedules for additional creep tests (Paper III)

3.4.2 Short term test

The 24 sapwood and 24 heartwood control specimens were bent to failure in a four-point bending test performed with a custom-made fixture in a universal testing machine (UTM) type MTS®-810 (MTS® systems Corporation, Eden Prairie, USA). The test was performed to get an indication of the variation experienced in material parameters obtained between the different cardinal and intercardinal wind directions at either annual ring 13 (heartwood) or 25 (sapwood). Before testing, the moisture content of each specimen was brought down from green-state to an EMC of 30%. During the test, the F and u were recorded. This data was used to determine E and f_b. The mean value of f_b was used to make a deliberate estimation of the load-level needed in the LT-experiment and additional creep tests. Oven-dry density ρ_0 and w_v at time of testing were determined using the oven-dry method (EN 13183-1 2003).

3.5 Experiment under natural climate

3.5.1 Background

Three plain-sawn solid timber beams (195 × 45 × 3100 mm) were tested in four-point bending in large custom-made testing rigs (capacity 50 kN) located in a test facility in Asa Research Park in Southern Sweden; see **Fig. 3-15**. The facility did not have insulation or heating, but did prevent exposure to the direct influence of wind, rain and sunlight.
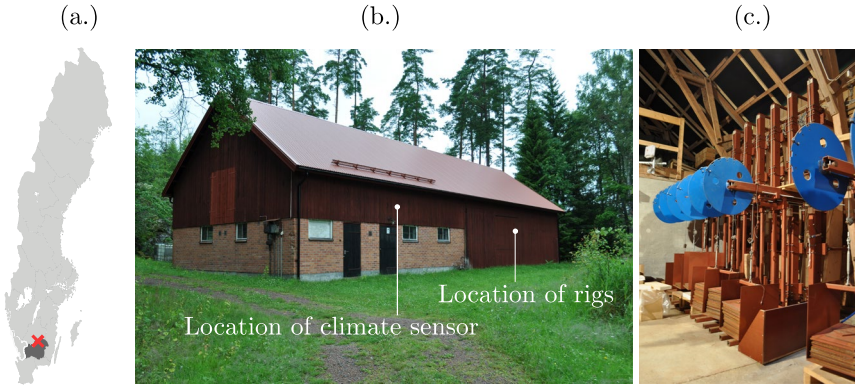
Fig. 3-15: *(a.) Location Asa Research Park in Southern Sweden, (b.) the research facility, and (c.) a selection of the* 30 *large testing rigs (Paper IV)*

A visualisation of the details of the experimental setup can be found in **Fig. 3-16**. The beams were subjected to low-level bending by applying a total load of 6900 N. The experimental procedure provided continuous recordings of T and ϕ, and total deflection u at 20 mm from the lower surface; see **Fig. 3-16a**. For a more detailed description of the test set-up and procedure, Paper IV can be consulted.
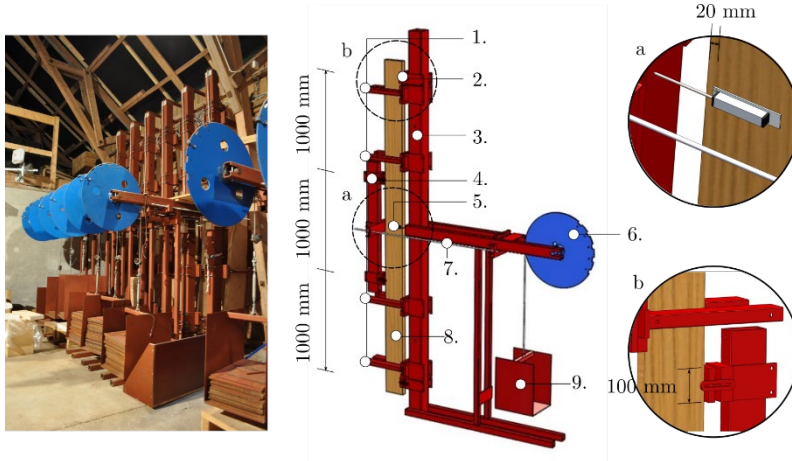
Fig. 3-16: *Photo and render of the four-point loading rig: (1.) lateral supports, (2.) roller supports, (3.) base steel beam used to vertically support timber beam, (4.) steel load evener, (5.) potentiometer, (6.) gear wheel, (7.) rod used to distribute load between wheel and load evener, (8.) solid timber beam, (9.) load basket, (a.) detail of location potentiometer, and (b.) detail of roller and lateral support (Paper IV)*

3.5.2 Climate recordings

The raw data for T, ϕ and u (grey) recorded in the test facility in Asa Research Park over a span of 18 months (23-10-2018 to 30-04-2020) is presented in **Fig. 3-17**. The recorded temperature ranges between -2 and $20°C$, and the RH between 50% and 90%. The T and ϕ data are added to the numerical model as so-called tabulated data, which is automatically averaged by the FE-program between each time increment and made available in all user-subroutines. The validation of the numerical model is performed with the averaged u between the three timber beams; see black line **Fig. 3-17b**.
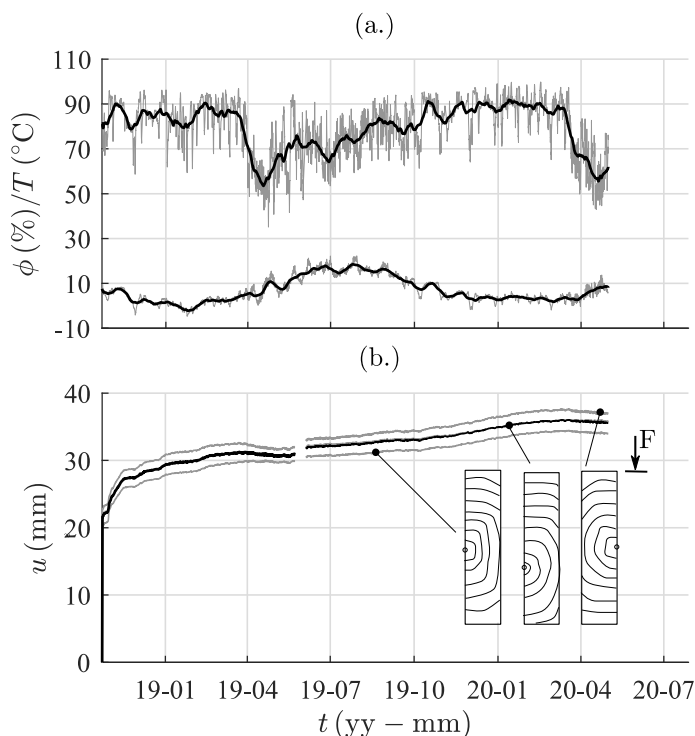
Fig. 3-17: *(a.) The original (grey) and averaged (black) RH ϕ and temperature T from Asa Research Park, and (b.) the original (grey) and averaged (black) deflection u measured at mid-span at a distance of 20 mm to the lower surface of the beams, including the orientation of the cross-section with respect to the direction of load (Paper IV)*

40

4 Results and discussion

4.1 Influence of green-state on tangential stress

4.1.1 Fibre orientation and stress reversal (Paper I)

The areas where the annual rings align with the exchange surface of the timber boards are prone to high tensile and compressive stress in tangential direction σ_t; see **Fig. 4-1**. After initiation of drying, a steep moisture gradient quickly develops right underneath the exchange surface, which drops below FSP ($\approx 27\%$) and creates tension areas that have values above 0.5 MPa (the characteristic strength perpendicular to grain) (Porteous and Kermani 2007); see **Fig. 4-1** at 0.7 days. This makes the wood susceptible to surface and end-checking (McMillen 1958).
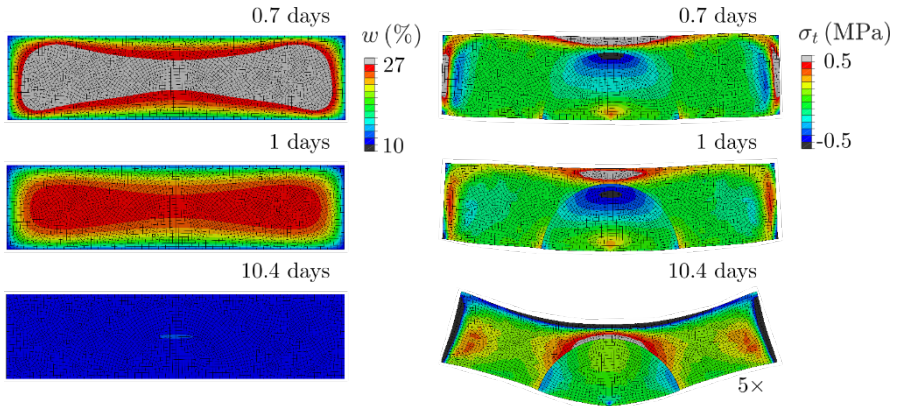
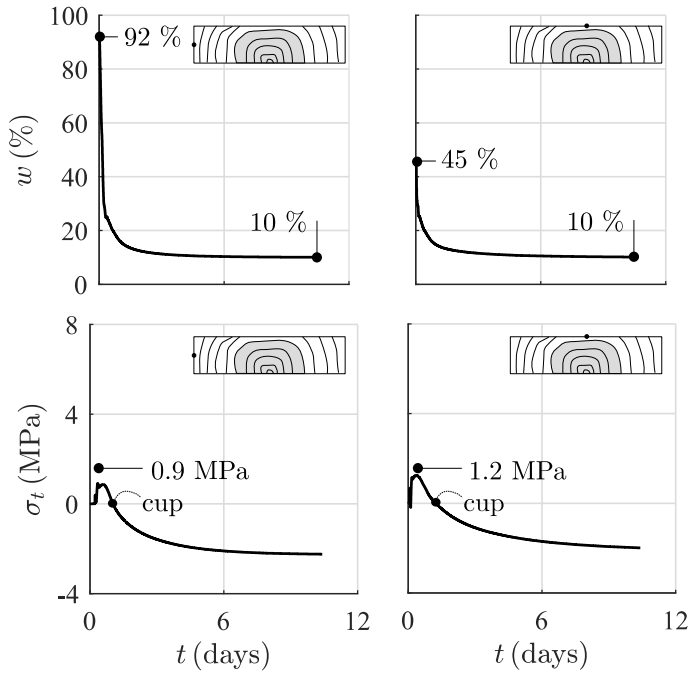

Fig. 4-1: *Moisture content w change and tangential stress σ_t development of timber board B₁ when dried from green-state to an EMC of 10% (FSP is 27%)*

Since the inner section of the timber boards is still above FSP, no shrinkage occurs in this part of the cross-section, and consequently forms an internal constraint. The

area adjacent to the tension field, therefore experiences a state of compression (McMillen 1958; Pang 2000).

The formation of the well-known cupping behaviour associated with timber board B_1 starts after about 1 day of drying, around the same time the complete inner section of the timber board reaches FSP; see **Fig. 4-1** and **Fig. 4-2**. At this moment, the board also experiences stress reversal, which indicates that the inner-section also starts to shrink and the tensile area close to the exchange surface start to move inwards and turns this area into compression (McMillen 1958; Svensson et al. 2002b). Stress reversal allows for the formation of inner-checks and former developed checks to turn into cracks.

Fig. 4-2: Moisture content w change and tangential stress σ_t development for two specific locations on the exchange surface of timber board B_1 obtained when dried from green-state to an EMC of 10%

The areas in compression close to the exchange surfaces seen at the end of drying (see **Fig. 4-1**) hardens the surface area of the timber boards. This is often referred to as case-hardening (McMillen 1958). **Fig. 4-3** shows that mechano-sorption is important in the development of this phenomenon. **Fig. 4-3a** present the change in σ_t in time when only elastic behaviour and hygro-expansion are included in the simulation, whereas in **Fig. 4-3b** also mechano-sorption is included. Due to the differences in hygro-expansion parameters between sapwood and heartwood, high values in tensile stress develop around the upper, left and right surface. Due to

mechano-sorption, these stresses are lowered and stress reversal is introduced. In the area where sapwood and heartwood intersect another tension area can be found, which is formed due to differences in hygro-expansion experienced between the sapwood and heartwood region (see **Fig. 4-1**). This creates an additional area where checks easily develop and under the right circumstances turn into cracks. Repeated drying and wetting can open and close checks and cracks in wood, and therefore can become invisible to the eye. Nevertheless, these damages can weaken timber elements, especially when loaded in shear (McMillen 1958).
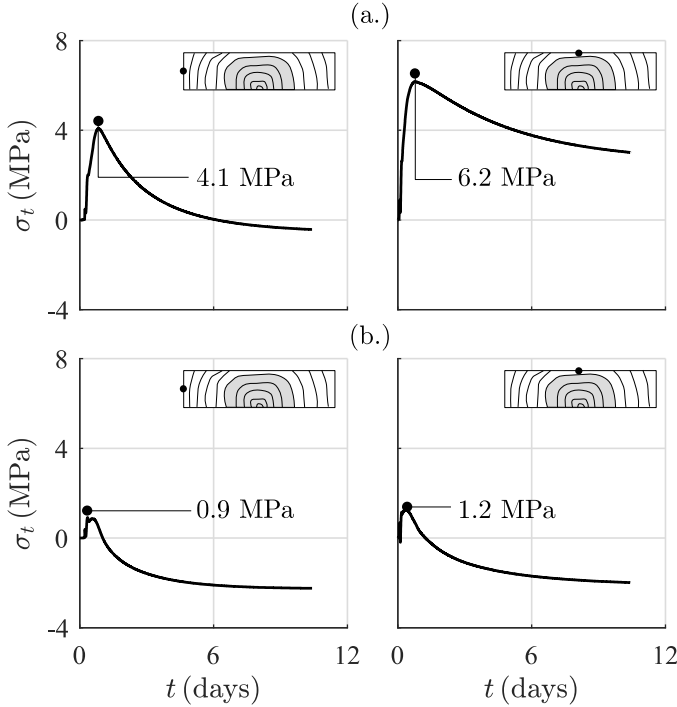
Fig. 4-3: *Tangential stress σ_t development during drying from green-state to an EMC of 10%, when (a.) the elastic behaviour and hygro-expansion are included in the analysis, and (b.) also the mechano-sorption is accounted for*

4.1.2 Initial moisture state (Paper I)

To illustrate the effect of green-state moisture content on the development of σ_t, two types of simulations were performed: 1) with an initial constant state just above FSP (30%) and 2) with an initial state at green-state, see **Fig. 3-5**. Although, the location of extreme stress is mainly influenced by material orientation and therefore independent of the initial moisture state, a slightly higher and more pronounced tension peak develops for the simulation that starts at a constant 30% moisture content. This peak quickly turns into compression, which is quantified by Δt_1; see

Fig. 4-4d. When green-state is the initial state, this peak occurs much later in time, and dependent on the location in the cross-section, are also present over a much longer period; see Δt_2 in **Fig. 4-4d**. Although the application is different, the order of magnitude of σ_t is similar to what was found by Pang (2000) with a one- dimensional model.

In green-state, the moisture content of timber board B_1 and the top and bottom surface of timber board B_2 are much closer to FSP than the left and right surface. These surfaces will start to shrink earlier on in the drying process. Consequently, an increased difference in time and time span with which the tensile σ_t occurs is experienced between the left and right and top and bottom surfaces; compare **Fig. 4-4a** and **c** with **Fig. 4-4b** and **d**. It is seen that the results obtained with an initial constant state at 30% moisture content experience stress peaks and a state of stress reversal that are quite consistent and similar between each plot.
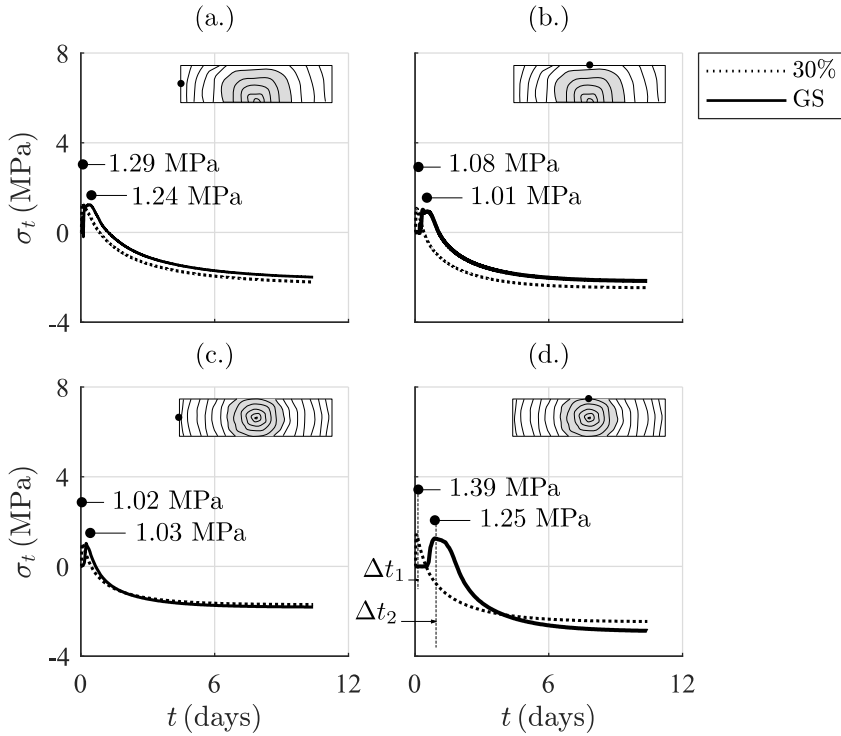

Fig. 4-4: Tangential stress σ_t development in (a. and c.) a location at the left surface and (b. and d.) in a point at the upper surface of (a. and b.) timber board B_1 and (c. and d.) timber board B_2 dried from green-state (GS) or 30% moisture content to EMC

4.2 Long-term behaviour under controlled climate

4.2.1 Analytical method

4.2.1.1 Short-term experiment (Paper III)

To create insight into the variation in material parameters within the cross-section of logs T1-2, T1-3 and T2-4 before long-term testing, the green-state moisture content w_{gs}, oven-dry density ρ_0, ultimate bending strength f_b and elastic modulus E were determined; see **Fig. 4-5**. By comparing the mean value μ of each wind direction, it is seen that no substantial variation is found within the cross-sections of the logs. The largest differences are seen between sapwood and heartwood.
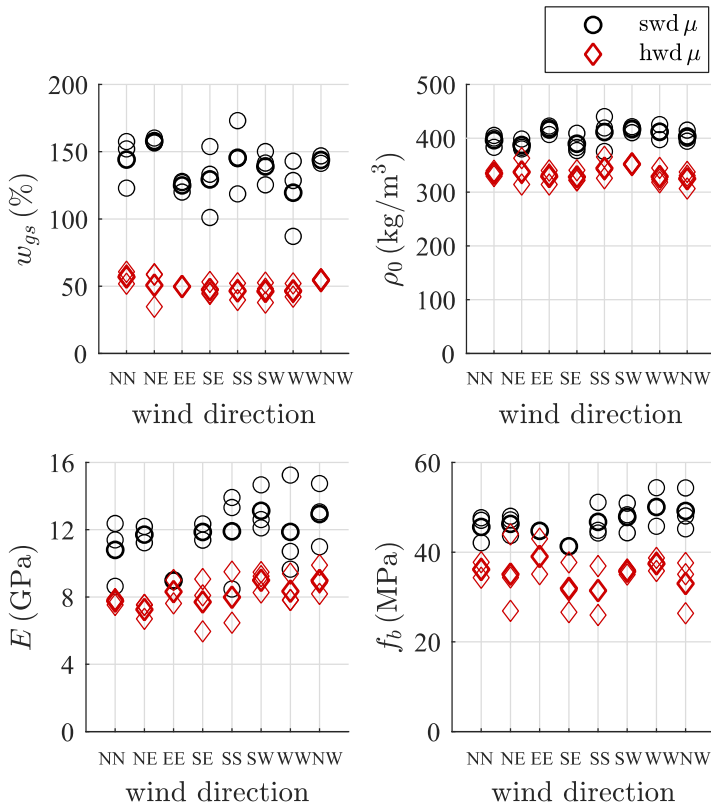
Fig. 4-5: *Green-state moisture content w_{gs}, oven-dry density ρ_0, ultimate bending strength f_b and elastic modulus E of sapwood (swd) and heartwood (hwd) specimens related to different wind directions, where μ is the mean value for each wind direction (Paper III)*

The obtained values for w_{gs} lie between 87% and 173% for sapwood and between 35% and 61% for heartwood. This complies with the expected range between 80% and 200% and between 30% and 80%, respectively (Absetz 1999; Larsen 2013;

Samuelsson and Arfvidsson 1994). The values found for ρ_0 range between 375 and 440 kg/m^3 for sapwood and 307 and 363 kg/m^3 for heartwood. For clear wood specimens of Norway spruce, van Blokland et al. (2019) presents a mean value and standard deviation of $427 \pm 9.2\%$ without making a clear distinction between heartwood and sapwood. For f_b, values between 41.3 and 54.4 MPa for the sapwood sample set and between 26 and 44 MPa for the heartwood sample set were found, which exceed the limits set by the Risbrudt et al. (2010), which are 32 and 42 MPa. The E found for sapwood ranges between 8.5 and 15.3 GPa and for heartwood between 6.0 and 9.9 GPa, which exceed the values given by the Risbrudt et al. (2010) of 7.1 and 9.5 GPa. The differences in characteristics observed in specimens harvested from sapwood and heartwood zones may be attributed to the content of juvenile wood, however we were not able to determine the content of juvenile wood directly and we cannot make such conclusion with definite or even measurable margin of confidence.

4.2.1.2   Deflection (Paper III and IV)

The experimentally obtained total deflection u and the deflection components obtained with the analytical method are collected in **Fig. 4-6**. The initially dry wood is subjected to low-level bending ($\sigma_x / f_b \leq 34\%$) and experiences a mentionable increase in u for the first ad- and desorption (the period between 5 and 15 days). This initiates a decreasing deflection rate phase (first ± 30 days), followed by a constant deflection rate phase. After 90 days of testing, a wide range in u is found between the individual specimens of either the sapwood or heartwood sample set, which highlights the strong effect of location within the log from which the specimens are taken. This is stronger than seen for the ST-test.

The elastic deflection u_e is the largest component that makes up u (46-60%); **Fig. 4-6** and **Table 4-1**. u_e slightly fluctuates, which is caused by the competing changes in E, b and h initiated by changing ϕ-phases. The mechano-sorptive deflection u_{ms} is the second most largest deflection component, with values between 27% and 43%. The smallest contributing component is the creep deflection u_c (9-15%). This component experiences a significant increase in the first 30 days of testing, after which no measurable growth is observed. It seems that the series of Kelvin modules used to describe u_c fits the experimental data, but make it challenging to predict the behaviour beyond the fit, since it will eventually trend towards a horizontal asymptote; see **Fig. 4-7**. When calibrated at 5 days, an underestimation of 78.5% was seen for 40 days for the random example given in **Fig. 4-7**. The results obtained with the heuristic approach (see section 3.3.4 'Creep under controlled climate) used to get an indication of what the effect is of the ϕ-phases on creep after 90 days of testing is also collected in **Table 4-1**. By comparing $u_{c,40-80}$, $u_{c,40}$ and $u_{c,80}$, it is seen that the climate in the first 5 days of testing have a much bigger effect on u_c than the subsequent ϕ-phases (between 0 and 3%) in the considered time frame.
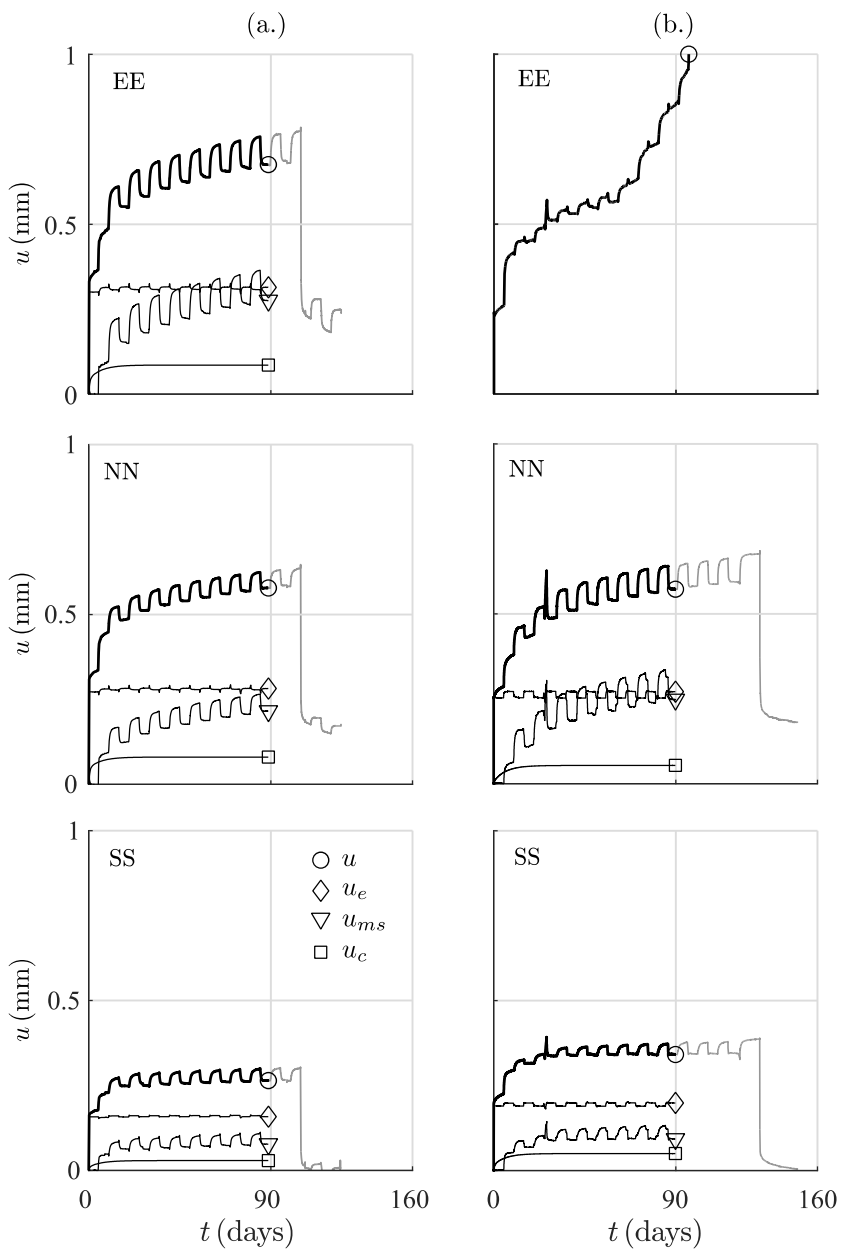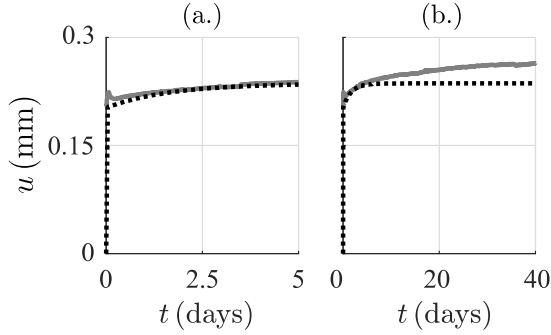
Fig. 4-6: *Separation of the total deflection curves u of (a.) the sapwood and (b.) the heartwood specimens into an elastic u_e, creep u_c and mechano-sorptive u_{ms} component (Paper III)*

Table 4-1. *Contribution of each deflection component to the total deflection u after 90 days of testing, including the elastic deflection right after loading, u_e^* and the creep deflection expected at 80% RH, $u_{c,80}$ and when subjected to RH-phases, $u_{c,40-80}$ (Paper III)*

	Total (mm)	Elastic (mm)		Creep (mm)			Mechano-sorption (mm)
	u	u_e^*	u_e	$u_{c,40}$	$u_{c,80}$	$u_{c,40-80}$	u_{ms}
Sapwood							
EE	0.676	0.310	0.314	0.0856	0.1062	0.0856	0.2757
% of total	**100**		**46**	**13**	**18**	**13**	**41**
NN	0.578	0.275	0.281	0.0803	0.0990	0.0803	0.2156
% of total	**100**		**49**	**14**	**17**	**14**	**37**
SS	0.264	0.157	0.158	0.0289	0.0397	0.0289	0.0773
% of total	**100**		**60**	**11**	**15**	**11**	**28**
Heartwood							
NN	0.573	0.250	0.271	0.0539	0.1026	0.0555	0.2478
% of total	**100**		**47**	**9**	**18**	**10**	**43**
SS	0.342	0.190	0.199	0.0499	0.0865	0.0512	0.0927
% of total	**100**		**58**	**15**	**25**	**15**	**27**

Fig. 4-7: Total deflection u obtained for specimen T1-3-NW-LT-s at $60°C$ and 80% RH, where (a.) is a fit made with the numerical model to u obtained in the first 5 days of testing and (b.) shows the trend the fit follows over a period of 40 days

4.2.1.3   Mechano-sorption deflection (Paper III)

A mentionable fit is found between the isolated mechano-sorptive deflection u_{ms} and the analytical method in the cumulative moisture content domain v; see **Fig. 4-8**. Initially u_{ms} experiences a decreasing deflection rate phase, while v is still below a value of 0.3 (-). For values of v higher than 0.3 (-), the constant deflection rate phase is seen. The sample sets are too small to perform a statistical analysis, however a trend is seen between the u_{ms} and the E or u_e^* of each specimen. Where, the specimen SS (see **Fig. 4-8**) experiences the lowest amount of u_{ms} after 90 days of testing and the highest E, where specimen EE experiences the highest amount of u_{ms} and the lowest E or u_e^*.
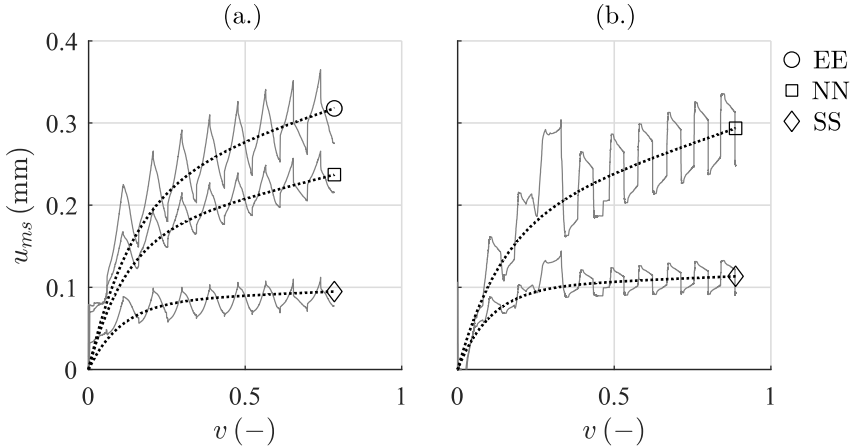
Fig. 4-8: Mechano-sorptive deflection u_{ms} (grey line) and fit made with the analytical method (dotted line) for (a.) the sapwood and (b.) the heartwood specimens (Paper III)

4.2.2 Numerical model

4.2.2.1 Fit moisture content data (Paper II)

For a correct interpretation of moisture-induced stress and distortion, it is important that the moisture flow analysis can represent the speed of moisture content change and the formation of moisture gradients just below the exchange surfaces. To assess these abilities of the current moisture flow model, a fit was made to experimentally obtained moisture content profiles from Rosenkilde (2002); see **Fig. 4-9**. These profiles relate to a specific flow direction (l, r or t) and were obtained with specimens of Scots pine ($29 \times 29 \times 29$ mm) dried from green-state to EMC at $60°C$ and 59% RH, either using a so-called slicing technique (**Fig. 4-9a**) or computed tomography scans (**Fig. 4-9b**).
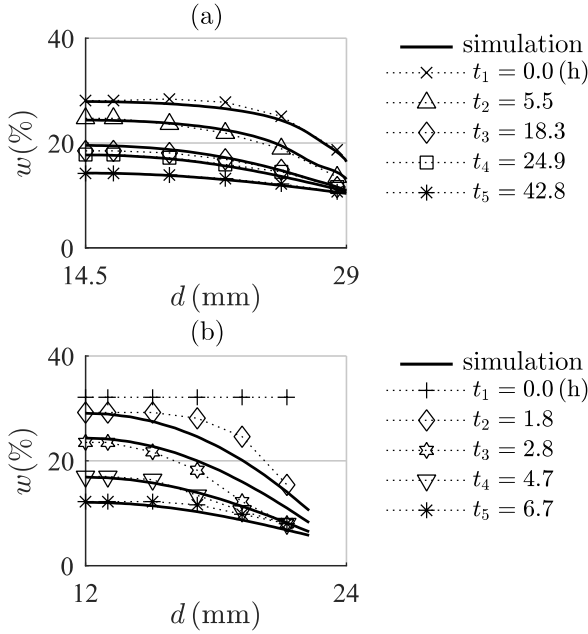
Fig. 4-9: *Comparison of simulated (solid line) and experimentally obtained moisture content profiles (scattered data) below FSP in (a) radial/tangential and (b) longitudinal direction (Rosenkilde 2002) (Paper II)*

Although, a more accurate set of w and T dependent D and s can be obtained with a fit made to moisture content profiles, continuous readings of a specimens overall weight, parallel to recordings made of long-term deflection, showed beneficial due to its simplicity in execution; see **Fig. 3-13**. For the long-term bending test subjected to controlled climate, the experimentally obtained average volumetric moisture content w_v is presented in **Fig. 4-10**. The result belongs to the sapwood specimen labelled WW. The w_v ranges between 7 and 13%, which complies with what was

previously seen for wood species in general (Wood Handbook 2010), where values between 6.3% and 13.6% were reported for a constant temperature of 60℃ and RH of 40% and 80%, respectively.
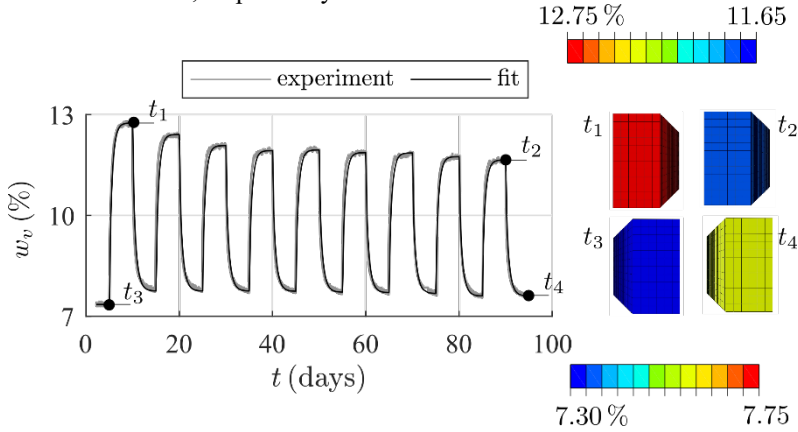
Fig. 4-10: *Fit made with the numerical model to the average volumetric moisture content w_v, including colour plots to indicate hysteretic behaviour (Paper II)*

The precision of the fit presented in **Fig. 4-10** is dependent on the fact that D and s are a function of moisture and temperature. To show this, a parametric study was performed; see **Fig. 4-11**. Simulation s_1 is also presented in **Fig. 4-10** and is performed with D and s both dependent on w and T. Simulations s_2 and s_3 are ran with constant values of D and s, which correspond to the upper and lower values, respectively, of the w and T dependent D and s used in s_1 in the considered w (7.3% and 12.75%) and T-domain (60℃). With s_1 as reference, it can be observed that s_2 and s_3 lead to quite a difference in curvature between ad- and desorption. In adsorption, s_3 lies closer to s_1, whereas in desorption s_2 lies closer to s_1; see relative difference (RD) in **Fig. 4-11**.
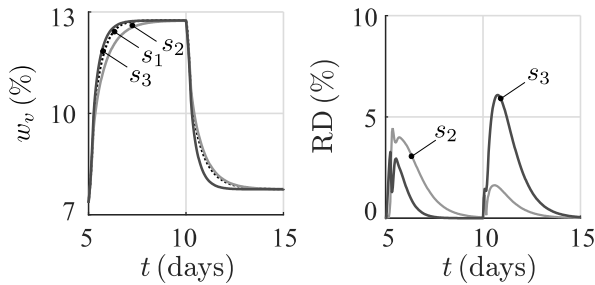
Fig. 4-11: *Average volumetric moisture content w_v obtained for three different simulations and the relative difference (RD) with respect to simulation s_1, where s_1 is obtained with a moisture and temperature dependent diffusion and surface emission coefficient, and s_2 and s_3 with constant values for the same coefficients*

4.2.2.2   Sorption hysteresis (Paper II)

The w_v-curve presented in **Fig. 4-10** clearly shows sorption hysteresis in both ad- and desorption, a phenomenon important in the accurate description of moisture content change and gradients. The values for w_v found at the end of each ϕ-phase, which correspond to an EMC w_{eq}, are illustrated in **Fig. 4-12** as circles. Cycling wood between two ϕ-phases will result in closed hysteresis loops (scanning curves), bound by the first adsorption and desorption curves. With Eq. (24) and (25), and the parameters provided in **Table 3-2**, an interpretation of these scanning curves is made and presented in **Fig. 4-12**. The scanning curves generally do not follow a straight line, and develop with the same curvature seen for the boundary curves (Salin 2011; Shi et al. 2017a; Time 2002a).
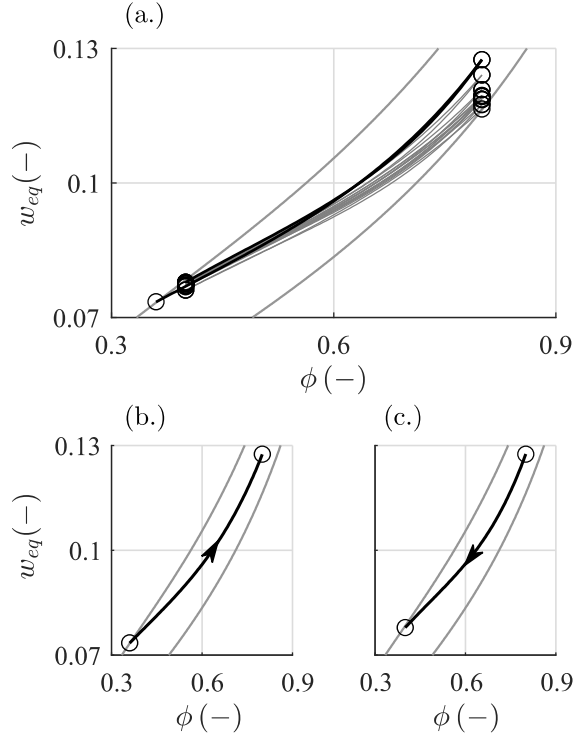
Fig. 4-12*: Interpretation of sorption behaviour at a constant temperature of 60℃ using a heuristic approach: (a.) approximation of scanning curves, (b.) interpolation data points at first adsorption, and (c.) interpolation data points at first desorption (Paper II)*

4.2.2.3   Fit deflection data (Paper IV)

Subjected to low-level bending ($< 34\%$) and systematic ϕ-cycles, the deflection curves u of the small clear-wood beams show an increasing deflection rate phase in the first 30 days of testing, followed by a constant deflection rate phase until the

end of testing; see **Fig. 4-13a**. A mentionable fit is found with the numerical model. However, the model cannot describe the characteristic waves that show a decrease in deflection during adsorption except for the first wetting phase. In **Fig. 4-13b**, the fit made with a 2-module creep model is presented.
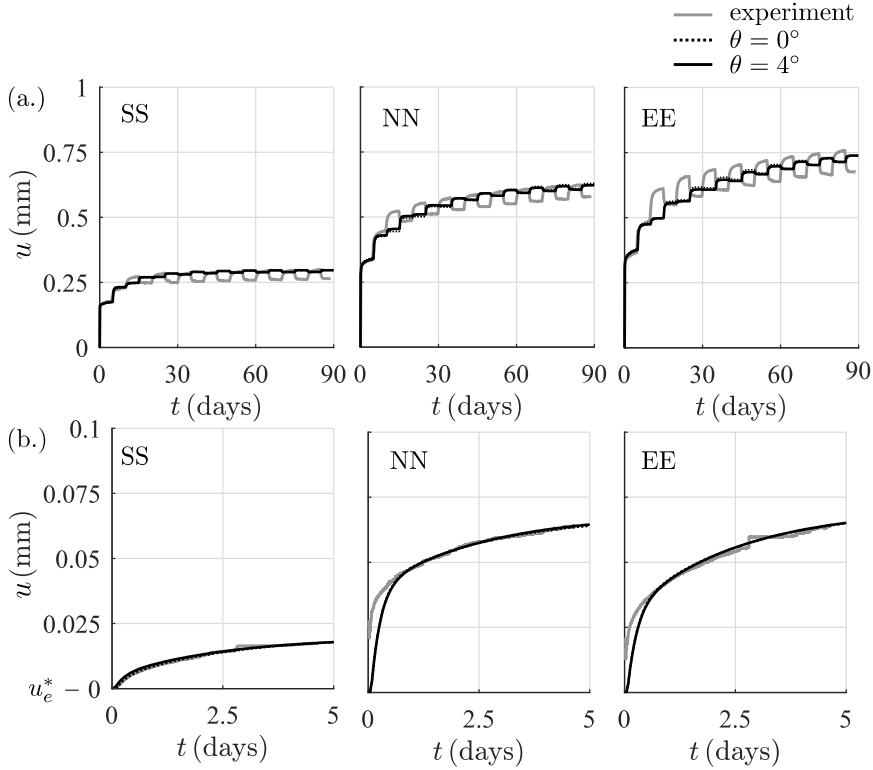
Fig. 4-13:Results calibration, where (a.) is the fit made with the numerical model to 90 *days of deflection data* u *and (b.) is the fit made to the first* 5 *days of testing with a simulation where the spiral grain θ was equal to* 0° *and one where θ was* 4°*. Note that b. starts where the elastic deflection right after loading* u_e^* *ends (Paper IV)*

4.2.2.4   Stress (Paper IV)

The longitudinal, tangential and longitudinal-tangential stress state experienced by the small clear-wood beams show normative and are affected by both spiral grain θ and climatic changes; see **Fig. 4-14** and **Fig. 4-15**. The stress development of σ_l presented in **Fig. 4-14a** is more affected by climate then by θ. The initial value of σ_l decreases with 2.1% due to a θ equal to 4°. However, at first desorption, the change in climate results in a vast increase in σ_l of 21.9% when θ is equal to 0°. This increase is even larger for θ equal to 4°, where a 33.4% increase is seen. For a stress state that is close to the ultimate limit state, such spikes in σ_l can possibly initiate or lead to failure. **Fig. 4-14b** shows that for small values of θ a significant

shear stress can occur in the longitudinal-tangential material plane, which enters the constant moment area. Due to drying, a 14.7% increase in τ_{lt} at first adsorption is seen for the simulation where θ equals 4° when compared to the initial stress state. For the simulation where θ is equal to 0°, a 4.7% increase is found.
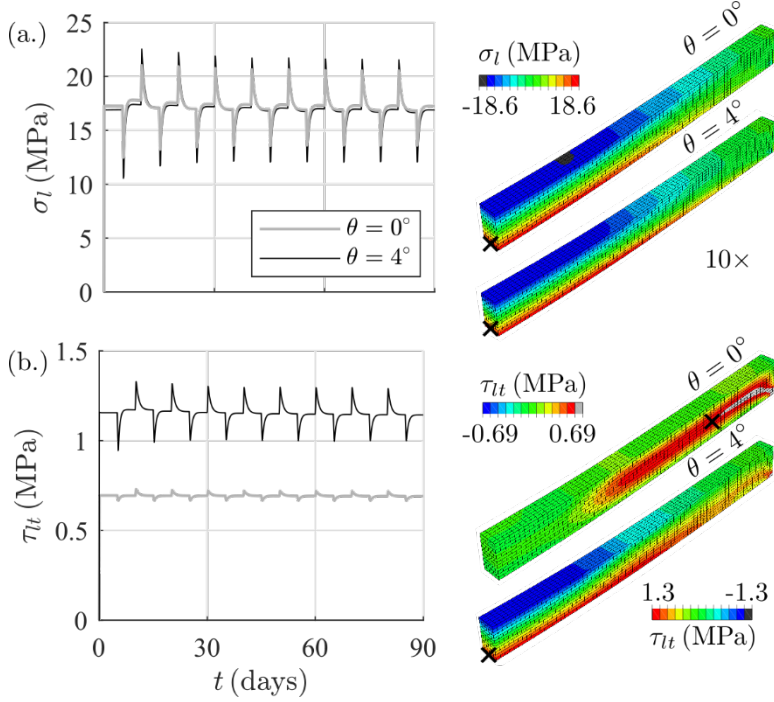
Fig. 4-14: (a.) Longitudinal stress σ_l and (b.) longitudinal-tangential shear stress τ_{lt} for a simulation were θ is 0° or 4°, where (×) indicates the mesh element from which the graphs are taken. Note: colour plots are taken directly after loading and only show half of the respected beam. The deflection is magnified by a factor 10 (Paper IV)

After 10.25 days of testing, the beam dries at the exchange surface, and a tensile σ_t-state as seen in **Fig. 4-15** is experienced. The stress state, which is caused by excessive shrinkage of the surface is compensated in the inner section of the beam by a stress state in compression (see colour plot **Fig. 4-15** after 15.25 days). How this stress state develops in time is also dependent on spiral grain. Higher stress peaks are found for the simulation without θ (surface: 1.68 MPa and centre: 1.5 MPa) compared to the simulation with θ (surface: 0.91 MPa and centre: 0.97 MPa). For Norway spruce, strength values in tangential direction between 1 and 3 MPa are reported for a temperature of 60℃ and different moisture content levels (Gustafsson 2003; Hanhijärvi 1998; Larsen 2013). However, no checks or cracks were observed upon visual inspection of the beam surfaces.
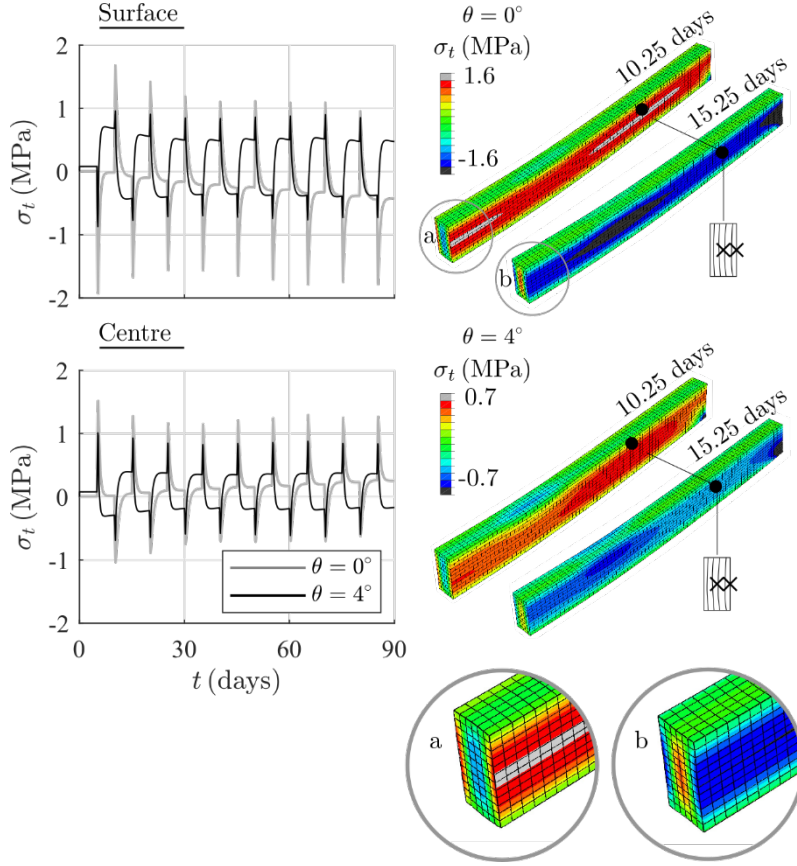
Fig. 4-15*: Tangential stress σ_t when θ is 0° or 4° for a specific mesh element at the surface and centre of beam SS. Note: the colour plots are obtained after either* 10.25 *or* 15.25 days *and show half of the respected beam. The deflection is magnified by factor* 10 *(Paper IV)*

4.3   Long-term behaviour under natural climate

4.3.1   Moisture content and strain (Paper IV)

In **Fig. 4-16**, for a solid timber beam (A2) and a small clear-wood beam (A3), the moisture content w and strain component ε_l are presented. The moisture content at the surface of the beams varies between 11% and 21%. The smaller beam A3 interacts much quicker with the surrounding air, than the larger beam A2, which is seen in **Fig. 4-16** in the smaller differences in w between the different plots obtained at different locations over the depth of the beams. After 120 and 185 days, a much large difference in w between surface and centre is seen for beam A2. However, due to the large cross-section, the moisture gradients are smaller than seen for beam

A3; see **Fig. 4-17**. The largest difference in *w* is seen in May after 185 days of testing (see **Fig. 4-16**), which is also confirmed by the colour plots presented in **Fig. 4-17b** and **d**.
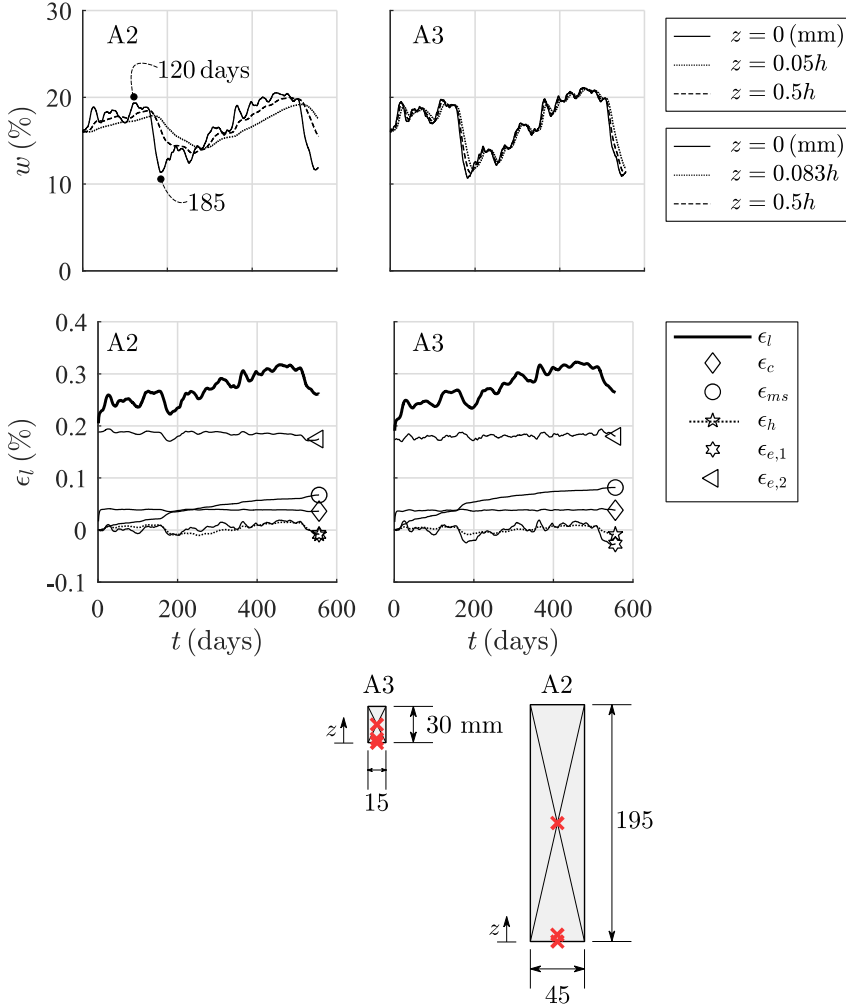
Fig. 4-16: *Moisture content w in three specific nodes over the depth of the beams h at mid-span, and the longitudinal strain ε_l component with its strain terms obtained in a mesh element located at the bottom surface of the beams at mid-span (Paper IV)*

The material point used to analyse strain is located at different distances from the bottom exchange surface for both beams. **Fig. 4-16** shows that the strain component ε_l follows a seasonal change for both beams A2 and A3, which is similar to the change seen in w. After about 550 days of testing, the larges strain term that makes up ε_l is $\varepsilon_{e,2}$, followed by ε_{ms}. The creep strain ε_c gives a considerable contribution to ε_l, but trends towards an asymptote almost directly after loading. ε_h and $\varepsilon_{e,1}$ show the most variation in value due to climate. Possible differences seen in ε_h between the two beams, among other things, can be caused by the radial variation in α_l. The size of this coefficient between both beams differs in the studied locations. There, the value for beam A2 is 0.0036 (-) and for beam A3 is 0.0018 (-).
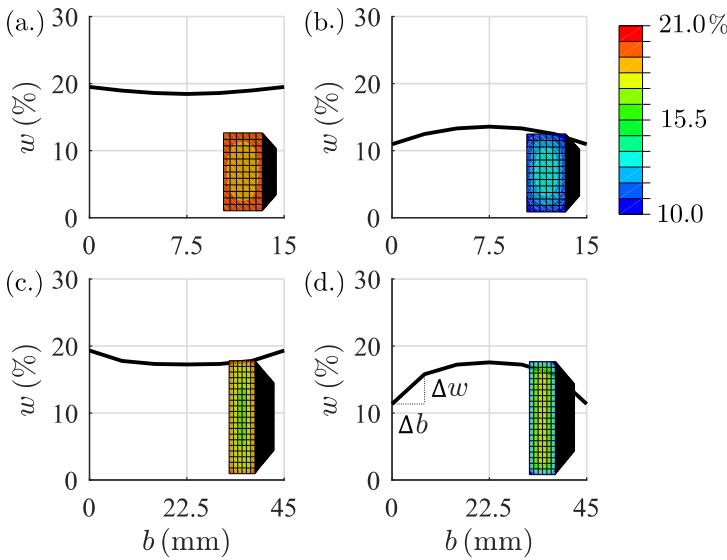
Fig. 4-17: *Moisture content profiles covering the width b of beam A3 after (a.)* 120 days *and (b.)* 185 days*, and of beam A2 after (c.)* 120 days *and (d.)* 185 days*.*
Note: colour plots are not scaled (Paper IV)

4.3.2   Stress (Paper IV)

The timber beams are subjected to a combination of mechanical load and natural climate. The stress states initiated by mechanical load, see σ_l and τ_{lt}, are visualised in **Fig. 4-18** for specific locations at the exchange surface. The size in stress shows to be seasonal, encountering tension peaks in springtime. The variation in σ_l and τ_{lt} due to climate is more pronounced for the larger beam A2 than the smaller beam A3. The larger beam A2 experiences a spike in σ_l (13.7 MPa) around 185 days of testing, which is an 17.1% increase with respect to the initial stress state right after loading. For the smaller beam A3, this spike (11.7 MPa) is smaller, with only

an 3.2% increase. Due to radial variation in α_l, the value of α_l is quite small in the analysed locations (see previous paragraph 4.3.1). **Fig. 4-18a** shows (dashed lines) the effect of the size of α_l on σ_l with an additional simulation for both beams, which are performed with an α_l equal to 0.012 (-). This value corresponds to values found by Bengtsson (2001) for fast growing stands of Norway spruce. The peak experienced for beam A2 after 185 days shows a 23.9% increase with the initial state due to the larger hygro-expansion coefficient. For beam A3, this increase is only 4.8%. The distribution of τ_{lt} over the cross-section of the beams is very much dependent on the pith location.
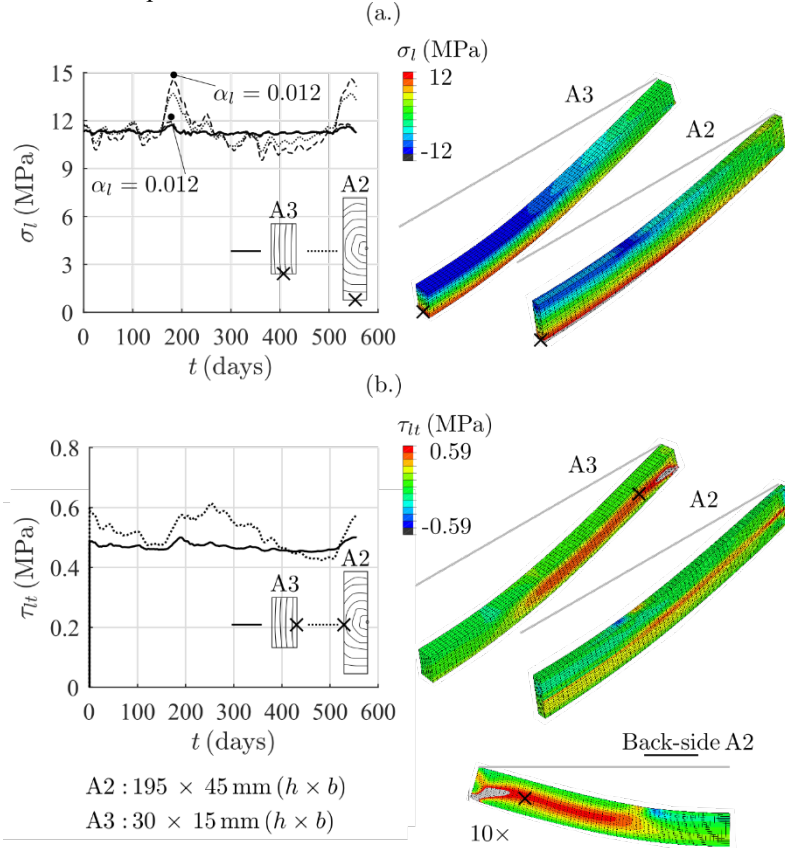
Fig. 4-18: Longitudinal stress σ_l and longitudinal-tangential shear τ_{lt} stress development for beams A2 and A3 obtained in a specific mesh element located at the exchange surface. Note: deformed shape is magnified by a factor 10 (Paper IV)

The tangential stress σ_t develops quite differently for beam A2 compared to beam A3; see **Fig. 4-19**. The stress state is influenced by pith location and the stress peaks are more pronounced for the smaller beam A3. However, also similarities can be found. The area where the tangential material direction aligns with the exchange surface is prone to high tensile stress during drying of this surface. These tension

areas are compensated with adjacent compression areas; see close-up **Fig. 4-19**. Since the beams are subjected to continuous drying and wetting, the stress state between surface and centre continuously changes between tension and compression, which can contribute to the opening and closing of checks and cracks. For beam A2, σ_t-spikes up to 1.4 MPa (surface) are found, while for beam A3 spikes up to 0.68 MPa (centre) are seen. These values exceed the characteristic strength perpendicular to grain of 0.5 MPa (Porteous and Kermani 2007), and can contribute to the development of drying related checks and cracks in the longitudinal-radial plane. Such cracks can influence the aesthetical appearance of the structural element and lead to weakening of the shear capacity of beams.
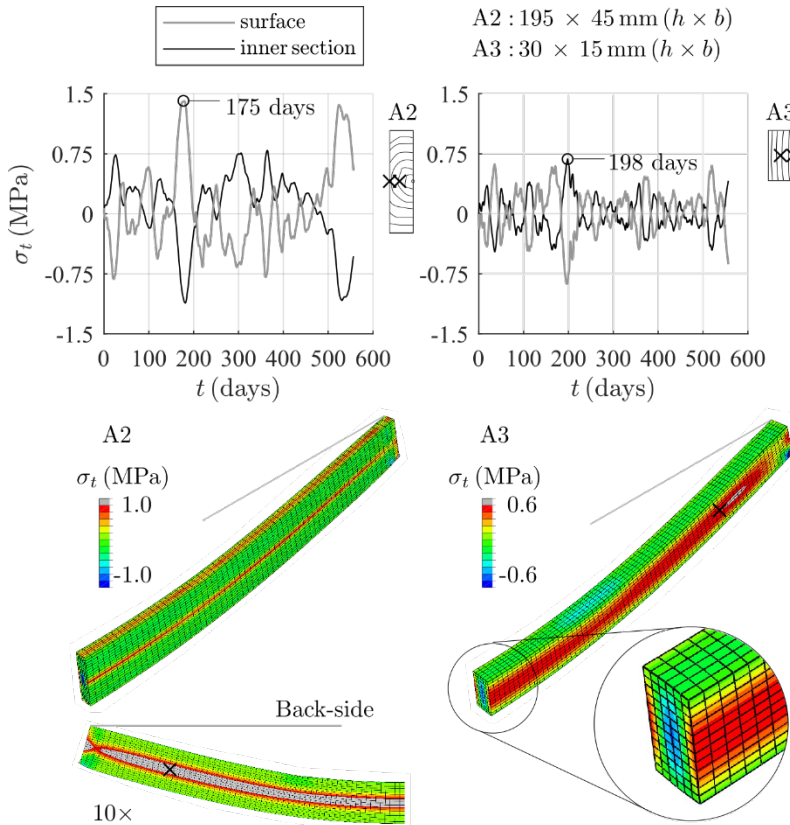
Fig. 4-19: *Tangential stress σ_t development for beams A2 and A3 obtained in a specific mesh element located at the exchange surface or centre.*
Note: deformed shape is magnified by a factor 10 *(Paper IV)*

5 Concluding remarks

5.1 Conclusions

A *three-dimensional numerical model* is presented that can describe the nonlinear transient moisture transport in wood and moisture-induced distortion of wood. User-subroutines compatible with the FE-program made the model more flexible in defining the constitutive models, boundary conditions and material orientation (spiral grain angle, conical angle and annual ring curvature). The results indicated that the three-dimensional character of the numerical model, together with the graphical interface and pre- and post-processing options of the FE-program contributed to the analysis and visualisation of the moisture content change, and the different stress and deformation states experienced by wood. These phenomena were each affected by material properties that vary (i.e. from pith to bark, between heartwood and sapwood, and due to temperature and moisture content), material orientation and climate.

The various calibrations and validations performed in this doctoral thesis indicated that the numerical model is able to describe moisture change and gradients in the considered temperature range between $-2℃$ and $60℃$, and the RH range between 40% and 80%, as well as the deflection of timber beams subjected to controlled and natural climate. The analysis of timber boards as part of the first application clarified phenomena, such as stress reversal and casehardening associated with wood drying, and showed that the green-state moisture content affected the time, size and frequency with which extremes in tangential tensile stress developed inside the timber during drying. The results of the second application showed that the nonlinearity of the analysis, *i.e.* the moisture- and temperature-dependency of the diffusion and surface emission coefficient, and sorption hysteresis are important in the correct description of moisture flow in wood. In addition, it showed the strong effect that the spiral grain within the small clear-wood beams and climate have on the size of deflection, the calibrated material parameters and the normative stress states. The analysis of different beam sizes as part of the third application showed that larger beams experienced a slower change in moisture,

smaller moisture gradients, more seasonal fluctuation in longitudinal stress, tangential stress and longitudinal-tangential shear stress, and high drying stress in tension.

The experimental methodology and analytical method designed as part of the second application led to a successful identification of each deflection component and isolation of the mechano-sorptive deflection curves of small-clear wood beams that were subjected to low-level bending (stress level/ultimate bending strength < 34%) and a controlled climate generated inside a climate chamber. At the end of the respected time, the elastic deflection was the highest contributor (46-60%) to the total deflection, followed by mechano-sorption (27-43%). Despite the lowest contribution, the creep deflection was non-negligible (9-15%). The calibration of the numerical model in the second application benefitted from the experimental methodology. The recordings of average volumetric moisture content were useful, seen the simplicity of the equipment and the possibility to perform these measurements parallel to the recordings of deflection. However, it was also seen that moisture content profiles, obtained with techniques such as X-ray computed tomography scanning or the slicing technique, led to a more coherent set of w and T dependent s and D. The developed heuristic approach used to describe sorption hysteresis based on the experimentally obtained average volumetric moisture content was useful for a better description of moisture content gradients. However, the approach should be regarded as a simplification of reality, since hysteresis is a process associated with the cell wall. The adopted climate and load schedule allowed for a subsequent calibration of elastic, creep and mechano-sorption behaviour. The adopted material models to describe these phenomena led to a reasonable fit to the experimental data. A similar conclusion could be drawn for the validation of the numerical model performed in the third application. However, the process would have benefitted from continuous recordings of mass change as part of the experiment.

For all three applications, in the areas where the tangential material direction aligned with the exchange surface of the timber boards and beams, high tensile stress in the same direction developed during drying. Due to the uneven change in moisture content over the cross-section, differential shrinkage is experienced between the inner section and surface area of the boards and beams. Therefore, adjacent to the tension area, in the inner section of the wood elements, the results showed that this stress field is always compensated by a compression field. For the first application, these tension areas showed prone to stress-reversal and casehardening, which caused the stress field to change from tension to compression during drying at the same time as the compression state in the inner section of the beam changed to tension. For the beams tested in the second and third application, the tangential tension fields below the exchange surface continuously changed between tension and compression due to phases of desorption and adsorption, respectively. The results showed that these particular type of stress fields were strongly affected by changes in climate and material orientation, and resulted in values that can make the material prone to cracking (0.68-1.7 MPa). Since the

beams studied in the second and third application were exposed to both mechanical load and fluctuating climate, the changes in moisture content also led to a mentionable increase in stress related to the longitudinal material direction (3.2- 33.4%) and longitudinal-tangential shear plane (2.4-14.7%).

In conclusion, a powerful numerical tool for scientists and engineers is created, which is compatible with a commercially available FE-program. The tool can be used to study the combined effect of load and climate on states of stress and deformation experienced by various (engineered) timber products in a wide field of applications. The three-dimensional numerical model contributed to the understanding of phenomena associated with wood drying and long-term behaviour of wood. It reopened the discussion whether moisture flow can be described by the more simple single Fickian approach by taking advantage of recent developments in the experimental work conducted on the moisture and temperature dependency of the surface emission coefficient. The work also contributed to the selection of suitable experimental methodologies and techniques to benefit the calibration and validation of numerical models.

5.2   Future studies

The range of applications for the numerical model is wide: from possible simulations made of drying processes of timber elements, to the storage of timber elements on site during the construction phase, to the actual long-term behaviour of wood elements. The model can be applied to predict the performance of engineered products, such as glue-laminated timber, cross-laminated timber or laminated veneer lumber, or the behaviour of window frames, lining, wood floors and wood walls during production or when in use. The model can also be used to predict the long-term behaviour of dowel behaviour subjected to low-level stress and climate, which is still in early stages of research (Fortino and Toratti 2010). The model can also be easily coupled to the extended finite element method (XFEM) provided by Abaqus FAE®. This allows for the analysis of moisture-induced crack propagation, which is visualised in **Fig. 5-1** for an arbitrary piece of wood that is dried from 12% to 7.7% moisture content using the version of the numerical model presented in paper IV. The crack initiation takes place once a tangential stress in tension is reached equal to 1.2 MPa.

The construction industry and the development of the Eurocode could greatly benefit from numerical models that can quickly analyse timber structures (moment, stress and displacement) subjected to both mechanical load and climate. Such a model is now available and is based on a more advanced FE-beam element (Ormarsson et al. 2013; Ormarsson and Gíslason 2016; Ormarsson and Steinnes 2014). The moisture and distortion analysis that are part of this frame model are, just as the numerical model presented in this thesis, uncoupled. The current moisture flow analysis can be used in conjunction with the frame model, to provide the two-dimensional moisture content data, related to the cross-section of the simulated

timber elements. In addition, the current distortion model can be used to analyse the stress also related to the cross-section, since this is not possible with the frame model (Ormarsson and Gíslason 2016).
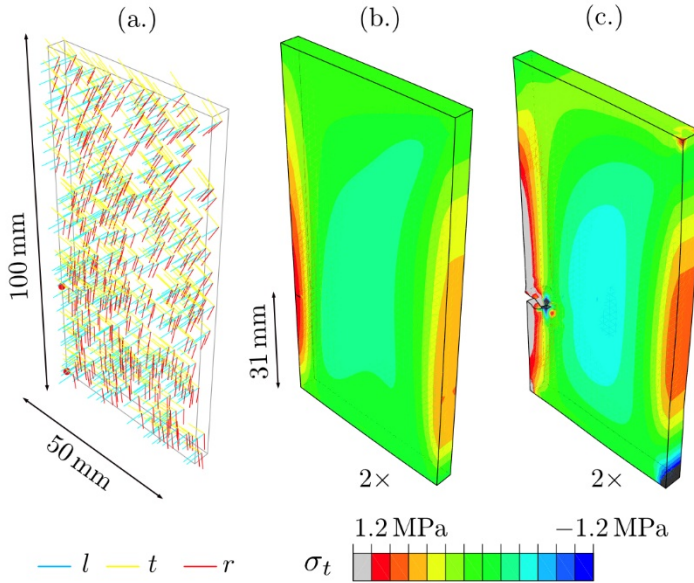
Fig. 5-1: *Tangential stress σ_t development and crack propagation for a piece of wood dried from 12% to 7.7% moisture content: a) material orientation, b) crack initiation after 14 days, and c) crack state after 208 days. Note: deformed shape is magnified by a factor 2*

The experiments conducted in the doctoral thesis as part of the second application are also suitable to be used to calibrate the frame model. To widen the range in which the frame model can be calibrated, additional tests at different temperatures and lower RH-ranges should be performed that relate both to indoor and outdoor climate using the proposed methodology. The experiments used in the current work are of relatively simple nature. The understanding of the moisture-induced mechanical behaviour of wood can benefit from the developments made in digital engineering (Muszyński 2006). A more thorough calibration and validation can be made of simulations using a combination of techniques such as X-ray computed tomography and digital image correlation, to get a better understanding of how moisture change and strain development relate. To the author's knowledge, these studies have been conducted separately (Couceiro et al. 2020; Larsen 2013), but never combined. Such experiments can also benefit the harvesting of material properties for specific wood species, specimen sizes, climate conditions and material models, and the subsequent validations of numerical models. In this process, it would be important to use end-matched specimens that follow the grain direction.

References

EN 13183-1 (2003) Moisture content of a piece of sawn timber - Part 1: Determination by oven dry method. European Committee for Standardization (CEN), Brussels.

EN 408 (2012) Structural timber - structural timber and glued laminated timber - determination of some physcial and mechanical properties. European Committee for Standardization (CEN), Brussels.

Absetz I (1999) The moisture equilibrium of softwoods above the fibre saturation point at the heartwood-sapwood boundary, TKK-TRT-101. Helsinki University of Technology, Espoo, Finland

Alexandersson M, Askfelt H, Ristinmaa M (2016) Triphasic model of heat and moisture transport with internal mass exchange in paperboard. Transport Porous Med, 112:381-408 doi:https://doi.org/10.1007/s11242-016-0651-9

Angst-Nicollier V (2012) Moisture induced stresses in glulam. Doctoral thesis, Norwegian University of Science and Technology (NUST), Trondheim, Norway

Angst V, Malo KA (2012) Moisture-induced stresses in glulam cross sections during wetting exposures. Wood Sci Technol, 47:227-241 doi:https://doi.org/10.1007/s00226-012-0493-8

Armstrong LD, Christensen GN (1961) Influence of moisture changes on deformation of wood under stress. Nature, 4791:869-870

Autengruber M, Lukacevic M, Füssl J (2020) Finite-element-based moisture transport model for wood including free water above the fibre saturation point. Int J Heat Mass Transf, 161 doi:https://doi.org/10.1016/j.ijheatmasstransfer.2020.120228

Avramidis S, Siau JF (1987) An investigation of the external and internal resistance to moisture diffusion in wood. Wood Sci Technol, 21:249-256 doi:https://doi.org/10.1007/BF00351396

Bengtsson C (2001) Variation of moisture induced movements in Norway spruce (*Picea abies*). Ann For Sci, 58:569-581 doi:https://doi.org/10.1051/forest:2001146

Bodig J, Jayne BA (1982) Mechanics of wood and wood composites. Van Nostrand Reinhold company, New York. ISBN 0894647776

Brandner R, Flatscher G, Ringhofer A, Schickhofer G, Thiel A (2016) Cross Laminated Timber (CLT): overview and development. Eur J Wood Prod doi:https://doi.org/10.1007/s00107-015-0999-5

Bratasz Ł, Kozłowska A, Kozłowski R (2012) Analysis of water adsorption by wood using the Guggenheim-Anderson-de Boer equation. Eur J Wood Prod, 70:445-451 doi:https://doi.org/10.1007/s00107-011-0571-x

Carlsson H, Thunell B (1975) Shrinking behaviour of wood during drying effect of tensile stresses. Paperi ja Puu, 7

Castera P Tensile creep of small wood specimens across the grain under drying conditions. In: IUFRO International Wood Drying Symposium, Seattle, 1989.

Couceiro J, Hansson L, Sehlstedt-Persson M, Vikberg T, Sandberg D (2020) The conditioning regime in industrial drying of Scots pine sawn timber timber studied by X-ray computed tomography: a case-study. Eur J Wood Wood Prod, 78:673-682 doi:https://doi.org/10.1007/s00107-020-01549-2

Dahlblom O (1987) Constitutive modelling and finite element analysis of concrete structures with regards to environmental influence, 1004, Report TVSM-1004. Lund Institute of Technology, Lund, Sweden

Dahlblom O, Persson K, Petersson H, Ormarsson S (1999) Inverstigation of variation of engineering properties of spruce. Paper presented at the IUFRO Wood Drying Conference: Wood Drying Research and Technology for Sustainable Forestry Beyond 2000, University of Stellenbosch, South Africa

Dassault Systèmes (2007) Writing user subroutines with ABAQUS. Dassault Systèmes, Vélizy-Villacoublay, France.

Dassault Systèmes (2017a) Simulia User Assistance 2017. Abaqus User Subroutines Reference Guide. Vélizy-Villacoublay, France

Dassault Systèmes (2017b) Simulia User Assistance 2017. Abaqus Theory Guide. Vélizy-Villacoublay, France

Di Blasi C (1997) Multi-phase moisture transfer in the high-temperature drying of wood particles. Chem Eng Sci, 53:353-366 doi:https://doi.org/10.1016/S0009-2509(97)00197-8

Dinwoodie JM (1981) Timber: its nature and behaviour, Second Edition. E&FN Spon Taylor & Francis Group. ISBN 0-419-25550-8

Dodoo A (2011) Life cycle primary energy use and carbon emission of residential buildings. Doctoral thesis, Mid Sweden University, Sundsvall, Sweden

Eitelberger J, Hofstetter K (2011) A comprehensive model for transient moisture transport in wood below the fiber saturation point: Physical background, implementation and experimental validation. Int J Therm Sci, 50:1861-1866 doi:https://doi.org/10.1016/j.ijthermalsci.2011.02.024

Engelund ET, Salmen L (2012) Tensile creep and recovery of Norway spruce influenced by temperature and moisture. Holzforsch, 66:959-965 doi:https://doi.org/10.1515/hf-2011-0172

Engelund ET, Thygesen LG, Hoffmeyer P (2010) Water sorption in wood and modified wood at high values of relative humidity. Part 2: Appendix. Theoretical assessment of the amount of capillary water in wood microvoids. . Holzforsch, 64:325-330 doi:https://doi.org/10.1515/hf.2010.061

Engelund ET, Thygesen LG, Svensson S, Hill CAS (2013) A critical discussion of the physics of wood-water interactions. Wood Sci Technol, 47:141-161 doi:https://doi.org/10.1007/s00226-012-0514-7

Eriksson J, Johansson H, Danvind J (2007) A mass transport model for drying wood under isothermal conditions. Dry Technol, 25:433 - 439 doi:https://doi.org/10.1080/07373930601183785

Everett DH, Whitton WI (1952) A general approach to hysteresis. Transactions of the Faraday Society, 48:749-757

Fick A (1995) On liquid diffusion. J Membr Sci, 100:33-38 doi:https://doi.org/10.1080/14786445508641925

Fortino S, Genoese A, Genoese A, Rautkari L (2013) FEM simulation of the hygro-thermal behaviour of wood under surface densification at high temperature. J Mater Sci, 48:7603-7612 doi:https://doi.org/10.1007/s10853-013-7577-1

Fortino S, Hradil P, Genoese A, Genoese A, Pousette A (2019a) Numerical hygro-thermal analysis of coated wooden bridge members exposed to Northern European climates. Constr Build Mater, 208:492-505

Fortino S, Hradil P, Koski K, Korkealaakso A, Fülöp L, Burkart H, Tirkkonen T (2021) Health monitoring of stress-laminated timber bridges assisted by a hygro-thermal model for wood material. Appl Sci, 11 doi:https://doi.org/10.3390/app11010098

Fortino S, Hradil P, Metelli G (2019b) Moisture-induced stresses in large glulam beams. Case study: Vihantasalmi bridge. Wood Mater Sci Eng, 14:366-380

Fortino S, Toratti T (2010) A three-dimensional moisture-stress FEM analysis for timber structures. Paper presented at the World Conference of Timber Engineering (WCTE), Italy, Trentino,

Frandsen HL (2007) Selected constitutive models for simulating the hygromechanical response of wood. Doctoral thesis, Aalborg University Aalborg, Denmark

Frandsen HL, Damkilde L, Svensson S (2007) A revised multi-Fickian moisture transport model to describe non-Fickian effects in wood. Holzforsch, 61:563-572 doi:https://doi.org/10.1515/HF.2007.085

Fredriksson M (2019) On wood-water interactions in the over-hygroscopic moisture range: mechanisms, methods and influence of wood modification. Forests, 10:779 doi:https://doi.org/10.3390/f10090779

Fredriksson M, Engelund ET (2018) Scanning or desorption isotherms? Characterising sorption hysteresis of wood. Cellulose, 25:4477-4485 doi:https://doi.org/10.1007/s10570-018-1898-9

Gerhards CC (1982) Effect of moisture content and temperature on the mechanical properties of wood: an analysis of immediate effects. Wood Fiber Sci, 14:4-36

Gowda S, Kortesmaa M, Ranta-Maunus A (1998) Duration of load effect on curved glulam beams, VTT Publications 334. VTT Building Technology, Espoo, Finland

Gustafsson PJ (2003) Timber Engineering. John Wiley & Sons Ltd., West-Sussex, England. ISBN 0-470-48869-8

Gustafsson PJ, Hoffmeyer P, Valentin G (1998) DOL behaviour of end-notched beams. Eur J Wood Prod, 56:307-317 doi:https://doi.org/10.1007/s001070050325

Hanhijärvi A (1998) Deformation properties of Finnish spruce and pine wood in tangential and radial directions in association to high temperature drying. Eur J Wood Prod, 56:373-380 doi:https://doi.org/10.1007/s001070050415

Hanhijärvi A (2000) Advances in the knowledge of the influence of moisture changes on the long-term mechanical performance of timber structures. Mater Struc, 33:43-49 doi:https://doi.org/10.1007/BF02481695

Hearmon RFS, Paton JM (1964) Moisture content changes and creep of wood. Forest Prod J, 8:357-359

Hering S, Niemz P (2012) Moisture-dependent, viscoelastic creep of European beech wood in longitudinal direction. Eur J Wood Prod, 70:667-670 doi:https://doi.org/10.1007/s00107-012-0600-4

Holzer SM, Loferski JR, Dillard DA (1988) A review of creep in wood: concepts relevant to develop long-term behavior predictions for wood structures. Wood Fiber Sci, 21:376-392

Huč S (2019) Moisture induced strains and stresses in wood. Doctoral thesis, Uppsala University, Uppsala, Sweden

Hunt DG (1989) Linearity and non-linearity in mechano-sorptive creep of softwood in compression and bending. Wood Sci Technol, 23:323-333 doi:https://doi.org/10.1007/BF00353248

Hunt DG (1999) A unified approach to creep of wood. R Soc, 455:4077-4095 doi:https://doi.org/10.1098/rspa.1999.0491

Hunt DG, Shelton CF (1988) Longitudinal moisture-shrinkage coefficients of softwoods at the mechano-sorption creep limit. Wood Sci Technol, 22:199-210 doi:https://doi.org/10.1007/BF00386014

International Energy Agency (2021) Buildings: A source of enormous untapped efficiency potential. International Energy Agency. URL: https://www.iea.org/topics/buildings.

Janssen H, Blocken B, Carmeliet J (2007) Conservative modelling of the moisture and heat transfer in building components under atmospheric excitation. Int J Heat Mass Transf, 50:1128-1140 doi:https://doi.org/10.1016/j.ijheatmasstransfer.2006.06.048

Johannesson B (2019) Thermodynamics of single phase continuous media: lecture notes with numerical examples. Lecture notes. Linnaeus University, Växjö, Sweden.

Johannesson B, Janz M (2009) A two-phase moisture transport model accounting for sorption hysteresis in layered porous building constructions. Build Environ, 44:1285-1294 doi:https://doi.org/10.1016/j.buildenv.2008.09.018

Keunecke D, Sonderegger W, Pereteanu K, Lüthi T, Niemz P (2007) Determination of Young's and shear moduli of common yew and Norway spruce by means of ultrasonic waves. Wood Sci Technol, 41:309-327 doi:https://doi.org/10.1007/s00226-006-0107-4

Kollmann FFP, Côté WA (1968) Principles of wood science and technology Part I: Solid wood. Springer-Verlag, Berlin, Heidelberg. ISBN 978-3-642-87930-2 doi:https://doi.org/10.1007/978-3-642-87928-9

Konopka D, Kaliske M (2018) Transient multi-Fickian hygro-mechanical analysis of wood. Comput Struct, 197:12-27 doi:https://doi.org/10.1016/j.compstruc.2017.11.012

Krabbenhøft K (2003) Moisture transport in wood a study of physical & mathematical models and their numerical Implementation. Doctoral thesis, Technical University of Denmark, Copenhagen, Denmark

Krabbenhøft K, Damkilde L (2004) Double porosity models for the description of water infiltration in wood. Wood Sci Technol, 38:641-659 doi:https://doi.org/10.1007/s00226-004-0253-5

Larsen F (2013) Thermal/moisture-related stresses and fracture behaviour in solid wood members during forced drying: modelling and experimental study. Doctoral thesis, Technical University of Denmark, Copenhagen, Denmark

Malo KA, Abrahamsen RB, Bjertnæs MA (2016) Some structural design issues of the 14-storey timber framed building 'Treet' in Norway. Eur J Wood Prod, 74:407-424 doi:https://doi.org/10.1007/s00107-016-1022-5

McMillen JM (1958) Stresses in wood during drying, 1652, 1652. Forest Products Laboratory Madison S. Wisconsin, Wisconsin, United States

Mmari W, Johannesson B (2020) Modeling transient and hysteretic hygrothermal processes in wood using the hybrid mixture theory. Int J Heat Mass Transf, 163 doi:https://doi.org/10.1016/j.ijheatmasstransfer.2020.120408

Mohager S, Toratti T (1993) Long term bending creep of wood in cyclic relative humidity. Wood Sci Technol, 27:49-59

Morlier P (1994) Creep in timber structures Rilem report 8. Rilem Technical Committee, London

Muszyński L (2006) Empirical data for modeling: methodological aspects in experimentation involving hygro-mechanical characteristics of wood. Dry Technol, 24:1115-1120 doi:https://doi.org/10.1080/07373930600778254

Muszyński L, Lagaňa R, Shaler SM, Davids W (2005) Comments on the experimental methodology for determination of the hygro-mechanical properties of wood. Holzforsch, 59:232-239 doi:https://doi.org/10.1515/HF.2005.037

Mårtensson A, Svensson S (1997) Stress-strain relationship of drying wood Part 2: Verification of a one-dimensional model and development of a two-dimensional model. Holzforsch, 51:565-570

Rijksdienst voor Ondernemend Nederland (2015) Infoblad energieneutraal bouwen: definitie en ambitie, RVO-035-1401/BR-DUZA. Ministerie van Binnenlandse Zaken en Koninkrijksrelatie, Utrecht, the Netherlands

Olsson L (2019) Fuktsäkerhet vid KL-träbyggande utan väderskydd: Fallstudie, fältmätningar och intervjuer, ID: 13548. Research Institute of Sweden (RISE), Kalmar, Sweden

Ormarsson S (1999) Numerical analysis of moisture related distortion in sawn timber. Doctoral thesis, Chalmers University of Technology, Gothenburg, Sweden

Ormarsson S, Dahlblom O (2013) Finite element modelling of moisture related and visco-elastic deformations in inhomogeneous timber beams. Eng Struct, 49:182-189 doi:https://doi.org/10.1016/j.engstruct.2012.10.019

Ormarsson S, Dahlblom O, Johansson M (2010) Numerical study of how creep and progressive stiffening affect the growth stress formation in trees. Trees, 24:105-115 doi:https://doi.org/10.1007/s00468-009-0383-3

Ormarsson S, Dahlblom O, Petersson H (1998) A numerical study of the shape stability of sawn timber subjected to moisture variation Part 1: Theory. Wood Sci Technol, 32:325-334 doi:https://doi.org/10.1007/BF00702789

Ormarsson S, Dahlblom O, Petersson H (1999) A numerical study of the shape stability of sawn timber subjected to moisture variation Part 2: Simulation of drying board. Wood Sci Technol, 33:407-423 doi:https://doi.org/10.1007/s002260050126

Ormarsson S, Gíslason Ó, V. (2016) Moisture-induced stresses in glulam frames. Eur J Wood Prod, 74:307-318 doi:https://doi.org/10.1007/s00107-016-1006-5

Ormarsson S, Steinnes JR (2014) An enhanced beam model for glued laminated structures that takes moisture, mechano-sorption and time effects into account. Paper presented at the World Conference of Timber Engineering, Quebec, Canada, August 10-14

Ormarsson S, Vessby J, Johansson M, Kuai L Numerical and experimental study on modular-based timber structures. In: Modular and Offsite Construction (MOC), Banff, Alberta, Canada, May 21-24 2019.

Ottosen N, Petersson H (1992) Introduction to the Finite Element Method. Prentice Hall, Lund. ISBN 0-13-473877-2

Ottosen N, Ristinmaa M (2005) The mechanics of constitutive modeling. Elsevier Science, Lund. doi:https://doi.org/10.1016/B978-0-08-044606-6.X5000-0

Pang S (2000) Modelling of stress development during drying and relief during steaming in *Pinus Radiata* lumber. Dry Technol, 18:1677-1696 doi:https://doi.org/10.1080/07373930008917806

Pang S (2007) Mathematical modeling of kiln drying of softwood timber: model development, validation, and practical application. Dry Technol, 25:421-431 doi:https://doi.org/10.1080/07373930601183751

Pang S, Keey RB, Langrish TAG (1995) Modelling the temperature profiles within boards during the high-temperature drying of *Pinus radiata* timber: the influence of airflow reversals. Int J Heat Mass Transf, 38:189-205 doi:https://doi.org/10.1016/0017-9310(95)90001-2

Peralta PN (1995) Sorption of moisture by wood within a limited range of relative humidities. Wood Fiber Sci, 27:13-21

Perré P, Turner IW (1999) A 3-D version of TransPore: a comprehensive heat and mass transfer computational model for simulating the drying of porous media. Int J Heat Mass Transf, 42:4501-4521 doi:https://doi.org/10.1016/S0017-9310(99)00098-8

Persson K (2000) Micromechanical modelling of wood and fibre properties. Doctoral thesis, Lund University, Lund, Sweden

Porteous J, Kermani A (2007) Structural timber design to Eurocode 5. Blackwell Publishing, United Kingdom. 978-14051-4638-8

Ramage MH et al. (2017) The wood from the trees: The use of timber in construction. Renew Sust Energ Rev, 68:333-359 doi:http://dx.doi.org/10.1016/j.rser.2016.09.107

Ranta-Maunus A (1975) The viscoelasticity of wood at varying moisture content. Wood Sci Technol, 9:189-205 doi:https://doi.org/10.1007/BF00364637

Ranta-Maunus A, Gowda S, Kortesmaa M (1998) Duration of load effect on LVL beams, 1899, 1899. VTT Building Technology, Espoo, Finland

Rémond R, Perré P, Mougel E (2005) Using the concept of thin dry layer to explain the evolution of thickness, temperature, and moisture content during convective drying of Norway Spruce boards. Dry Technol, 23:249-271 doi:http://dx.doi.org/10.1081/DRT-200047883

Risbrudt CD, Ritter MA, Wegner TH (2010) Wood handbook: wood as an engineering material. Forest Product Laboratory, Madison, Wisconsin.

Rosenkilde A (2002) Moisture content profiles and surface phenomena during drying of wood. Doctoral thesis, Royal Institute of Technology (KTH), Stockholm, Sweden

Rowell RM (2012) Handbook of Wood Chemistry and Wood Composites. CRC Press Inc, Boca Raton, Florida, USA. ISBN 9781439853818

Rybarczyk W (1973) Study on the development of mathematical model of mechanical properties of some wood materials undergoing changes in their moisture content 2, 66. Prace Institute of Technology Drewna, Poland

Salin J-G (1992) Numerical prediction of checking during timber drying and a new mechano-sorptive creep model. Eur J Wood Prod, 50:195-200 doi:https://doi.org/10.1007/BF02663286

Salin J-G (2008) Drying of liquid water in wood as influenced by the capillary fiber network. Dry Technol, 26:560–567 doi:https://doi.org/10.1080/07373930801944747

Salin J-G (2010) Problems and solutions in wood drying modelling: History and future. Wood Mater Sci Eng, 5:123-134 doi:https://doi.org/10.1080/17480272.2010.498056

Salin J-G (2011) Inclusion of the sorption hysteresis phenomenon in future drying models: some basic considerations. Maderas: Ciencia y Tecnologia, 13:173-182

Salin J-G, Wamming T (2008) Drying of timber in progressive kilns: simulation, quality, energy consumption and drying cost considerations. Wood Mater Sci Eng, 3:12-20 doi:https://doi.org/10.1080/17480270802561003

Samuelsson A, Arfvidsson J (1994) Measurement and calculation of moisture content distribution during drying. Paper presented at the 4th Internation IUFRO Wood Drying Conference, Rotorua, New Zealand, 1994, August 9-13

Santaoja K, Leino T, Ranta-Maunus A, Hanjijärvi A (1991) Mechano-sorptive structural analysis of wood by the ABAQUS finite element program. Laboratory of Structural Engineering, Espoo, Finland

Schniewind AP, Barrett JD (1972) Wood as a linear orthotropic viscoelastic material. Wood Sci Technol, 6:43-57

Serrano E, Enquist B, Vessby J Long term in-situ measurements of displacement, temperature and relative humidity in a multi storey residential CLT building. In: World Conference of Timber Engineering (WCTE), Quebec City, Canada, 10-14 August 2014.

Shi J, Avramidis S (2017a) Water sorption hysteresis in wood: I review and experimental patterns - geometric characteristics of scanning curves. Holzforsch, 71:307-316 doi:https://doi.org/10.1515/hf-2016-0120

Shi J, Avramidis S (2017b) Water sorption hysteresis in wood: II mathematical modeling - functions beyond data fitting. Holzforsch, 71:317-326 doi:https://doi.org/10.1515/hf-2017-0115

Siau JF, Avramidis S (1996) The surface emission coefficient of wood. Wood Fiber Sci, 28:178-185

Simpson W (1980) Sorption theories applied to wood. Wood Fiber Sci, 12:183-195

Simpson WT (1971) Equilibrium moisture content prediction for wood. For Prod J, 21:48-49

Skaar C (1988) Wood-water relations. Springer series in wood science. Springer-Verlag, Berlin. 3-540-19258-1

Swedish Wood (2021) Wood is a sustainable construction material. URL: https://www.swedishwood.com/wood-facts/about-wood/wood-and-the-environment/wood-is-a-sustainable-construction-material/.

Svensson S, Mårtensson A (2002a) Simulation of drying stresses in wood Part II: Convective air drying of sawn timber. Eur J Wood Prod, 60:72-80 doi:https://doi.org/10.1007/s00107-001-0266-9

Svensson S, Toratti T (2002b) Mechanical response of wood perpendicular to grain when subjected to changes of humidity. Wood Sci Technol, 36:145-156 doi:https://doi.org/10.1007/s00226-001-0130-4

Svensson S, Turk G, Hozjan T (2011) Predicting moisture state of timber members in a continuously varying climate. Eng Struct, 33:3064-3070 doi:https://doi.org/10.1016/j.engstruct.2011.04.029

Säll H (2002) Spiral grain in Norway spruce. Doctoral thesis, Linnaeus University, Växjö, Sweden

Thelandersson S, Larsen HJ (2003) Timber Engineering. John Wiley & Sons Ltd, The Atrium, Southern Gate, Chichester, West Sussex, England. ISBN 0-470-84469-8

Thygesen LG, Engelund ET, Hoffmeyer P (2010) Water sorption in wood and modified wood at high values of relative humidity. Part I: Results for untreated, acetylated, and furfurylated Norway spruce. Holzforsch, 64:315-323 doi:https://doi.org/10.1515/hf.2010.044

Time B (1998) Hygroscopic Moisture Transport in Wood. Doctoral thesis, Norwegian University of Science and Technology, Trondheim, Norway

Time B (2002a) Studies on hygroscopic moisture transport in Norway spruce (*Picea abies*) - Part 1: Sorption measurments of spruce exposed to cyclic step changes in relative humidity. Eur J Wood Prod, 60:271-276 doi:https://doi.org/10.1007/s00107-002-0303-3

Time B (2002b) Studies on hygroscopic moisture transport in Norway spruce (*Picea abies*) - Part 2: Modelling of transient moisture transport and hysteresis in wood. Eur J Wood Prod, 60:405-410 doi:https://doi.org/10.1007/s00107-002-0334-9

Toratti T (1992) Creep of timber beams in a variable environment. Doctoral thesis, Helsinki University of Technology, Helsinki, Finland

Wadsö L (1993) Unsteady-state water vapor adsorption in wood: an experimental study. Wood Fiber Sci, 26:36-50

van Blokland J, Olsson A, Oscarsson J, Adamopoulos S (2019) Prediction of bending strength of thermally modified timber using high-resolution scanning of fibre direction. Eur J Wood Prod, 77:327-340 doi:https://doi.org/10.1007/s00107-019-01388-w

Wiberg P (1996) CT-scanning during drying. Moisture distribution in Pinus Silvestris. Paper presented at the 5th International IUFRO Wood Drying Conference, Quebec, Canada, August 13-17

Wiberg P (1998) CT-scanning of moisture distributions and shell formation during wood drying. Doctoral thesis, Luleå University of Technology, Skellefteå, Sweden

Wiberg P, Morén TJ (1999) Moisture flux determination in wood during drying above fibre saturation point using CT-scanning and digital image processing. Eur J Wood Prod, 57:137-144

Wu Q, Milota MR (1994) The effect of creep and mechano-sorptive effect on stress development during drying. Dry Technol, 12:2057-2085 doi:https://doi.org/10.1080/07373939408962219

Yahiaoui K (1991) A rheological model to account for mechano-sorptive behaviour, Fundamental aspects on creep in wood. COST Workshop 508, Lund, Sweden

Yeo H, Eom C-D, Han Y, Kang W, Smith WB (2008) Determination of internal moisture transport and surface emission coefficients for Eastern white pine. Wood Fiber Sci, 40:553-561

Yeo H, Smith WB, Hanna RB (2002) Mass transfer in wood evaluated with a colorimetric technique and numerical analysis. Wood Fiber Sci, 34:557-665

Younsi R, Kocaefe D, Poncsak S, Kocaefe Y (2007) Computational modelling of heat and mass transfer during the high-temperature heat treatment of wood. Appl Therm Eng, 27:1424-1431

A NUMERICAL STUDY OF THE EFFECT OF GREEN-STATE MOISTURE CONTENT ON STRESS DEVELOPMENT IN TIMBER BOARDS DURING DRYING

S. Florisson*†

PhD Student
E-mail: sara.florisson@lnu.se

S. Ormarsson†

Professor
E-mail: sigurdur.ormarsson@lnu.se

J. Vessby†

Senior lecturer
E-mail: johan.vessby@lnu.se

(Received February 2018)

Abstract. Timber boards manufactured with a traditional sawing pattern often contain both heartwood and sapwood. In such boards, internal constraints can occur during drying because of a radial variation in green-state (GS) MC between the heartwood (30-60%) and sapwood region (120-200%). Despite such knowledge, the initial MC is seldom considered when evaluating kiln-drying schedules. The effect of GS MC on the development of tangential tensile stress during drying is studied for four types of timber boards. A numerical model was developed that can simulate transient nonlinear orthotropic moisture flow and moisture–induced stress and distortion in wood with the use of the finite element method. The stress analysis considers elastic, hygroscopic, and mechano-sorptive strain. The study shows that the GS MC does not significantly influence the maximum stress state, but that it does influence the time at which the maximum tangential tensile stress occurs at different exchange surfaces. This results in several periods in the drying schedule where unfavorable high stress situations in the tangential direction arise, which could lead to crack propagation.

Keywords: Green state, nonlinear, numerical, moisture transport, transient, timber drying, tangential stress.

INTRODUCTION

A variation in initial MC exists in timber boards fabricated from Norway spruce with a plain, rift, or quarter sawn. This variation occurs because such boards often contain both heartwood and sapwood in their cross-section. This article will focus on the effect of such green-state (GS) MC on the time, location, and size of critical tangential tensile stress values when they are dried from GS to EMC. These aspects are important to consider when the quality of timber boards needs to be managed against possible cracking and distortion during kiln-drying.

---

* Corresponding author
† SWST member

Physical Phenomenon of Moisture Transport in Wood

GS MC. The MC when felling a tree is referred to as the GS MC (Skaar 1988). For softwood species, such as Norway spruce (*Picea abies*) and Scots pine (*Pinus sylvestris*), this state of MC equilibrium is characterized by a radial variation that can range from 30% to 60% in the heartwood region and 120-200% in the sapwood region (Salin 1992; Samuelsson and Arfvidsson 1994; Absetz 1999; Larsen and Ormarsson 2012b; Larsen 2013). The variation is most clear and abrupt at the intersection of heartwood and sapwood, as seen in Fig 1. The pits in green sapwood are unaspirated and allow for an undisturbed flow of liquid water between the tracheids (Pang et al 1995). The cells in heartwood
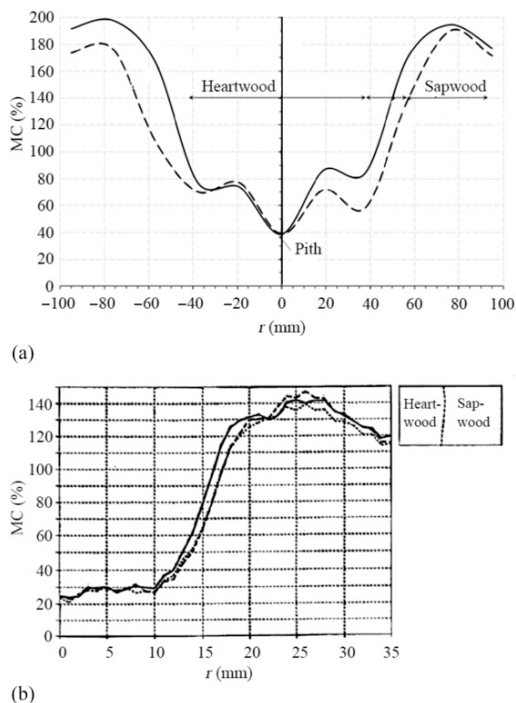
(a)

(b)

Figure 1.   Green state moisture variation in the radial direction r (a) obtained by slicing the cross-section and applying the oven-dry method (Larsen 2013, p. 41; Larsen and Ormarsson 2012b) and (b) obtained with X-ray attenuation (Absetz 1999, p. 12) for Norway spruce.

are dead, resulting in lower GS MC. The heartwood is also less permeable to moisture because of pit aspiration that occurs during the formation of heartwood and when felling the tree (Pang et al 1995).

Drying above fibre saturation point (FSP). The physical phenomena experienced during drying separate the wood-drying process into two significant phases; one above fibre saturation point (FSP) and one below FSP. Research shows that the physical behavior of moisture transport above FSP is still under great discussion. Most research articles indicate that the free water in sapwood migrates, because of capillary forces, toward an exchange surface or evaporation plane, where the bound-water diffusion controls the drying rate. Whether the position of the evaporation plane coincides with the exchange

surface, ie the physical surface of wood is not always determined. Wiberg (1996) simply suggests, based on MC profiles obtained with computerized tomography (CT) scanning, that the free water in sapwood migrates because of capillary forces toward the exchange surface, which results in gradient-free drying up to where the cross-section reaches FSP, as in Fig 2 (Wiberg 1998).

Pang et al (1995) and Rémond et al (2005) introduce the concept of evaporation plane, which is not necessarily located at the exchange surface. This plane divides the wood material into a wet zone underneath the plane and a dry zone above the plane. They state that free water in the wet zone moves according to the principles of capillary force in the direction of the evaporation surface. In the dry zone, the bound water and water vapor flow is governed by diffusion. Pang
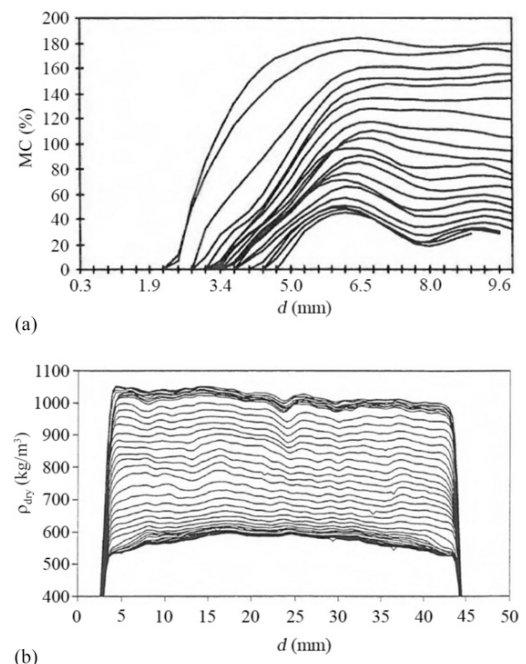

(a)

(b)

Figure 2.   (a) MC profile from surface to center of sample and (b) density profile from surface to surface obtained with CT scanning and digital image processing for timber boards of Scots pine (Wiberg 1996, 1998).

et al (1995) and Rémond et al (2005) suggest that the evaporation plane recedes into the material in the first phase of drying. Rémond et al (2005) propose a division of this first phase into two distinctive periods; a *constant drying rate period* and a *pseudo-constant drying rate period.*

At the beginning of the first period the evaporation surface moves slightly inward, creating a *dry shell* just below the exchange surface, as seen in Fig 2 (Pang et al 1995; Wiberg 1998). A balance between heat and mass transfer exists at the boundary and the drying rate is constant (Rémond et al 2005). The end of the *constant drying period* is indicated by the *point of irreducible saturation* (Eriksson 2005; Eriksson et al 2007). Some researchers believe that below this point, the flow governed by capillary pressure is no longer possible because of the interruption of the liquid path (Spolek and Plumb 1981; Nijdam et al 2000; Rosenkilde 2002). Krabbenhøft (2003), however, mentions that at lower degrees of saturation, free water collects at the ends of the tapered tracheids, and transport mainly takes place through the bordered pits. Salin (2008, 2010) suggests that a continuation of the liquid phase is established through possible links between water-filled clusters in the form of films, as seen with other materials.

The *pseudo-constant drying rate period* is characterized by a reduction in the drying rate, an increase in temperature, and a sensitivity to surface cracking. Pang et al (1995) and Rémond et al (2005) explain these phenomena as an inwardly receding evaporation front. This recession leads to an increasing length, that the water vapor needs to bridge to reach the exchange surface. Nonetheless, Wiberg (1996, 1998) presented experimental data in Fig 2 that does not indicate such further penetration of the evaporation surface. Rémond et al (2005) present experimental data that do show a drop in the drying rate during this second period. Finally, heartwood experiences similar phenomena. However, the drying process is only initiated in the *pseudo-constant drying rate period* because of the lower initial MC state and not in the *constant drying rate period* as seen

with sapwood (Pang et al 1995; Rémond et al 2005).

Dry shell. The aforementioned dry shell is signified by a rapidly receding evaporation surface, just below the material surface, at the beginning of the *constant drying-rate period*. This receding surface results in a steep gradient at the material surface and a high neighboring uniform MC level, Fig 2 (Pang et al 1995; Wiberg 1996; Wiberg and Morén 1999; Rosenkilde 2002; Salin 2010). The dry shell can develop because of damaged surface cells and aspiration of pits because of the processing of wood. The steepness of the gradient is dependent on the roughness of the surface layer (Eriksson 2005; Salin 2008). Wiberg and Morén (1999), and Pang et al (1995) suggest a gradient between 0.2 and 1.0 mm. This value should provide a distinction between the dry shell and the previously discussed receding evaporation front that was suggested by Pang et al (1995) and Rémond et al (2005) during the *pseudo-constant drying rate period*. Rémond et al (2005) question the existence of the thin dry shell, and, thus, call the recession of the evaporation plane during the *pseudo-constant drying rate period* the thin dry layer.

Drying below FSP. The second drying phase starts after the MC level reaches FSP, ie the *decreasing drying rate period* or the *hygroscopic range* (Pang et al 1995; Rémond et al 2005).The FSP indicates whether the cell walls are completely saturated with water, and no capillary water exists in the lumen or voids (Siau 1995; Dinwoodie 2000). According to Eitelberger and Hofstetter (2011), such a situation agrees with a RH of about 98%. In the hygroscopic range, the drying process is controlled by bound-water diffusion in the cell walls and the water vapor flow in the lumen. Hygroscopic strain occurs in this range, and the mechanical material properties are influenced by MC, eg see Ormarsson et al (1998).

Surface emission and diffusion. The previously mentioned dry shell contributes to the external resistance against moisture transport and

translates into an external mass transfer coefficient, or the more commonly used surface emission coefficient (SEC). The coefficient is a function of fluid characteristics such as temperature, velocity, and viscosity, and wood characteristics such as specific gravity, MC, and surface conditions (Siau and Avramidis 1996; Perré 2007). Similarly, the internal resistance against moisture transport is expressed by the diffusion coefficient (DC), which is a function of properties such as the composition of wood, temperature, and MC.

A correct mutual correlation between DC and SEC is vital to drying speed and the formation of moisture gradients close to the exchange surface. A relatively high SEC with regard to DC leads to receding steep gradients, whereas a relatively low SEC in terms of DC leads to flat MC profiles. Both coefficients are MC dependent. Siau (1995) shows how the value of DC exponentially decays with decreasing MC, whereas Yeo and Smith (2005) show the opposite effect for SEC. This difference contributes to the observation made by Wiberg (1998), where the dry shell starts to move inward only when the MC reaches FSP, indicating a lower resistance at the exchange surface and a higher SEC value; see Fig 2.

Modeling of Moisture Transport in Wood

Current state of knowledge. Total moisture diffusion models and phase separation models are used to model the moisture transport above and below FSP. The total moisture diffusion models, ie the Fickian models, describe the flux to be driven by a moisture gradient, and should be proportional to the DC. *Fick's first law* is a constitutive law and describes the moisture flux, whereas *Fick's second law* is a differential equation and is applicable when the MC is changing in time (Fick 1995). Fick's laws assume internal moisture equilibrium to be a function of RH given by the sorption isotherm (Krabbenhøft 2003). Applying these laws seems to give acceptable results below FSP, when relative slow transfer under isothermal conditions is assumed, and only one material property to simulate the

physical behavior of flow is required, viz the DC. The application seems less fruitful when only a small internal resistance to water vapor diffusion is encountered compared with the rate of sorption into the cell wall (Krabbenhøft 2003). This phenomenon might be because vapor penetrates the wood rapidly along available paths and voids, but absorbs moisture into the cell wall rather slowly (Salin 2010).

A more advanced way to model mass transport is via the phase separation model, also mentioned as the dual diffusion model or model for multi-Fickian behavior (Pang et al 1995; Perré and Turner 1999; Krabbenhøft 2003; Salin 2010; Eitelberger and Hofstetter 2011; Eitelberger et al 2011; Fortino et al 2013). Phase separation models treat the transport of free water, bound water, water vapor, and dry air with separate conservation equations, and use coupling terms to create links between the different phases (Krabbenhøft 2003; Salin 2010). For high-temperature drying, the conservation of mass needs to be complemented with the conservation of enthalpy or energy, which considers the conduction of heat, the changes in enthalpy due to phase change, and the convection of heat transfer (Krabbenhøft 2003; Fortino et al 2013). In Rémond et al (2005), such models are still incapable of describing all physical phenomena, especially for transport above FSP. Such phenomena can be referred to as non-Fickian effects.

The phase separation model is used in combination with Darcy's law for capillary flow and a separate Fick's law for bound-water diffusion and water vapor transport. The flow of liquid water through wood can be described as a gradient-driven phenomenon, when the capillary pressure can be established. Spolek and Plumb (1981) accomplish this by associating the capillary pressure with the level of saturation. Nevertheless, the use of Darcy's equation (Darcy 1856) seems to deviate from experimental results when applied for heartwood or kiln-dried interior sapwood, whereas it does not consider random blockage of tracheids due to aspirated pits (Bramhall 1971). In addition, this equation does not seem to account for physical phenomena, such as dry shell, gradient-free drying, and length

scale effect. To enclose these phenomena, Salin (2006a, 2006b, 2008, 2010) proposes the application of percolation theory, where a stochastic process describes the transport of moisture between tracheids.

Moisture and stress model. In this article, a three-dimensional numerical model will be presented, which is able to simulate moisture flow and moisture-induced stress development in timber boards. The model operates on a continuum level and consists of a total diffusion model, ie a transient nonlinear orthotropic Fickian model, and a moisture-induced stress model, ie distortion model, that regard elastic, hygroscopic, and mechano-sorptive strain behavior with the use of the finite element method. Ormarsson (1999) and Ormarsson et al (1998, 1999a, 1999b) previously developed the distortion model, which was extended in this article by adding a transient nonlinear moisture flow model that is able to simulate flow above and below FSP and regards an initial variation in MC and a boundary layer resistance, ie a convective boundary condition.

Transient Nonlinear Moisture Flow

The nonlinear orthotropic moisture transport above and below FSP is modeled using Fick's first law of diffusion as introduced in the section *Current state of knowledge*. As discussed in this section, the application of this law is straightforward and effective when applied for low isothermal drying conditions and requires only one type of material property, specifically the DC for orthotropic material. Although this law does not represent the exact physical behavior above FSP, it can simulate gradient-free drying fairly well. In this chapter, a brief description of the three-dimensional finite element (FE) formulation of nonlinear transient flow is given.

Constitutive equation. Fick's first law, Eq 1, describes the moisture flux $\bar{\mathbf{q}}$ to be proportional to the moisture-dependent diffusion matrix $\bar{\mathbf{D}}(w)$ governed by the moisture gradient vector $\bar{\nabla}w$. The bar indicates that the orthotropic material

directions refer to the orientation of the orthogonal local coordinate system. The same formulation in rate form is presented in Eq 2, where the dot indicates a change with respect to time.

$$\bar{\mathbf{q}} = -\bar{\mathbf{D}}\bar{\nabla}w \tag{1}$$

$$\dot{\bar{\mathbf{q}}} = -\dot{\bar{\mathbf{D}}}\bar{\nabla}w - \bar{\mathbf{D}}\bar{\nabla}\dot{w} \tag{2}$$

The moisture flux $\bar{\mathbf{q}}$, diffusion matrix $\bar{\mathbf{D}}(w)$, and moisture-gradient vector $\bar{\nabla}w$ can be transformed between the local and global coordinate systems by means of the transformation matrix $\mathbf{A}$; see Eqs 3-5. This matrix can account for pith direction and annual ring orientation $\mathbf{A}_0$, conical shape $\mathbf{A}_c$, and spiral grain $\mathbf{A}_s$, and is presented in Eq 6. The origins of these matrices are found in Ormarsson (1999) and Ormarsson et al (1998).

$$\mathbf{q} = \mathbf{A}\bar{\mathbf{q}} \tag{3}$$

$$\nabla w = \mathbf{A}\bar{\nabla}w \tag{4}$$

$$\mathbf{D} = \mathbf{A}\bar{\mathbf{D}}\mathbf{A}^T \tag{5}$$

$$\mathbf{A} = \mathbf{A}_0\mathbf{A}_c\mathbf{A}_s = \begin{bmatrix} l_{0x} & r_{0x} & t_{0x} \\ l_{0y} & r_{0y} & t_{0y} \\ l_{0z} & r_{0z} & t_{0z} \end{bmatrix} \begin{bmatrix} cos\phi & -sin\phi & 0 \\ sin\phi & cos\phi & 0 \\ 0 & 0 & 1 \end{bmatrix} \begin{bmatrix} \cos\theta & 0 & \sin\theta \\ 0 & 1 & 0 \\ -\sin\theta & 0 & \cos\theta \end{bmatrix} \tag{6}$$

Strong formulation. The strong formulation of the transient nonlinear flow is given in Eq 7. The formulation is known as Fick's second law of diffusion as presented in the section *Current state of knowledge*, and is nonlinear because of moisture dependency of the diffusion matrix $\bar{\mathbf{D}}(w)$. Eq 8 presents the convective boundary condition, Eq 9 the natural boundary condition, and Eq 10 the essential boundary condition,

$$\frac{\partial w}{\partial t} = div(\mathbf{D}(w)\nabla w) + Q \text{ in region } V \qquad (7)$$

$$q_n = s(w)(w - w_\infty) \text{ on surface } S_c \qquad (8)$$

$$q_n = \mathbf{q}^T\mathbf{n} = h \text{ on surface } S_h \qquad (9)$$

$$w = g \text{ on surface } S_g \qquad (10)$$

where $\partial w/\partial t$ is the rate of moisture change, Q is the moisture supplied to the body per unit time, and q_n is the flux normal to the exchange surface. The convective boundary condition described by Eq 8 is vital to this article. The condition describes the flux to be proportional to the MC-dependent SEC $s(w)$ and the driver $(w - w_\infty)$ expressed as the difference between surface MC and the MC of the ambient air.

Finite element formulation. The nonlinear finite-element formulation is presented in Eq 11, and Eqs 12-16 present an elaboration of the different matrices. The used approximation $w(x, y, z, t) = \mathbf{N}(x, y, z)\mathbf{a}(t)$ for the MC shows the shape functions to be position dependent and the nodal point values to be time dependent. The derivation of $w(x, y, z, t)$ with respect to time gives $dw/dt = \mathbf{N}\dot{\mathbf{a}}$, where $\dot{\mathbf{a}} = d\mathbf{a}/dt$. The convective boundary condition results in a complementary matrix, but is also present in the boundary vector $\mathbf{f}_b$.

$$(\mathbf{K} + \mathbf{K}_c)\mathbf{a} + \mathbf{C}\dot{\mathbf{a}} = \mathbf{f}_b + \mathbf{f}_l \qquad (11)$$

$$\mathbf{K} = \int_V \mathbf{B}^T\mathbf{D}(w)\mathbf{B} \, dV \qquad (12)$$

$$\mathbf{K}_c = \int_{S_c} s(w) \, \mathbf{N}^T\mathbf{N} \, dS \qquad (13)$$

$$\mathbf{C} = \int_V \mathbf{N}^T\mathbf{N} \, dV \qquad (14)$$

$$\mathbf{f}_b = -\int_{S_h} \mathbf{N}^T h \, dS - \int_{S_g} \mathbf{N}^T q_n \, dS + w_\infty \int_{S_c} \mathbf{N}^T s(w) \, dS \qquad (15)$$

$$\mathbf{f}_l = \int_V \mathbf{N}^T Q \, dV \qquad (16)$$

Ottosen and Petersson (1992) present a more detailed description of the finite-element formulation for convective boundary condition and Zienkiewicz and Taylor (1991) present nonlinear transient moisture flow.

Moisture-Related Deformations and Stress

The constitutive relation for the stress simulation is given as

$$\dot{\bar{\boldsymbol{\sigma}}} = \bar{\mathbf{C}}^{-1}\left(\dot{\bar{\boldsymbol{\varepsilon}}} - \dot{\bar{\mathbf{C}}}\bar{\boldsymbol{\sigma}} - \dot{\bar{\boldsymbol{\varepsilon}}}_h - \dot{\bar{\boldsymbol{\varepsilon}}}_{ws}\right) \qquad (17)$$

where the total strain and the elastic strain are given by

$$\dot{\bar{\boldsymbol{\varepsilon}}} = \dot{\bar{\boldsymbol{\varepsilon}}}_e + \dot{\bar{\boldsymbol{\varepsilon}}}_h + \dot{\bar{\boldsymbol{\varepsilon}}}_{ws} \qquad (18)$$

$$\dot{\bar{\boldsymbol{\varepsilon}}}_e = \bar{\mathbf{C}}\dot{\bar{\boldsymbol{\sigma}}} + \dot{\bar{\mathbf{C}}}\bar{\boldsymbol{\sigma}}. \qquad (19)$$

The constitutive relation consists of the elastic strain rate $\dot{\bar{\boldsymbol{\varepsilon}}}_e$, hygroscopic strain rate $\dot{\bar{\boldsymbol{\varepsilon}}}_h$, and mechano-sorptive strain rate $\dot{\bar{\boldsymbol{\varepsilon}}}_{ws}$. The elastic strain rate is expressed as the generalized Hooke's law using the local compliance matrix $\bar{\mathbf{C}}$ and its rate $\dot{\bar{\mathbf{C}}}$, and the local stress matrix $\bar{\boldsymbol{\sigma}}$ and its rate $\dot{\bar{\boldsymbol{\sigma}}}$. The matrix formulation for the different strain components and the finite element formulation are found in Ormarsson (1999) and Ormarsson et al (1998).

Problem Description

Model description. A three-dimensional numerical model was created in the finite element software ABAQUS[©] (Johnston, RI), patch number 2016. The simulation model consists of two types of analysis: a transient nonlinear moisture-flow analysis and the stress analysis that considers elastic, hygroscopic, and mechano-sorptive strain. Output data from the moisture analysis function as input data for the stress analysis. A general purpose linear brick element

Table 1. Impression of material properties and their relation to temperature and MC used in stress simulation.

$E_r = E_{r0} \cdot (1 + E_{rT}(T_0 - T)) + E_{rw}(w_f - w_a)$	Eq 20
$G_{rt} = G_{rt0} \cdot (1 + G_{rtT}(T_0 - T)) + G_{rtw}(w_f - w_a)$	Eq 21
$w_f = w_{f0} \cdot (1 + w_{fT}(T_0 - T))$	Eq 22
$m_r = m_{r0} \cdot (1 - m_{rT}(T_0 - T))$	Eq 23

is used for both moisture (DC3D8) and stress (C3D8) analyses. The element type combined with a characteristic edge length of 2 mm prevents spurious oscillation in the transient moisture analysis, which can be caused by steep gradients and perpendicular flow to the exchange surface. The model is scripted in Python© (Wilmington, DE) to generate flexibility and the ability to perform parametric studies.

The three-dimensional formulation of the moisture-dependent material behavior of wood was implemented in the user subroutine UMAT. All transformations of matrices between local and global coordinate systems for both moisture and

Figure 3. Four analyzed timber boards with a unique location of the pith with dimensions 50×200 mm containing both heartwood (dark area) with radius of 40 mm and sapwood (light area): (a) timber board B_1, (b) timber board B_2, (c) timber board B_3, and (d) timber board B_4.

stress simulations are implemented in the user subroutine ORIENT. The local coordinate system is used to define the orthotropic nature of wood and specify the longitudinal, radial, and tangential direction.

The material data needed to perform the nonlinear transient flow simulation can be found in section *Green State MC* and *Surface Emission and Diffusion Coefficient*. The material data needed to perform the stress analysis originates from Ormarsson et al (1998). A selection of parameters and their relation to temperature and MC can be found in Table 1. In this table, E_r is the modulus of elasticity in the radial direction, G_{rt} is the shear modulus in the radial-tangential plane, w_f is the FSP, and m_r is the mechano-sorption property in the radial direction. The parameters $E_{r0}, G_{rt0}, w_{f0}, m_{r0}$ are the basic values at the reference temperature of $T = T_0 = 20$°C. The parameters $E_{rT}, G_{rtT}, w_{fT}, m_{rT}$ describe the effect of temperature, and E_{rw}, G_{rtw} describe the effect of MC. The shrinkage properties for heartwood ($\alpha_r = 0.1$ and $\alpha_t = 0.2$) and sapwood ($\alpha_r = 0.17$ and $\alpha_t = 0.35$) are taken from Larsen and Ormarsson (2012a) and Larsen (2013).

Study description. The simulation model in this article will be used to study the effect of initial MC variation on the development of tensile stress in the tangential direction σ_t. A tensile strength of 0.5 MPa is assumed. This value corresponds to the weakest characteristic strength values of solid wood perpendicular to the grain. Figure 3 shows the four theoretical plain-sawn timber boards that were analyzed in this study. The boards have dimensions of 50×200 mm and a unique pith location. The radius of the heartwood area was chosen according to the experimental data in Fig 1(a) and has a value of 40 mm.

Two types of simulations were made for each timber board. The first simulation considered constant initial MC over the cross-section of 31%. The second simulation took into account a variation in initial MC. This variation was created with the method presented in the following section.
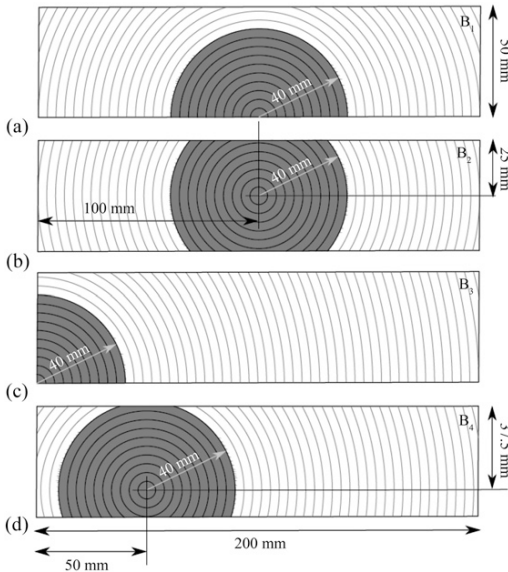
Green State MC

The initial moisture variation in the radial direction for the four timber boards is based on experimental data published by Larsen (2013). A polynomial expression was created by curve-fitting the data using the least square method. The expression can be used in the simulation model to automatically generate an initial MC field based on the location of the pith, see Fig 4. The expression results in an MC variation, which runs from 28.4% in the pith location to a value between 105% and 190% at the exchange surfaces. The exact value is dependent on the distance between the pith and outermost surface.

Surface Emission and Diffusion Coefficient

In literature, it is difficult to find a coherent set of experimentally obtained moisture-dependent SEC and DC (Siau and Avramidis 1996) that can be used for the transient nonlinear moisture simulation. The experimentally obtained moisture profiles by Rosenkilde (2002) were used to obtain a sufficient set of moisture-dependent coefficients to simulate realistic MC profiles. This was carried out by adjusting the set of moisture-dependent SECs from Yeo and Smith (2005) and DCs from Siau and Avramidis (1996) until the simulations fitted the drying speed and

curvature of the moisture profiles. The same climatic conditions apply for the experimental data and the simulation. The fitting is presented in Fig 5. The initial variation seen in Fig 5(a) was neglected because it is the result of premature drying and averaging of the MC of the wood slices.

The SEC data presented by Yeo and Smith (2005) and the data found with the fitting is presented in Fig 6. The values found with the fitting are much lower than the values found in literature. This implies a greater resistance at the boundary surface than for the experimentally obtained

(a)

(b)
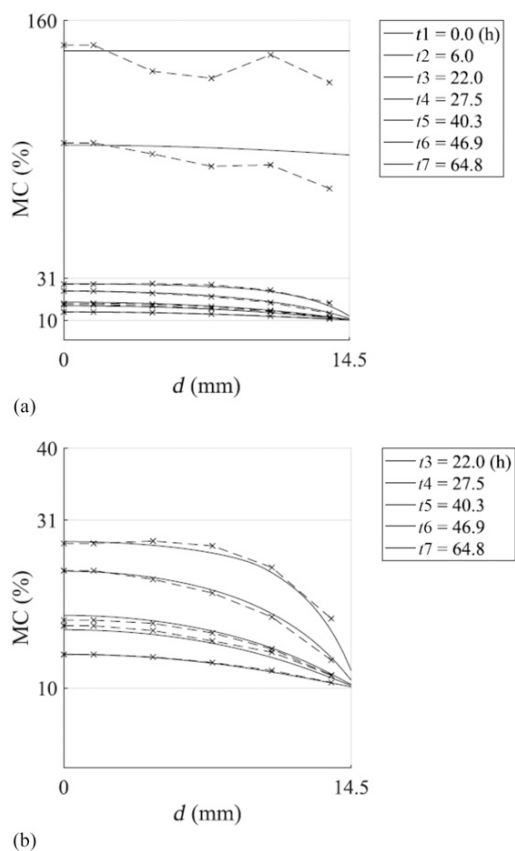
Figure 5. MC profiles obtained experimentally by Rosenkilde (2002) (dashed lines) and with nonlinear transient flow simulation model (solid lines) (a) MC profiles from center to surface, above and below FSP (b) MC profiles from center to surface, below FSP. The simulation was used to obtain SEC and DC data.

$$p(X,Y) = 0.434 - 5.3 \cdot 10^{-03}X - 3.87 \cdot 10^{-16}Y$$
$$+ 69.56X^2 - 1.29 \cdot 10^{-14}XY$$
$$+ 69.55Y^2 + 0.119\,X^3 + 3.5 \cdot 10^{-16}\,X^2Y$$
$$+ 9.89 \cdot 10^{-02}XY^2 - 2.78 \cdot 10^{-17}Y^3 - 748.1X^4$$
$$+ 2.86 \cdot 10^{-13}X^3Y - 1496X^2Y^2$$
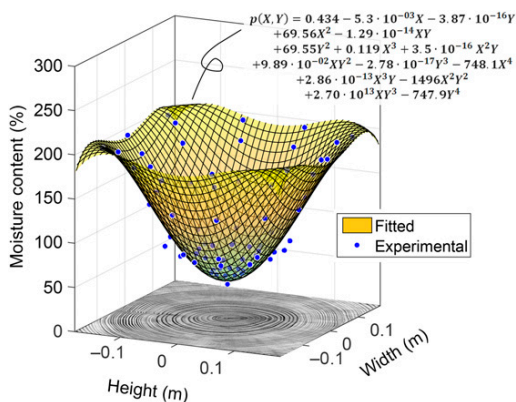$$+ 2.70 \cdot 10^{13}XY^3 - 747.9Y^4$$

Figure 4. Green state MC data as presented in Figure 1 by Larsen (2013) and curve-fitted polynomial function used for the numerical simulations.

Figure 6.   Moisture-dependent surface emission coefficient *s* obtained experimentally and with the simulation model for the MC profiles illustrated in Fig 5.

values. This is especially the case at the beginning of the drying process, when the samples are above FSP.

The DC data presented by Siau and Avramidis (1996) and the data found with the fitting is presented in Fig 7. The values found with the fitting are much higher than the values found in literature. This mainly indicates that the process above FSP is much quicker. Under the section *Drying above FSP*, it was seen that the drying process can be divided into three phases. These phases are clearly seen in the diffusion data. The *point of irreducible saturation*, which divides the *constant drying rate period* and the *pseudo-constant drying rate period*, is clearly seen around 105% MC.
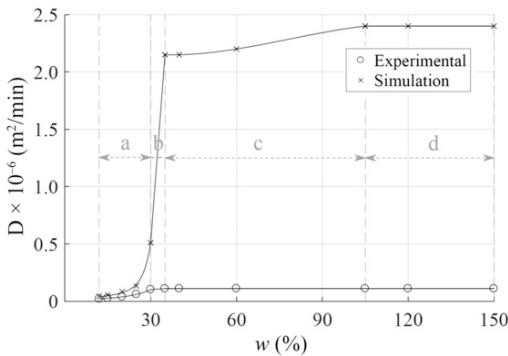
Figure 7.   Moisture-dependent diffusion coefficient *D* obtained experimentally and with the simulation model for MC profiles illustrated in Fig 5.

It can also be seen that at 31% MC the *decreasing drying period* is starting, because of the large decrease in DC.
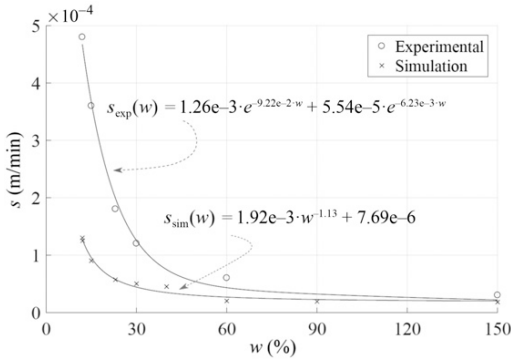
In the section *Physical Phenomenon of Moisture Transport in Wood*, different suggestions are given on how the moisture profiles look above FSP according to recent literature. The aforementioned fitting showed that a correct drying speed and shape of moisture profiles can only be found with a combination of specific SEC and DC data. The SEC mainly influences the formation of moisture gradients at the exchange surface, whereas the DC largely influences the drying speed.

RESULTS AND DISCUSSION

The two different simulations of boards introduced under the subchapter *Problem Description* will be indicated as $B_{n,c}$ and $B_{n,v}$, where index c refers to the simulation with a constant initial MC, v refers to the simulation with variation in initial MC, and n is the number
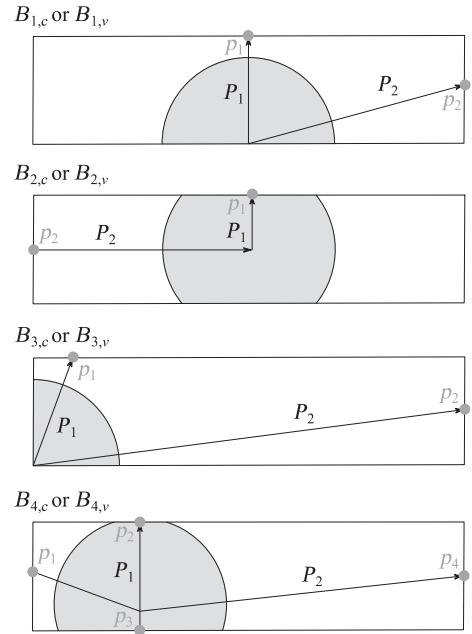
Figure 8.   Orientation of paths P_1 and P_2 and location of material points $p_{i,c}$ and $p_{i,v}$ for the different types of timber boards that were illustrated in Fig 3.

corresponding to the board type as illustrated in Figs 3 and 8. The results will, among other things, be presented along two paths, which are indicated by P_1 and P_2. The results presented in material points will be indicated by $p_{i,c}$ and $p_{i,v}$, where i is the number of the material point. Figure 8 shows the orientation of paths and location of material points for the different timber boards.

## Moisture and Stress Development in Timber Board B_1

In this section, a general discussion of the first timber board B_1 will be given based on the results found for the simulation that takes into account an initial variation in MC $B_{1,v}$. This is done to clarify most phenomena that can be expected when drying timber boards from GS to EMC and to enable an easier discussion in the next sections.

Timber boards that are subjected to drying conditions will experience a continuous change in the tangential stress state σ_t. In this situation, the change in state is mainly influenced by the hygroscopic and mechano-sorptive behavior of wood and can be described as *stress-overturn* or *stress reversal*. Figures 9(b) and (d) and 10(b) and (d) show this phenomenon along paths P_1 and P_2, respectively, whereas Figs 9(a) and (c) and 10(a) and (c) show the corresponding moisture profiles. It should be noted that the jump in the stress field is caused by the abrupt change in shrinking properties between heartwood and sapwood.

Norway spruce experiences a strong variation in MC between the heartwood and sapwood region in GS as was discussed in section *GS MC*. The moisture profile in Figs 9(a) and 10(a) at the beginning of the drying process shows an initial MC between 30% and 40% for the heartwood region (*d* between 0 and 40 mm) and between 40% and 105% for the sapwood region. This means that the heartwood area lies closer to the FSP of 27%. The color plots in Figs 9(c) and 10(c) clearly show that the initial variation in MC results in a nonuniform moisture gradient along the exchange surface, which develops more

rapidly below FSP in the heartwood region because of the low initial MC in this area.

The highest tensile stress values are found in the areas where the annual rings run parallel to the board's exchange surface. At the beginning of the drying process, these areas develop into a tension front, which slowly moves into the timber board, leaving behind an area in compression. This process occurs within the first 2.5 da of the drying process for path P_1 and can be seen in Fig 9(b) and (d). A similar situation is seen for path P_2 in Fig 10(b) and (c), but for a shorter period of time.

The concept of *stress reversal* together with the movement of the tension area creates a risk for cracks to initiate at the exchange surface and with a possible propagation into the timber board. It is seen that this process along path P_1 and P_2 takes place at different times. The maximum tensile stress for path P_2 takes longer to develop and remains greater than the critical value of 0.5 MPa for a shorter period of time. In next section, it can be seen that this difference in process is caused by the initial moisture variation.

The area around the intersection between the sapwood and heartwood region also develops into a tension area during the drying process. This development is clearly seen in Figs 9(d) and 10(d). The tension area that develops in this region is partly caused by the difference in shrinkage properties between heartwood and sapwood, and does not show any sign of *stress reversal*. It is important to notice that this tension front occurs at the end of the drying process and creates a third situation where high enough tensile stress values in the tangential direction can initiate cracks. This time, the high level of tensile stress occurs within the cross-section.

Maximum Tensile Stress for Boards B_1 to B_4

Figure 11 shows the tangential stress profiles for the points in time at which the maximum stress values are found for all the simulations $B_{n,c}$ and $B_{n,v}$. The illustrations are used to analyze the influence of constant and varying initial MC on time and maximum stress size. The graphs show
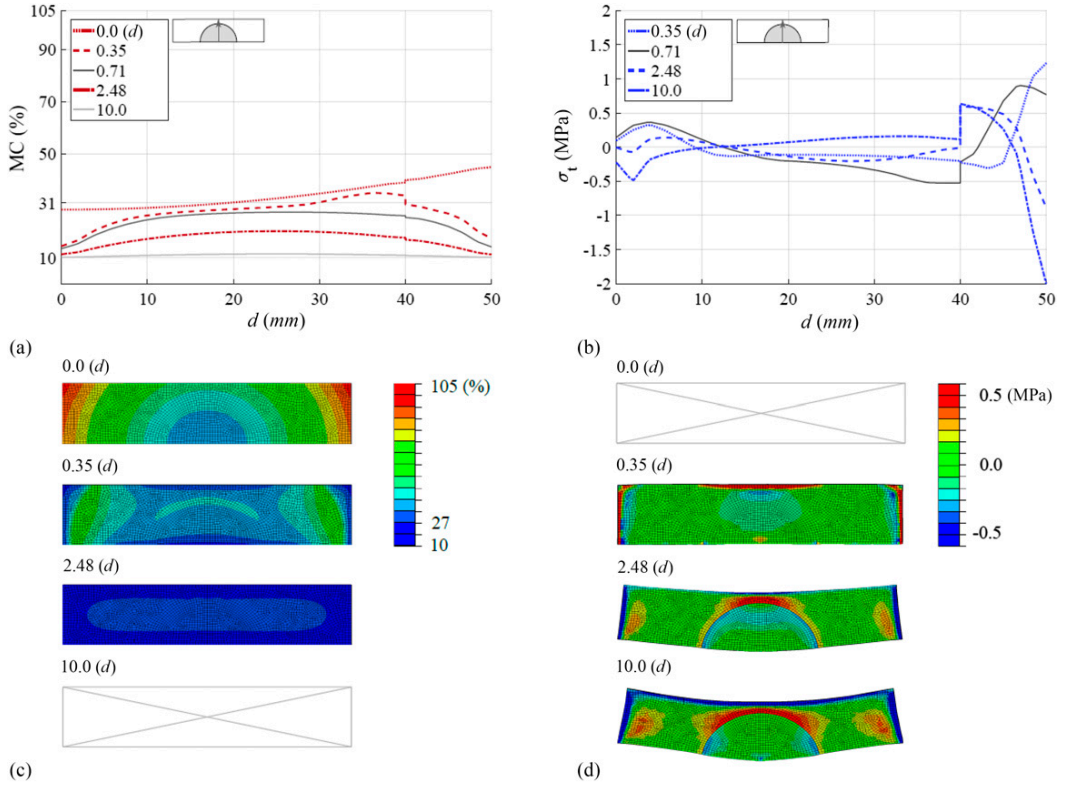
Figure 9.   Illustration of MC and stress variation for board $B_{1,v}$: (a) MC profiles along path P_1 for significant times, (b) tangential stress profiles along path P_1, (c) complementary MC color plots for some of the times used in (a), and (d) complementary tangential stress color plots for some of the times in (b). (The distortion of the cross-section is magnified 3 times.)

the tangential stress variation for the four boards presented in Figs 3 and 8 along paths P_1 and P_2.

The variation in initial MC influences the formation of MC-gradients early on in the drying process. The simulations with a constant initial MC showed an MC gradient that is uniform along the entire exchange surface because of the identical diffusion properties in the radial and tangential direction. The simulations with an initial variation in MC showed a nonuniform MC gradient, which in the beginning of the drying process quickly developed in the heartwood region in contrast to the sapwood region because of the low MC. This phenomenon results in an area within the timber boards that will start to shrink early on in the drying process and will influence

the cupping behavior. The simulations showed that cupping is only visible when a sufficient gradient below FSP is created along most of the exchange surface.

The graphs in Fig 11 show that the location in which the maximum tangential tensile stress occurs is not influenced by an initial variation in MC. However, the sawing pattern does have a great influence on the location. It is observed that the maximum tangential tensile stress occurs in the areas where the annual rings align in a parallel fashion to the exchange surface. The maximum stress level is generally higher for simulations in $B_{n,c}$ as compared with $B_{n,v}$ and occurs much earlier on in the drying process. The initial variation in MC seems to decrease the maximum
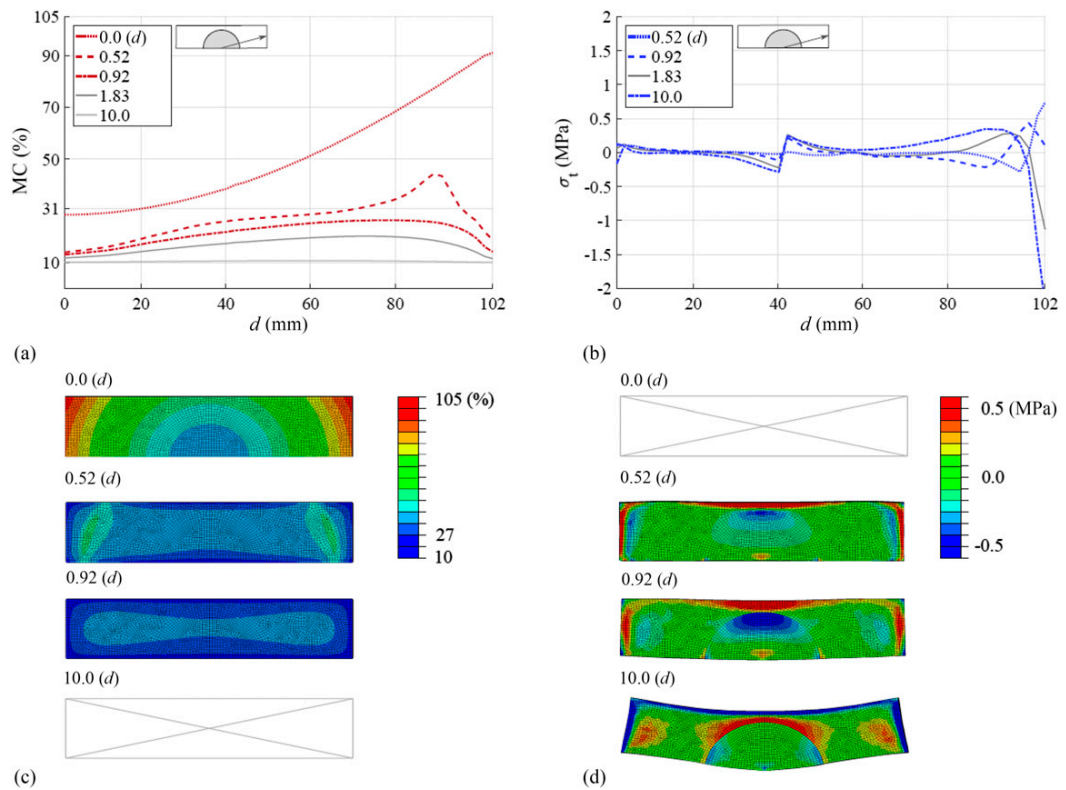
Figure 10.   Illustration of MC and stress variation in board $B_{1,v}$: (a) MC profiles along path P_2 for significant times, (b) tangential stress profiles along path P_2, (c) complementary MC color plots for some of the times used in (a), and (d) complementary tangential stress color plots for some of the times in (b). (The distortion of the cross-section is magnified 3 times.)

stress level because of the nonuniform MC gradient in the beginning of the drying process, which leads to a nonuniform shrinking pattern. Nevertheless, the stress level is still high enough to cause initiation of cracks.

The first row of graphs in Fig 11 corresponds to path P_1. This path runs from the lower surface to the upper surface through the pith. The second row of graphs in Fig 11 corresponds to path P_2, which runs from the left surface to the right surface through the pith. The difference in stress values between the simulations $B_{n,c}$ and $B_{n,v}$ can be found in the caption of Fig 11 in percentages. The highest stress values and the highest difference in stress values between simulations $B_{n,c}$ and $B_{n,v}$ are mostly found for path P_2. This path is most

affected by the high variation in moisture. One exception is found for the symmetrical board B_3. This board experiences very little cupping deformation at the end of drying, which suggests that the initial variation in MC and the annual ring orientation strongly influence the development of the maximum tangential tensile stress.

The time at which the highest tensile stress levels occur differ significantly between the simulations that take into account a constant initial MC and a variation in initial MC. In addition, the comparison made between the paths P_1 and P_2 shows that the highest stress levels for the simulations $B_{n,c}$ occur almost simultaneously in the drying process. This is not seen for the simulations $B_{n,v}$, where

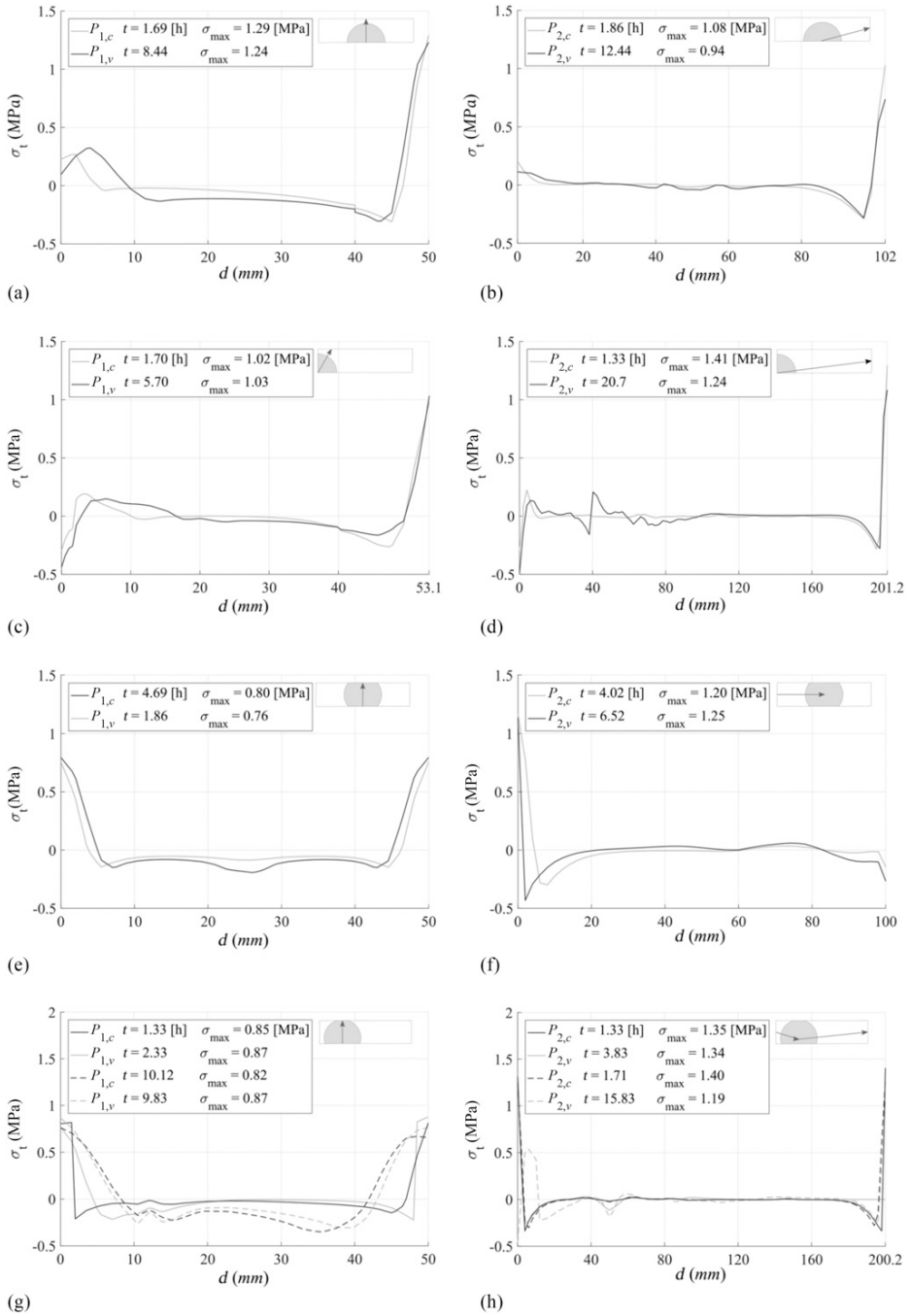Figure 11.   Path plots for tangential tensile stress states for boards $B_{n,c}$ and $B_{n,v}$ at times when maximum stress values occur. The difference in percentage between $B_{n,c}$ and $B_{n,v}$ are for (a) P_1: -3.9%, (b) P_2: -13.0%, (c) P_1: $+1.0\%$, (d) P_2: -12.1%, (e) P_1: -5.0%, (f) P_2: $+4.2\%$, (g) P_1: $+2.34\%$ and $+6.1\%$, and (h) P_2: -0.7% and -15%.

the variation in MC at GS seems to increase the time interval at which high stress levels between different exchange surfaces occur. This means that the initial variation in MC leads to a drying process where multiple points in time exist when cracks can develop at the exchange surface.

It is also noted that the highest tensile stress does not necessarily occur once the boards start to cup. For boards $B_{n,c}$, this would be the case, but for $B_{n,v}$, it was not. The cupping of the cross-section occurs once most of the exchange surface is sufficiently below FSP, which often does not align with the time period at which the maximum tensile stress values are formed. As a last note, it should be said that no significant trend could be found on whether the absolute difference in the GS moisture variation had an impact on the size of the tangential tensile stress.

Stress Development over Time for Boards B_1 to B_4

Figure 12 shows the development of the maximum tangential tensile stress in time. This can be done because the area in which the maximum stress occurs is not affected by the way in which the initial MC variation is defined. Each graph in Fig 12 corresponds to a specific timber board. For each board, the material points that have been proven relevant based on the results presented in Fig 11 were analyzed.

The graphs presented in Fig 12 give more insight into the concept of *stress reversal*. This phenomenon is present for all simulations $B_{n,c}$ and $B_{n,v}$, and at every exchange surface, unless the pith is located directly at the surface. The graphs clearly show that the most critical stress areas first develop into a tension front, whereafter they gradually turn into a compression front. It also confirms what has been suggested in the previous section. There, it was seen that this happens in multiple points at the exchange surface and at different points in time. It is also seen that the boards with an initial variation in MC experience a *stress reversal* that generally takes a
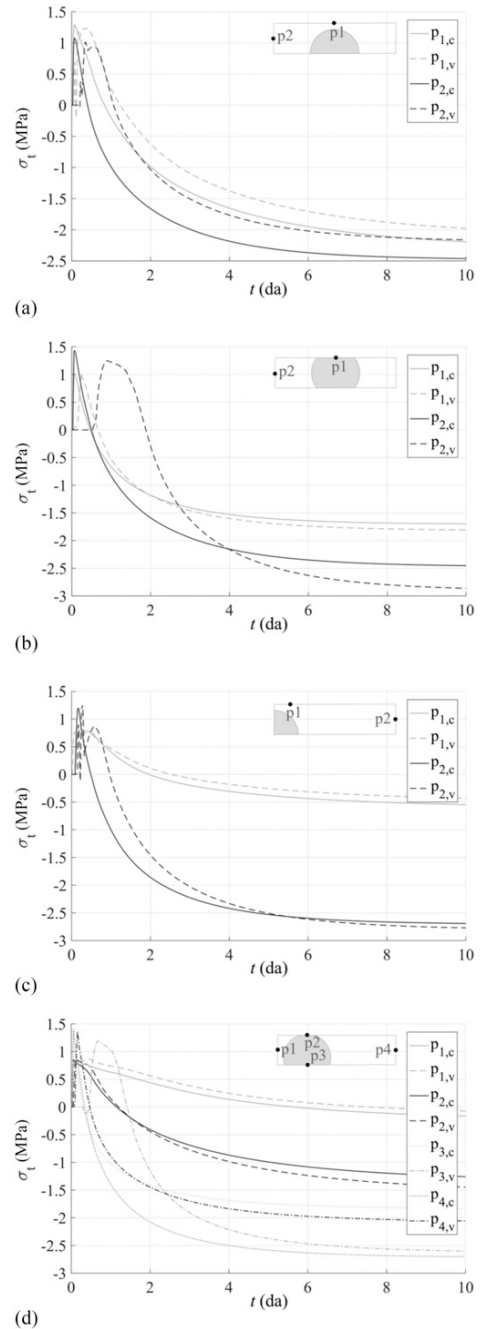

Figure 12.   History plots for material points with maximum tangential tensile stress in (a) board B_1, (b) board B_2, (c) board B_3, and (d) board B_4. The maximum stress values can be found in Fig 11.

longer period of time. This means that the peaks in tangential tensile stress continue and create a situation where it is vulnerable to crack development.

CONCLUSIONS

The development of moisture-induced tangential tensile stress has been studied by means of numerical simulations for four different configurations of Norway spruce timber boards, which were dried from GS to EMC below FSP. The results were compared with numerical results of the same boards, but with constant initial MC. The following conclusions can be drawn from the presented results and discussion:

1. The change of the moisture profiles in time over the cross-section of the studied boards is very important for the accurate prediction of moisture-induced stress development and distortion of the cross-section. The shape of these profiles and the speed in which they change is very much dependent on the correct correlation between diffusion and SEC.
2. The initial variation in MC at GS results in a nonuniform moisture gradient close to the exchange surface, which influences the shrinking and distortion behavior of the cross-section in the early stages of drying.
3. The variation in initial MC does not influence the location where the maximum tangential tensile stress occurs. It is seen that the areas where the annual rings align parallel to the exchange surface are prone to high levels of tensile stress and *stress reversal* in the early stages of drying. The areas where the heartwood and sapwood regions intersect also seem prone to high tangential tensile stress. However, the highest tensile stress in these areas often only occur at the end of the drying process and do not show any signs of *stress reversal.*
4. The size of the highest level of tensile stress in the tangential direction for boards $B_{n,v}$ was generally lower than that of the boards $B_{n,c}$. For boards $B_{n,v}$, the tensile stress often took a longer time to develop, was present over a longer period of time, and was high enough to cause cracking.

5. It is very important to carefully simulate the variation in MC when an accurate prediction is desired for the periods at which the highest tensile stress occurs at different exchange surfaces. At three different periods of time, high tensile stress values can be expected; two at the exchange surface where the *stress reversal* occurs early during the drying, and one at the interface between heartwood and sapwood at the end of the drying process.
6. All four timber boards simulated in the current study show the phenomenon of *stress reversal* at multiple exchange surfaces early on in the drying process. This phenomenon creates a situation where a crack can initiate and subsequently propagate, but also close later on in the drying process.
7. The previous conclusions give a picture on how critical stress situation in the tangential direction develop during the drying of timber boards. The results show that it is not only important to take into account the initial variation in MC to obtain a better prediction of the critical stress level, but also to get an idea of when, where, and for how long such critical situations can be experienced. The study contributes to the understanding of crack initiation and possible propagation in timber boards during drying. The picture can also greatly benefit the optimization of drying schedules designed by kiln operators.

REFERENCES

Absetz I (1999) The moisture equilibrium of softwoods above the fibre saturation point at the heartwood-sapwood boundary. Helsinki University of Technology, Espoo, Finland, TKK-TRT-101.

Bramhall G (1971) The validity of Darcy's law in the axial penetration of wood. Wood Sci Technol 5: 121-134.

Darcy H (1856) Les fontaines publiques de la ville de Dijon, exposition et application des principes a suivre et des formules a employer dans les questions de distribution d'eau. Dalmont V Editeur, Paris, France.

Dinwoodie JM (2000) Timber: Its nature and behaviour, 2nd Edition. E&FN Spon Taylor & Francis Group, London, UK. ISBN 0-419-25550-8.

Eitelberger J, Hofstetter K (2011) A comprehensive model for transient moisture transport in wood below the fiber saturation point: Physical background, implementation and experimental validation. Int J Therm Sci 50: 1861-1866.

Eitelberger J, Hofstetter K, Dvinskikh SV (2011) A multiscale approach for simulation of transient moisture transport processes in wood below the fiber saturation point. Compos Sci Technol 71:1727-1738.

Eriksson J (2005) Moisture transport and moisture induced distortion in timber—An experimental and numerical study. PhD thesis, Department of Structural Engineering, Chalmers University of Technology, Gothenburg, Sweden.

Eriksson J, Johansson H, Danvind J (2007) A mass transport model for drying wood under isothermal conditions. Dry Technol 25:433-439.

Fick A (1995) On liquid diffusion. J Membr Sci 100: 33-38.

Fortino S, Genoese A, Genoese A, Nunes L (2013) Numerical modelling of the hygro-thermal response of timber bridges during their service life: A monitoring case-study. Constr Build Mater 47:1225-1234.

Krabbenhøft K (2003) Moisture transport in wood a study of physical and mathematical models and their numerical implementation. PhD thesis, Department of Civil Engineering, Technical University of Denmark, Copenhagen, Denmark.

Larsen F (2013) Thermal/moisture-related stresses and fracture behaviour in solid wood members during forced drying: Modelling and experimental study. PhD thesis, Department of Civil Engineering, Technical University of Denmark, Copenhagen, Denmark.

Larsen F, Ormarsson S (2012a) Numerical and experimental study of moisture-induced stress and strain field developments in timber logs. Wood Sci Technol 47: 837-852.

Larsen F, Ormarsson S (2012b) A numerical and experimental study of temperature and moisture related fracture behaviour in timber logs. Holzforschung.

Nijdam JJ, Langrish TAG, Keey RB (2000) A high-temperature drying model for softwood timber. Chem Eng Sci 55:3585-3598.

Ormarsson S (1999) Numerical analysis of moisture related distortion in sawn timber. PhD thesis, Department of Structural Mechanics, Chalmers University of Technology, Gothenburg, Sweden.

Ormarsson S, Dahlblom O, Petersson H (1998) A numerical study of the shape stability of sawn timber subjected to moisture variation part 1: Theory. Wood Sci Technol 32: 325-334.

Ormarsson S, Dahlblom O, Petersson H (1999a) A numerical study of the shape stability of sawn timber subjected to moisture part 2: Simulation of drying board. Wood Sci Technol 33:407-423.

Ormarsson S, Dahlblom O, Petersson H (1999b) A numerical study of the shape stability of sawn timber subjected to moisture variation part 3: Influence of annual ring orientation. Wood Sci Technol 34:207-219.

Ottosen N, Petersson H (1992) Introduction to the finite element method. Prentice Hall, London, UK. ISBN 0-13-473877-2.

Pang S, Keey RB, Langrish TAG (1995) Modelling the temperature profiles within boards during the high-temperature drying of *Pinus radiata* timber: The influence of airflow reversals. Int J Heat Mass Transfer 38(2):189-205.

Perré P (2007) Fundamentals of wood drying. A.R.BO.LOR: Nancy, France, European COST.

Perré P, Turner IW (1999) A 3-D version of transPore: A comprehensive heat and mass transfer computational model for simulating the drying of porous media. Int J Heat Mass Transfer 42:4501-4521.

Rémond R, Perré P, Mougel E (2005) Using the concept of thin dry layer to explain the evolution of thickness, temperature, and moisture content during convective drying of Norway spruce boards. Drying Technol 23: 249-271.

Rosenkilde A (2002) Moisture content profiles and surface phenomena during drying of wood. PhD thesis, Building materials, KTH Royal Institute of Technology, Stockholm, Sweden.

Salin J-G (1992) Investigation of heartwood/sapwood and wood anisotropy influence on timber drying by a two-dimensional simulation model. 8th International Drying Symposium, August 2-5, Montreal, Quebec, Canada.

Salin J-G (2006a) Modelling of the behaviour of free water in sapwood during drying. Wood Mater Sci Eng 1(1): 4-11.

Salin J-G (2006b) Modelling of the behaviour of free water in sapwood during drying. Wood Mater Sci Eng 1(2): 45-51.

Salin J-G (2008) Drying of liquid water in wood as influenced by the capillary fiber network. Dry Technol 26: 560-567.

Salin J-G (2010) Problems and solutions in wood drying modelling: History and future. Wood Mater Sci Eng 5(2): 123-134.

Samuelsson A, Arfvidsson J (1994) Measurement and calculation of moisture content distribution during drying. 4th International IUFRO Wood Drying Conference, August 9-13, 1994, Rotorua, New Zealand.

Siau JF (1995) Wood: Influence of moisture on physical properties. Virginia Polytechnic Institute and State University, Keen, NY. ISBN 0-9622181-0-3.

Siau JF, Avramidis S (1996) The surface emission coefficient of wood. Wood Fiber Sci 28(2):178-185.

Skaar C (1988) Wood-water relations. Springer series in wood science. Springer-Verlag, Berlin, Germany. ISBN 3-540-19258-1.

Spolek GA, Plumb OA (1981) Capillary pressure in softwoods. Wood Sci Technol 15:189-199.

Wiberg P (1996) CT-scanning during drying. Moisture distribution in *Pinus sylvestris*. 5th International IUFRO

Wood Drying Conference, August 13-17, 1996, Quebec, Canada.

Wiberg P (1998) CT-scanning of moisture distributions and shell formation during wood drying. Thesis, Division of Wood Physics, Luleå University of Technology, Skellefteå, Sweden.

Wiberg P, Morén TJ (1999) Moisture flux determination in wood during drying above fibre saturation point using CT-scanning and digital image processing. Holz Roh Werkst 57:137-144.

Yeo H, Smith WB (2005) Development of a convective mass transfer coefficient conversion method. Wood Fiber Sci 37(1):3-13.

Zienkiewicz OC, Taylor RL (1991) The finite element method. McGraw-Hill, London, UK.

II

ORIGINAL

Three-dimensional orthotropic nonlinear transient moisture simulation for wood: analysis on the effect of scanning curves and nonlinearity

Sara Florisson[1] · Johan Vessby[1] · Winston Mmari[1] · Sigurdur Ormarsson[1]

Abstract

This paper introduces, with the development of user-subroutines in the finite-element software Abaqus FEA®, a new practical analysis tool to simulate transient nonlinear moisture transport in wood. The tool is used to revisit the calibration of moisture simulations prior to the simulation of mechanical behaviour in bending subjected to climate change. Often, this calibration does not receive sufficient attention, since the properties and mechanical behaviour are strongly moisture dependent. The calibration of the moisture transport simulation is made with the average volumetric mass data experimentally obtained on a paired specimen of Norway spruce (*Picea abies*) with the dimensions $30 \times 15 \times 640\,\text{mm}^3$. The data, from a 90-day period, were measured under a constant temperature of 60 °C and systematic relative humidity cycles between 40 and 80%. A practical method based on analytical expressions was used to incorporate hysteresis and scanning behaviour at the boundary surface. The simulation tool makes the single-Fickian model and Neumann boundary condition readily available and the simulations more flexible to different uses. It also allows for a smoother description of inhomogeneity of material. The analysis from the calibration showed that scanning curves associated with hysteresis cannot be neglected in the simulation. The nonlinearity of the analysis indicated that a coherent set of moisture dependent diffusion and surface emission coefficient is necessary for the correct description of moisture gradients and mass transport.

✉ Sara Florisson
sara.florisson@lnu.se

Johan Vessby
johan.vessby@kau.se

Winston Mmari
winston.mmari@lnu.se

Sigurdur Ormarsson
sigurdur.ormarsson@lnu.se

[1]   Linnaeus university Faculty of Technology, Växjö, Sweden

🙂 Springer

Introduction

Lack of standard test method leads to diversity

A popular method to determine the strength and stiffness of wood is the three- or four-point bending test. This method is not the most straightforward, though in bending the beam experiences both tension and compression simultaneously and therefore cannot result in valid material level properties (Morlier 1994; Muszyński 2006). However, the flexural test is still a common method to experimentally calibrate (numerical) models, especially long-term behaviour when subjected to dynamic changes in climate (Honfi et al. 2014; Ma et al. 2017; Mohager and Toratti 1993). Here, the definition of calibration is the iterative process of adjusting material properties and comparing the model to experimental data until good agreement is found.

There are no standard test methods available to study the long-term behaviour of timber beams. Therefore, much diversity is found between published experimental setups (Morlier 1994), but also between the calibrations from simulations based on experimental data. Often, only the total deflection measured between the bearing supports is used and no elaboration is given of the measurements made of mass change or hygro-expansion. The flow (Skaar 1988; Yeo and Smith 2005; Yeo et al. 2002) and mechanical properties (Dinwoodie 1981; Siau 1995) as well as the mechanical behaviour associated with long-term behaviour under climate variations are strongly dependent on moisture (Ormarsson 1999; Ranta-Maunus 1975). Therefore, the importance of performing a calibration of the moisture flow model (moisture model) prior to the calibration of the moisture induced mechanical behaviour (distortion model) (Angst-Nicollier 2012) is understood. However, in the context of the four-point bending test, this is not always sufficiently exercised.

The moisture model presented in this paper is part of a more thorough study that focuses on improving the calibration of models based on long-term experimental data obtained with the traditional four-point bending setup subjected to variations in climate. The overall experiment is based on the methodology, where the deflection curve is conceptually separated into an elastic, creep, hygro-expansion and mechano-sorptive component. A climate and load schedule is used to stimulate the dissection of the curve and, together with measurements of mass change, helps to isolate the effects of mechano-sorption. The mechano-sorption is a second order phenomenon, i.e. it cannot be measured independently, such as the elastic and creep component (Muszyński 2006). The current publication will focus on the calibration of the moisture model based on experimental data. The calibration of the distortion model will be treated in a future publication.

Single-Fickian model more suitable in practice

Moisture transport in wood at the microscopic level is observed below the fibre saturation point (FSP) as water vapour diffusion in the lumen, bound water diffusion in the cell walls and as sorption processes between these two phases (Frandsen 2007; Krabbenhøft 2003). The most traditional way to simulate moisture transport is with

a single-Fickian model (Fick 1855–1995), which can describe moisture transport below FSP on the scale of annual rings. A more advanced model is the multi-Fickian model (Eitelberger and Hofstetter 2011; Eriksson et al. 2007; Fortino et al. 2013a; Frandsen et al. 2007a; Johannesson 2019; Konopka and Kaliske 2018) or the multiphase moisture transport model (Alexandersson et al. 2016; Di Blasi 1997; Fortino et al. 2013b; Janssen et al. 2007; Krabbenhøft and Damkilde 2004; Pang et al. 1995; Perré and Turner 1999; Younsi et al. 2007). The multi-Fickian model uses separate equations to describe each moisture phase and coupling terms to describe the sorption rate between phases. The classical multiphase model assumes equilibrium between moisture phases at all times. The equations are not separated, and a total diffusion tensor or matrix is used to combine the phases (Krabbenhøft and Damkilde 2004).

Hence, the multiphase models are more accurate from a physics standpoint. The single-Fickian models tend to be suitable at lower relative humidity (RH) (below 65%) (Frandsen 2007; Konopka and Kaliske 2018; Krabbenhøft 2003). Here, the moisture transport is characterised by slow bound water transport and relatively fast sorption, and the ratio between surface emission and diffusion coefficient used to describe the transport is high (Konopka and Kaliske 2018). Compared to the multiphase model, the single-Fickian model is simpler to implement and a more efficient model to simulate engineering problems.

The importance of modelling sorption hysteresis

For wood, the sorption isotherm plays a fundamental role in the numerical simulations of moisture transport, both for the single-Fickian and multiphase models. The sorption isotherm, i.e. the relation between equilibrium moisture content (EMC) (0–FSP%) and ambient RH (0–100%), is characterized by an envelope created from the so-called border desorption (drying) and adsorption (wetting) isotherms, which are obtained at the first complete drying and wetting (Frandsen 2007; Time 1998). Traditionally, the sorption isotherm for wood is determined on wood fibres (Shi and Avramidis 2017a, c), but the effect is also present on large-scale wooden and timber elements (Svensson et al. 2011).

The difference in EMC between the desorption and adsorption isotherms for equal ambient climatic conditions is referred to as sorption hysteresis (Engelund et al. 2013; Fredriksson and Engelund 2018). This indicates that the EMC is not only dependent on RH, but also on moisture history. Between the border isotherms, the EMC follows a unique path that is dependent on the previous moisture content (MC) changes experienced, which creates so-called intermediate or scanning curves (Frandsen 2007). The paths occur under a slope that is not necessarily identical for desorption and adsorption curves. It is not uncommon to use the average sorption isotherm, without the effect of hysteresis, to describe the relation between EMC and RH when performing simulations (Salin 2011). However, such an assumption can lead to a significant deviation from the measured MC (Frandsen et al. 2007b; Time 2002b) and will affect the moisture gradients and rate of moisture change, important to describe the moisture dependent mechanical behaviour.

The most traditional way to model hysteresis and its associated scanning curves is with the independent domain model (Everett and Whitton 1952). Peralta (1995) first applied this model to wood. The challenges with this model are the lack of experimental data on scanning curves and the double integral that needs to be solved to obtain EMC (Frandsen 2007; Shi and Avramidis 2017b). A more recent hysteresis model was proposed by Frandsen et al. (2007b), which is largely used in the hygroscopic computational literature for wood, and other building materials (Fortino et al. 2019; Huč 2019; Johannesson and Janz 2009; Svensson et al. 2011). The model can be used in combination with the multi-Fickian model, where both RH and MC are driving forces behind moisture transport below FSP.

Novelty is of technical nature

The purpose of the current work is to present a new practical tool to simulate nonlinear transient moisture transport. The user-subroutine frameworks associated with this tool are provided by finite-element software Abaqus FEA® (Dassault Systemes, Vélizy-Villacoublay, France). The work further develops the research previously published by Florisson et al. (2019). The research objectives related to the development of the simulation tool are: (1) the implementation of the single-Fickian approach and the moisture-dependent diffusion coefficient in user-subroutine UMATHT, which is usually used in the field of polymers, freezing soil and fire engineering; (2) the implementation of the moisture flux vector normal to the boundary surface in user-subroutine FILM, which is described by the moisture dependent material property named the surface emission coefficient (Yeo and Smith 2005; Yeo et al. 2002); (3) implementation of a practical method in user-subroutine FILM to describe sorption hysteresis and scanning behaviour at the boundary surface. Unique expressions are used for each adsorption and desorption curve to interpolate between RH and the experimentally obtained EMC at the end of each RH-period.

The simulation tool will be used to revisit the calibration of moisture transport model made prior to the simulation of moisture-dependent mechanical behaviour in bending. The calibration is based on experimentally obtained volumetric average moisture content. The experimental method is relatively simple compared to other methods, such as nuclear magnetic resonance (NMR) and computerised tomography (CT), which give a more detailed representation of the moisture gradient and change in wooden components (Rosenkilde 2002; Wiberg 1998). However, the test method is chosen to allow for the simultaneous measurement of mass and deflection in the same climatic environment for a long period of time. The research objectives related to the analysis of the calibration are: (1) to use the simulation tool to perform a fit on moisture content profiles obtained under similar climatic conditions and thus obtain a coherent set of moisture dependent diffusion and surface emission coefficients prior to the calibration of the moisture transport model, and (2) to visualise the effect of moisture gradients and mass transport by analysing sorption behaviour and nonlinearity of analysis.

Material and methods

The following section will introduce the governing equation for the nonlinear transient moisture transport together with the constitutive laws. A finite element formulation for the problem will be presented and the Jacobian matrix will be derived to iteratively solve the nonlinear equation system. The implementation of the equation system into Abaqus, using the user-subroutines, will be highlighted as well. Finally, the simulation model, the experiment used to calibrate this model, and the method used to evaluate the calibration will be discussed.

Moisture transport model

A single-Fickian approach is used to analyse the orthotropic nonlinear transient moisture flow in wood. The governing equation is derived from the mass balance law and expressed as

$$c\rho\frac{\partial w}{\partial t} + \boldsymbol{\nabla} \cdot (\boldsymbol{q}) = 0 \tag{1}$$

where c is the moisture capacity in m³/kg, ρ is the density of liquid moisture in kg/m³, w is the unit-less moisture content, t is time in h, $\boldsymbol{\nabla}$ is the divergence and $\boldsymbol{q}$ is the moisture flux in m/h. The $(\cdot)$ denotes the operation where the components of $\boldsymbol{\nabla}$ are applied to the corresponding components of $\boldsymbol{q}$ and summated. The constitutive law for the moisture flux is described by Fick's law of diffusion defined as

$$\bar{\boldsymbol{q}} = -\bar{\boldsymbol{D}}(w, T)\bar{\boldsymbol{\nabla}}w \tag{2}$$

where $\boldsymbol{D}$ is a moisture and temperature dependent diffusion matrix in m²/h and T is temperature in °C. The parameter with the over-line, i.e. $(\bar{\cdot})$ in Eq. (2) refers to the orthogonal local coordinate system. The constitutive law for the flux normal to the boundary q_n in m/h is defined as

$$q_n = s(w, T)\big(w - w_\infty\big) \tag{3}$$

where s is a moisture and temperature dependent surface emission coefficient in m/h and w_∞ the unit-less moisture content in the ambient air. The geometry is assumed to be discretized into finite elements, each with an approximation of the moisture content, weight function, and their respective gradients as

$$\begin{aligned} w = \boldsymbol{Na}, \quad v = \boldsymbol{c}^{\mathrm{T}}\boldsymbol{N}^{\mathrm{T}}, \\ \boldsymbol{\nabla}w = \boldsymbol{Ba}, \quad \boldsymbol{\nabla}v = \boldsymbol{c}^{\mathrm{T}}\boldsymbol{B}^{\mathrm{T}} \end{aligned} \tag{4}$$

where $\boldsymbol{N}$ is a shape function vector, $\boldsymbol{a}$ is a nodal moisture content vector, $\boldsymbol{c}$ is an arbitrary vector and $\boldsymbol{B} = \boldsymbol{\nabla N}$. A backward Euler time integration scheme is used to account for the derivative in time and by following the steps suggested by Johannesson (2019) leads to the definition of the residual $\boldsymbol{\psi}$ for each finite element as

$$\boldsymbol{\psi}(\boldsymbol{a}_{n+1}) =: \frac{1}{\Delta t} \int_V \boldsymbol{N}^{\mathrm{T}} c\rho \boldsymbol{N}(\boldsymbol{a}_{n+1} - \boldsymbol{a}_n) \mathrm{d}V$$
$$+ \int_V \boldsymbol{B}^{\mathrm{T}} \boldsymbol{DB} \boldsymbol{a}_{n+1} \mathrm{d}V \qquad (5)$$
$$+ \int_A \boldsymbol{N}^{\mathrm{T}} s \boldsymbol{N} \boldsymbol{a} \, \mathrm{d}A - \int_A \boldsymbol{N}^{\mathrm{T}} s w_\infty \, \mathrm{d}A$$

where the subscript to a quantity, $(\cdot)_{n+1}$ denotes the value of the quantity at the current time step, and $(\cdot)_n$ the value at previous known time step at equilibrium, separated by a time increment Δt. The last two terms in Eq. (5) will only be nonzero for the elements at the boundary of the domain.

Numerical solution

The Newton–Raphson method is used to iteratively solve the nonlinear system of equations, see Eq. (5). Assuming an initially known iteration state $i-1$, with known residual $\boldsymbol{\psi}^{i-1} = \boldsymbol{\psi}(\boldsymbol{a}_{n+1}^{i-1})$ and known $\boldsymbol{a}_{n+1}^{i-1}$ and $\boldsymbol{a}_n$, a truncated Taylor expansion is performed to achieve the residual $\boldsymbol{\psi}^i = \boldsymbol{\psi}(\boldsymbol{a}_{n+1}^i)$ at the next iteration i as

$$\boldsymbol{\psi}^i = \boldsymbol{\psi}^{i-1} + \left(\frac{\partial \boldsymbol{\psi}^{i-1}}{\partial \boldsymbol{a}_{n+1}^{i-1}} \right) (\boldsymbol{a}_{n+1}^i - \boldsymbol{a}_{n+1}^{i-1}) \qquad (6)$$

For the iteration, i to be at equilibrium, i.e. $\boldsymbol{\psi}^i = 0$, Eq. (6) can be rewritten into a system of linearized equations used to determine $\boldsymbol{a}_{n+1}^i$. More on how to derive and solve this linearized equation can be found in Johannesson (2019). The Jacobian (or tangent diffusion matrix), $\boldsymbol{K}_{\mathrm{t}}$ is defined as

$$\boldsymbol{K}_{\mathrm{t}} = \left(\frac{\partial \boldsymbol{\psi}^{i-1}}{\partial \boldsymbol{a}_{n+1}^{i-1}} \right) = \frac{\boldsymbol{C}^{i-1}}{\Delta t} + \tilde{\boldsymbol{C}}^{i-1} + \boldsymbol{K}^{i-1} + \tilde{\boldsymbol{K}}^{i-1} + \boldsymbol{K}_{\mathrm{c}}^{i-1} + \tilde{\boldsymbol{K}}_{\mathrm{c}}^{i-1} - \boldsymbol{F}_{\mathrm{b}} \qquad (7)$$

where using Eq. (5), we have

$$\boldsymbol{C} = \int_V \boldsymbol{N}^{\mathrm{T}} c\rho \boldsymbol{N} \, \mathrm{d}V \qquad (8)$$

$$\tilde{\boldsymbol{C}} = \int_V \boldsymbol{N}^{\mathrm{T}} \frac{\partial c}{\partial w} \boldsymbol{N} (\boldsymbol{a}_{n+1}^{i-1} - \boldsymbol{a}_n) \boldsymbol{N} \mathrm{d}V \qquad (9)$$

$$\boldsymbol{K} = \int_V \boldsymbol{B}^{\mathrm{T}} \boldsymbol{DB} \mathrm{d}V \qquad (10)$$

$$\tilde{\boldsymbol{K}} = \int_V \boldsymbol{B}^{\mathrm{T}} \frac{\partial \boldsymbol{D}}{\partial w} \boldsymbol{B} \boldsymbol{a}_{n+1}^{i-1} \boldsymbol{N} \mathrm{d}V \qquad (11)$$

$$K_c = \int_A N^T s N dA \tag{12}$$

$$\tilde{K}_c = \int_A N^T \frac{\partial s}{\partial w} N a^{i-1} N dA \tag{13}$$

$$\tilde{F}_b = \int_A N^T \frac{\partial s}{\partial w} w_\infty N dA \tag{14}$$

The Jacobian is updated in each Newton–Raphson iteration.

Implementation user-subroutines

Abaqus uses the Newton Raphson method as a default numerical technique to solve the nonlinear equilibrium equations (Dassault Systèmes 2017a). The motivation for this choice is primarily the convergence rate obtained with this method. Abaqus FAE® enters user-subroutines UMATHT and FILM at each iteration (Dassault Systèmes 2017b). The routines are used by Abaqus FAE® to derive the Jacobian and define the necessary matrices and load vectors. Results are available at the beginning and end of each time increment. The subroutines are written in programming language FORTRAN (The Fortran Company, Colorado, USA). Routine UMATHT requires the user to define the following items:

- The moisture capacity c
- The derivative of the capacity towards moisture $\partial c/\partial w$
- The derivative of the capacity towards the spatial gradients of moisture $\partial c/\partial \bar{\nabla} w$
- The flux vector $\bar{q}$
- The derivative of the flux vector towards moisture $\partial \bar{q}/\partial w = \partial \bar{D}/\partial w \bar{\nabla} w$
- The derivative of the flux vector towards the spatial gradients of moisture $\partial \bar{q}/\partial \bar{\nabla} w = \bar{D}$

The routine also provides so-called state variables that can be used to store and reintroduce certain variables. Because the flux vector and moisture content are automatically reintroduced by the routines, and all other variables only need to be defined at the end of the time increment, state variables were not used in this analysis.

By assigning the subroutine FILM to the necessary surface, the routine can find the corresponding elements that need to be considered for the analysis. Important variables sent into the routine are the current moisture content values and corresponding time. The routine requires the user to define the following items:

- The ambient MC of the air w_∞
- The surface emission coefficient s
- The derivative of the surface emission coefficient towards moisture $\partial s/\partial w$

For simplicity, it is assumed that Eq. (1) is divided by the density and capacity and that this inverse of density and capacity is implicitly taken care of by the diffusion coefficient later obtained from calibration. Further, the analysis is performed under constant temperature, simplifying the diffusion matrix. The orthotropic material orientation was defined in user-subroutine ORIENT as a local coordinate system (longitudinal, radial and tangential). The local system was described by direction cosiness, based on the global coordinate system (x, y, and z). A more detailed description of theory and implementation can be found in Ormarsson (1999) and Ormarsson et al. (1998).

Abaqus model

A three-dimensional model was created to simulate the nonlinear transient moisture transport in a wood beam. The beam was obtained from the cross section of a log at a distance of 130 mm from pith, see Fig. 1. The cut followed the conical slope of the tree. The wood beam had a constant width of 15 mm, a constant height of 30 mm and a total length of 640 mm. The beam had a spiral grain angle θ of 4°.

The moisture transport analysis was performed with a fixed time increment Δt, see "Numerical solution" section, of 0.1 h over a total period of 2880 h (120 days). The increment size, chosen based on the distortion simulation subsequent to the moisture transport simulation, was small enough to assure satisfactory results and large enough to get acceptable computation time. The simulation was performed with element type DC3D8 and an element size of 2.5 mm over the cross section of the beam and 5 mm over the length of the beam, see Fig. 2. The orthotropic material orientation of the beam as defined in user-subroutine ORIENT is also shown in Fig. 2.
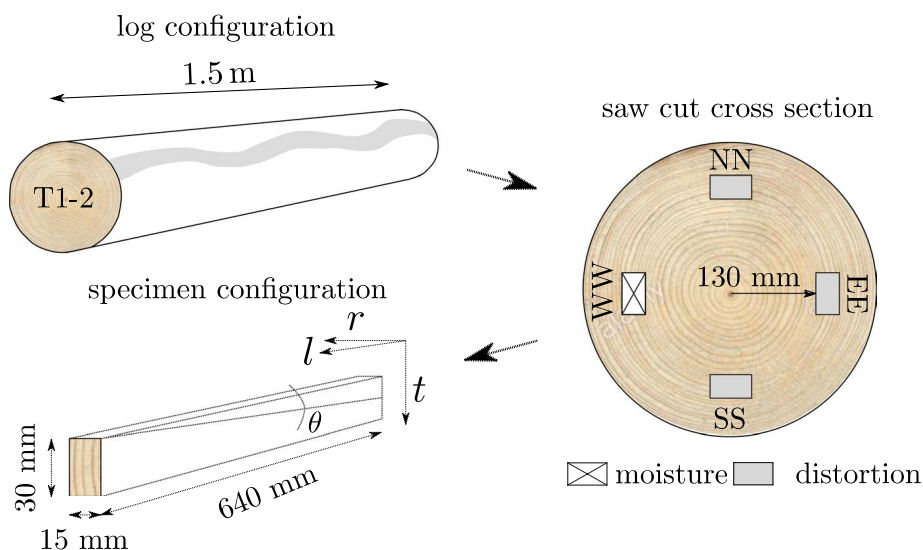
Fig. 1 Origin of the beam used for the moisture simulation
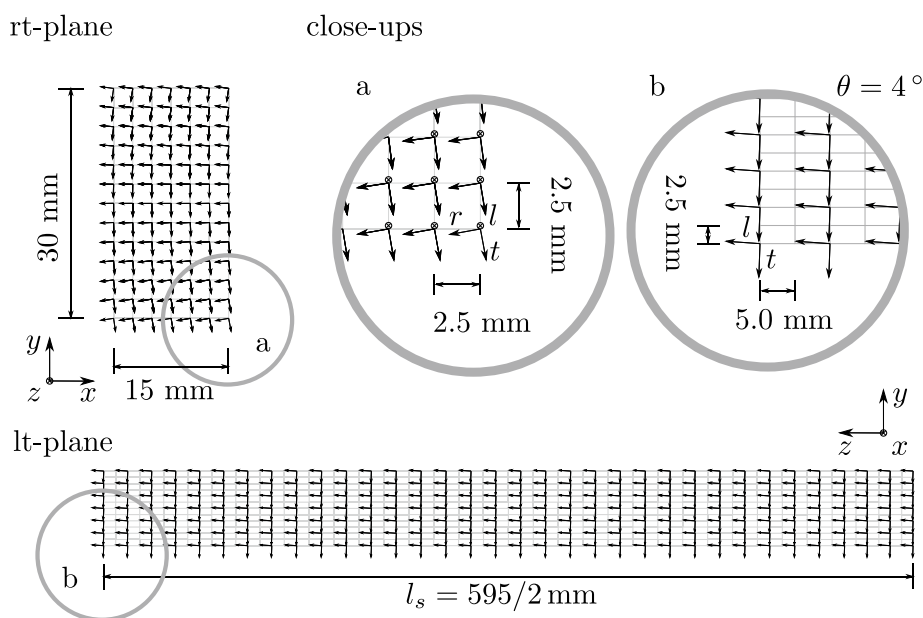
Fig. 2 Local material orientation radial–tangential plane (front side beam including annual ring curvature) and longitudinal–tangential plane (right side beam including spiral grain angle θ of 4°) presented together with dimensions and mesh size

Figure 3 illustrates the temperature and RH schedules used to define the MC of the ambient air. A relatively high temperature and differential between subsequent RH were chosen to stimulate the development of mechano-sorption. This meant a constant temperature of 60 °C was used and systematic RH-cycles were initiated, covering 10 day-periods and consisting of two RH-phases; one at 40%
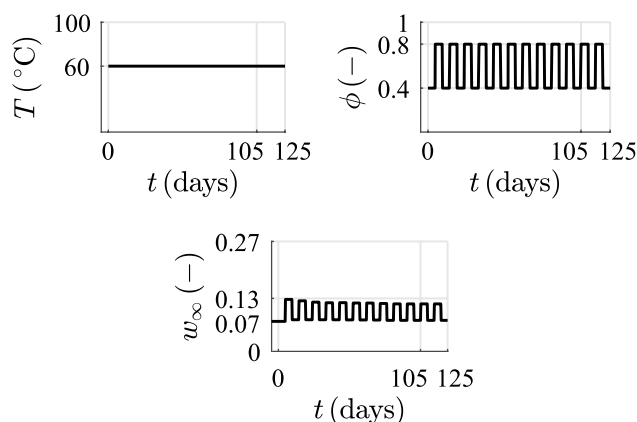
Fig. 3 Schedules used for temperature (T), relative humidity (ϕ) and ambient moisture content $\left(w_\infty\right)$, where 0.27 is the fibre saturation point $\left(w_\mathrm{f}\right)$

and one at 80%. Each phase resulted in EMC, which was used as the ambient moisture content w_∞ as initiated by Eq. (3).

The RH-schedule (see Fig. 3) was defined in user-subroutine FILM. Each new phase was introduced under a slight slope that covered six hours (60 increments) to ensure numerical stability. The relation between RH (ϕ) and the experimentally obtained EMC (w_{eq}) was established with scanning curves. An approximation of these curves was made with Eq. (15) and (16) (Johannesson 2019). Equation (15) describes w_∞ when in adsorption, and Eq. (16) when in desorption. The constants a and b are used to describe the shape of the curves, and w_f is the moisture content at fibre saturation point as defined in Fig. 3. To increase the flexibility with which parametric studies and post-processing of results were done, scripts written in programming language Python® (PSF, Delaware, United States) were used.
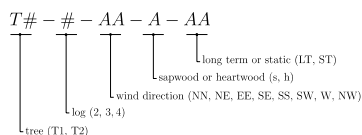
$$w_\infty^a = \frac{a \cdot \phi^{0.4} + b \cdot \phi^5}{5} \cdot w_f \tag{15}$$

$$w_\infty^d = \left(\frac{a \cdot \phi^{0.4} + b \cdot \phi^5}{6} + 0.08 \cdot \sin(\pi \cdot \phi) \right) \cdot w_f \tag{16}$$

Calibration of numerical model based on experiments

Because the hygro mechanical behaviour is strongly dependent on moisture gradient and mass transport, calibration of the numerical model used to perform the moisture simulation is essential. In this section, the experiment is presented that was needed for this calibration. The timber log of Norway spruce used in the experiment came from a private stand named *Engaholms skogar*, located near *Lyngsåsa* in southern Sweden. The specimens were obtained with the procedure previously illustrated in Fig. 1. Figure 4 illustrates the method to identify the beams. The first object in the identifier indicated the tree, the second was the log number and the third pointed towards the primary wind direction. Additionally, a fourth object was used to show whether the beam was tested in the long-term (for calibration) experiment or the static experiment (future publication). The beams used for the moisture simulation were identified as T1–2-WW-s-LT.

Fig. 4 Adopted method for identification of beams

$$T\# - \# - AA - A - AA$$

tree (T1, T2)
log (2, 3, 4)
wind direction (NN, NE, EE, SE, SS, SW, W, NW)
sapwood or heartwood (s, h)
long term or static (LT, ST)

The specimens used for the long-term experiment were all provided with a silicone sealant to prevent moisture transport in the lengthwise direction. The limited space inside the climate chamber allowed for one specimen to be monitored for mass change. This was justified by the fact that between the specimens in the sample

set of four, only a 10% difference in density was found, and therefore, a similar thickness of cell wall and lumen size can be assumed. Further, the specimens had similar MC, and a similar amount of latewood on visual inspection, and therefore, a comparable moisture transport.

The temperature and RH-schedules used in the experiment are displayed in Fig. 3. Each RH-phase resulted in a mass equilibrium state. This state was reached when the change in mass was below 1% between consecutive days. The recorded average volumetric mass change was converted to average volumetric MC (w_a^{exp}) by means of the oven-dry method (EN 13183-1 2003), see Eq. (17). Here, m_w indicates the wet mass and m_d the oven dry mass of the beam. The oven dry mass was reached when a change in mass of less than 1% was determined between two consecutive hours. The experimental results were compared with the simulated volumetric average MC w_a^{sim}, see Eq. (18),

$$w_a^{exp} = \left(\frac{m_w - m_d}{m_d} \right) \times 100 \tag{17}$$

$$w_a^{sim} = \left(\frac{1}{V} \sum_{i=1}^{m} w_i V_i \right) \times 100 \tag{18}$$

where V is the total volume, and w_i is the MC and V_i is the effected volume for each nodal point i corresponding to the finite element mesh. The calibration of the moisture transport model based on the experimentally obtained average volumetric MC resulted in a moisture-dependent diffusion and surface emission coefficient. The expressions that were used to describe the coefficients mathematically are presented by Eq. (19) and (20), where D indicates the diffusion coefficient, s the surface emission coefficient, w the MC and indexes a to c reference the constant parameters needed to describe each coefficient. The constants were established by calibration. Here, index k refers to the orthotropic material directions l, r or t.

$$D_k = D_a \cdot w^{D_b} + D_c \tag{19}$$

$$s = s_a \cdot w^{s_b} + s_c. \tag{20}$$

Accuracy of calibration

The calibration was evaluated by determining the relative difference (RD) between experimental data and simulation data, see Eq. (21). The RD is based on the absolute difference between the simulation y_m^{sim} and the experimental y_m^{exp} value of each data point m. The most optimal value for the RD is zero per cent. Such value indicates accurate calibration, though it does not indicate possible experimental measuring errors or simulation errors due to geometric simplification, discretisation, numerical imperfections, or the fact that the finite element method is based on approximations.

$$RD = \frac{abs\left(y_m^{sim} - y_m^{exp}\right)}{y_m^{exp}} \times 100 \qquad (21)$$

$$RD = \frac{abs\left(s_m^x - s_m^1\right)}{s_m^1} \times 100 \qquad (22)$$

The method of RD was also used to analyse the outcome of the parametric studies presented in the results and discussion chapter, see Eq. (22). Here, the reference value is s_m^1, indicating the data corresponding to the calibrated numerical model. The variable s_m^x refers to specific data obtained from the parametric study and x is a number between 2 and 8, referring to a specific simulation.

Results and discussion

In the first "Moisture content profiles" section, the numerical model will be used to simulate MC-profiles associated with flow in radial, tangential and longitudinal directions separately. The profiles come from Rosenkilde (2002). To validate the routines, the moisture-dependent diffusion and surface emission coefficient obtained from this analysis are compared to the coefficients obtained in a previous publication by Florisson et al. (2019). In the second "Hysteresis" section, the experimentally observed hysteretic behaviour, together with its implementation into the routine that covers the boundary condition, is discussed. The flow properties found in the first section are used as a starting point for the calibration presented in the third "Calibration of numerical model based on experiment" section. The calibrated model is used to analyse the effect of scanning curves and nonlinearity in the final "Moisture change and gradients" and "Nonlinearity analysis" sections of this chapter. These items have significant effect on moisture flow and gradients, which are fundamental to describe the hygro mechanical behaviour of wood.

Moisture content profiles

To assess numerical models for moisture transport, it is recommended to validate the models with moisture profiles. Rosenkilde (2002) provides MC-profiles in radial, tangential and longitudinal directions for Scots pine dried from green state to EMC at 60 °C and 59% RH. The profiles were obtained on specimens with dimensions $29 \times 29 \times 29$ mm^3. The results in radial direction were obtained with a combination of the so-called slicing technique and oven-dry method, and in longitudinal direction with CT-scanning. More about these techniques and the experiment can be read in Rosenkilde (2002). The fits of the MC-profiles in the radial, tangential and longitudinal directions below FSP using the numerical moisture transport model are presented in Fig. 5.

Fig. 5 Comparison of simulated (solid line) and experimentally obtained moisture content profiles (scattered data) below fibre saturation point in **a** radial/tangential, **b** longitudinal direction (Rosenkilde 2002)
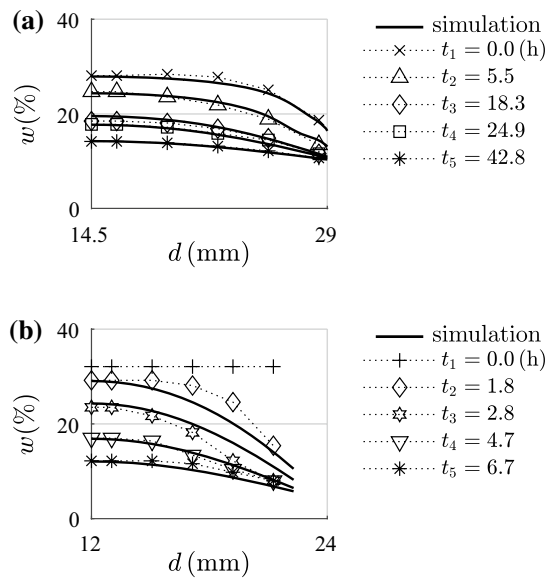
Fig. 6 Moisture-dependent diffusion and surface emission coefficient obtained in fit (solid line) on moisture content profiles covering **a** radial and tangential direction, together with data (scattered) obtained in Florisson et al. (2019), **b** longitudinal direction
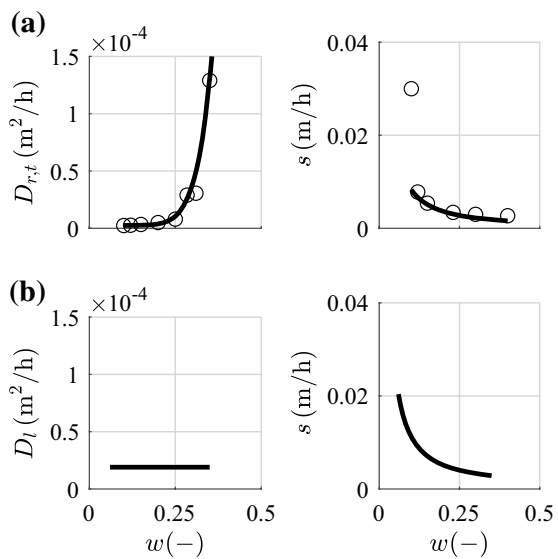
The distribution of the moisture-dependent flow parameters obtained, with the fit on the data by Rosenkilde (2002), is presented in Fig. 6. The diffusion coefficient is the same in both the radial and tangential directions. Figure 6a presents these coefficients together with the values obtained in Florisson et al. (2019). Great similarities are found between the simulation made with the standard analysis (without routines) provided by Abaqus FAE® in combination with tabulated flow properties, and the simulation made using the user-subroutines in combination with the expressions provided by Eq. (19) and (20). Figure 6b presents the flow properties associated with

Table 1 Variables needed to describe the diffusion coefficient (D) in the orthotropic directions (l, r, t) and corresponding surface emission coefficient (s) used to describe the flux vector normal to the boundary. Values are obtained with fit made of moisture content profiles by Rosenkilde (2002) in the MC-range 8–30% at 60 °C (a) and (b) relate to Fig. 6

		$(\cdot)_{(a)}$	$(\cdot)_{(b)}$	$(\cdot)_{(c)}$
(a)	$D_{r,t}$	0.70	8.2	2.5×10^{-6}
	s	5.1×10^{-4}	-1.21	0.5×10^{-3}
(b)	$D_l{}^*$			1.9×10^{-5}
	s	6.6×10^{-4}	-1.21	0.5×10^{-3}

*Constant value

Fig. 7 Interpretation of sorption behaviour at a constant temperature of 60 °C used in calibration of numerical model based on long-term experiment, **a** plot of sorption isotherm of spruce at 20 °C (solid line) (Bratasz et al. 2012) including an adjustment of this plot to enclose the data points at 40 and 80% RH obtained in long-term experiment (dotted line), **b** interpolation data points between 40 and 80% RH at first adsorption, **c** interpolation data points between 40 and 80% RH at first desorption, **d** approximation of scanning curves for all data points in long-term experiment
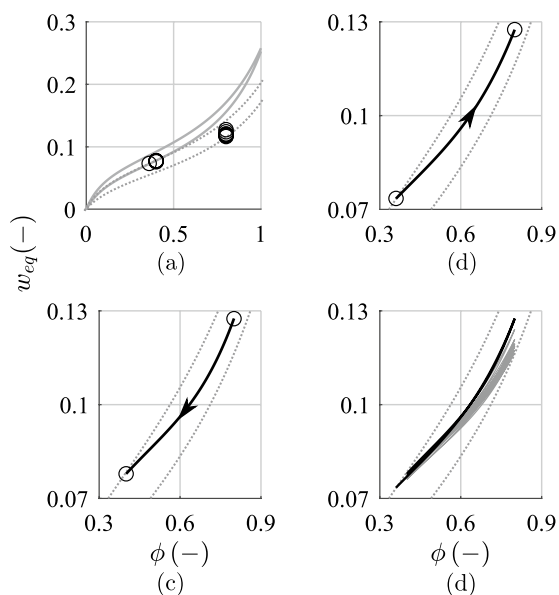
the longitudinal direction. The diffusion coefficient is constant with respect to moisture change, which was also seen in Rosenkilde (2002). The distribution of the surface emission coefficient is similar to that of the radial/tangential directions, which have an RD of maximum 21% and a minimum of 19% in the MC-domain between 10 and 35%. The variables that describe the flow properties by using Eq. (19) and (20) are collected in Table 1.

Hysteresis

The analysis of hysteresis and the scanning behaviour experienced due to the cyclic movement between 40 and 80% RH are illustrated in Fig. 7. Figure 7a presents the experimentally obtained values for EMC at 40 and 80% RH, together with a plot of a sorption isotherm of Norway spruce obtained at a temperature of 20 °C by Bratasz

et al. (2012). The sorption isotherm was obtained with the Guggenheim, Anderson and de Boer (GAB) method, presented by Eq. (23). Here, V_m is the monolayer capacity, c_e is the energy constant related to the difference of free enthalpy of water molecules in the upper sorption layers and monolayers, and k is the free enthalpy of water molecules in the pure liquid and upper sorption layers. The method assumes water molecules to be present in a monolayer or upper layer in the cell wall, as well as capillary condensation in the lumen, dependent on the RH. The water molecules in the monolayer have direct contact with the surface layer, whereas those in the upper layer do not. In this context, enthalpy is the thermodynamic quantity, which is equivalent to the total heat content of a system.

$$w_{eq} = \frac{V_m \cdot c_e \cdot k \cdot \phi}{(1 - k \cdot \phi)(1 + (c_e - 1) \cdot k \cdot \phi)} \tag{23}$$

Cycling the wood between two RH-values will result in closed hysteresis loops (scanning curves) bound by the adsorption and desorption isotherm. To get an indication of the two boundary curves at 60 °C, the variables used to describe the sorption isotherm at 20 °C were adjusted to enclose the experimentally obtained datapoints. The results show that the sorption isotherm lowers for higher temperatures (Engelund et al. 2013; Shi and Avramidis 2017a; Skaar 1988), as seen when the average EMC of 12.0 and 7.7% (80 and 40% RH) obtained in the present study is compared with the average of 16.4 and 8.5% MC found for the sorption isotherm by Bratasz et al. (2012) at the same RH-levels. The variables needed to describe both sorption isotherms are collected in Table 2.

The scanning curves generally do not develop in a straight manner (Salin 2011; Shi and Avramidis 2017a; Time 2002a), but in a similar trend to the boundary curves. With Eq. (15) and (16), an approximation is made of what these scanning curves could look like. In Fig. 7b, c, the interpolation between the experimentally obtained data points at first desorption and adsorption are presented. In Fig. 7d, all scanning curves are collected. It can be seen that the hysteretic behaviour results in larger differences in EMC at 80% RH (Δ1.1%) than at 40% RH (Δ0.4%). It is difficult to compare the experimental results with other publications (Fredriksson and Engelund 2018; Shi and Avramidis 2017a), where the scanning curves are limited and often start at adsorption. However, it is seen in Fredriksson and Engelund (2018) that the distance between desorption and adsorption boundary curve is much smaller at 40% RH than at 80% RH, also suggesting a similar scanning range. Additionally, this difference is seen in Johannesson and Janz (2009), as an example of the hysteretic behaviour simulated with the hysteresis model by Frandsen et al. (2007b)

Table 2 Three parameters needed to describe the sorption isotherm using the GAB method presented in Eq. (23) and illustrated in Fig. 7

T (°C)		V_m	c_e	k
20	ad	0.068	10.00	0.740
	de	0.080	12.00	0.700
60	ad	0.058	8.00	0.685
	de	0.073	10.49	0.660

Table 3 Variables used to describe the scanning curves at adsorption (ad) and desorption (de) with a fibre saturation point of 0.27 (−)

Cycle		a	b		a	b
1	ad	2.033	1.530	de	1.797	2.774
2		2.063	1.255		1.798	2.535
3		2.062	1.073		1.794	2.325
4		2.058	1.000		1.793	2.225
5		2.056	1.015		1.782	2.270
6		2.047	0.995		1.783	2.215
7		2.047	0.991		1.775	2.225
8		2.040	0.945		1.747	2.228
9		2.020	0.945			

Fig. 8 Average moisture content (w_a) and relative difference (RD) between experiment (e) and simulation (s) data for **a** simulation made with flow properties obtained with fit of moisture content profiles presented by (Rosenkilde 2002), **b** calibration made of moisture model based on long-term experiment
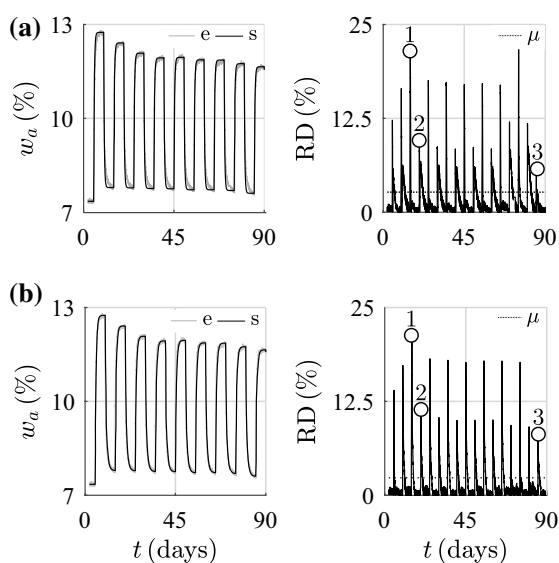
starting from the adsorption curve and scanning between 74 and 88% RH. All variables needed to make the scanning curves illustrated in Fig. 7 are collected in Table 3.

Calibration of numerical model based on experiment

Figure 8 presents the results of the calibration made from the moisture transport model based on the average MC. The calibration started with the flow properties obtained in "Moisture content profiles" section, see Table 1. Figure 8a presents these results, together with the experimental data. This figure also shows the RD between simulated and experimental data, which was determined based on Eq. (21). The next step was to adjust the flow properties until a better RD distribution was found. Figure 8b illustrates the final fit made in the calibration process. The flow properties

Table 4 Variables needed to describe the diffusion coefficient (D) in orthotropic directions (l, r, t) and surface emission coefficient (s) used to describe the flux vector normal to the boundary. Values are obtained with calibration made of numerical model based on experimental data between 7−13% MC and 60 °C

	$(\cdot)_a$	$(\cdot)_b$	$(\cdot)_c$
$D_{r,t}$	2.0	7.0	1.05×10^{-6}
D_l^*			1.9×10^{-5}
s	2.9×10^{-4}	-1.5	5.52×10^{-4}

*Constant value
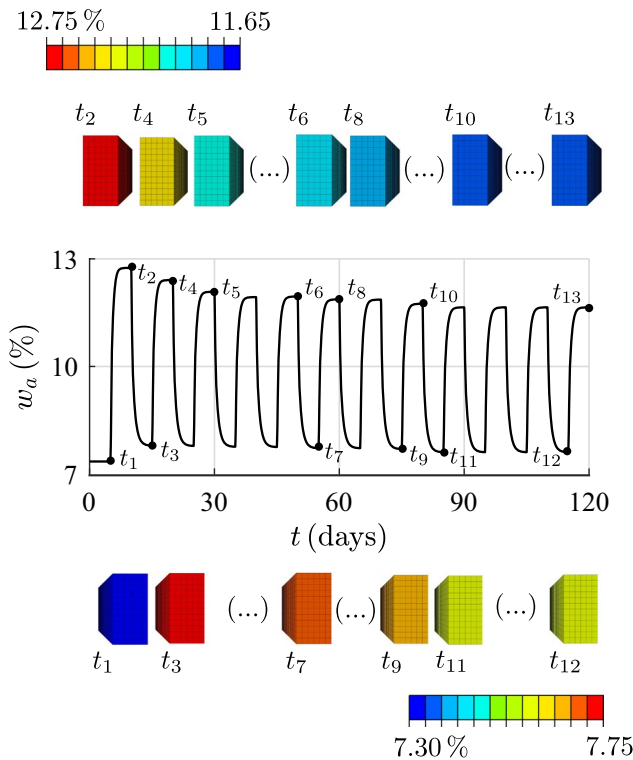
Fig. 9 Simulated average volumetric moisture content (w_a) including colour plots emphasising the effect of hysteresis on adsorption and desorption side for specific points in time (t_1 to t_{13})

related to this fit are collected in Table 4. To emphasize the EMC after each RH-phase and the effect hysteresis has on the EMC, Fig. 9 is presented.

The obtained RD-datasets were statistically analysed with a built in function of MATLAB®. The analysis showed that both sets were not normally distributed. The RD-dataset presented in Fig. 8a had a mean value of 2.7%. By adjusting the diffusion and surface emission coefficient, a better fit between simulation and experiment was obtained in Fig. 8b. The mean value of this dataset is 2.3%.

Although the mean RD-values did not reduce significantly, a visual inspection of the graphs in Fig. 8a, b shows considerable differences. In the RD-plot, three locations are highlighted. The peaks, indicated by the first point, are largely caused by the subtle difference in an initial rapid increase or decrease in MC after a change in RH. These points have a significant influence on the mean RD, but are difficult to eliminate. However, the RH is initiated under a time span in the simulation to avoid numerical instability issues. The second and third points highlight the beginning of a desorption and adsorption phase. Despite the higher peaks seen in adsorption, the general fit results in similar values for RD. Figure 9 shows that with hysteresis included in the numerical model, the EMC has considerably different values after every RH-phase.

To finalise the discussion about the calibration of the model, the flow properties of Table 1 are compared with those collected in Table 4. For the diffusion coefficient corresponding to the radial/tangential direction, a maximum RD is found of 82% around 10% MC and a minimum RD of 18% around 35% MC. The RD for the surface emission coefficient finds a maximum of 15.7% at 35% MC and a minimum of 0% at 15% MC. The diffusion coefficient in the longitudinal direction was adopted from Table 1. However, despite the spiral grain, no large reduction in the RD presented in Fig. 8 could be established by changing this property in value.

The radial/tangential diffusion coefficient and surface emission coefficient presented in Table 4 are shown in Fig. 10. The variation of these properties with respect to MC at various times and at different locations across the beam-section is shown. Figure 10a, c illustrate, in particular, the opposing behaviour of diffusion and surface emission coefficient to moisture, which has been observed by many researchers, such as Siau and Avramidis (1996), Yeo and Smith (2005) and Yeo et al. (2002). Especially interesting, shown by Fig. 10b, d, is the effect of hysteresis on the flow properties, and, in Fig. 10e, the variation of the diffusion coefficient over the cross section with respect to time seen for the first two RH-phases.

Moisture change and gradients

The average sorption isotherm is often used to simulate the moisture transport needed to analyse the moisture dependent mechanical behaviour. These choices influence the rate with which moisture changes, and the steepness of the gradients are experienced inside the material, which can have a significant effect on strain development in wood. In this section, the simulation from "Calibration of numerical model based on experiment" section (simulation 1) will be compared with a simulation where hysteresis at the boundary is neglected (simulation 2). The latter simulation uses the final values found in the calibration experiment, which is a constant EMC of 11.65% at 80% RH and an EMC of 7.6% at 40% RH as boundary condition.

In Fig. 11, the development of the average volumetric MC with respect to time is presented for both simulations. Eight points in time are selected for further study, which are strategically chosen 25 h after an increase in RH, when a moisture gradient is clearly present. The points were chosen in adsorption, when the hysteretic effects on the sorption isotherm are most significant. Colour plots were provided to
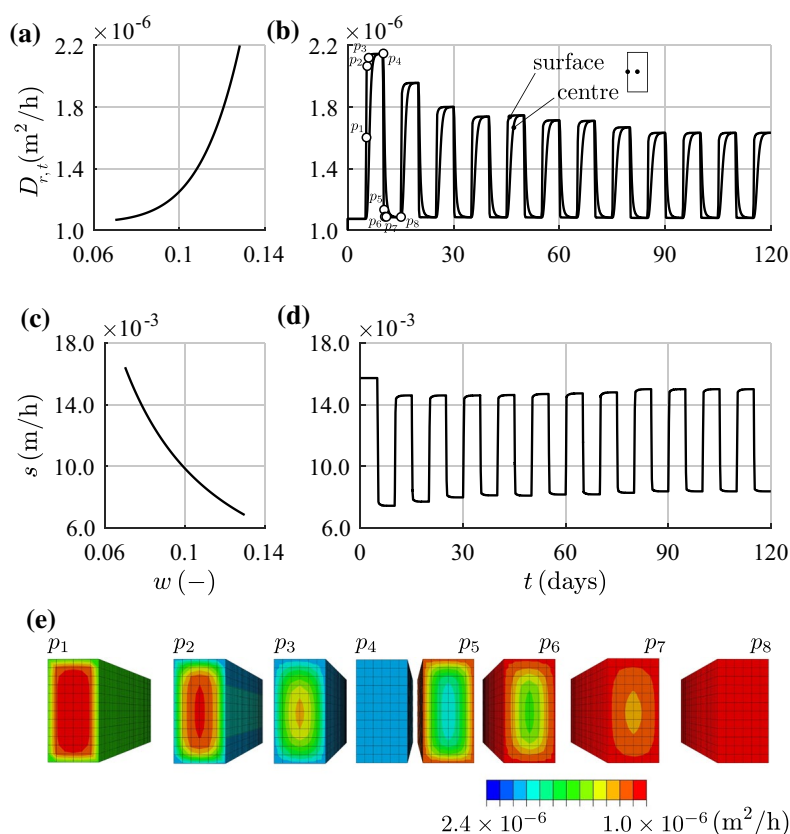
Fig. 10 Calibrated flow properties, **a** moisture-dependent diffusion coefficient in radial/tangential direction (D), **b** variation of the same D over time for a nodal point at the surface and the centre of the cross section, **c** moisture dependent surface emission coefficient (s), **d** variation of s with respect to time for a nodal point at the surface, **e** colour plots of D corresponding to the points illustrated in **b** (colour figure online)

visualise the MC-distribution over the cross section. The last plot in the sequence of colour plots shows the point where simulations 1 and 2 coincide.

For the eight points illustrated in Fig. 11, path plots that run from the upper exchange surface to the lower exchange surface for both simulations 1 and 2 were created, see Fig. 12. As a reference, the volumetric average MC belonging to the eight points are also plotted. The MC during adsorption shows to be systematically higher for simulation 1 than for simulation 2.

To increase the understanding of the path plots presented in Fig. 12, values of the average MC, the MC at the centre of the path plot and the moisture gradient at a 2.5 mm distance from the upper and lower exchange surface are collected in Table 5. Between the two simulations, a significant difference is found in the average MC and MC at the centre of the path plot, where both find their maximum at around 10% RD. The moisture gradient is unaffected by spiral grain and is higher for simulation 2 than for simulation 1, with a maximum RD of 10% after 385 h of testing. For simulation 1, the gradient gradually increases with increasing test time.
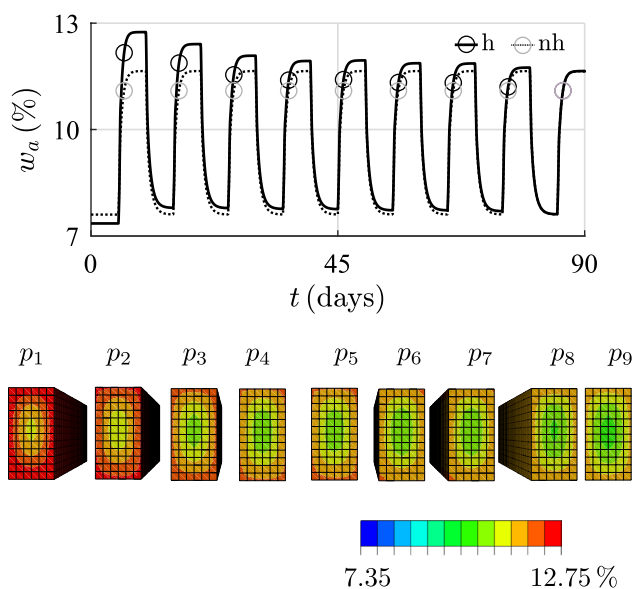
Fig. 11 Simulated average volumetric moisture content (w_a) with respect to time (t) for a simulation with (solid line) and without (dotted line) the scanning curves included at the boundary, together with colour plots that show the cross sectional variation of moisture at eight specific points in time (p_1 to p_8) for the simulation with and one colour plot for the simulation without (p_9) sorption effects (colour figure online)
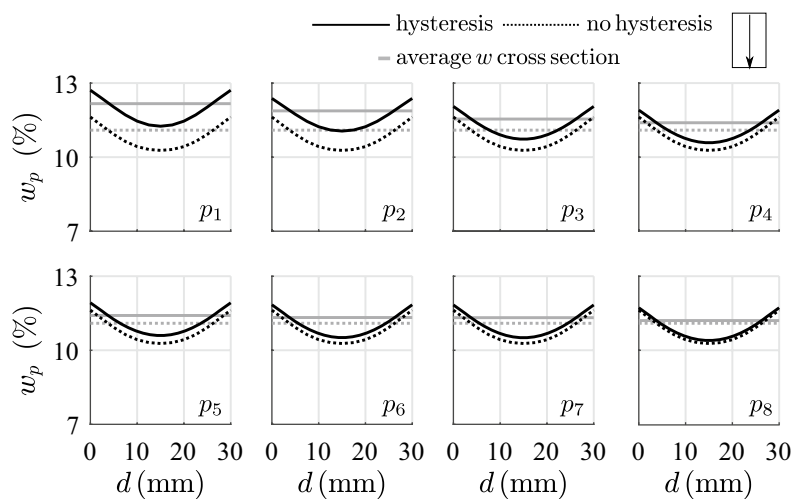
Fig. 12 Moisture content plots (w_p) over the height of the cross section at unique nodes for eight specific points in time previously illustrated in Fig. 11 for the simulation where hysteresis was and was not included as a boundary condition

Table 5 Data from the eight points in time treated in Figs. 11 and 12 for a simulation with (h) and without (nh) the effect of hysteresis included at the boundary

|	t (h)	Average MC			MC centre cross section			MC gradient at surface		
		w_h(%)	w_{nh}(%)	RD(%)	w_h(%)	w_{nh}(%)	RD(%)	$\mathrm{abs}|\nabla_x w_h|\,(m^{-1})$	$\mathrm{abs}|\nabla_x w_{nh}|\,(m^{-1})$	RD(%)
P_1	145	12.2	11.1	9.7	11.25	10.27	9.5	1.34	1.42	5.6
P_2	385	11.9	11.1	7.0	11.06	10.27	7.7	1.28	1.42	9.9
P_3	625	11.5	11.1	4.1	10.73	10.27	4.5	1.32	1.42	7.0
P_4	865	11.4	11.1	2.7	10.59	10.27	3.1	1.34	1.42	5.6
P_5	1015	11.4	11.1	2.9	10.60	10.27	3.2	1.34	1.42	5.6
P_6	1345	11.3	11.1	2.2	10.52	10.27	2.4	1.36	1.42	4.2
P_7	1585	11.3	11.1	2.1	10.51	10.27	2.3	1.35	1.42	4.9
P_8	1825	11.2	11.1	1.0	10.41	10.27	1.3	1.36	1.42	4.2

Nonlinearity analysis

When simulating moisture transport, it is generally known to incorporate the moisture dependency of flow properties, where they can have a strong effect on the speed with which MC changes and the formation of moisture gradients (Angst-Nicollier 2012; Florisson et al. 2019; Toratti 1992). To show the effect regarding the properties obtained in this paper, simulation 1 from the previous section will be compared to simulations where either constant flow properties are assumed or a mixture between constant and moisture dependent properties.

In total, six additional simulations were made, numbered 3–8. Simulations 3 and 4 were performed with a moisture-dependent diffusion coefficient and a constant surface emission coefficient. Simulations 5 and 6 were performed with moisture-dependent surface emission coefficient, but with a constant diffusion coefficient, and simulations 7 and 8 both ran with constant coefficients and therefore did not experience any nonlinearity. All simulations used the constant diffusion coefficient in longitudinal direction presented in Table 4.

For the moisture-dependent properties, the curves in Fig. 10a, c are used. The constant values are based on the minimum and maximum values presented in these curves. The constant surface emission coefficient in simulation 3 had a value of 0.0153 m/h found at 7.35% MC. For simulation 4, the value of 0.007 m/h corresponded to 12.75% MC. The constant diffusion coefficient used in simulation 5 was the value of 1.07×10^{-6} (mm^2/h), corresponding to 7.35% MC. The value in simulation 6 was a value of 2.15×10^{-6} (mm^2/h) at 12.75% MC. Finally, simulation 7 runs with the constant values of simulations 3 and 5, where simulation 8 runs with the constant values of simulation 4 and 6.

To show the general difference between constant and moisture-dependent properties, the volumetric average MC with respect to time for the first two RH-phases is presented in Fig. 13 for simulations 1, 7 and 8. The experimental data presented in Fig. 8 showed a difference between the curvatures of the average MC-curve in adsorption and desorption. Figure 13 shows that this behaviour is only visible in simulation 1, where the equilibrium moisture state of the volume is reached sooner in adsorption than in desorption due to the moisture dependency of the properties. This behaviour is not present when constant properties are used as in simulations 7 and 8. The RD-distribution in Fig. 13 shows that in

Fig. 13 Average volumetric moisture content $\left(w_a\right)$ change in first two RH-phases for simulations 1, 7 and 8 together with a display of the relative difference (RD)
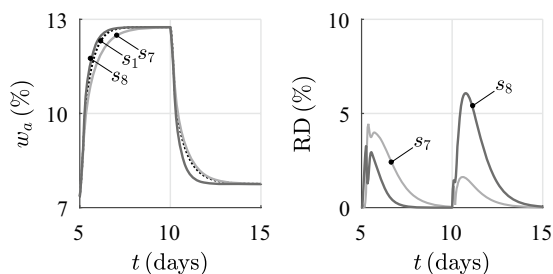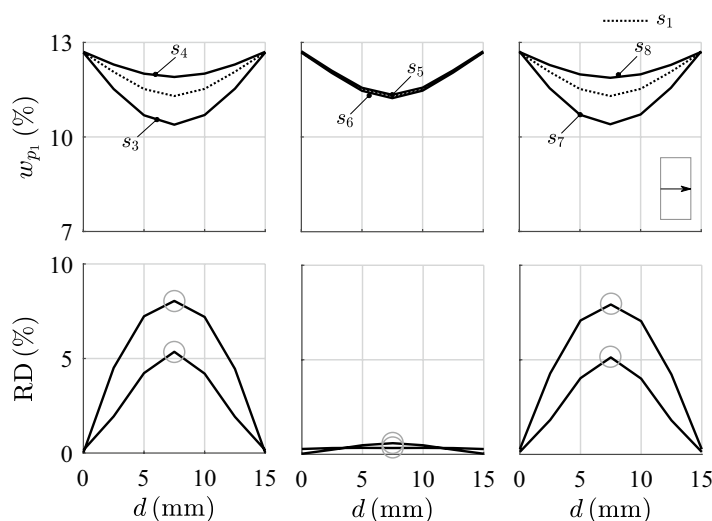
Fig. 14 Moisture content plots over the width of the cross section at unique nodes at time period p_1 (145 h) illustrated in Fig. 12 for the different simulations in the nonlinearity analysis including estimation of the relative difference (RD)

adsorption simulation 8 comes closer to simulation 1, where in desorption simulation 7 comes closer to simulation 1.

A brief impression of the effect of nonlinearity of the analysis on moisture profiles is given in Fig. 14. The profiles are taken 145 h into the analysis. The results of simulation 1 presented in Fig. 14 agree with the first point illustrated for simulation 1 in Fig. 11. Compared with the surface emission coefficient (simulations 5 and 6), the moisture dependency of the diffusion coefficient (simulations 3 and 4) has the most effect on the flow speed and formation of gradients, with a maximum RD of 8% compared to 0.59%.

Conclusion

The simulation tool makes the nonlinear orthotropic single-Fickian model and Neumann boundary condition readily available and the simulations more flexible to different uses. It allowed for the practical incorporation of the scanning curves associated with hysteresis at the boundary and a smoother definition of the moisture-dependent flow properties. The analysis of the calibration made with this tool on volumetric average moisture content data obtained in a bending test subjected to systematic climate changes showed that: (1) the continuous recordings of average moisture content is beneficial due to its simplicity and should be a standard measurement when performing bending tests subjected to climate; (2) the calibration benefitted from the fit made of MC-profiles, where it gives a better representation of moisture content gradient; (3) it is necessary to incorporate hysteresis into the moisture simulation to obtain moisture profiles that best describe the moisture-dependent

mechanical behaviour; and (4) for the same reasons, a coherent set of moisture-dependent diffusion and surface emission coefficients are needed to perform a moisture simulation.

The experimental methodology presented in this paper will be used in future publications to analyse mechano-sorption analytically and with simulations. The results obtained in this paper will be used as input to the moisture-induced distortion simulation. The routines can easily be extended by including inhomogeneity of material properties and effects due to temperature on diffusion and surface emission coefficient, making it suitable in conjunction with kiln drying operations. The simulation tool could benefit from a simple hysteresis model that is able to describe hysteresis as a boundary condition in combination with a single-Fickian model based on theoretical equations that are derived from underlying theory. To better incorporate the scanning behaviour and the temperature and moisture dependency of the flow properties, more experiments are needed with different RH-ranges and temperature levels.

References

Alexandersson M, Askfelt H, Ristinmaa M (2016) Triphasic model of heat and moisture transport with internal mass exchange in paperboard. Transp Porous Med 112:381–408

Angst-Nicollier V (2012) Moisture induced stresses in glulam. Doctoral thesis, Norwegian University of Science and Technology

Bratasz Ł, Kozłowska A, Kozłowski R (2012) Analysis of water adsorption by wood using the Guggenheim–Anderson–de Boer equation. Eur J Wood Prod 70:445–451

Dassault Systèmes (2017a) SIMULIA user assistance 2017. Abaqus Theory Guide, Providence

Dassault Systèmes (2017b) SIMULIA user assistance 2017. Abaqus User Subroutines Reference Guide, Providence

Di Blasi C (1997) Multi-phase moisture transfer in the high-temperature drying of wood particles. Chem Eng Sci 53:353–366

Dinwoodie JM (1981) Timber: its nature and behaviour, 2nd edn. E&FN Spon Taylor & Francis Group, London

Eitelberger J, Hofstetter K (2011) A comprehensive model for transient moisture transport in wood below the fiber saturation point: physical background, implementation and experimental validation. Int J Therm Sci 50:1861–1866

EN 13183-1 (2003) Moisture content of a piece of sawn timber part 1: determination by oven dry method. European Committee for Standardization (CEN), Brussels

Engelund ET, Thygesen LG, Svensson S, Hill CAS (2013) A critical discussion of the physics of wood–water interactions. Wood Sci Technol 47:141–161

Eriksson J, Johansson H, Danvind J (2007) A mass transport model for drying wood under isothermal conditions. Dry Technol 25:433–439

Everett DH, Whitton WI (1952) A general approach to hysteresis. Trans Faraday Soc 48:749–757

Fick A (1855) On liquid diffusion. J Membr Sci 100:33–38 **(1995)**

Florisson S, Ormarsson S, Vessby J (2019) A numerical study of the effect of green-state moisture content on stress development in timber boards during drying. Wood Fiber Sci 51:41–57

Fortino S, Genoese A, Genoese A, Nunes L, Palma P (2013a) Numerical modelling of the hygro-thermal response of timber bridges during their service life: a monitoring case-study. Constr Build Mater 47:1225–1234

Fortino S, Genoese A, Genoese A, Rautkari L (2013b) FEM simulation of the hygro-thermal behaviour of wood under surface densification at high temperature. J Mater Sci 48:7603–7612

Fortino S, Hradil P, Genoese A, Genoese A, Pousette A (2019) Numerical hygro-thermal analysis of coated wooden bridge members exposed to Northern European climates. Constr Build Mater 208:492–505

Frandsen HL (2007) Selected constitutive models for simulating the hygromechanical response of wood. Doctoral degree, Aalborg University

Frandsen HL, Damkilde L, Svensson S (2007a) A revised multi-Fickian moisture transport model to describe non-Fickian effects in wood. Holzforschung 61:563–572

Frandsen HL, Svensson S, Damkilde L (2007b) A hysteresis model suitable for numerical simulation of moisture content in wood. Holzforschung 61:175–181

Fredriksson M, Engelund ET (2018) Scanning or desorption isotherms? Characterising sorption hysteresis of wood. Cellulose 25:4477–4485

Honfi D, Mårtensson A, Thelandersson S, Kliger R (2014) Modelling of bending creep of low- and high-temperature-dried spruce timber. Wood Sci Technol 48:23–36

Huč S (2019) Moisture induced strains and stresses in wood. Doctoral thesis, Uppsala University

Janssen H, Blocken B, Carmeliet J (2007) Conservative modelling of the moisture and heat transfer in building components under atmospheric excitation. Int J Heat Mass Transf 50:1128–1140

Johannesson B (2019) Thermodynamics of single phase continuous media: lecture notes with numerical examples. Lecture notes. Linnaeus University, Växjö

Johannesson B, Janz M (2009) A two-phase moisture transport model accounting for sorption hysteresis in layered porous building constructions. Build Environ 44:1285–1294

Konopka D, Kaliske M (2018) Transient multi-Fickian hygro-mechanical analysis of wood. Comput Struct 197:12–27

Krabbenhøft K (2003) Moisture transport in wood a study of physical and mathematical models and their numerical implementation. Doctoral thesis, Technical University of Denmark

Krabbenhøft K, Damkilde L (2004) Double porosity models for the description of water infiltration in wood. Wood Sci Technol 38:641–659

Ma X, Smith LM, Wang G, Jiang Z, Fei B (2017) Mechano-sorptive creep mechanism of bamboo-based products in bending. Wood Fibre Sci 49:1–8

Mohager S, Toratti T (1993) Long term bending creep of wood in cyclic relative humidity. Wood Sci Technol 27:49–59

Morlier P (1994) Creep in timber structures Rilem report 8. Rilem Technical Committee, London

Muszyński L (2006) Empirical data for modeling: methodological aspects in experimentation involving hygro-mechanical characteristics of wood. Drying Technol 24:1115–1120

Ormarsson S (1999) Numerical analysis of moisture related distortion in sawn timber. Doctoral thesis, Chalmers University of Technology

Ormarsson S, Dahlblom O, Petersson H (1998) A numerical study of the shape stability of sawn timber subjected to moisture variation part 1: theory. Wood Sci Technol 32:325–334

Pang S, Keey RB, Langrish TAG (1995) Modelling the temperature profiles within boards during the high-temperature drying of *Pinus radiata* timber: the influence of airflow reversals. Int J Heat Mass Transf 38:189–205

Peralta PN (1995) Sorption of moisture by wood within a limited range of relative humidities. Wood Fibre Sci 27:13–21

Perré P, Turner IW (1999) A 3-D version of TransPore: a comprehensive heat and mass transfer computational model for simulating the drying of porous media. Int J Heat Mass Transf 42:4501–4521

Ranta-Maunus A (1975) The viscoelasticity of wood at varying moisture content. Wood Sci Technol 9:189–205

Rosenkilde A (2002) Moisture content profiles and surface phenomena during drying of wood. Doctoral thesis, KTH Royal Institute of Technology

Salin J-G (2011) Inclusion of the sorption hysteresis phenomenon in future drying models: some basic considerations. Maderas Ciencia Technol 13:173–182

Shi J, Avramidis S (2017a) Water sorption hysteresis in wood: I review and experimental patterns—geometric characteristics of scanning curves. Holzforschung 71:307–316

Shi J, Avramidis S (2017b) Water sorption hysteresis in wood: II mathematical modeling—functions beyond data fitting. Holzforschung 71:317–326

Shi J, Avramidis S (2017c) Water sorption hysteresis in wood: III physical modeling by molecular simulation. Holzforschung 71:733–741

Siau JF (1995) Wood: influence of moisture on physical properties. Virginia Polytechnic Institute and State University, Virginia

Siau JF, Avramidis S (1996) The surface emission coefficient of wood. Wood Fiber Sci 28:178–185

Skaar C (1988) Wood–water relations. Springer series in wood science. Springer, Berlin

Svensson S, Turk G, Hozjan T (2011) Predicting moisture state of timber members in a continuously varying climate. Eng Struct 33:3064–3070

Time B (1998) Hygroscopic moisture transport in wood. Doctoral thesis, Norwegian University of Science and Technology

Time B (2002a) Studies on hygroscopic moisture transport in Norway spruce: part 1 sorption measurements of spruce exposed to cyclic step changes in relative humidity. Holz Roh Werkst 60:271–276

Time B (2002b) Studies on hygroscopic moisture transport in Norway spruce: part 2 modelling of transient moisture transport and hysteresis in wood. Holz Roh Werkst 60:405–410

Toratti T (1992) Creep of timber beams in a variable environment Doctoral thesis, Helsinki University of Technology

Wiberg P (1998) CT-scanning of moisture distributions and shell formation during wood drying. Licentiate thesis, Luleå University of Technology

Yeo H, Smith WB (2005) Development of a convective mass transfer coefficient conversion method. Wood Fiber Sci 37:3–13

Yeo H, Smith WB, Hanna RB (2002) Mass transfer in wood evaluated with a colorimetric technique and numerical analysis. Wood Fiber Sci 34:557–665

Younsi R, Kocaefe D, Poncsak S, Kocaefe Y (2007) Computational modelling of heat and mass transfer during the high-temperature heat treatment of wood. Appl Therm Eng 27:1424–1431

III

ANALYSIS OF HYGRO-MECHANICAL BEHAVIOR OF WOOD IN BENDING[1]

S. Florisson*†

Doctoral Candidate
Department of Building Technology
Linnaeus University
Växjö, Sweden
E-mail: sara.florisson@lnu.se

L. Muszyński†

Professor
Wood Science and Engineering
Oregon State University
Corvallis, OR
E-mail: lech.muszynski@oregonstate.edu

J. Vessby†

Senior Lecturer
Department of Engineering and Chemical Sciences
Karlstad University
Karlstad, Sweden
E-mail: johan.vessby@kau.se

Abstract.   The empirical test developed as validation for a new beam element model that can account for both mechanical and environmental load action in finite element analysis is presented. The testing protocol allows for the identification and analysis of contributing deflection components in bending under varying MC conditions, including mechano-sorption. The components of deflection in the shear-free span of a four-point bending test and their responses to varying moisture are evaluated with an analytical procedure. The experiment was conducted on clear, straight-grained sapwood and heartwood specimens of Norway spruce (*Picea abies*) ($30 \times 15 \times 640$ mm^3). The program consisted of three phases: 1) long-term (LT) experiments under constant temperature of 60°C and RH cycles between 40% and 80%, 2) a short-term static experiment to determine the variation in the sample set and the load level of the LT experiment on end-matched specimens, and 3) creep tests at 60°C and constant humidity at either 40% or 80% to determine the effect of moisture on the viscoelastic creep. Mass changes and hygro-expansion measured on matched specimens were used in the analytical method. Constitutive models used for describing the material-level response to loads and moisture changes were applied to the shear-free segment of the specimens disregarding actual moisture gradients and fiber orientation inside the test specimens. A successful identification of each deflection component and isolation of mechano-sorption component was accomplished. In the 90 da of testing, the dominant component of the total deflection was the elastic component, followed by the mechano-sorptive component. Creep was found to be nonnegligible and important in the correct description of mechano-sorption. The effect of moisture on the viscoelastic behavior showed most important during loading and first stages of decreasing deflection rate phase.

Keywords: Bending, solid wood, Norway spruce, creep, experimental methodology, mechano-sorption, viscoelasticity.

INTRODUCTION

When wood is subjected simultaneously to stress and MC changes below the FSP, the mechano-sorptive phenomenon may be observed as an additional deformation that cannot be explained by a simple superposition of elastic deformation, free shrinkage or swelling, and creep at constant MC (Muszyński et al 2005). Mechano-sorption is a second-order phenomenon, which means that the mechano-sorptive deformation cannot be measured directly, as it is always accompanied by viscoelastic and free hygro-expansion deformation. To properly isolate the mechano-sorptive deformation, these components must be measured independently in reference tests on matched specimens and subtracted from the total deformation of the specimens tested in changing climatic conditions (Bengtsson 1999; Muszyński et al 2005; Hering et al 2012). This is rarely carried out in published empirical studies (Morlier 1994; Muszyński et al 2006; Lagaňa et al 2011). When properly isolated, the mechano-sorptive deformation appears somewhat similar to viscoelastic creep. Under high stress levels and long series of moisture cycles, three stages of deformation may be observed, which correspond to the three stages of viscoelastic creep: a *primary stage*, with a decreasing deflection rate, followed by a *secondary stage*, with a constant deflection rate, and, potentially, a *tertiary stage*, characterized by an increasing deflection rate that can lead to failure (Armstrong and Christensen 1961; Hearmon and Paton 1964; Hunt 1989; Hunt 1999). Thanks to this analogy, the first two stages may be adequately described by phenomenological models resembling simple spring–dashpot models, where the time domain needed to describe visco-elastic behavior is replaced with the cumulative MC change defined as follows:

$$v = \int_0^t |\dot{w}|\, dt. \qquad (1)$$

Here, $\dot{w}$ is momentary MC change rate in the time domain. In reference to these models, an analogue to the Newton dashpot, proposed independently by Rybarczyk (1973) and Ranta-Maunus (1975) may be presented as follows:

$$\varepsilon_{ms} = \alpha \sigma v, \qquad (2)$$

where α is a parameter analogue to an inverse of viscosity and σ is a constant stress value. An analogue to a Kelvin element is obtained by adding a parallel spring parameter E_{ms}, as proposed independently by Rybarczyk (1973) and Salin (1992):

$$\varepsilon_{ms} = \frac{\sigma}{E_{ms}} \left(1 - e^{-\alpha E_{ms} v} \right). \qquad (3)$$

Since the first reports in 1960s (Armstrong and Christensen 1961), mechano-sorption has been extensively researched. The progress made in the state of knowledge is summarized in Holzer et al (1988), Morlier (1994), Hunt (1999), Hanhijärvi (2000) and Muszyński et al (2005). However, Morlier (1994), Hunt (1999), and Muszyński et al (2005) pointed out that the experimental programs used in published studies show a lot of variation and often a superficial analysis of results. Typically, the total deflection between the bearing supports is recorded, which includes effects of shear, and indentation under loads and over bearing supports (Brancheriau et al 2002). When the separation of deflection components is attempted, many authors only subtracted the effect of shrinkage and swelling, whereas in general, the viscoelastic creep is neglected (Hering and Niemz 2012). To properly isolate the mechano-sorptive effect, Muszyński et al (2005) and Muszyński et al (2006) have proposed an experimental methodology based on the commonly accepted concept that the total strain ε_t may be considered a separable superposition of an elastic ε_e component, hygro-expansion ε_h, creep component ε_c, and mechano-sorptive ε_{ms} component, as in Eq 4.

$$\varepsilon_t = \varepsilon_e + \varepsilon_h + \varepsilon_c + \varepsilon_{ms} \qquad (4)$$

This methodology was then applied to tests on specimens of red spruce loaded in tension parallel to the grain with a load level equal to 70% of the green-state ultimate tensile stress, subjected to a constant temperature of 21°C and 18 RH cycles between 30 and 98%. Subsequently, Lagaňa et al (2011) proved that mechano-sorptive characteristics measured on small clear wood specimens in tension and

compression along the grain can be successfully used in predicting complex behavior of beams subjected to loads and varying climatic conditions.

Recently, a beam element model that can account for both mechanical and environmental load action was developed (Ormarsson and Dahlblom 2013; Ormarsson and Steinnes 2014; Ormarsson and Gíslason 2016). This model builds on the essential feature of the beam theory proposed by Bernoulli, such that the plane section normal to the beam axis remains plane and normal to the beam axis during deformation (Ottosen and Petersson 1992). This means that ε_t as described by Eq 4 has to vary linearly over the cross section, whereas the strain portions ε_e, ε_h, ε_c, and ε_{ms} can vary arbitrarily (Ormarsson and Dahlblom 2013). In the three-dimensional plane, the input parameters to the beam model are the compliance matrix, which contains the elastic and shear moduli, the vector γ of hygro-expansion coefficients, the mechano-sorption matrix $\boldsymbol{m}$ including the mechano-sorption parameter α, the spring parameter of Kelvin creep model ϕ_σ^n, and the dashpot viscosity of Kelvin creep model τ_n, where n indicates the amount of the Kelvin model modules arranged in series. The transformation from the local coordinate system (l, r, t), which accounts for the fiber orientation, to the global coordinate system (x, y, z) is carried out by means of transformation matrices. These matrices are also used to transform the three-dimensional notation of ε_h, ε_c, and ε_{ms} to a suitable notation for the beam theory. As output, the beam model generates the bending moment, deflection diagrams, and the cross-section stress distribution. The model accounts for two-dimensional moisture gradients within the beam elements (Ormarsson and Gíslason 2016). Compared with the solid finite element models used to simulate moisture-induced strains, the beam model is much more computationally efficient and can therefore be applied on structural-level modeling. However, the beam model still needs an experimental validation to determine its accuracy and to identify its potential limitations.

Therefore, the primary motivation for this work is the calibration of the beam model with empirical data from carefully controlled bending tests in

variable climatic conditions. A meaningful validation requires that the experimental procedure allows for clear separation of the contributing components of the total deflection, as listed in Eq 4, so that the contribution made by mechano-sorption to the total deflection of the beam can be isolated. Although such procedures have been successfully demonstrated for tension and compression (Muszyński et al 2006), it is a serious challenge in case of bending in varying climatic conditions, where nonuniform stress distribution coincides with nonuniform development of moisture gradients within the same specimen's volume (Muszyński et al 2005). To the authors' knowledge, no successful attempt for such procedure allowing clear separation of the deflection components in beams had been reported at the time of the inception of the project presented in this article. The purpose of the current article is to describe the experimental methodology, analytical procedures, and outcomes of tests on small clear wood specimens subjected to bending in varying climatic conditions, and the validation of the beam model will be described in a separate publication.

The specific objectives of this experimental study were 1) to develop the experimental setup and analytical procedure applied to separate components of the total deflection measured on beams subjected to bending in varying climate; 2) to determine the expected variation of the material properties in the material used for the tests described in objective 1), as represented by strength and stiffness of specimens extracted from various positions in the harvested logs; 3) to analyze the effect of moisture on the viscoelastic creep to enhance the analytical procedure; 4) to determine the hygro-expansion coefficients of the test material; and 5) to fit the isolated mechano-sorption deflection curve with a suitable model.

EXPERIMENTAL PROGRAM

The testing protocol was designed based on the assumption that the total deflection of beams subjected to sustained load under varying climatic conditions is separable into individual components. The mechano-sorptive deflection

u_{ms} was isolated from the total deflection u_t by subtracting the elastic component u_e, creep u_c, and hygro-expansion u_h, determined with reference tests (Eq 5).

$$u_{ms} = u_t - (u_e + u_c + u_h) \qquad (5)$$

The main part of the experimental program was of a long-term four-point bending test conducted under varying climatic conditions on sapwood and heartwood specimens of Norway spruce. A four-point bending test was used to obtain deflection data from the shear-free section to exclude shear and indentation under loads and over supports. The tests were conducted in a constant temperature of 60°C and nine 10-d humidity cycles varying between equal 5-d stages at 40% and 80% RH. Before testing, the specimens were preconditioned in the test chamber at 60°C and 40% RH. These conditions were kept through the first 5 d. This procedure allowed recording of the immediate elastic deflection u_e and the initial viscoelastic creep trajectory, before the RH cycles were launched. The specimens were unloaded in the conditions similar to those at the beginning of the test and left unloaded for two additional RH cycles to measure the recovery of deflection.

The reference tests were designed to isolate the mechano-sorptive component of deflection:

1. Creep tests in constant climate at 40% and 80% RH were used to determine the effect of moisture on the viscoelastic response.
2. Short-term (ST) static tests (at an MC close to the FSP) were conducted on end-matched specimens to estimate the variation in the modulus of rupture f_b and the elastic modulus E in the test material, to provide context for the variability of elastic deflection u_e values determined from loading and unloading procedures in the main test, and to determine the stress level for the long-term (LT) tests in reference to f_b.
3. The mass of unloaded matched specimens was recorded to approximate the average MC of the loaded specimens, neglecting the moisture gradients within the specimens.
4. The hygro-expansion of the depth of an unloaded matched specimen was monitored to

estimate the cross section's dimensional change of the loaded specimens and their effect on the modulus of inertia.

The outline of the experimental program with an overview of the type of tests performed, the load levels, the provenience, the number of specimens used, the deflection components measured, and expected types of results is presented in Table 1. The following sections are concerned with the description and the treatment of the specimens, presentation of the test setup and procedures, and the discussion of the analytical approach and its limitations.

Materials and Specimen Fabrication

All test specimens were fabricated from three logs of Norway spruce related to 60-yr-old trees acquired from a private stand named Engaholms skogar located near Lyngsåsa in Southern Sweden. The logs were harvested in winter time and kept in frozen state before and after further processing at Asa försökspark. The cutting scheme followed the conical shape and annual ring pattern in the logs but could not eliminate spiral grain. Eight sapwood and eight heartwood specimens (25th and 13th annual ring, respectively) were extracted from each 1.5-m log. The distinction between sapwood and heartwood was made on the green-state MC right after felling the tree. The specimens were marked according to their position within the log, related to a specific wind direction (Fig 1). The 1.5-m rectangular sections extracted from the logs were subsequently cut in two equal segments to obtain end-matched specimen pairs marked for static and LT tests (Fig 1).

After cutting, the specimens covered in plastic sheets to minimize drying were transported to Linnaeus University's laboratory and stored in a freezer until the final cutting and planing to 30 mm × 15 mm × 640 mm (depth × width × length) while in frozen state. The span-to-depth ratio over 18 allowed the mitigation of the effect of shear deformation to below 6% of the total deflection measured on the full span

Table 1. Outline of the experimental plan.

Test	Data type	Load levels**	Specimen labels	Number of specimens swd/hwd*	Deflection components				Material parameters			
					u_e	u_c	u_h	u_{ms}	E	ϕ_σ	τ	f_b
Main (LT) (40-80% RH 60°C)			T1–2									
	Deflection	34%	NN/SS/EE	3/3	×	×		×	×	×	×	
Reference (LT) (40-80% RH 60°C)												
	Hygro-expansion	0%	WW	1/1			×					
	Mass change	0%										
ST (98% RH 21°C)	ultimate	T1-3, T1-3, T2-4	24/24						×			×
Creep (40% RH 60°C)			T1-3									
	Deflection	34%	NN/SS/EE	3/3	×	×			×	×	×	
	Mass	0%	WW	1/1								
Creep (80% RH 60°C)			T1-3									
	Deflection	34%	NW/SE/NE	3/3	×	×			×	×	×	
	Mass	0%	SW	1/1								

*Sapwood (swd) and heartwood (hwd).
**Percentage of the mean $(\mu)\, f_b$ at 30% MC.

of the beam. The specific dimensions were dictated by the constraints of the loading setup inside the climate chamber.

The specimen's ID system, as shown in Fig 2, marked the tree (T1 or T2), the log (2–4), the specimen's orientation in the log (NN, NE, EE, SE, SS, SW, WW, NW), the radial position (sapwood or heartwood: *s* or *h*), and their designation to the LT or static tests (LT or ST). Logs labeled T1-2, T1-3, and T2-4 resulted in 24 pairs of sapwood specimens and 24 pairs of heartwood specimens. The 48 crown-end specimens were used in the static tests, whereas the root-end specimens were used in the LT and creep tests. The summary of specimen assignment to specific
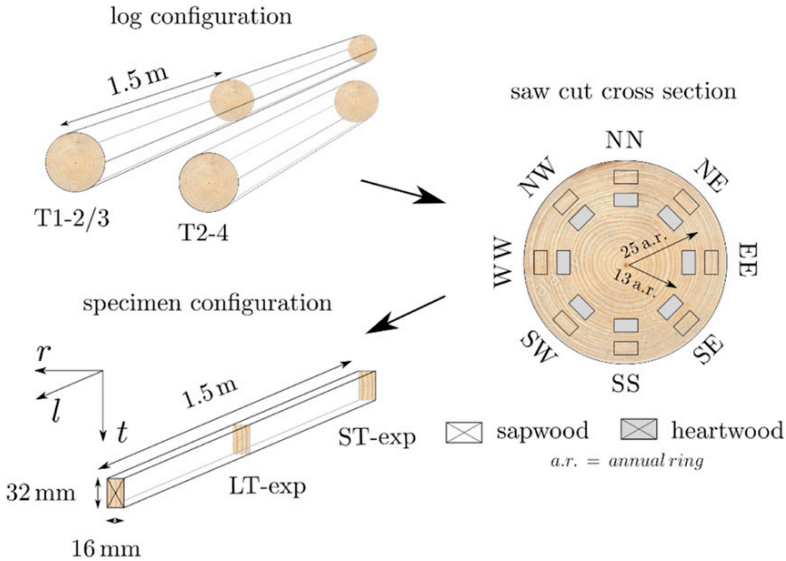

Figure 1. Diagram illustrating processing of the material samples from tree trunks, through logs, toward paired bending specimens.
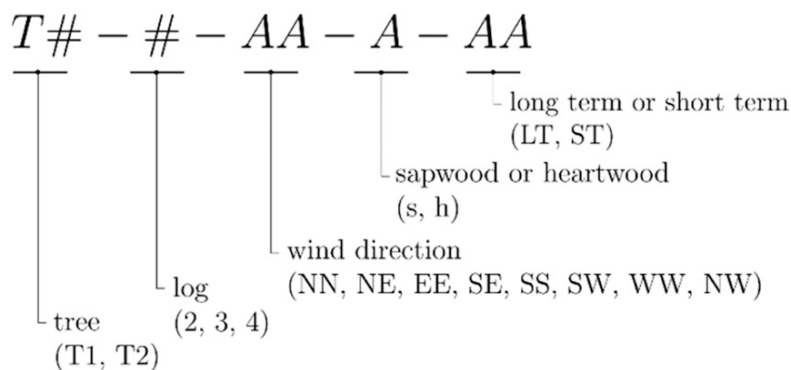
$$T\# - \# - AA - A - AA$$

- long term or short term (LT, ST)
- sapwood or heartwood (s, h)
- wind direction (NN, NE, EE, SE, SS, SW, WW, NW)
- log (2, 3, 4)
- tree (T1, T2)

Figure 2.   Identification method for specimens.

tests is summarized in the fourth column of Table 1.

Specimen Treatment and Storage

Specimens for LT and creep tests. Both ends of the frozen LT-specimens were sealed with a silicone sealant (Sikaflex® AT-connection, Sika AG, Baar, Switzerland) to prevent moisture gradients along the grains. Five days before testing, the specimens were conditioned inside the climate chamber in the climate used for testing (for creep tests in steady conditions) or in the climate related to the initial RH phase (for LT tests conducted in varying conditions): 60°C and 40% RH ($\approx 7.2\%$ EMC) or 60°C and 80% RH ($\approx 15\%$ EMC) At the end of each test, the MC of all specimens was determined by using the oven-dry method (EN13183-1 2003).

Specimens for static tests. The sample set of 24 sapwood and 24 heartwood specimens was tested in static bending at an MC above the FSP to obtain the lower limit values of E and f_b, meant to understand the contribution of individual logs and specific positions within the logs to the variability of the results of the LT tests, and to determine the load level used in the LT and creep tests. To prevent sorption hysteresis, the specimens were dried from green state to an MC close to the FSP in five sealed plastic boxes equipped with fans, salt boxes, and heaters (IGLOO IMR2/ A, Amiga AB, Vara, Sweden) for a period of

110 d before testing. A potassium sulfate solution was used to maintain high humidity. For sapwood specimens, the conditioning regimen was 95% RH at 70°C for the first 40 da and 98% RH at 21°C for the rest of the conditioning period. Heartwood specimens were conditioned at 98% RH and 21°C all the time. The progress of the drying was monitored by recording the weight of the specimens every 5 d on average using a ± 0.001 g Sartorius LP620S analytical balance (Sartorius AB, Göttingen, Germany). The RH and temperature inside these boxes was monitored with Testo 635 sensors ($\pm 0.7\%$ of the measured temperature value and $\pm 1.8\%$ of the RH value). In these conditions, the specimens dried very slowly from green condition to 30% MC, until the daily mass differences were less than 1%, an MC still above 26% FSP reported for Norway spruce (Bratasz et al 2012). To prevent mold or rot, the specimens were cleaned with ethanol on a daily basis.

Test Setup

LT tests. The LT tests with varying climate and creep tests at constant humidity were conducted in a Vötsch VCR 4033/S climate chamber (Vötsch Industrietchnik GmbH, Balingen, Germany). A custom-made loading fixture was used to test three specimens simultaneously in bending (Fig 3). The fixture consisted of a steel test frame, movable lateral supports (Fig 3[a]), mechanical supports consisting of a roller and a pinned

connection type (Fig 3[b] and [c]), an aluminum loading rig (Fig 3[d]), and dead loads. The loading fixture was held up by struts attached to the interior of the climate chamber. The climate inside the chamber was regulated by a water bath with a temperature range between 10°C and 90°C and an RH range between 30% and 80%. During the tests, the climate in the chamber was monitored by three external pin-type temperature (±0.3°C) and humidity (±1.8% RH) sensors (SHT75 Sensirion, Stäfa, Switzerland) placed in the upper left back, upper right back, and lower right front of the climate chamber. A comparison with the recording made by the sensors built in the climate chamber showed a difference in temperature below 0.1% and a difference in RH within 5%.

The deflection over a length of 160 mm shear-free section of the beams (Figs 4-3/4 and u_l in Fig 4[a] [b]) was measured by linear variable differential transformers (LVDT) (HBM WI, Darmstadt, Germany) with a measuring range of 10 mm (±1 μm) mounted in a yoke that was attached to the beam at the neutral axis (Figs 3[d] and 4-4). The tip of the LVDT was loosely pressed under an L-shaped element that was also placed in the neutral axis at midspan (Figs 3[d] and 4-5). Full span deflection was measured as well, but the measurements are not used in this article.

Static tests. An MTS®-810 universal testing machine (UTM: MTS® systems Corporation, Eden Prairie, MN) was used to perform the static bending tests. The UTM was equipped with a 100 kN ± 2 N load cell and a custom-made four-point bending steel testing fixture, as illustrated in Fig 4b. The specimen was supported on two rollers at a 595-mm span, anchored on a base steel beam nested in the UTM. The load was transferred through an aluminum load evener pivoted at the upper grip of the UTM and then to the beam through two steel rollers at a heart distance of 190 mm (Fig 4[b]). The force between the rollers and the specimen was distributed by steel bearing plates with a 5-mm thickness, a 16-mm width, and a 55-mm length. The deflection over a length of 160 mm shear-free section of the beams was measured with an LVDT with an accuracy of ±0.01 mm attached to the neutral axes at midspan using an L-shaped element (see close-up Fig 4 [b]). The deflection over the full span was also measured, but not included in this article. The same setup was also used to determine E and f_b after the specimens were tested in the LT tests and additional creep tests.

Measurement of MC. The moisture changes in specimens tested in the climate chamber were estimated based on changes in mass of an
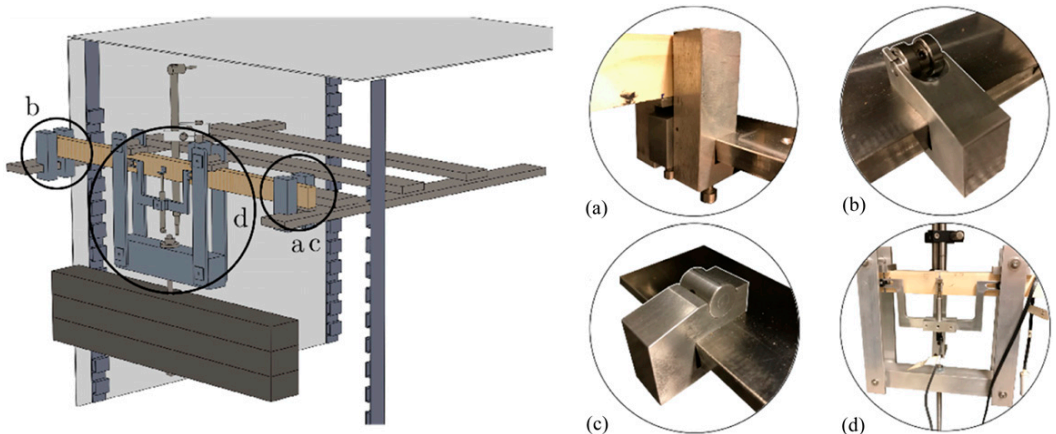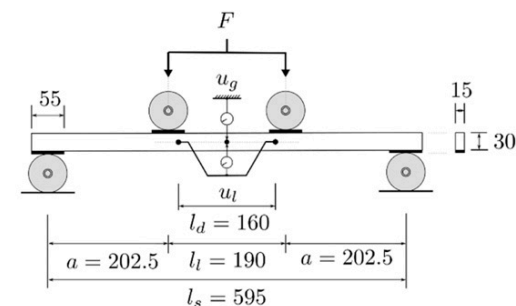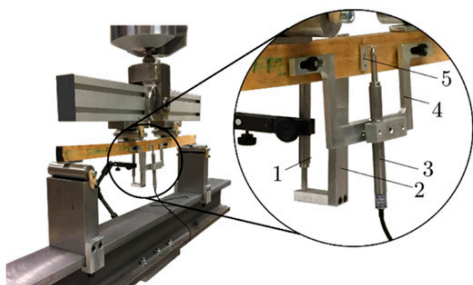

Figure 3. Rendering of the setup for long-term tests under varying and constant climate conditions, including details of the (a) lateral support, (b) roller support, (c) pinned support, and (d) displacement transducers and aluminum loading rig.

(a)

(b)

Figure 4. (a) Schematic representation of the static setup and (b) photos, where 1) is the LVDT measuring over the span of the specimen, 2) is the L-shaped element to support the LVDT and locate it in the neutral axis of the specimen, 3) is the LVDT measuring in the shear-free area of the specimen, 4) is the gauge used to position the LVDT, and 5) is the L-shaped element to place the LVDT at the neutral axis of the specimen.

unloaded reference specimen monitored with a waterproof Vibra CJ 820 CE ±0.01 g balance with a 820 g range (Lidén Weighing AB, Kungälv, Sweden, see Fig 5[b]) placed inside a
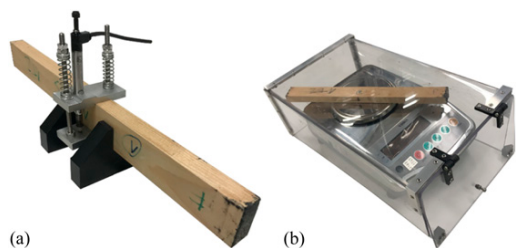
(a)   (b)

Figure 5. Additional equipment to the climate chamber, where (a) is the fixture to measure shrinkage and swelling over the depth of the specimen and (b) is a waterproof electronic scale including plastic coverage to measure the change in mass.

ventilated plastic box to avoid the interference of the internal air current. At the end of the test, the MC of each specimens was determined with the oven-dry method (EN 13183-1 2003).

Measurement of free hygro-expansion. The free hygro-expansion u_h in specimens tested in the climate chamber was estimated based on measurements of the depth of a matched unloaded specimen using a custom fixture shown in Fig 5[a]. An HBM WI displacement transducer was used with a measuring range of 10 mm (± 1 μm).

Data acquisition and storage. Signals from the humidity sensors and the transducers were collected with a QuantumX box (HBM), connected to a DAQ application Catman (HBM), whereas the signal from the scale was sent to a separate custom DAQ application by Saab AB (Sweden). The two systems were not synchronized and had different time stamps.

Testing Procedures

LT experiment and creep tests. The specimens tested in the climate chamber were loaded manually with calibrated dead loads in increments of 100 N on a rod attached to the loading rig, which added 13 N to the total load. For this procedure, the testing frame was partially slid out of the chamber using a custom supporting frame. A total load of 413 N was used for the sapwood specimens and 313 N for the heartwood specimens (Fig 6[a]), calibrated to achieve a target nominal bending stress below 40% of f_b at the FSP measured in the static tests, to prevent early failure of specimens. The related nominal bending stress for sapwood specimens was 18.6 MPa (bearing stress at the supports of 0.25 MPa) and 14.1 MPa for the heartwood specimens (bearing stress 0.19 MPa). It is important to keep in mind that the stress values change with changing geometry during RH cycles.

Both the LT tests and creep tests have been conducted at a constant temperature of 60°C (Fig 6[b]) to accelerate the development of deformations compared with lower temperature. The
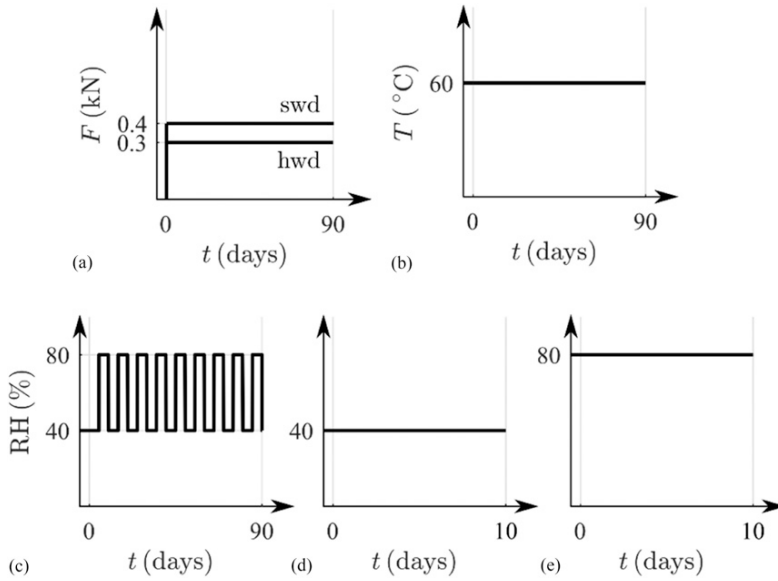
Figure 6.   Climate and load schedules for sapwood (swd) and heartwood (hwd) specimens used in the long-term experiment and creep tests: (a) load (*F*), (b) temperature (*T*), (c) RH schedule for LT experiment, (d) RH schedule for creep tests at 40% RH, and (e) RH schedule for creep tests at 80% RH.

creep and mechano-sorptive response rates are higher at elevated temperatures, as shown by Carlsson and Thunell (1975), Bodig and Jayne (1982), and Castera (1989). The RH schedule used in the main LT test illustrated in Fig 6(c) consisted of nine 10-d cycles: 5 d at 40% RH and 5 d at 80% RH. The RH schedule used in the creep tests is presented in Fig 6(d) and (e). Specimens EE, NN, and SS were tested for 10 d at a constant RH of 40%, and specimens NE, SE, and NW were tested at a constant RH of 80%.

The LT tests were continued until a constant deformation rate was confirmed by $R^2 \geq 0.95$ in a linear regression analysis on deflection values obtained at the end of the four consecutive RH phases of both the adsorption and desorption curves. At the end of the tests, specimens were unloaded and the elastic recovery was measured. After that, the humidity cycles continued with no load for 25 more days. Once the recovery phase was completed, the specimens were removed from the loading fixture and stored in a constant climate of 60°C and 40% RH until tested in static bending to obtain the residual E and f_b. The static

tests were performed at a room temperature of 21°C and an RH of 35% (EMC ≈ 6.9%). At the end of the test, the MC of each specimens was determined with the oven-dry method (EN 13183-1 2003).

Static tests. To minimize drying between mounting and testing (±5 min), the test specimens were pulled one at a time from the climate boxes located next to the UTM. The specimens were loaded with a displacement rate of 1 mm/s. The specimens were first preloaded to 300 N, unloaded to 50 N, and then loaded to failure. Load and displacement data were collected at a sampling rate of 5 Hz. At the end of the test, the MC of each specimens was determined with the oven-dry method.

Analysis of Results

Tests with cyclic climate changes. To resolve the components of the total deflection curve u_t measured in the shear-free section of the beam span, an analytical procedure was developed.

This procedure uses the description of u_t presented in Eq 6, and Eqs 7–9 to describe u_e, u_c, and u_{ms}, respectively. In the formulation of u_e according to Eq 7 (EN 408 2012), the effects of hygro-expansion are only included to describe the variation in the modulus of inertia of the cross-section during cyclic moisture changes. It can be safely assumed that the hygro-expansion along the beam axis does not affect the deflection in the plane of loading. However, u_h is added to the measured h at 40% RH and 60°C, and 0.33 u_h to the measured b at 40% RH and 60°C (Bengtsson 2001).

$$u_t = u_e + u_c + u_{ms} \tag{6}$$

$$u_e = \frac{3Fal_l^2}{4E(w)b(w)h^3(w)} \tag{7}$$

$$u_c = u_e^* \sum_{n=1}^{2} \phi_\sigma^n(w)\left(1 - e^{-t/\tau_n}\right) \tag{8}$$

$$u_{ms}(v) = u_e^*\left(\frac{1}{E_{ms}}\left(1 - e^{-v\alpha_1 E_{ms}}\right) + v\alpha_2\right) \tag{9}$$

A 2-module Kelvin model is used to describe u_c for all specimens (see Eq 8). The model is modified such that the elastic deflection right after loading u_e^* is used to scale u_c, which is an analogue to the description of ε_c in the beam element model, as described in the introduction. To describe u_{ms}, the analogues of the Newton and Kelvin models presented by Eqs 2 and 3 are combined in Eq 9. The deflection is scaled using the same elastic deflection right after loading u_e^*. Eq 9 is best analyzed in the cumulative moisture change or v-domain (rather than in the time domain). Because the cumulative MC change adds absolute values of all minuscule values of the recorded MC change, it is sensitive to noise in the MC signal. In fact, the level of noise was high enough to substantially affect the total length of the recorded cumulative moisture change v. The noise in the MC data was therefore removed by moving the average each 14 min.

Linear expressions (10–12) were used to describe the effect of MC w below the FSP (w_a) on the viscoelastic model parameters and to describe the shift in the FSP (w_f) at elevated temperature. In Eq 10, T_0 is a reference temperature of 20°C and T the test temperature of 60°C. The term ψ_{fT} describes the shift in the FSP due to a unit increment in temperature. The value for w_f for Norway spruce at reference temperature is 26% (Bratasz et al 2012) and holds a value of ψ_{fT} was assumed 0.0033°C^{-1} (Dinwoodie 1981). The expression 11 for E is based on experimental work carried out by Dinwoodie (1981). The reference value E_0 is unique for each specimen and determined from the instantaneous elastic deflection in the total deflection curve obtained in the LT tests under cyclic climate. The term Y_{w0} indicates the change in E_0 due to unit MC increment, and holds a value of 21000 MPa (Keunecke et al 2007). The reference values $\phi_{\sigma0}^n$ were unique for each specimen and obtained with a fit on the creep deflection data monitored in the first 5 d until the first climate cycle, whereas the term χ_{w0} that describes the change in ϕ_σ due to unit MC increment was determined from the reference creep tests. The complete analytical procedure was implemented in MATLAB® (MathWorks, Natick, MA).

$$w_f = 0.26\left(1 + \psi_{fT}(T_0 - T)\right) \tag{10}$$

$$E = E_0 + Y_{w0}\left(w_f - w_a\right) \tag{11}$$

$$\phi_\sigma^n = \phi_{\sigma0}^n + \chi_{w0}^n\left(w_f - w_a\right) \tag{12}$$

Creep at constant climate. The creep tests at constant climate were used to obtain χ_{w0}^n for both the sapwood and heartwood sample sets (see Eq 12). The creep deflection was isolated from the total deflection curve by subtracting u_e^*. The individual and the average values of u_c fitted Eq 8. To obtain χ_{w0} for each of the two Kelvin modules, a linear relation was assumed between the obtained average values for ϕ_σ at 40% and 80% RH with Eq 12.

The procedure used to analyze the effect of moisture on u_c for each specimen tested in the LT experiment is visualized in Fig 7. In this figure, the expected creep curves at a constant RH levels of 40% and 80% are drawn. The MC influences the deflection rate du_c/dt during either of the two RH

phases of the climate cycle (Engelund and Salmen 2012; Hering and Niemz 2012). Instead of simulating a gradual change in the deflection rate following the MC change in the specimens, a simplified but conservative assumption was made that the creep rate changes immediately with EMC corresponding the 40% or 80% RH phase of the cycle. The effect of the moisture cycles on u_c is estimated by a summation of deflection increments Δu_c at 40% and 80%RH for each of the 9 cycles analyzed in the LT test.

Static tests. The ST test was used to determine reference E and f_b based on Eqs 13 and 14, respectively

$$E = \frac{3}{4} \frac{a l_d^2}{b h^3} \frac{\Delta F}{\Delta u_l} \tag{13}$$

$$f_b = 3Fa/bh^2, \tag{14}$$

where $\Delta F / \Delta u_l$ is the slope of the linear section of the load–displacement curve measured in the shear-free section of the beam over a displacement range Δu_l between 0.1 and 0.25 mm. The slope $\Delta F / \Delta u_l$

Figure 7. Procedure used to analyze the increase in creep deflection u_c due to systematic changes in RH between 40% and 80%, where Δu_c is the increase in deflection after each respective RH phase and i indicates the amount of RH cycles.

was estimated using a linear regression analysis. A satisfying result was obtained, when a coefficient of correlation larger than 0.99 was found (EN 408 2012). The mean values for E, f_b, and w were determined for sapwood and heartwood specimens harvested from different positions of the logs and, separately, for pooled data for all positions.

Hygro-expansion. The hygro-expansion coefficient γ is needed in the beam model to describe the strain related to shrinkage and swelling of the cross section ε_h and the resulting changes in the section modulus of inertia. The γ for each RH cycle was determined for both the sapwood and heartwood specimens using Eqs 15 and 16

$$\varepsilon_h = \frac{h_{80} - h_{40}}{h_{80}} \tag{15}$$

$$\gamma = \frac{\varepsilon_h}{w_{80} - w_{40}}, \tag{16}$$

where ε_h is determined using the depth of the specimen at an EMC corresponding to 80% RH, h_{80}, and at an EMC corresponding to 40% RH, h_{40}. The slight curvature of the annual rings in the cross-section was neglected.

RESULTS AND DISCUSSION

The following section presents the primary results obtained with the procedures described in Section 2. To isolate the mechano-sorptive deformations in the LT tests with variable climate conditions, it is necessary to subtract the other components of the total deflection based on measurements obtained from the reference and creep tests, as described in Eq 6. Therefore, first, the results from the static tests, creep tests, mass measurements, and hygro-expansion measurements are discussed, and the resulting mechano-sorptive deflection curves and the results of fitting the mechano-sorption deflection model are presented last.

Static Tests

In Table 2, the mean values for w, f_b, and E are collected for the all-sapwood and all-heartwood sample sets as well as for the individual wind
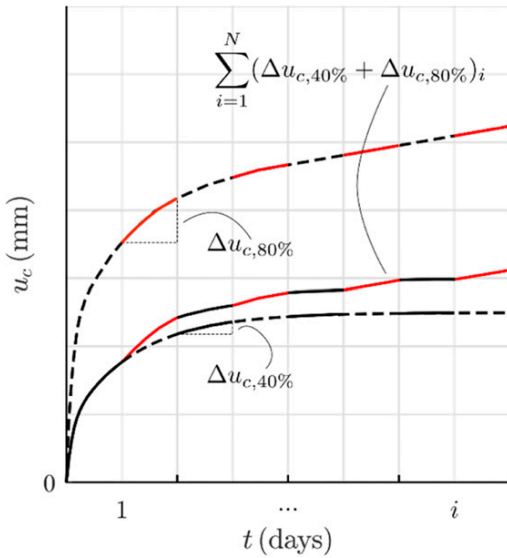
Table 2. Mean μ for MC w measured at the end of the experiment, the modulus of rupture f_b, and the elastic modulus E for either the whole sapwood (swd) or heartwood (hwd) sample set or individual wind directions

Specimen location in the log		w (%)				f_b (MPa)				E (GPa)			
		#	swd	#	hwd	#	swd	#	hwd	#	swd	#	hwd
NN	μ	3	30.3	3	30.1	3	45.6	3	36.1	3	10.8	3	7.76
EE	μ	2	31.2	3	30.0	1	44.8	2	39.0	1	9.0	2	8.32
SS	μ	3	30.1	3	29.9	3	46.8	2	31.4	3	11.9	2	7.99
WW	μ	3	30.5	3	29.7	2	50.1	3	37.4	3	11.9	3	8.35
NE	μ	3	30.0	3	29.7	3	46.3	3	35.1	2	11.7	3	7.25
SE	μ	3	30.6	3	30.0	1	41.3	3	31.9	2	11.9	3	7.71
SW	μ	3	30.4	3	29.8	3	47.9	3	35.7	3	13.1	3	9.00
NW	μ	3	30.3	3	33.6	3	49.2	3	33.0	3	12.9	3	8.98
All	μ	23	30.3	24	30.4	19	47.0	22	34.9	20	11.9	22	8.2

directions. The results found for w confirm that specimens were at 30% MC during testing. For f_b, a mean value of 47 MPa for the all sapwood sets and 35 MPa for the all heartwood sets were found. The sapwood values exceed those published in the FLP Wood Handbook for clear wood specimens in green state for several spruce species, which where between 42 and 32 MPa (Wood Handbook 2010). The same is seen for E, where the mean values for sapwood and heartwood were 11.9 and 8.2 GPa, respectively, whereas the reported values by the FLP Wood Handbook were between 9.5 and 7.1 GPa (Wood Handbook 2010).

The largest difference in E was found between the all-sapwood and all-heartwood data sets (Fig 8). The differences in characteristics observed in specimens harvested from sapwood and heartwood zones may be attributed to the content of juvenile wood; however, we were not able to determine the content of juvenile wood directly, and we cannot make such conclusions with definite or even measurable margin of confidence. Minor differences in E between mean values for the wind direction from NN to NW were found in the sapwood and heartwood sample sets (11.9–13.1/7.7–9.0 GPa).

Based on the mean f_b for the all sapwood and all heartwood sample sets, a load level of 34% of the ultimate value was chosen for both the sapwood and heartwood specimens used in the LT tests under varying and constant climate conditions. However, f_b measured in the static tests on specimens subjected to the LT tests indicated that the actual load levels were between 15 and 30%.

Creep Tests

The results of the creep tests at 40% and 80% RH are presented in Fig 9, along with the individual
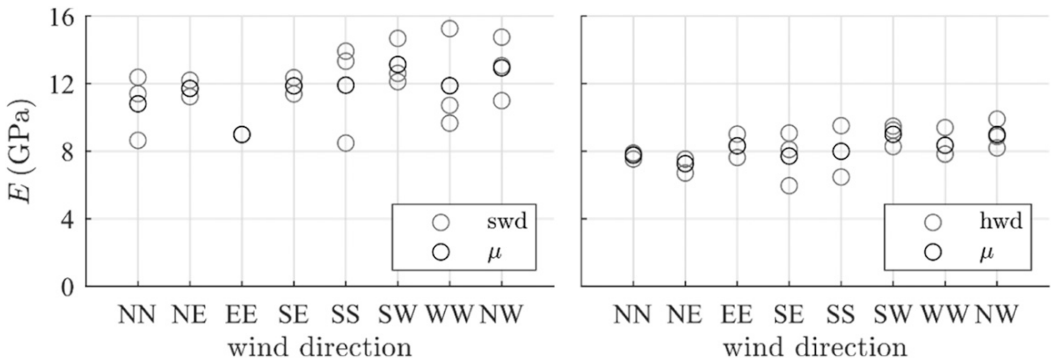

Figure 8.   Raw data (gray) and mean values (black) for the elastic modulus E obtained for the different wind directions (presented clockwise on the x-axis) in the sapwood (swd) and heartwood (hwd) sample sets.
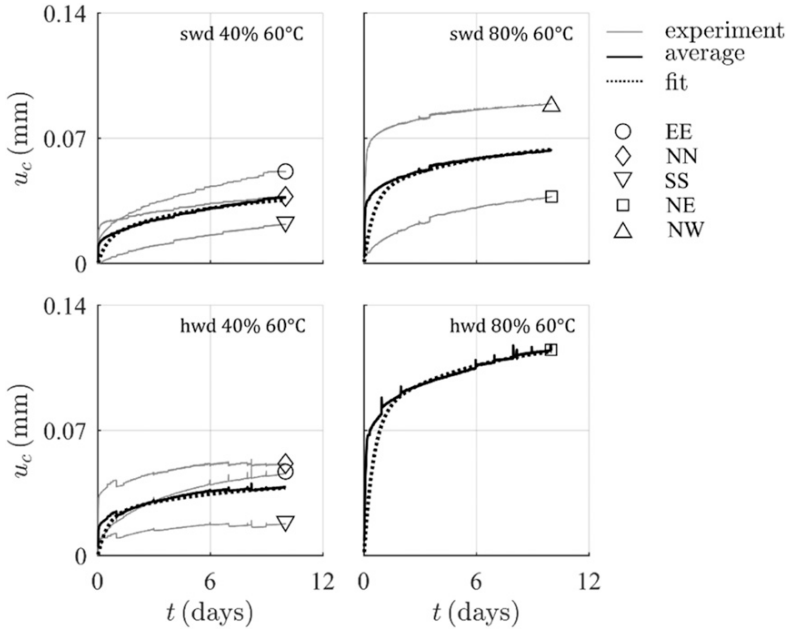
Figure 9.   Individual and mean creep deflection curves u_c obtained in the creep tests performed on log T1-3, together with a fit made with the 2-module Kelvin model.

creep deflection component u_c of each specimen (from different locations in the log), the averaged curves, and a best fit based on Eq 8. Results of one sapwood and two heartwood specimens tested at 80% RH could not be used because of LVDT failure. Despite the low variation in E seen in the ST experiment, the results of each individual creep test show a noticeable variation in u_c between specimens, which gives a mixed effect of position within the log and MC.

For sapwood, the averaged value of u_c after 10 d of testing was 0.037 mm at 40% RH and 0.063 mm at 80% RH. For heartwood, these values were 0.038 mm and 0.120 mm, respectively. A 70% difference in u_c for the all sapwood sets and a 200% difference for the all heartwood sets are observed when tests performed at 40% RH and 80% RH are compared. Table 3 summarizes the material parameters of Eqs 7 and 8 obtained with the fitting made with Eqs 7 and 8 fitted to the experimental data and the resulting χ_{w0} parameter of Eq 12 used to express the moisture effect on each module of the Kelvin model.

MC Change

The changes in average MC (neglecting internal moisture gradients) in the reference sapwood and heartwood specimens labeled T1-2-WW during the LT experiment are presented in Fig 10. For both specimens, the MC fluctuated between 7% and 13%, which agrees with the EMC values published in 2010 FPL Wood Handbook: 6.3% MC for 40% RH and 13.6% MC for 80% RH (Wood Handbook 2010). The initial value for sapwood is 7.4% and for heartwood 7.7% at 40% RH, and 12.8% and 12.7% at 80% RH, respectively. The MC at the FSP for 60°C calculated using Eq 10 was 23%.

Shrinkage and Swelling

The hygro-expansion u_h measured over the depth of the unloaded sapwood and heartwood reference specimens labeled T1-2-WW is presented in Fig 11, together with the hygro-expansion coefficient γ. Because of the RH cycle, γ changes in

Table 3. Creep parameters ϕ_σ^n and τ_n determined with the fit on the individual and average creep deflection curves using the 2-module Kelvin model, including the calculated values for χ_{w0} for both sapwood and heartwood

	Moisture	Elastic	Creep			
	w (%)	E^* (GPa)	ϕ_σ^1 (−)	τ_1 (h)	ϕ_σ^2 (−)	τ_2 (h)
Sapwood						
40% 60°C						
EE	4.89	14.7	0.080	0.5	0.160	6.0
NN	4.95	24.4	0.140	0.5	0.120	6.0
SS	5.56	19.3	0.010	0.5	0.130	6.0
μ	5.13	19.5	0.075	0.5	0.130	6.0
80% 60°C						
NE	13.8	16.3	0.050	0.5	0.160	6.0
NW	14.0	12.9	0.270	0.5	0.090	6.0
μ	13.9	14.6	0.170	0.5	0.130	6.0
χ_{w0}	—	—	1.25	—	0.00	—
Heartwood						
40% 60°C						
EE	7.38	12.9	0.080	0.5	0.180	6.0
NN	7.25	13.4	0.200	0.5	0.080	6.0
SS	7.33	27.6	0.080	0.5	0.120	6.0
μ	7.32	18.0	0.150	—	0.130	—
80% 60°C						
NE	12.9	10.2	0.315	0.5	0.175	6.0
μ	12.9	10.2	0.315	—	0.175	—
χ_{w0}	—	—	3.06	—	0.84	—

Figure 10.   Average MC changes of the total volume before filtering for (a) sapwood and (b) heartwood specimen T1-2-WW recorded during LT-tests.

value, and the values fluctuate slightly from cycle to cycle (Fig 11). Values between 0.39 and 0.35(−) are estimated for sapwood and between 0.17 and 0.09(−) for heartwood, of which the initial values of 0.39 and 0.17(−) found for sapwood and heartwood, respectively, correspond to values reported by Perstorper et al (2001) and Bengtsson (2001) for Norway spruce, where between pith and bark, an average is found around 0.35(−) and extremes between 0.18 and 0.5(−). The lower values for the heartwood specimen can be due to juvenile wood, which tends to experience a decrease in tangential hygro-expansion (Persson 2000). However, as mentioned previously, we were not able to determine the content of juvenile wood directly.

Long-Term Experiment

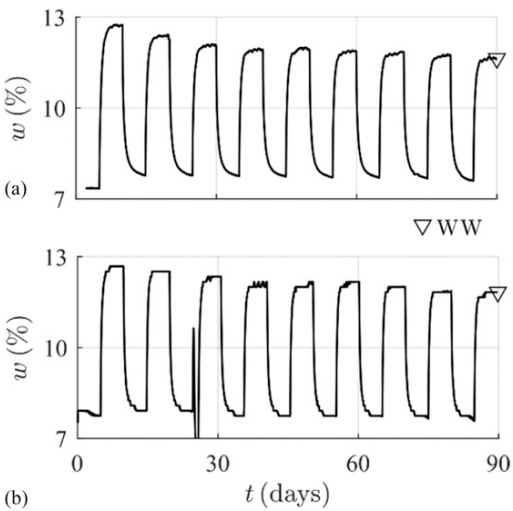***End-of-the-test criterion.*** Fig 12 shows the minimum (adsorption) and maximum (desorption) values of the total deflection u_t recorded at the end of each half-cycle of the climate schedule for each specimen tested in the LT experiment with linear regression curves fitted to the last four extreme cycle points. The coefficient of determination (R^2) for all lines exceeded 0.963, indicating that all beams reached a stage with constant deflection rate, the assumed criterion for the termination of the LT test. The regression lines are also shown in Fig 12.

Separation of the components of total deflection curves. The process of separation of the components of the total deflection of the test beams leading to the isolation of the mechano-sorptive component is shown in Fig 13. The first set of curves (marked with a circle) represent the total deflection u_t measured in the shear-free section of the beams subjected to LT load at variable climate conditions, separately for the sapwood and heartwood specimens. The part used in the analytical procedure is marked black. The recorded u_t show characteristics similar to these first reported by Armstrong and Christensen (1961); Armstrong and Kingston (1962) for initially dry wood at relatively low load-level bending. The first adsorption (moisture intake)
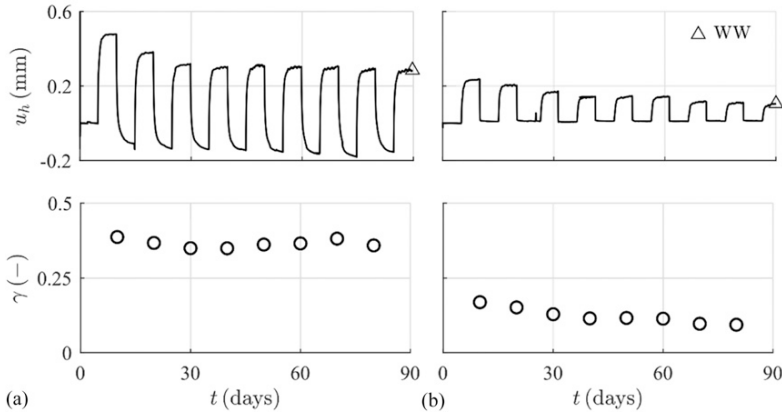
Figure 11.   Hygro-expansion u_h and swelling coefficient γ obtained in the plane of loading (along the depth of specimen) for (a) sapwood and (b) heartwood specimen T1-2-WW tested in LT experiment.

and subsequent desorption (moisture release) result in substantial increase in deflection. When one neglects the fluctuation between high- and low-humidity cycles, a decreasing deflection rate in the first days of testing and a constant deflection rate for the remaining time are seen.

A wide range in u_t is seen between the individual specimens of the all sapwood and all heartwood sample sets, highlighting the strong effect of the location within the log. When the load is chosen proportional to the mean f_b, this effect is more significant than the differences seen between sapwood and heartwood. The first graph in Fig 13(b) shows the early failure of specimen EE later traced back to the presence of a large knot with strong grain deviation around, despite the careful specimen selection procedure.

Looking at the individual deflection components, the u_{ms} curves (marked with triangle) show a decreasing deflection rate, followed by a constant deflection rate. The u_e curve (marked with diamond) is generally constant, showing a slight fluctuation change due to a difference in competing changes in $E(w)$ and modulus of inertia caused by cyclic moisture changes, leaving the resulting stiffness $E(w)I(w)$ almost unchanged. The tiny peaks in the curves are caused by a slight time difference between hygro-expansion and MC collected by different DAQ applications. For u_c, a decreasing deflection rate is found for the first 30 d of testing, after which no measurable growth is observed. This is in contrary to what is seen in Fig 9, where the creep curves show constant deformation rates at the end of the test. The series of Kelvin modules used to describe u_c
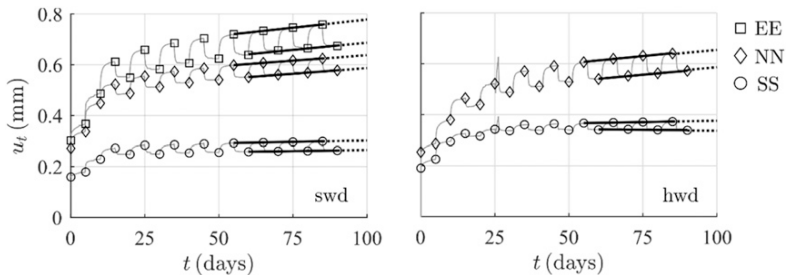

Figure 12.   Analysis to determine the end of the long-term experiment based on linear regression lines for each specimen EE (squares), NN (diamonds), and SS (circles) in the sapwood (swd) and heartwood (hwd) sample sets.
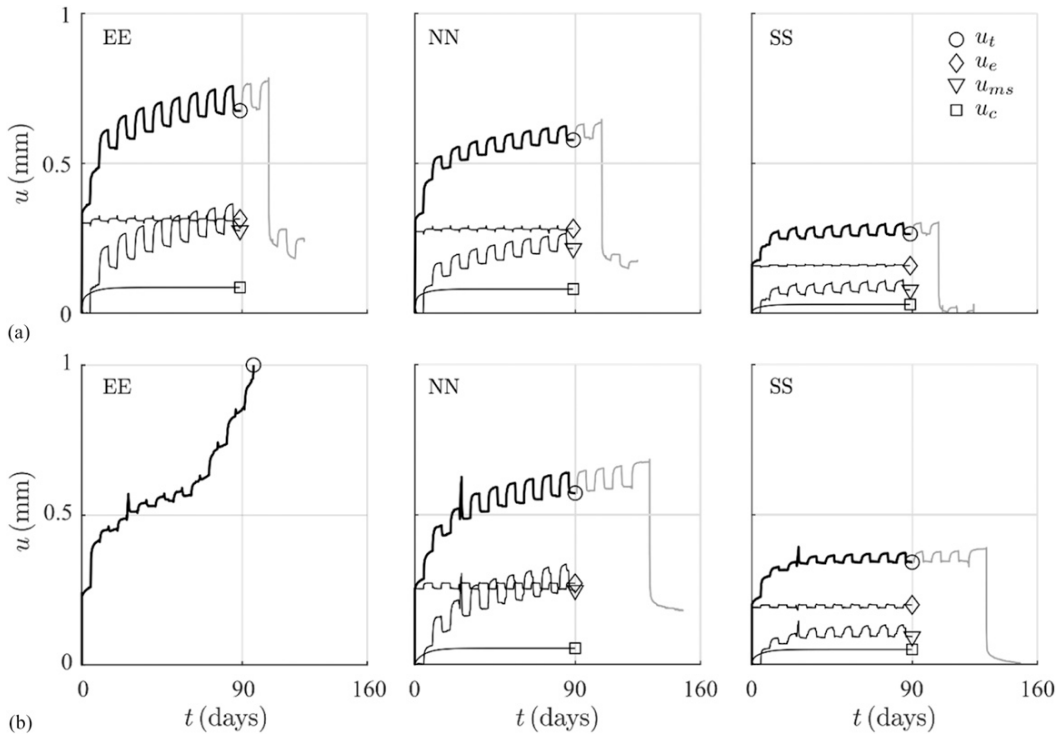
Figure 13.   Separation of the total deflection u_t curves into an elastic u_e, creep u_c, and mechano-sorptive u_{ms} component for 90 da of LT tests (a) sapwood and (b) heartwood.

result in a good fit with the experimental data time range, but making it challenging to predict the behavior beyond the fit range because it will eventually trend toward a horizontal asymptote.

The largest contributor to u_t measured in the shear-free section of the beam after 90 d of testing is u_e (46-60%), followed by u_{ms} (27-43%) and u_c (10-15%) (Table 4). This is consistent with observation made in the study on red spruce using a similar experimental methodology (Muszyński et al 2006). The values for u_c are not negligible and prove essential for proper isolation of the mechano-sorptive deflection curve (Hering and Niemz 2012). With the chosen 2-module Kelvin model chain (see Eq 8), it is found that the MC at time of loading is more decisive for the magnitude of u_c after 90 d of testing than the following RH cycles (see $u_{c,40}$, $u_{c,80}$, and $u_{c,40-80}$ in Table 4). With the scale of these adjustments

relatively small compared with the total creep deformation and the scale of other components, it was deemed safe to use the creep curve fit made at 40% RH in the analysis. The parameters of Eq 11 obtained at loading and unloading at 80% RH are collected in Table 5, together with the parameters of the 2-module Kelvin model chain fitted to u_c obtained from the first 5 d of testing until the first climate cycle and corresponding to 80% RH estimated with Eq 12.

The values for E^* show a more distinct variation between specimens than previously seen in Fig 8. The values found for E^* and E^{**} do not show much difference between loading and unloading, both performed at the end of the 40% RH part of the cycle. The creep parameters describing the initial deformation rate with the 2-module Kelvin model and collected in the creep tests (see Table 3) and the LT experiment (see Table 5) are

Table 4. Total deflection u_t at the end of 90-d tests in cycling climate conditions, compared with the values for the elastic u_e, creep u_c and mechano-sorptive deflection u_{ms} components calculated from the reference tests, including the elastic deflection right after loading u_e^* and the percentage difference of each component with respect to u_t

	Total (mm)	Elastic (mm)		Creep (mm)			Mechano-sorption (mm)
	u_t	u_e^*	u_e	$u_{c,40}$	$u_{c,80}$	$u_{c,40-80}$	u_{ms}
Sapwood							
EE	0.676	0.310	0.314	0.0856	0.1062	0.0856	0.2757
% of total	100	—	46	13	18	13	41
NN	0.578	0.275	0.281	0.0803	0.0990	0.0803	0.2156
% of total	100	—	49	14	17	14	37
SS	0.264	0.157	0.158	0.0289	0.0397	0.0289	0.0773
% of total	100	—	60	11	15	11	28
Heartwood							
NN	0.573	0.250	0.271	0.0539	0.1026	0.0555	0.2478
% of total	100	—	47	9	18	10	43
SS	0.342	0.190	0.199	0.0499	0.0865	0.0512	0.0927
% of total	100	—	58	15	25	15	27

visualized in Fig 14 to show the effect of moisture on ϕ_1 and ϕ_2 and detect possible differences between the parameters obtained with the two tests. The effect of moisture is mainly seen in ϕ_1, which is primarily used to describe the decreasing deflection rate, and complies with that in Table 4. No specific differences are found between the two test types.

Analysis of the Mechano-Sorption Curves

The mechano-sorptive deflection curves presented in Fig 15 in the cumulative MC domain develop in a similar manner as the strain curves presented for red spruce in tension parallel to the grain (Muszyński et al 2006). First, a decreasing deflection rate phase is experienced, followed by

a constant deflection rate phase segment. The values of the fitted mechano-sorption parameters (used in Eq 9) are collected in Table 6 for each specimen tested in the LT experiment. A general difference observed between the data presented by Muszyński et al (2006) and Fig 15 is the presence of substantial oscillation that is clearly visible for the specimens tested in bending, which may be an effect of neglecting the internal moisture gradients within the specimens as they react to the rapid changes in the humidity of the ambient air between the 40% and 80% humidity.

In Table 6, the mechano-sorptive parameters belonging to each specimen tested in the LT experiment are collected. Because of the limited data sets, it is difficult to find a statistical correlation with a considerable confidence level

Table 5. Elastic modulus E determined with the initial elastic deflection $(\bullet)^*$, unloading $(\bullet)^{**}$ and Eq 11 at 80% RH, and creep parameters ϕ_σ^n and τ_n corresponding to the 2-module Kelvin model obtained from the first 5 d of testing under constant RH of 40% for each sapwood and heartwood specimens tested in the LT experiment, and estimated at 80% RH with Eq 12 and values for χ_{w0} presented in Table 3

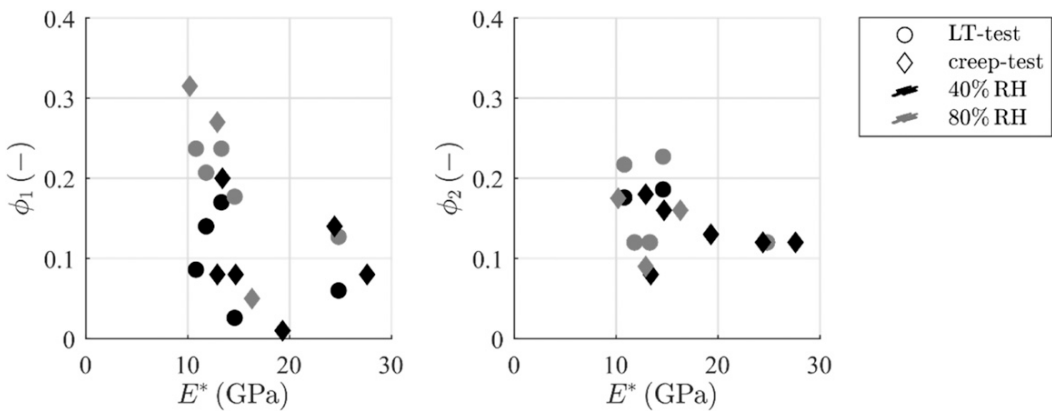|	Elastic			Creep							
	E^* (GPa)	E^{**} (GPa)	E_{80} (GPa)	$\phi_{\sigma,40}^1$ (−)	$\phi_{\sigma,80}^1$ (−)	$\phi_{\sigma0}^1$ (−)	τ_1 (h)	$\phi_{\sigma,40}^2$ (−)	$\phi_{\sigma,80}^2$ (−)	$\phi_{\sigma0}^2$ (−)	τ_2 (h)
Sapwood											
EE	12.2	12.6	11.0	0.140	0.207	0.33	0.5	0.120	0.120	0.14	6.0
NN	13.8	12.9	12.6	0.170	0.237	0.36	0.5	0.120	0.120	0.12	6.0
SS	25.7	25.6	24.5	0.060	0.127	0.25	0.5	0.120	0.120	0.12	6.0
Heartwood											
NN	11.3	11.6	10.2	0.086	0.237	0.48	0.5	0.176	0.217	0.31	6.0
SS	15.3	13.4	14.3	0.026	0.177	0.54	0.5	0.186	0.227	0.30	6.0

Figure 14.   Initial deformation rate of the 2-module Kelvin model ϕ_1 and ϕ_2 obtained in the LT experiment (circles) and creep tests (diamonds) at 40% (black) and 80% (gray) RH, previously presented in Tables 3 and 5 plotted against the elastic modulus at loading E^*.

between E, and E_{ms} and α_2. Also, it should be stressed again that it is inherently difficult to obtain reliable material-level mechano-sorptive characteristics because of the coincidence of internal moisture gradients, complex nonuniform stress patterns, and deviating material orientation (Muszyński et al 2005).

CONCLUSIONS

The purpose of the study is to provide the empirical validation to the beam element model developed by Ormarsson and Dahlblom (2013). The constitutive models similar to those used in

that beam element model were used to extract the mechano-sorptive component of the total deflection by subtracting the moisture-dependent viscoelastic components.

The primary findings for the beam geometry presented in this article are as follows:

1. The experimental and analytical procedures led to a successful identification of each deflection component and isolation of mechano-sorptive deflection curves. The chosen constitutive model used to describe mechano-sorption allowed a reasonable fit and was able to describe both the
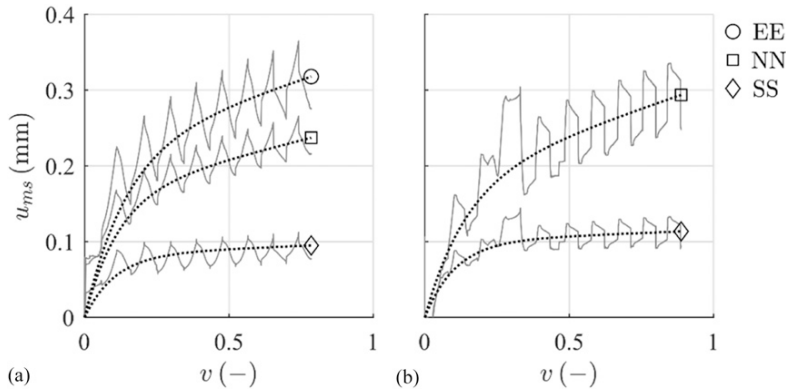

Figure 15.   Mechano-sorption deflection u_{ms} component plotted in respect to cumulative MC change v for each individual specimens part of (a) the sapwood and (b) the heartwood sample sets.

Table 6.   Mechano-sorptive model parameters E_{ms}, α_1, and α_2 obtained by fitting Eq 9 in the cumulative MC change domain v

	Mechano-sorption		
	E_{ms} (MPa)	α_1 (MPa^{-1})	α_2 (MPa^{-1})
Sapwood			
EE	1.4	5.0	0.40
NN	1.7	5.0	0.35
SS	1.9	5.0	0.10
Heartwood			
NN	1.4	5.0	0.52
SS	1.9	5.0	0.08

decreasing and constant deflection rate phases seen in the overall shape of the curves.

2. Over a period of 90 d of cyclic climate testing program, the elastic deflection was the most dominant component, followed by mechano-sorption, and creep. Still, the creep deflection was nonnegligible and showed to be important for proper identification of the mechano-sorptive deflection component in the total deflection. The applied creep model gave good results over the period which was used to make the fit.

3. Although no considerable variation in the elastic modulus and modulus of rupture determined in static tests was found between specimens extracted from different positions in the logs (described by wind directions), the viscoelastic creep and mechano-sorptive deformations varied substantially. However, with just three specimens sourced from each position in the log, it is impossible to conclude on correlation. Nevertheless, we may conclude that in future projects, specimens should be grouped by end-matching along the grain.

4. The effect of moisture on creep behavior showed especially important during loading and the first stages of the decreasing deflection phase, after which the contribution decreased rapidly.

5. For the selected load level and range of cumulative moisture changes, no asymptotic limit of the mechano-sorptive deflection could be detected.

FUTURE RESEARCH

The quantities measured in this study will be used to validate the beam element model. MC, constitutive model parameters, and material characteristics are needed for the inputs, whereas total deflection and deflection components are needed for the outputs. To widen the range in which the beam model will be validated, additional tests at different temperatures and lower RH ranges should be performed. Also, to be able to make a statistical analysis, the number of specimens should be increased for each test.

REFERENCES

Armstrong LD, Christensen GN (1961) Influence of moisture changes on deformation of wood under stress. Nature 4791:869-870.

Armstrong LD, Kingston RST (1962) The effect of moisture content changes on the deformation of wood under stress. Aust J Appl Sci 13:257-276.

Bengtsson C (1999) Mechano-sorptive creep in wood: Experimental studies of the influence of material properties. Doctoral thesis, Chalmers University of Technology, Gothenburg, Sweden.

Bengtsson C (2001) Variation of moisture induced movements in Norway spruce (*Picea abies*). Ann Sci 58: 569-581.

Bodig J, Jayne BA (1982) Mechanics of wood and wood composites. Van Nostrand Reinhold Company, New York, NY.

Brancheriau L, Bailleres H, Guitard D (2002) Comparison between modulus of elasticity values calculated using 3 and 4 point bending tests on wooden samples. Wood Sci Technol 36:367-383.

Bratasz Ł, Kozłowska A, Kozłowski R (2012) Analysis of water adsorption by wood using the Guggenheim-Anderson-de Boer equation. Eur J Wood Wood Prod 70:445-451.

Carlsson H, Thunell B (1975) Shrinking behaviour of wood during drying effect of tensile stresses. Paperi ja Puu, 7.

Castera P (1989) Tensile creep of small wood specimens across the grain under drying conditions. *In* IUFRO International Wood Drying Symposium, Seattle, WA.

Dinwoodie JM (1981) Timber: Its nature and behaviour, 2nd edition. E&FN Spon Taylor & Francis Group.

EN 13183-1 (2003) Moisture content of a piece of sawn timber - Part 1: Determination by oven dry method. European Committee for Standardization (CEN), Brussels, Belgium.

EN 408 (2012) Structural timber - structural timber and glued laminated timber - determination of some physcial and mechanical properties. European Committee for Standardization (CEN), Brussels, Belgium.

Engelund ET, Salmen L (2012) Tensile creep and recovery of Norway spruce influenced by temperature and moisture. Holzforschung 66:959-965.

Hanhijärvi A (2000) Advances in the knowledge of the influence of moisture changes on the long-term mechanical performance of timber structures. Mater Struct 33:43-49.

Hearmon RFS, Paton JM (1964) Moisture content changes and creep of wood. Forest Prod J 8:357-359.

Hering S, Niemz P (2012) Moisture-dependent, viscoelastic creep of European beech wood in longitudinal direction. Eur J Wood Wood Prod 70:667-670.

Holzer SM, Loferski JR, Dillard DA (1988) A review of creep in wood: Concepts relevant to develop long-term behavior predictions for wood structures. Wood Fiber Sci 21:376-392.

Hunt DG (1989) Linearity and non-linearity in mechano-sorptive creep of softwood in compression and bending. Wood Sci Technol 23:323-333.

Hunt DG (1999) A unified approach to creep of wood. R Soc 455:4077-4095.

Keunecke D, Sonderegger W, Pereteanu K, Lüthi T, Niemz P (2007) Determination of Young's and shear moduli of common yew and Norway spruce by means of ultrasonic waves. Wood Sci Technol 41:309-327.

Lagaňa R, William GD, Muszyński L, Shaler SM (2011) Moment-curvature analysis of coupled bending and mechano sorptive response of red spruce beams. Wood Fiber Sci 43:280-292.

Morlier P (1994) Creep in timber structures Rilem report 8. Rilem Technical Committee, London, UK.

Muszyński L, Lagaňa R, Shaler SM (2006) Hygro-mechanical behavior of red spruce in tension parallel to the grain. Wood Fiber Sci 38:155-165.

Muszyński L, Lagaňa R, Shaler SM, Davids W (2005) Comments on the experimental methodology for determination of the hygro-mechanical properties of wood. Holzforschung 59:232-239.

Ormarsson S, Dahlblom O (2013) Finite element modelling of moisture related and visco-elastic deformations in inhomogeneous timber beams. Eng Struct 49:182-189.

Ormarsson S, Gíslason ÓV (2016) Moisture-induced stresses in glulam frames. Eur J Wood Wood Prod 74:307-318.

Ormarsson S, Steinnes JR (2014) An enhanced beam model for glued laminated structures that takes moisture, mechano-sorption and time effects into account. Paper Presented at the World Conference of Timber Engineering, August 10-14, 2014, Quebec, Canada.

Ottosen N, Petersson H (1992) Introduction to the finite element method. Prentice Hall, Lund, Sweden.

Persson K (2000) Micromechanical modelling of wood and fibre properties. Doctoral thesis, Lund University, Lund, Sweden.

Perstorper M, Johansson M, Kliger R, Johansson G (2001) Distortion of Norway spruce timber: Part I variation of relevant wood properties. Eur J Wood Wood Prod 59:94-103.

Ranta-Maunus A (1975) The viscoelasticity of wood at varying moisture content. Wood Sci Technol 9:189-205.

Risbrudt CD, Ritter MA, Wegner TH (2010) Wood handbook: Wood as an engineering material. Forest Product Laboratory, Madison, WI.

Rybarczyk W (1973) Study on the development of mathematical model of mechanical properties of some wood materials undergoing changes in their moisture conten (in Polish). Prace Instytutu Technologii Drewna 66(2):17-138.

Salin JG (1992) Numerical prediction of checking during timber drying and a new mechano-sorptive creep model. Eur J Wood Wood Prod 50:195-200.

APPENDIX

Abbreviations	
EMC	EMC
LT	Long-term, in reference to duration of tests and related specimens
ST	Static, in reference to the tests and related specimens
UTM	Universal testing machine

NOTATIONS and units		
a	mm	Shear span (between load and support)
b	mm	Width of specimen
E	MPa	Pure elastic modulus
E_{ms}	MPa	Parameter of mechano-sorptive model (analogue of Hooke's spring parameter in Kelvin model)
Y_{w0}	MPa	Term to indicate relation of E to moisture
E_0	MPa	Reference value to describe E
F	kN	Total bending load
f_b	MPa	Modulus of rupture (bending strength)
h	mm	Depth of specimen
I	mm^4	Moment of inertia
l_d	mm	Gauge length for the determination of elastic modulus
l_l	mm	Shear-free span (between loads)
l_s	mm	Full span in bending
m	kg	Mass
T	°C	Temperature
T_0	°C	Reference temperature of 20°C
u_c	mm	Creep deflection component
u_e	mm	Elastic deflection component
u_g	mm	Deflection measured over the full span
u_h	mm	Free hygro-expansion
u_l	mm	Deflection measured in shear-free section beam, see l_d
u_{ms}	mm	Mechano-sorptive deflection component
u_t	mm	Total deflection
v	—	Cumulative MC change
w	—	MC
w_a	—	MC below FSP
w_f	—	FSP
α	MPa^{-1}	Parameter of mechano-sorptive model (analogue of dashpot viscosity in Kelvin model)
γ	—	Hygro-expansion coefficient
ε_c	—	Creep strain
ε_e	—	Elastic strain
ε_h	—	Free hygro-expansion strain
ε_{ms}	—	Mechano-sorption strain
ε_t	—	Total strain
μ	—	Mean
τ	h	Retardation time in Kelvin creep model
ϕ_σ	—	Initial deformation rate in Kelvin creep model
$\phi_{\sigma0}$	—	Reference term to describe ϕ_σ
χ_{w0}	—	Term to indicate relation of ϕ_σ to moisture
ψ_{fT}	–	Term to describe relation of w_f to temperature
Δ	—	Range in reference to variables universal testing machine
$(\bullet)^*$	—	Material properties corresponding to loading stage
$(\bullet)^{**}$	—	Material properties corresponding to unloading stage

IV

A Three-dimensional Numerical Analysis of Moisture Flow in Wood and of the Wood's Hygro-mechanical and Visco-elastic Behaviour

Sara Florisson[1,✉] · Johan Vessby[2] · Sigurdur Ormarsson[1]

Abstract A three-dimensional numerical model developed using the finite element (FE) software Abaqus FEA® was employed in simulating nonlinear transient moisture flow in wood, and the wood's hygro-mechanical and visco-elastic behaviour under such conditions, account being taken of the fibre orientation of the wood. The aim of the study was to assess the ability of the model to simulate the response of wood beams to bending and to the climate of northern Europe. Four-point bending tests of small and clear wood specimens exposed to a constant temperature and to systematic changes in relative humidity (RH) were conducted to calibrate the numerical model. A validation of the model was then performed on the basis of a four-point bending test of solid timber beams subjected to natural climatic conditions but sheltered from the direct effects of rain, wind and sunlight. The three-dimensional character of the model enabled a full analysis of the effects of changes in moisture content and in fibre orientation on stress developments in the wood to be carried out. The results obtained showed there to be a clear distinction between the effects of moisture on the stress developments caused by mechanical loads and the stress developments caused solely by changes in climate. The changes in moisture that occurred were found to have the strongest effect on the stress state that developed in areas in which the tangential direction of the material was aligned with the exchange surface of the beams. Such areas were found to be exposed to high-tension stress during drying and to stress reversal brought about by the uneven drying and shrinkage differences that developed between the outer surface and the inner sections of the beams.

1 Introduction

The renewable character and the low carbon footprint of wood as compared with concrete (Dodoo 2011), for example, has made wood increasingly popular for use in structural applications (Malo et al. 2016). Due to the natural process of sorption that takes place, wood interacts very readily with the surrounding climate, making an equilibrium moisture content (EMC) more readily reached, even when the direct effects of rain, solar radiation or wind are lacking (Gustafsson et al. 1998). When wood is subjected to a combination of a change in moisture content (MC) and a state of stress brought on by external load (*e.g.* mechanical load) or internal constraint (*e.g.* through differential shrinkage or swelling), a continuous change in the level of stress and the occurrence of deformations can be the result. In bending, an unfavourable state of stress can lead to an exponential increase in deflection and, in consequence of this, to failure (Armstrong et al. 1962; Bodig et al. 1982) or to fracture in the longitudinal-radial plane (TL- and TR-oriented cracking)

---

[1] Department of Building Technology, Linnaeus University, Växjö, Sweden

✉ Sara Florisson, sara.florisson@lnu.se, ORCID 0000-0001-7322-7052

[2] Department of Engineering and Chemical Science, Karlstad University, Karlstad, Sweden

that can weaken the shearing capacity of beams (Larsen 2013; McMillen 1958). The techniques available for monitoring changes in MC and hygro-mechanical viscoelastic behaviour in-situ can only be employed in specific locations in or around the wood (Fortino et al. 2019a; Fortino et al. 2019b). With recent developments in three-dimensional modelling, predictions can be made both of moisture flow and of moisture-induced stress and distortion in three-dimensional space.

Many studies regarding the impact of moisture gradients on beam bending in which simulations have been involved have been carried out. These have concerned both controlled changes in climate (Honfi et al. 2014; Ranta-Maunus 2001) and changes in climate that occur naturally (Fortino et al. 2019b; Franke et al. 2019; Müller et al. 2007; Toratti 1992). A variety of constitutive models have been used in such studies, these involving one-, two- or three-dimensional space considerations. Yet the fibre orientations that can be present in three-dimensional space (such as annual ring patterns, conical shapes or spiral grain formations) have thus far never been fully incorporated into such studies, despite the strong effects these can have on the stress distribution and thus on the deformations that the wood can be subjected to (Angst-Nicollier 2012; Ormarsson et al. 1999). Spiral graining is a phenomenon in which the wood fibres spiral around the pith that lies at the centre of the log. The magnitude of the spiral graining at each point in the material can be expressed as an angle θ in the lt-plane (Ormarsson et al. 1998). Between the pith and the bark, θ can vary between a value of $+8$ and $-5°$ over a distance of some 200 mm (Dahlblom et al. 1999; Säll 2002). Spiral graining can strongly affect both the deflection to which the beams are subjected and the stress fields involved (Ormarsson 1999; Schniewind et al. 1972). Together with changes in moisture content, this can lead to complex stress states that can change continuously.
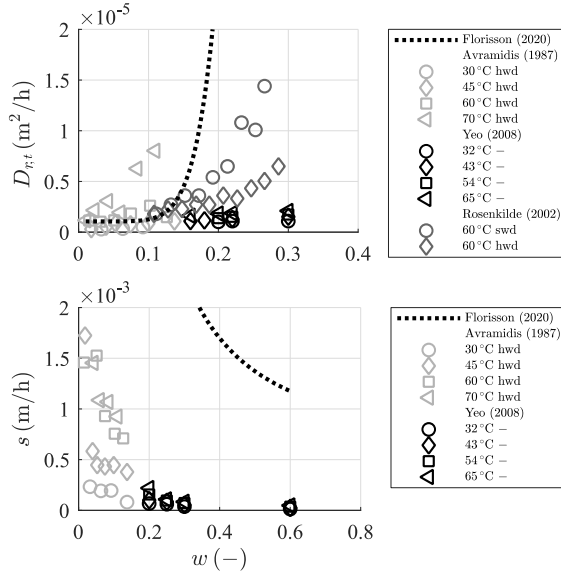
Fig. 1: Moisture- w and temperature- T dependent radial and tangential diffusion coefficient $D_{r,t}$, as well as surface emission coefficient s, as reported on in different literature sources, hwd referring to heartwood and swd to sapwood.

It was shown recently that use of a nonlinear single-Fickian model in connection with nonlinear Neumann boundary conditions is able to describe not only slow MC-changes (Konopka et al. 2018), but also quick MC-changes (Florisson et al. 2020). One challenge that brings this model about, is that there is not enough experimental data available to cover the moisture and temperature dependent diffusion coefficient (Avramidis et al. 1987; Rosenkilde 2002) and surface emission coefficient (Yeo et al. 2008; Yeo et al. 2005; Yeo et al. 2002). Most of the additional data available in this area concerns only a specific temperature or moisture content, though often in a wide variety of wood species, only certain material directions, or only simply sapwood and heartwood generally. An overview of various sets of data dealt with in the literature concerning the moisture dependency of the coefficients obtained is presented in **Fig. 1**.

For a moisture-sensitive and visco-elastic material such as wood, it is common to describe the total strain rate as a summation of the elastic, hygro-expansive creep and mechano-sorptive strain rates (Ormarsson et al. 1998). The elastic component is defined according to Hook's law and the hygro-expansion as the relationship between the hygro-expansion coefficient and the rate of change in moisture content. The most conventional way of describing mechano-sorption is with use of a model presented by Salin (1992). This is a model describing both the decreasing deflection rate phase and the constant deflection rate phase, two phases of mechano-sorption deflection that usually take place under moderate levels of stress, or low-level bending as it has also been called (Florisson et al. 2021). The most commonly used model for describing creep is the hereditary model (Dahlblom 1987). Similar to the mechano-sorption model, this approach is used to describe not only the decreasing deflection rate and the constant deflection rate, but also the unloading response of the material.

One difficulty in connection with three-dimensional modelling of moisture-induced distortion is the vast amount of experimental data needed to describe the material parameters that are involved. For Norway spruce, sufficient experimental data is available to cover both the moisture- and the temperature-dependent elastic and hygro-expansive behaviour that can occur; see **Table 1**. However, for mechano-sorption the data is limited to tension and compression in the principle material directions l, r and t (Aicher et al. 1998; Hunt 1984; Kangas et al. 1989; Ranta-Maunus 1993; Toratti et al. 2000). To the author's knowledge, not much has been reported on shear, although the work in this area of Hearmon et al. (1964) can be cited. A small dataset concerned with mechano-sorption in the rt-plane was studied by Kangas and Ranta-Maunus (1989). Experimental data on creep is available, both in the principal material directions and in the lr- and lt-planes, yet it is scattered in the sense of only certain wood species being involved (Hayashi et al. 1993; Ozyhar et al. 2013; Schniewind and Barrett 1972; Svensson 1995; Svensson 1996), and often only short-term test periods ($< 1\,\text{day}$) being dealt with, so that there is a lack of predictors of long-term behaviour ($> 50\,\text{days}$) when use is made of exponential expressions to describe creep deflection (Florisson et al. 2021).

A three-dimensional numerical model was created in the FE-software Abaqus FEA® to simulate both the transient nonlinear moisture flow and the moisture-dependent distortion and stress that normally takes place in wood, account being taken of the fibre orientation. To determine whether the model was able to simulate in an adequate way the beam bending that occurs under northern European climatic conditions, the following steps were taken: 1) on the basis of experimental data available in the literature, a set of expressions was created to determine the moisture- and temperature-dependent diffusion

3

coefficient and surface emission coefficient that appeared to be appropriate, 2) experimental results obtained for small beams tested under constant temperature and systematic RH-cycle (controlled climatic) conditions were used to calibrate an appropriate numerical model, account being taken of the spiral grain that applied and the annual ring curvature, and 3) test results for solid beams tested under natural climatic conditions were used to validate the numerical model, account being taken of the fibre orientation. Here, calibration involved the iterative process of changing material parameters until the simulation obtained agreed closely with the experimental data. This process indicated the order of range of the hygro-mechanical and the visco-elastic material parameters. Validation involved the assessment of whether the numerical model accurately described reality.

2 Material and methods

2.1 Theory

2.1.1 Moisture flow model

The constitutive relationship used to describe the nonlinear transient moisture flow in wood was defined as

$$\bar{q} = -\bar{D}(w, T)\bar{\nabla}w \qquad (1)$$

where q is the moisture flux vector, D is a moisture- and temperature-dependent diffusion matrix, w is the unit-less moisture content, T is the temperature and ∇ defines gradients. The over-line ($\bar{\bullet}$) in Eq. (1) refers to the orthogonal local coordinate system for the wood. The Neumann boundary condition that describes the flux that is normal for the exchange surface q_n is defined as

$$q_n = s(w, T)(w - w_\infty) \qquad (2)$$

where s is a moisture- and temperature-dependent surface emission coefficient and w_∞ is the unit-less moisture content of the ambient air. Further information concerning derivation of the FE-formulation and how to iteratively solve the nonlinear system of equations here can be found in Florisson et al. (2020) and Johannesson (2019).

2.1.2 Stress model

The moisture-related total strain rate (column matrix) $\dot{\bar{\varepsilon}}$ is described by the constitutive equation presented in Eq. (3) as a summation of the elastic strain rate $\dot{\bar{\varepsilon}}_e$, the strain associated with hygro-expansion $\dot{\bar{\varepsilon}}_h$, the mechano-sorption strain rate $\dot{\bar{\varepsilon}}_{ms}$, and the creep strain rate $\dot{\bar{\varepsilon}}_c$. The notation ($\bullet$) refers to the time derivative $\partial/\partial t$ of the strains. The different matrix expressions used to calculate each strain rate in the constitutive model (see Eq. (3)) are presented in Eq. (4) to (7)

Table 1: An inventory of literature on the elastic, hygro-mechanical, creep and mechano-sorption properties of Norway spruce, the moisture- and temperature-dependency these possess, and the constitutive models used in the present paper to explain such properties.

Properties	Model	Literature	Notes	Limitations		
				T/w	$l/r/t$	$tr/lt/rt$
Elastic	Hook's law	Keunecke et al. (2007)	Experimentally obtained	w	$l/r/t$	$tr/lt/rt$
Hygro-expansion	Moisture induced strain	Ormarsson et al. (1998)	Expressions not all experimentally verified	T/w	$l/r/t$	$tr/lt/rt$
		Florisson et al. (2021)	Experimentally obtained, with values for each RH-cycle	–	t	–
		Bengtsson (2001)	Experimentally obtained, including variation between pith and bark	–	$l/r/t$	–
Creep	Hereditary model (Dahlblom 1987)	Ormarsson (1999)	Only t experimentally verified and covers a time period of only 70h	–	$l/r/t$	$tr/lt/rt$
Mechano-sorption	Mechano-sorption limit model (Salin 1992)	Ormarsson et al. (1998)	Expressions not all experimentally verified	T	$l/r/t$	$tr/lt/rt$
		Svensson et al. (1997)	Experimentally verified	–	t	–

$$\dot{\boldsymbol{\varepsilon}} = \dot{\boldsymbol{\varepsilon}}_e + \dot{\boldsymbol{\varepsilon}}_h + \dot{\boldsymbol{\varepsilon}}_{ms} + \dot{\boldsymbol{\varepsilon}}_c \qquad (3)$$

$$\dot{\boldsymbol{\varepsilon}}_e = \dot{\boldsymbol{\varepsilon}}_{e,1} + \dot{\boldsymbol{\varepsilon}}_{e,2} = \overline{\boldsymbol{C}}(w,T)\dot{\boldsymbol{\sigma}} + \dot{\overline{\boldsymbol{C}}}(w,T)\overline{\boldsymbol{\sigma}} \qquad (4)$$

$$\dot{\boldsymbol{\varepsilon}}_h = \boldsymbol{\alpha}\dot{w}_a \qquad (5)$$

$$\dot{\boldsymbol{\varepsilon}}_{ms} = \overline{\boldsymbol{m}}(T)(\overline{\boldsymbol{\sigma}} - \overline{\boldsymbol{n}}\overline{\boldsymbol{\varepsilon}}_{ms})|\dot{w}_a| \qquad (6)$$

$$\dot{\boldsymbol{\varepsilon}}_c = \sum_{k=1}^{K} \frac{1}{\tau_k} e^{-\frac{t}{\tau_k}} \int_0^t e^{\frac{t'}{\tau_k}} \overline{\boldsymbol{C}}_{c_k}(w,T) \frac{\mathrm{d}\overline{\boldsymbol{\sigma}}(t')}{\mathrm{d}t'} \mathrm{d}t' \qquad (7)$$

where $\boldsymbol{C}$ is the compliance matrix, $\boldsymbol{\sigma}$ is the stress vector, $\boldsymbol{\alpha}$ is a vector that contains the hygro-expansion coefficients, $\dot{w}_a$ is the moisture content rate below FSP, $\boldsymbol{m}$ is the mechano-sorption property matrix, $\boldsymbol{n}$ is the retardation matrix, τ_k is a value that indicates in which time range the different creep terms have an effect on the change of sum, t' is the time corresponding to a recent stress change $\Delta\boldsymbol{\sigma}$, and $\boldsymbol{C}_{c_k}$ is the creep compliance matrix. The creep compliance matrix consists of $\boldsymbol{C}$ scaled with use of the creep parameter $\phi_{\sigma_l}^k$ $(-)$. The notation $|\bullet|$ indicates an absolute value. The time integral that is part of Eq. (7) is evaluated from time t to time Δt $(t + \Delta t)$, since the value of the integral is known at time t due to its storage in a so-called state variable (Dassault Systèmes 2017). More about the process of deriving the FE-formulation and of how to iteratively solve this set of equations can found, for example, in Ormarsson (1999) and Ottosen et al. (2005).

2.2 Numerical model

The three-dimensional numerical model employed used a sequential solution scheme, in terms of which first the transient nonlinear moisture flow problem was solved and it was used then as input (in terms of moisture content nodal values) to a moisture-induced distortion analysis; see **Fig. 2**. Both analyses used the same geometry and fibre orientation. The moisture flow model was supported by the material routine UMATHT and the boundary condition routine FILM (Florisson et al. 2020). The constitutive theory used for the distortion model was implemented in the user-subroutine UMAT. This routine was used very recently in Florisson et al. (2019) to simulate the drying behaviour of timber boards, and is extended here by the mechano-sorption model of Salin (1992) and the hereditary creep model of Dahlblom (1987). The orthotropic material orientation was determined by the user-subroutine ORIENT (Ormarsson et al. 1998), which describes the local coordinate system (l, r, t) in relation to the global coordinate system (x, y, z) being employed. In the present study, the numerical model was used in two different applications: 1) calibration of four-point bending behaviour under controlled climate conditions, and 2) validation of four-point bending behaviour under natural climate conditions. Both applications use experimental data from self-performed tests.
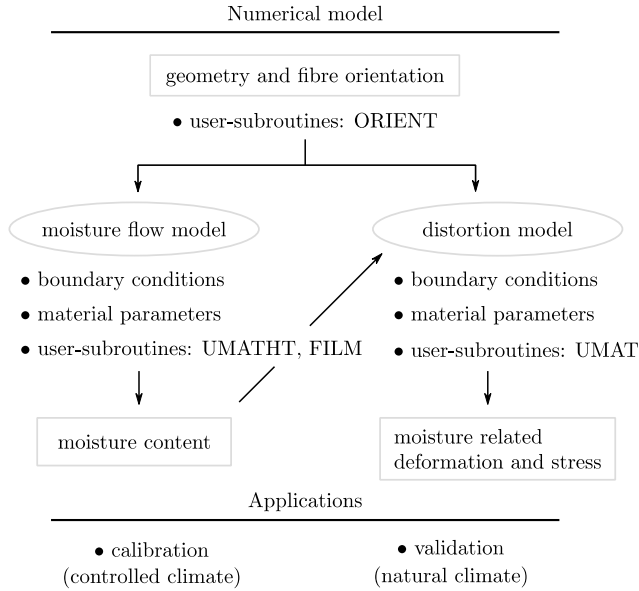
Fig. 2: The principal components of the numerical model developed in FE-software Abaqus FAE® and the applications for which it is used.

2.3 Experimental program

2.3.1 Application 1

Three beams (beams A1-SS/NN/EE) were tested in terms of four-point bending inside a climate chamber of type Vötsch VCR 4033/S (Vötsch Industrietchnik GmbH, Balingen, Germany). The beams were 30 mm in height, 15 mm in width, and 640 mm in length when testing began; see **Fig. 3**. A 5 mm thick steel plate was placed beneath the loads and above the supports, its having in each case an area of 16 by 55 mm, which resulted in beam spans there of 595 mm. A detailed account of the experimental methodology, the setup and the results obtained can be found in Florisson et al. (2021). The experiment provided data on mass change and hygro-expansion over the height of the beam, information regarding both being obtained from an unloaded specimen. In addition, deflection from the constant moment area $u_{y,1}$ was collected; see location LVDT in **Fig. 3**.
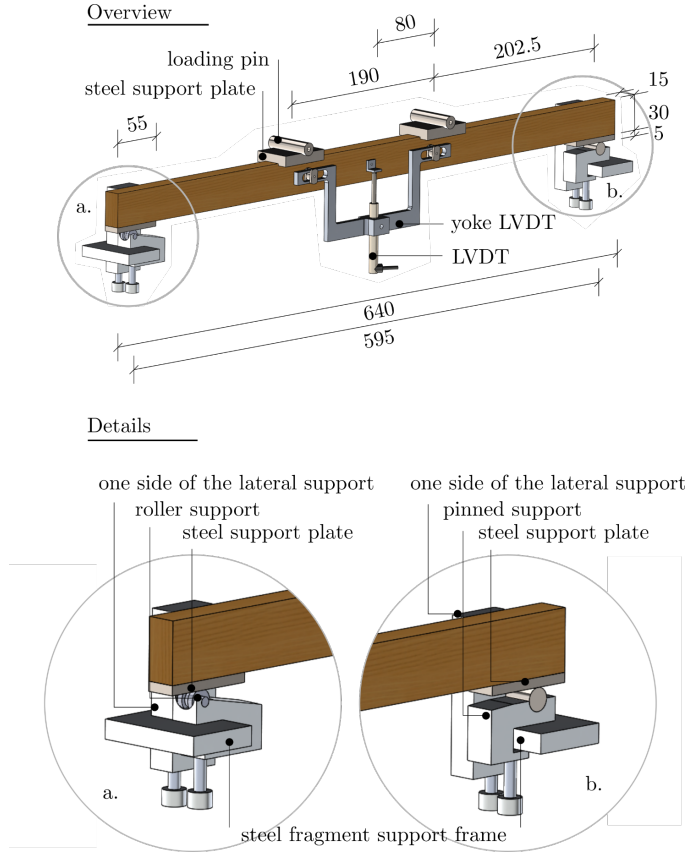
Fig. 3: Details concerning the four-point bending test setup for beam A1, testing of which was carried out under controlled climate conditions: (a.) a close-up of the custom-made roller support, and (b.) a close-up of the custom-made pinned support.

To show the effect of θ on calibration in the three long-term bending tests, two simulations were carried out for each specimen and for each of the deflection component (simulations of elastic creep and of mechano-sorption). To obtain the initial values, the first simulation was carried out with θ equal to 0°. There, the only contributing material parameters were those related to the l-direction. The second simulation was carried out using a positive θ of 4°. There, the material parameters belonging to the l- and to the t-direction and to the lt-plane affected the fit, and required an adjustment once again to meet $u_{y,1}$. The procedure is explained in greater detail in the section on numerical simulations.

2.3.2 Application 2

Three solid timber beams (each of them an A2 beam) were tested in terms of four-point bending and were subjected to natural climate conditions inside a research facility located in the Asa Research Park in Southern Sweden. The facility was not isolated, but it protected the test material against the direct effects of rain, wind and sunlight. The beams

8

were 195 mm in height, 45 mm in width, and 3100 mm in length, with a $\pm 12\%$ moisture content; see **Fig. 4**. The steel contact surface between the load points and the beam, or between the supports and the beam, had an area 45 mm by 100 mm in size. The beam spanned 3000 mm, which was divided up by the location of the load into 3 equal segments, each 1000 mm in length.

In a room adjacent to the setup, the temperature, T and the humidity, RH, ϕ were monitored by use of a pin-type SHT75 temperature ($\pm 0.3 C°$) and humidity ($\pm 1.8\%$ RH) sensor (Sensirion, Stäfa, Switzerland). The deflection $u_{y,2}$ of the wood beams was measured by an S18FLPA100 potentiometer (Sakae, Kawasaki, Japan) that had a measuring range of 100 mm (± 0.3 mm) at mid-span 20 mm from the lower surface and a measuring range of 100 mm (± 0.3 mm). The SAAB group (SAAB AB, Stockholm, Sweden) in Växjö developed the data collection system. T, ϕ and $u_{y,2}$ were logged every 10 min.
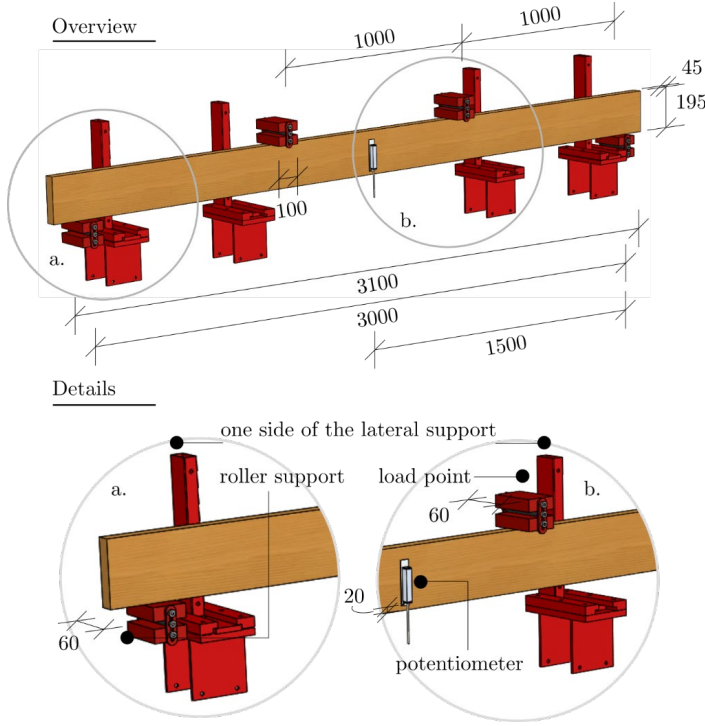
Fig. 4: Details of the test setup for the four-point bending test, performed under natural climate conditions, in the case of beam A2, where (a.) is a close-up of the roller support used for both the supports and for the loading points, and (b.) is a close-up of the potentiometer, located on the bearing frame (not shown).

The T and ϕ values that were recorded were used as input to the numerical model, whereas the average $u_{y,2}$ value of the three beams that were tested was used to carry out validation of beam A2. The effect of beam size on moisture transport and mechano-sorption was analysed by performing the simulation under natural climate conditions, also on the smaller geometry of beam A1, referred to here as beam A3. Beam A3 was assigned the same material parameters, the same expression for determining θ (the beam being

9

located 130 mm from the pith), and the same bending stress and climate as beam A2. The deflection $u_{y,2}$ was analysed at mid-span at a level 3 mm above the lower exchange surface, at a position corresponding to the location at which the data for beam A2 was analysed.

3 Numerical simulations

The numerical model was used in two different applications that differed in terms of geometry, fibre orientation, element mesh, boundary conditions and load configurations. These different aspects of the situation involved will be discussed here, together with an assessment of the instantaneous elastic stress state. For both applications, element type DC3D8 was used to create the mesh for the moisture flow analysis, and element type C3D8 was used for the distortion analysis.

3.1 Application 1

Application 1 concerned calibration of the numerical model on the basis of the experimentally obtained bending behaviour of three beams (A1-SS/NN/EE) that were tested under controlled climate conditions. The geometry of the model, as well as the element mesh, the boundary conditions and the load configuration, are shown in **Fig. 5**. The input parameters for the moisture flow analysis and its calibration are to be found in Florisson et al. (2020). The centre of the beams was located 137.5 mm from the pith, this resulting in a slight curvature of the annual rings in cross-section. The beams also had a positive spiral grain angle of 4°. In performing the calibration, the differences in the deflection data between nodes p_1 and p_2 $(p_1 - p_2)$ were determined and were compared with the experimentally obtained $u_{y,1}$ values; see **Fig. 5**. Here, p_1 and p_2 indicate the position of the head of the LVDT and of the right-hand side of the yoke, respectively, as can be seen in **Fig. 3**. The numerical analysis was carried out over a period of 90 days.
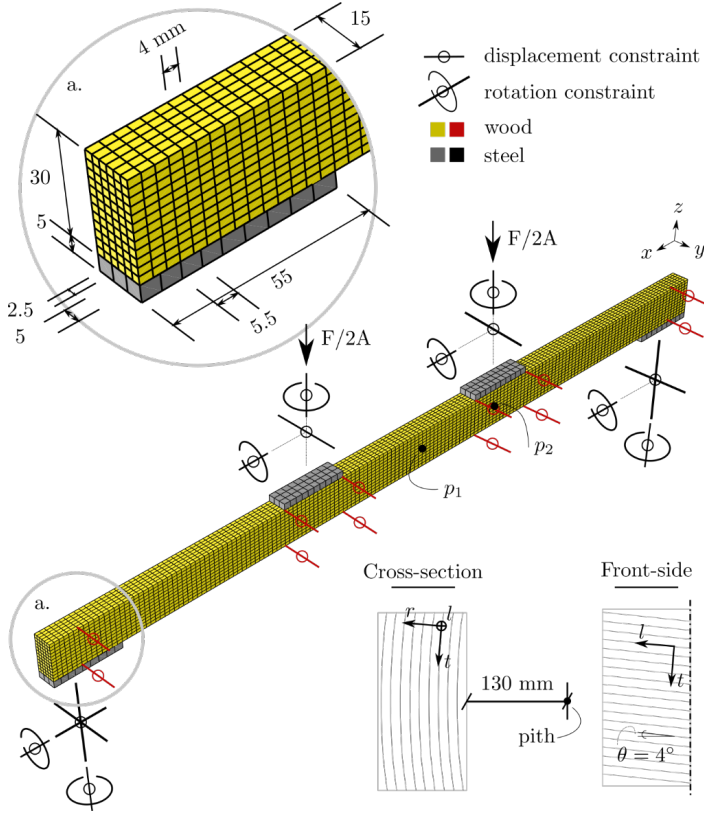
Fig. 5: The geometry, mesh, boundary conditions and material orientation used in the simulation of beam A1, *F* indicating load and *A* the area of the steel plate.

The simulation began after a 5-day period (when the value of t was 0) of constant climate conditions (60°C and 40% RH), after which conditions of pure elastic and creep deflection were established (and maintained for a period of 5 days) (**Fig. 6b & c**), this being followed by 85 days of testing at a constant T of 60°C and with systematic ϕ-phases of between 40 and 80% for generating deflection caused by mechano-sorption. The experimentally obtained EMC at the end of each ϕ-cycle was used to define w_∞ in the subroutine FILM, which is compared in **Fig. 6d** with values determined by use of Simpson's formula (Simpson 1971). This latter expression concerns the relationship between EMC and ϕ as well as T, without hysteresis being taken into account.
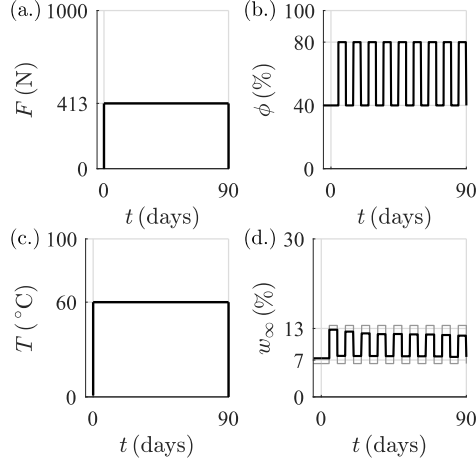
Fig. 6: Schedules used for (a.) load F, (b.) relative humidity ϕ, (c.) temperature T and (d.) the moisture content of the ambient air w_∞, in which (d.), the experimentally obtained w_∞ (black), is used as a boundary condition in the moisture analysis and as compared with values obtained with use of Simpson's formula (grey).

The total load F of 413 N was applied instantaneously and remained constant during the entire analysis; see **Fig. 6a**. Simple hand calculations based on elastic beam theory indicated that a maximum normal stress σ_x of 18.6 MPa could be expected for the outer fibres at mid-span, and that a maximum shear stress τ_{xz} of 0.69 MPa and a stress perpendicular to the beam direction σ_z beneath the loads and supports of 0.25 MPa could be expected. In **Fig. 7**, these values are compared with results of an elastic analysis performed in the global coordinate system. There, rigid shells were used to represent the steel plates above the supports and below the loads. The interaction between the steel plates and the wood was defined as involving a combination of normal (hard) friction and tangential friction (isotropic static friction with a friction coefficient of 0.3 ($-$)) behaviour.

Fig. 7 indicates there to be differences between the stress values obtained by hand calculations and those obtained by simulation. The load $F/2A$ applied to the top of the steel plates, where A is the contact area between the load and the steel, was found to result in a compression stress σ_z beneath the plates. This stress was found to vary between its being quite significant beneath the loading points and being zero on the bottom surface of the beam, this resulting in an asymmetric distribution of σ_x over the height of the beam. A similar stress situation was found to exist above the supports, due to the asymmetrical dividing up of the steel plate by the location of the line supports, the stress being concentrated at the ends of the beam. Simulation of the long-term behaviour was carried out without reference to the steel plates. The boundary conditions, in contrast, were directly associated with the wood surface.
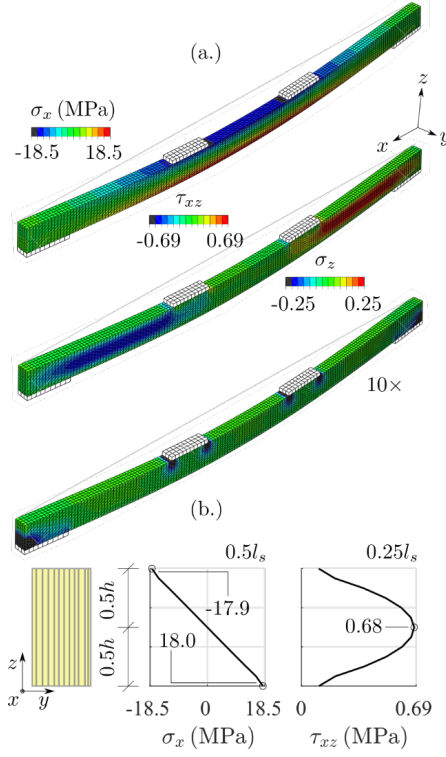
Fig. 7: (a.) Stress variation of σ_x, σ_z, and τ_{xz} directly after the loading of beam A1-SS, and (b.) variation in σ_x and τ_{xz} over the height of the beam h at a quarter and half of the span in bending l_s. Note that the magnification of deflection in the z-direction is $10 \times$.

3.1.1 Material parameters

The moisture flow analysis was performed with use of the w-and T-dependent $\boldsymbol{D}$ and $\boldsymbol{s}$ taken up in Florisson et al. (2020). Plots of D_r, D_t and s are shown in **Fig. 1**. The dependency of the elastic moduli E and the shear moduli G on T and w, and of the mechano-sorption moduli m on T were described using expressions presented by Ormarsson et al. (1998). The reference values needed for these expressions are indicated by $(\bullet)_0$; see **Table 2**. The reference values designated by $(\times)$ in **Table 2** were calibrated by use of the experimentally obtained $u_{y,1}$ value.

Table 2: The hygro-mechanical (reference) material parameters used in the stress analysis, and the parameters to be determined by calibration (×). Note that the size of the parameters is partly a function of the climate conditions for which they are calibrated.

	Elastic (MPa/−)					Hygro-expansion (−)		Creep (−)				Mechano-sorption (MPa⁻¹/MPa)			
E_l	×	E_{l0}	×	v_{lr}	0.35	α_l	0.0035	$\phi_{\sigma_l}^1$	×	$\phi_{\sigma_l}^2$	×	m_l	×	m_{l0}	×
E_r	1168	E_{r0}	1000	v_{tr}	0.6	α_r	0.17	$\phi_{\sigma_r}^1$	0.106*	$\phi_{\sigma_r}^2$	0.162*	m_r	0.28	m_{r0}	0.2
E_t	378	E_{t0}	500	v_{rt}	0.55	α_t	0.35–0.39	$\phi_{\sigma_t}^1$	0.07*	$\phi_{\sigma_t}^2$	0.09*	m_t	0.011*	m_{t0}	0.008*
G_{lr}	417	G_{lr0}	460									n_l	×		
G_{tt}	401	G_{tt0}	425									n_r	69		
G_{rt}	28	G_{rt0}	47									n_t	500*		

* Not verified on the basis of the experimental data
** $\tau_1 = 5$, $\tau_2 = 60$ (h)
*** The elastic and the creep parameters correspond to 60°C, a 7.35% moisture content and an FSP of 27%.
**** The mechano-sorption parameters correspond to those at 60°C.

The expressions describing the remaining elastic and shear moduli (r, t, lr, lt, rt) were calibrated using experimental data from Keunecke et al. (2007). The hygro-expansion coefficients are from Bengtsson (2001), except for α_t, which is from Florisson et al. (2021). Both E_l and the hygro-expansion coefficient α_l are assumed to be constant in the radial direction. In view of the lack of creep deflection data reported on in the literature, it was assumed that the creep parameters that pertained to the t-direction and the lt-plane were consistent with the relationship obtained by use of Eq. (7) and data reported by Schniewind and Barrett (1972). The mechano-sorption parameters stem from Ormarsson (1999), with the exception of the n_{lt} parameter, which was made consistent with the relationships of the other parameters.

3.2 Application 2

The second application concerned validation of the numerical model used to simulate the bending behaviour of beam A2 under natural climate conditions. The geometry of the model, the element mesh, the boundary conditions and the load configuration are shown in **Fig. 8**. At both ends of beam A2, the pith of the tree was located in about the centre of the beam's height h on the right exchange surface; see **Fig. 8**. The conical shape of the tree was taken to be $-0.5°$ and the spiral grain angle to be $\theta = 4 - 40r$, r being the radial distance (in m) between the pith and the material point (Ormarsson 1999). The numerical analysis concerned a period of 556 days altogether.
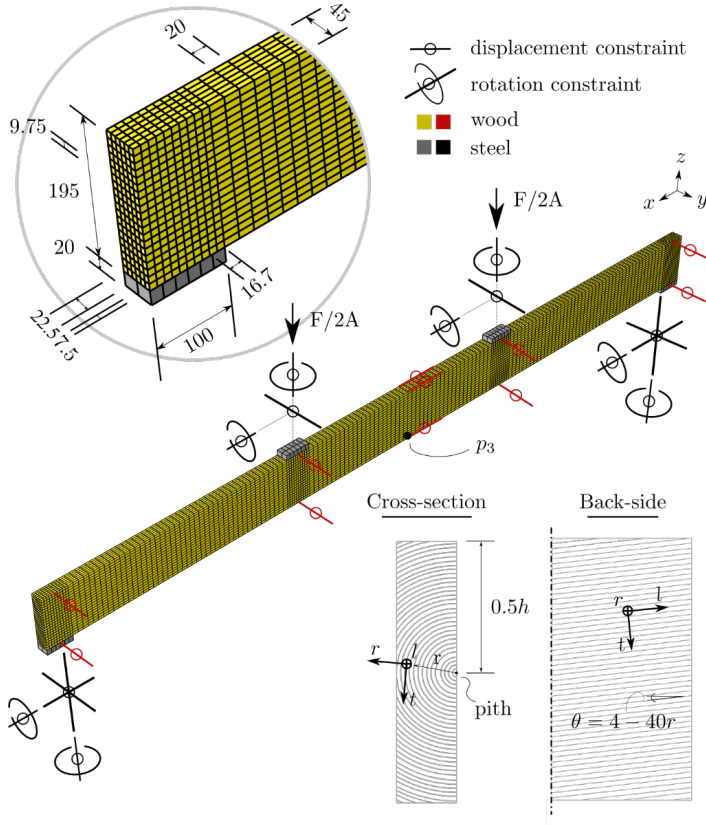
Fig. 8: The geometry, mesh, boundary conditions and material orientation used in the simulation of beam A2, F indicating load, A being the area of the steel plate, h the height of the beam and r the distance between pith and analyzed material point.

Fig. 9 presents the load and the climate schedules used in simulating beam A2. **Fig. 9b** and **c** present the experimentally obtained raw ϕ and T data, together with a 2-week average used as input to the numerical model. Subroutine FILM uses Simpson's formula to determine w_∞ (**Fig. 9d**) by use of the averaged ϕ and T values.
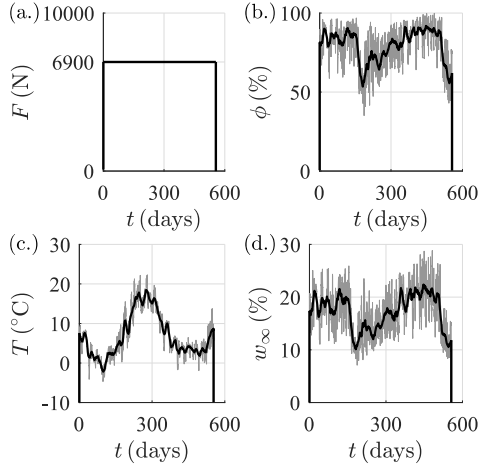
Fig. 9: Schedules used for (a.) the load F, (b.) the relative humidity ϕ, (c.) the temperature T, and (d.) the moisture content of the ambient air w_∞, where for ϕ, T and w_∞ both the raw data (grey) and the averaged data (black) are plotted over a 2-week time period.

The beam carried a total mechanical load F of 6900 N (see **Fig. 9a)**, which resulted in a bending stress of 12 MPa in the outer fibres, a nominal stress of 0.77 MPa perpendicular to the steel plates beneath the loading points and the supports, and a shear stress of 0.59 MPa. In **Fig. 10**, these results can be compared with the results of an elastic analysis carried out directly after the loading. Similar arguments apply in explaining the differences that can be seen in the stress values obtained for beam A1 (see **Fig. 7**). Similar simplifications were also made regarding the boundary conditions in the long-term analysis that was carried out.
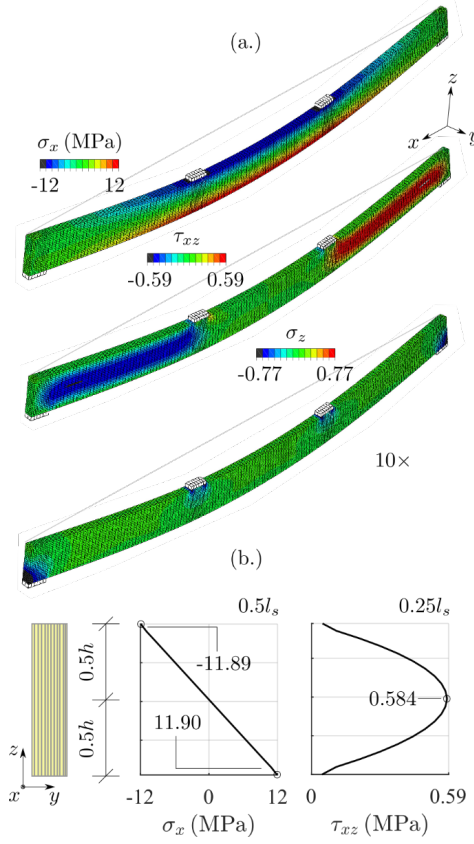
Fig. 10: (a.) Stress variations of σ_x, σ_z, and τ_{xz} directly after loading in the case of beam A2 and (b.) variations in σ_x and τ_{xz} over the height of the beam h at a quarter and half of the span in bending l_s. Note that the magnification of the deflection in the z-direction is 10 ×.

3.2.1 Material parameters

To describe the moisture flow under natural circumstances, exponential expressions were created for D and s with regard to w and T with the help of experimental data found in the literature; see **Fig. 11**. The experimental data used to determine D was from Avramidis and Siau (1987) (in the r- and t-directions), from Rosenkilde (2002) (in the l-direction), and for s from Yeo et al. (2008). The expressions are to be found in Eq. (8) to (10), where D_l is constant with regard to w, and – due to a lack of data – is assigned the same temperature dependency as $D_{r,t}$.
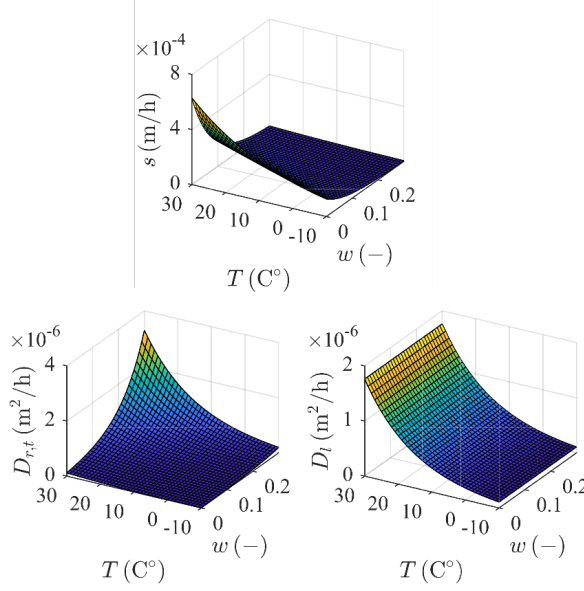
Fig. 11: The moisture- (w) and temperature- (T) dependent diffusion coefficient D as it relates to the l, t and r material directions, and the surface emission coefficient as presented in Eq. (8) to (10).

The hygro-mechanical parameters used in the distortion analysis of beam A2 are presented in **Table 3**. Here too, similar to what was found for beam A1, the expressions of Ormarsson (1999) are adopted to describe the w and T dependency of E and G, and the T dependency of m. The reference value E_{l0} and the values for m_{l0} and n_l were determined on the basis of $u_{y,2}$.

$$D_l(T) = 2.7 \times 10^{-8} \cdot (8e^{0.07T}) \qquad (8)$$

$$D_{r,t}(w,T) = (1.7 \times 10^{-9}e^{11w} + 9.3 \times 10^{-13}) \cdot (8e^{0.07T}) \qquad (9)$$

$$s(w,T) = (2.1 \times 10^{-4}e^{-13w} + 4.5 \times 10^{-6}) \cdot (0.9e^{0.04T}) \qquad (10)$$

The variation of α_l over the cross-section of the log is describes by the expression presented in **Table 3**, r being the distance between the pith and the bark (Ormarsson et al. 1998). The values for α_r and α_t are from Bengtsson (2001). All the other parameters were those adopted for beam A1. The creep parameters related to the r-direction, and the lr- and rt-plane are assumed to involve the same relationships as those applying to ϕ_{σ_l}, ϕ_{σ_t} and $\phi_{\sigma_{lt}}$. The mechano-sorption moduli and the retardation parameters for the same material direction and planes are from Ormarsson (1999).

19

Table 3: The hygro-mechanical (reference) material parameters employed in connection with the stress analysis. Note that the size of the parameters is a function of the climate conditions present at the beginning of analysis.

| Elastic [**] (MPa/−)				Hygro-expansion (−)		Creep [*] (−)		Mechano-sorption [***] (MPa^{-1}/MPa)					
E_l	6736	E_{l0}	2860	ν_{lr}	0.35	α_l	$0.0071 - 0.038r$	ϕ_{σ_l}	0.235	m_l	0.0004	m_{l0}	0.0004	n_l	12000
E_r	1525	E_{r0}	1000	ν_{lt}	0.6	α_r	0.12	ϕ_{σ_r}	0.25	m_r	0.15	m_{r0}	0.15	n_r	52
E_t	605	E_{t0}	500	ν_{rt}	0.55	α_t	0.35	ϕ_{σ_t}	0.30	m_t	0.2	m_{t0}	0.2	n_t	69
G_{lr}	610	G_{lr0}	460					ϕ_{lr}	0.15	m_{lr}	0.008	m_{r0}	0.008	n_{lr}	500
G_{lt}	575	G_{lt0}	425					$\phi_{\sigma_{lt}}$	0.15	m_{lt}	0.008	m_{lt0}	0.008	n_{lt}	500
G_{rt}	51	G_{rt0}	47					$\phi_{\sigma_{rt}}$	0.50	m_{rt}	0.8	m_{rt0}	0.8	n_{rt}	27.6

[*] $\tau = 40$ (h)

[**] The elastic parameters correspond to 20°C, a 16% moisture content and an FSP of 31%.

[***] The mechano-sorption parameters correspond to those found at 20°C.

4 Results and discussion

4.1 Application 1

4.1.1 Deflection

The experimentally obtained $u_{y,1}$ values (the grey line) presented in **Fig. 12a** show the usual characteristics observed in initially dry wood tested at low-level bending (Armstrong et al. 1961; Armstrong and Kingston 1962). The first adsorption (uptake of water molecules) and the subsequent desorption (release of adsorbed water molecules) were found to result in a substantial increase in $u_{y,1}$. When the waves observed between high and low ϕ-cycles are neglected, the expected decreasing deflection rate phase and its subsequent constant deflection rate phase were observed. The results obtained using the numerical model (the black line) show a good fit with these two phases. The model is unable, however, to predict the characterising waves.
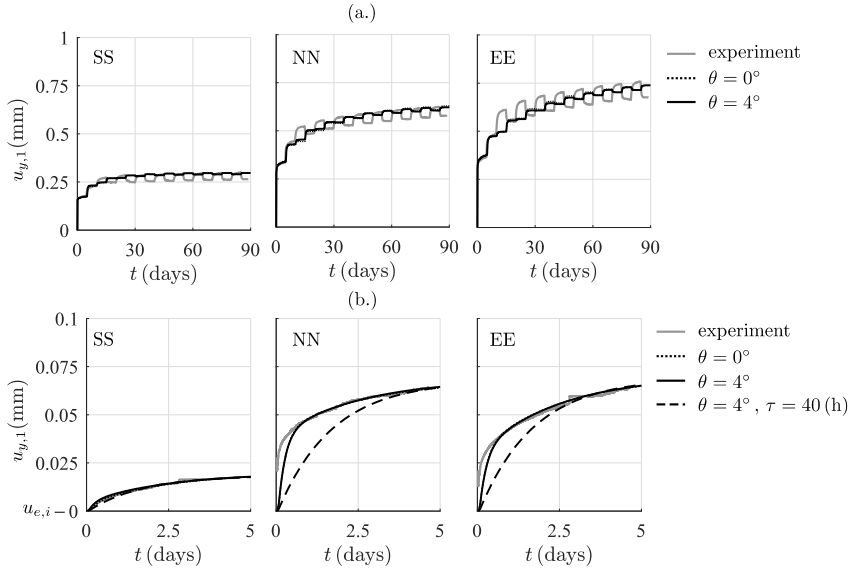
Fig. 12: The results of calibration, where (a.) is the fit with the experimentally obtained $u_{y,1}$ value during 90 days of testing and (b.) is the fit with the experimentally obtained $u_{y,1}$ value during the first 5 days of testing. Note that (b.) starts where the instantaneous elastic deflection $u_{e,i}$ ends.

Fig. 12b shows that the series of Kelvin modules used to describe u_c result in a good fit with the experimental results in the given time range of 5 days. The figure also shows the fit used to obtain the material parameters needed for the second application. Due to the numerical limitations placed on the exponent by the FE-program, the value selected for τ must be large enough for long-term analyses.

4.1.2 The effects of spiral grain on material parameters

Table 4 presents the material parameters obtained on the basis of calibrations made for beams A1-SS, NN and EE. The rotation of the longitudinal-tangential plane caused by the spiral grain results in an increase in the longitudinal elastic modulus E_l as compared with the values obtained for the simulations that include θ as 0°. The values obtained for E_l when θ is 4° show relative differences (RD) of 16.2, 19.7 and 41.4% (EE, NN and SS) as compared with E_l when θ is 0°. Since the other elastic and shear moduli do not change during the calibration, there is a lesser difference for stiffer specimens.

Since creep is described in terms of creep compliance $\boldsymbol{C}_{c_k}$, calibration of the curve when θ is 4° is considered to be made with E_l rather than with $E_{l,\theta=0}$. The approach adopted results, except in the case of beam A1-SS, in a slight increase in ϕ_{σ_l}, due to there being a spiral grain in all of the beams. In the case of mechano-sorption, a spiral grain leads to a decrease in m_l and an increase in n_l. The values obtained for m_l when θ is 4° show RD values of 30.4, 20.0 and 44.4% (EE, NN and SS) with respect to m_l when θ is 0°. When n_l is considered in combination with an θ of 4°, relative differences of 8.3, 22.2 and 51.4% (EE, NN and SS) were found with respect to n_l when θ is 0°.

4.1.3 Stress distribution

Under appropriate circumstances, a beam subjected both to bending and to climate change is prone to drying and to mechanically driven cracks. During the period of 90 days that was involved, no cracks were found to have occurred. The colour plots in **Fig. 13** show the stress distributions of σ_l and τ_{lt} for beam A1-SS directly after loading, as well as the effects of θ. The graphs that apply indicate the effects of climate on the various stress types. A spiral grain does not appear to have any particularly strong effect on σ_l for the mesh element adjacent to the lower surface at mid-span ($\times$). However, the change in moisture content after each change in RH-phase results in a spike in the stress, which is slightly greater when θ is equal to 4°. These spikes are the result of rapid changes in moisture content and of high moisture gradients close to the surface. With regard to the initial state, a significant increase, respectively, of 33.4% in σ_l can be observed at the first desorption when θ equals 4°. For a stress state close to the ultimate limit state, such a change may possibly lead to failure.

The shear stress distribution τ_{lt} is strongly affected by a spiral grain, which enters the so-called constant moment area when θ is 4°. The maximum positive τ_{lt} moves then from the side of the beam (see ($\times$) for $\theta = 0°$ in **Fig. 13**) to the lower surface of it at mid-span. This is caused by the translation of a much larger normal stress σ_x to τ_{lt}. This translation also results in a vast increase in the extreme stress state from a level of about 0.69 MPa to one of about 1.3 MPa, and to there being a much stronger effect of moisture on τ_{lt} (a 14.7% increase at the first desorption compared to the initial state). In Eurocode 5 (2004), the effect of moisture is incorporated into the design of timber elements as a reduction in strength through use being made of a modification coefficient, k_{mod}. Since the stress is a local effect and the peaks are affected by θ, the question remains of whether such a coefficient is able to adequately describe these effects, and of whether the climate effects should not instead be regarded as a load.

Table 4: Material (reference) parameters obtained in calibrations made in the case of simulations in which the spiral grain angle θ is and is not included, as regards beams A1-SS, NN and EE. Note that the size of parameters corresponds to the climate conditions in which they are calibrated

|	Elastic ***					Creep ***					Mechano-sorption ****							
	$E_{l,\theta=0}$ (GPa)	$E_{l0,\theta=0}$ (GPa)	E_l (GPa)	E_{l0} (GPa)	RD ** (%)	$\phi_{\sigma l,\theta=0}^k$ (–) 1*****	(–) 2	$\phi_{\sigma l}^k$ (–) 1	2	RD (%)	$m_{l,\theta=0}$ (MPa^{-1})	$m_{l0,\theta=0}$ (MPa^{-1})	m_l (MPa^{-1})	m_{l0} (MPa^{-1})	RD (%)	$n_{l,\theta=0}$ (MPa)	n_l (MPa)	RD (%)
EE	13.6	17.9	15.8	22.6	16.2	0.103	0.126	0.105	0.135	1.94/7.14	32.2*	23.0*	22.4*	16.0*	30.4	11000	12000	8.3
NN	15.2	21.4	18.2	27.6	19.7	0.148	0.103	0.158	0.110	6.76/6.80	28.0*	20.0*	22.4*	16.0*	20.0	14000	18000	22.2
SS	26.6	45.0	37.6	68.0	41.4	0.032	0.108	0.010	0.095	68.8/12.0	25.2*	18.0*	14.0*	10.0*	44.4	34000	70000	51.4

* Values that should be multiplied by · 10^{-5}

** The relative difference RD $= |(\bullet)_{l,\theta=0} - (\bullet)_l|/(\bullet)_{l,\theta=0} \cdot 100$

*** The elastic and the creep properties corresponding to 60°C, a 7.35% moisture content and an FSP of 27%

**** The mechano-sorption properties corresponding to a temperature of 60°C

***** 1 and 2 concern the two Kelvin-modules used to describe creep.
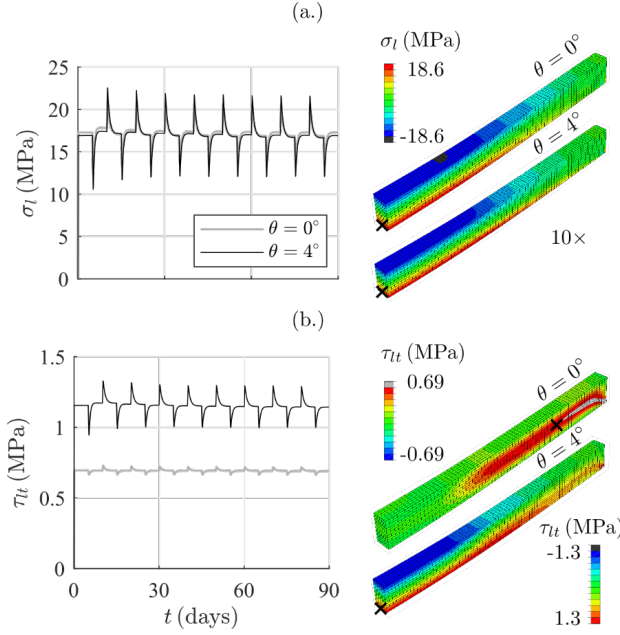
Fig. 13: Stress development (a.) σ_l and (b.) τ_{lt} for beam A1-SS when θ is 0 or 4°. Note that the graphs are taken from specific mesh elements ($\times$), that the stress field is obtained directly after loading and is projected onto half of the respected beam, and that the deflection is magnified by a factor of 10.

In addition, after each change in ϕ, a steep moisture gradient develops quickly at the exchange surface, and within a short period of time a σ_t stress field involving either compression or tension appears, depending upon whether it is swelling or shrinkage that is involved; see **Fig. 14**. As a counterreaction, the inner section of the beam develops a stress state opposite to that at the surface. Such moisture-induced stress states can result in surface or internal checks when the tensile stress exceeds the tangential strength, and under appropriate conditions cracks or so-called splits can develop. For Norway spruce, the tangential strength at 60℃ of different moisture content levels varies between 1 and 3 MPa (Gustafsson 2003; Hanhijärvi 1998; Larsen 2013). For simulations in which θ either is (0.91 MPa) or is not (1.68 MPa) accounted for, the strength is not exceeded (see **Fig. 14**). This can be confirmed by a visual inspection of specimens that are tested.
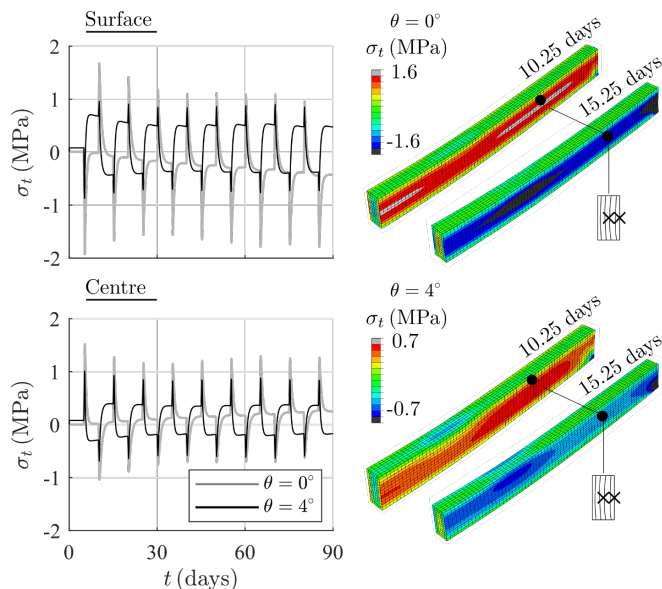
Fig. 14: The stress development σ_t for beam A1-SS when θ is 0 or 4°. Note that the graphs are taken from specific mesh elements (×), that the stress field is either obtained after 10.25 or 15.25 days and is projected onto half of the respective beam, and that the deflection is magnified by a factor of 10.

Due to the continuous change in RH, a continuous change in stress can be noted in the graphs presented in **Fig. 14** for the locations (×) that are selected, the surface and the centre alternating between a state of tension and of compression, depending upon whether the surface undergoes shrinkage or swelling. In following the stress peaks from the first to the last adsorption and desorption, the effects of hysteresis can be seen in the values for extreme stress moving closer and closer to zero. In addition, it was found, as can be seen in **Fig. 14**, that θ lowers the maximum σ_t level but does lead to a more permanent state of stress. A matter not dealt with here, but interesting to consider, is that, due to drying and the fact of there being a spiral grain, possible mixed failure modes that can lead to brittle failure become accessible. **Fig. 14** shows, for example, for a situation in which θ is 0°, a relatively high value for σ_t because of drying occurring at the same location and time as τ_{lt}, due to shear (see **Fig. 13**), and in **Fig. 13** due to a value for θ of 4°, σ_l and τ_{lt} on the upper and lower surfaces coinciding.

4.2 Application 2

4.2.1 Moisture data

The moisture content of the ambient air, w_∞, was determined on the basis of Simpson's formula and the raw T and ϕ-data recorded in Asa, showing a minimum value of 7 and a maximum value of 29%; see **Fig. 15**. The three service classes used by engineers in designing timber structures involve the following moisture content ranges: $< 12\%$, 12-20%, and $> 20\%$ (Eurocode 5 2004). Since in the wintertime ϕ exceeds 85% for a period of several weeks, the climate can be categorised as being of class 3 ($> 20\%$). However,

after a two-week averaging, the extremes change to 10 and 23%, respectively. Finally, after averaging done by the FE-software concerning the time increment, the extremes change to 11 and 20%, respectively (see the solid black line in **Fig. 15**). At this latter stage, the climate is classified as belonging to class 2 (12-20%). This averaging process eliminates spikes in w_∞, which affect mainly the moisture content of the surface of the wood and thus the drying stress.
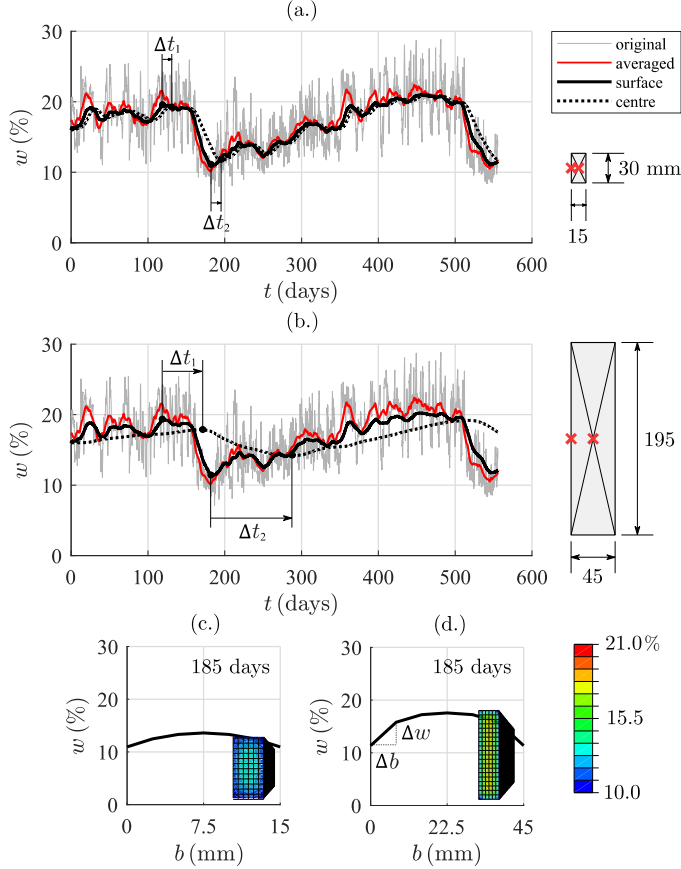

Fig. 15: Changes in moisture content w at the centre and the surface of (a.) beam A3 and (b.) beam A2, plotted together with the original and the averaged w_∞ values, determined by use of Simpson's formula and moisture content profiles over the width b of (c.) beam A3, and (d.) beam A2, after 185 days of testing.

Two different beam sizes are displayed in **Fig. 15**. As expected, beam A3 (**Fig. 15a**), which has a smaller cross-section, reacts much more quickly to changes in climate than beam A2 (see **Fig. 15b** and **c**), with its larger cross-section. To quantify this, Δt_1 and Δt_2 were introduced for analysing the shift in moisture content peaks that occurred around March (after 120 days) and in May (after 185 days); see **Fig. 15a** and **b**. For beam A3, the first shift takes place during a period of 10.6 days and results in a difference in moisture content of 0.2%. The second shift takes place during a period of 13.6 days, and

leads to a difference in moisture content of 0.77%. For beam A2, the shifts Δt_1 and Δt_2 extend over a much longer time frame than for beam A3. Periods of 51.1 and 103.2 days, respectively, are involved, and result in a difference in moisture content of 1.62 and 3.24%, respectively. Comparing beam A3 in **Fig. 15c** (blue in color in the figure) with beam A2 in **Fig. 15d** (yellow in color there), over the same period of time in both cases, shows there to be a much quicker drying process for beam A2 than for beam A3, the latter being much closer to having a 10% moisture content, and a larger moisture gradient between centre and surface.

4.2.2 Deflection

The experimentally obtained deflection curve $u_{y,2}$ (grey) was found to be smooth, with a slight decrease during the period between the months of April (about 150 days after the testing had begun) and November (about 400 days after it had begun); see **Fig. 16**. During these months, a relatively low w value and high T value could be noted (with extremes of 22.3°C and 10% MC) as compared with the winter months (extremes of 4.7°C and 23% MC). **Fig. 16** shows there to be a relatively close agreement between the simulation results and the experimental results. A discrepancy can be noted, however, between the experimental data for the first 200 days of testing and the simulation data (see $\Delta u_{y,2}$ in **Fig. 16**), which can be attributed to the choice of creep parameter, that will be discussed in the next section, In addition, the simulated deflection curve obtained showed decided fluctuations, caused by changes in moisture content.
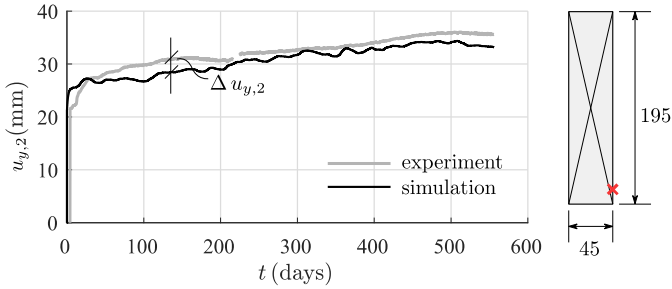

Fig. 16: Validation of the numerical model on the basis of experimentally obtained deflection $u_{y,2}$, obtained with use of the four-point bending test setup that was exposed to natural climate conditions.

4.2.3 Strain terms

The different terms that serve to define the strain component ε_l as it applies to beams A2 and A3 are to be found in **Fig. 17**. Values of the strain component for these two beams were measured in a mesh element located on the lower surface of the beams at mid-span, the strains to which beams A2 and A3 were subjected. Note that the material points related to the elements used for beam A2 and those related to the elements used for beam A3 are not located at the same distance from the surface. The total strain ε_l for both beams develops in a similar way, and in the same range order for both. The second elastic strain term, $\varepsilon_{e,2}$ (see Eq. (4)), is the most dominant one, its being followed then by the mechano-sorptive strain, ε_{ms}, which increases continuously over time. Hygro-expansion, ε_h and the first elastic strain term, $\varepsilon_{e,1}$ are the two measures most strongly affected by the climate, their values during the summer also differing markedly from those during the

winter. Regarding the creep parameters (see **Fig. 12b**), the creep strain variable ε_c moves in the direction of becoming an asymptote almost directly after loading. Since the different parameters here were obtained at a 7.35% moisture content level of the wood and are highly moisture-content dependent (Engelund et al. 2012), the creep strain is very likely to be underestimated.
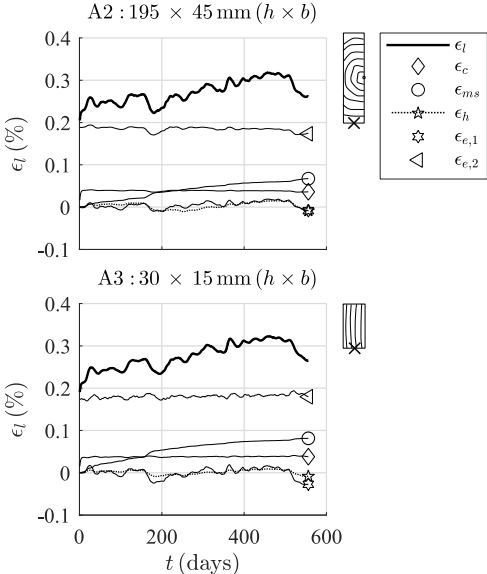
Fig. 17: Different strain-related terms that serve to define the strain component ε_l, which are taken from a specific mesh element located on the lower surface of (a.) beam A2 and (b.) beam A3 at mid-span (×). Note that h is the height of the beam, and b the width of the beam.

Comparing the strain terms for beam A2 with those for beam A3, one can note that the ε_h and ε_{ms} values are much higher for beam A3 than for beam A2. This is due to the fact that the interaction between the beam's cross-section and the surrounding climate is much greater in the A3 than in the A2 beam; see **Fig. 15** and **Table 5**, and in the case of ε_h also due to a radial variation in α_l, which results in a larger hygro-expansion coefficient for beam A2 in the location that is analyzed. For more details, see the next section 'Stress distribution'.

Table 5: The magnitude of different strain terms that make up ε_l, in the case of beam A2 and beam A3, respectively, after 556 days of testing.

	ε_l %	ε_e * %	ε_h %	ε_c %	ε_{ms} %
A2	0.257	0.176	−0.025	0.0387	0.067
c (%)	100	68.5	9.7	15.1	26.1
A3	0.225	0.152	−0.049	0.0391	0.083
c (%)	100	67.6	21.8	17.4	36.8

*$\varepsilon_e = \varepsilon_{e,1} + \varepsilon_{e,2}$

4.2.4 Stress distribution

In **Fig. 18** the effects of changes in the moisture level of the wood on the stress states σ_l and τ_{lt}, these stress states being brought about by mechanical loads, are shown for beams A2 and A3 when exposed to natural climate conditions. For beam A2, the pith was located within the cross-section of the beam ($y = 97.5$ mm, $z = 45$ mm), whereas for beam A3, it was located outside the cross-section ($y = 15$ mm, $z = 145$ mm). The graphs in the figure displaying the σ_l stress-level changes for beams A2 and A3, as obtained from a mesh element located at mid-span on the lower exchange surface, show there to be greater fluctuations for beam A3, and more seasonal variation for beam A2. The spikes that can be seen in the stress-level changes in beam A2 show a 17.1% increase to have been achieved at one point, as compared with the initial stress level. The differences that can be seen between beams A2 and A3 can be explained in terms of there being a much quicker change in moisture content in beam A3. Both beams have a hygro-expansion coefficient α_l that changes in a radial direction. At the location analysed in **Fig. 18a**, this results in a much lower value of 0.0019 ($-$) for beam A3 and a much higher value for beam A2 of 0.0035 ($-$). However, when a constant and much higher value of α_l for beam A3 was initiated, a value of 0.012 ($-$) (Bengtsson 2001), a 6.4% increase is seen for beam A2 and a 1.9% increase for beam A3 after around 185 days of testing. The results concerning the stress τ_{lt} variable were similar. This can be explained by the fact of the stress state here being a product of the translation of the much larger normal stress value σ_x.
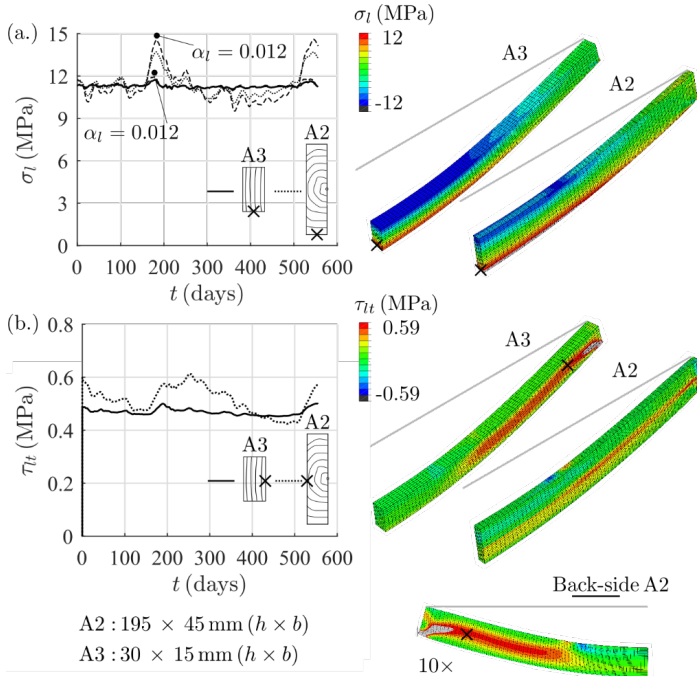
Fig. 18: Stress changes in σ_l and τ_{lt} for beams A2 and A3. Note that h is the height of the beam, b is the width of the beam, that the stress field is projected onto half of the beam, and that the deflection that occurs is magnified by a factor 10.

The changes that occur under natural climate conditions lead to phenomena similar to those that occur in beam A1 also being observed in beams A2 and A3; see **Fig. 14** and **Fig. 19**. In the areas in which the tangential material directions align with the exchange surface, high concentrations of σ_t develop. Here, steep moisture gradients located directly below the exchange surface result in shrinkage or swelling, which is counteracted by the inner section of the beam, which is still unaffected by the climate changes that have occurred; see **Fig. 19**.

Both beams are subjected to stress-reversal. However, the smaller geometry of beam A3 results in changes occurring more quickly, and in the stress values being lower than those in the larger beam, A2. The maximum tensile stress for σ_t, obtained in the month of May after about 200 days of testing, is much lower for beam A3 (≈ 0.68 MPa) than for beam A2 (≈ 1.4 MPa). For Norway spruce, the tangential strength of the wood at different moisture content levels and at a temperature of 20 ℃ is about 2 MPa (Hanhijärvi 1998). Since ϕ and T are averaged before being inserted into the analysis, and are averaged too in the analysis itself with each time increment, these stress peaks are readily underestimated.
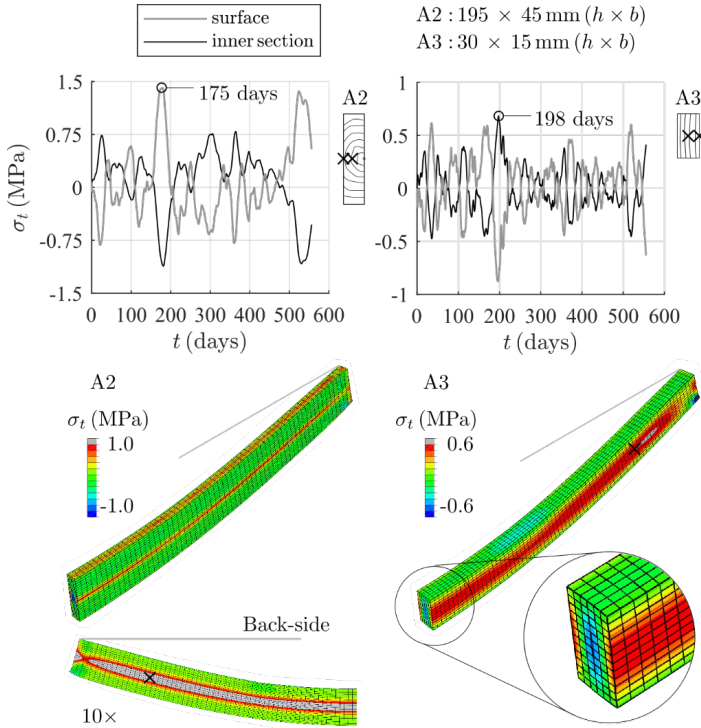
Fig. 19: The development of σ_t over time of beams A2 and A3 as obtained from the mesh element located on the exchange surface or at the centre ($\times$). Note that h is the height of the beam, b is the width of the beam, that the stress field is projected onto half of the beam, and that the deflection is magnified by a factor of 10.

5 Conclusions

The three-dimensional numerical model that was employed was found to be able to simulate long-term beam bending under both controlled and natural climate conditions. The model, implemented in a powerful FE-software, appeared to be ideal for computing and visualising complicated stress fields characterized by a combination of differing material orientations, as well as marked climate changes, long-term effects, and mechanical loads. On the basis of simulations made here for both applications, the following conclusions could be drawn:

- The small clear-wood beams analysed as part of the second application show the strong effect that spiral grain and climate have on deflection, calibrated material parameters and normative stress states.
- The results from the third application show that the larger beam exposed to mechanical load and natural climate experience a slower change in moisture, smaller moisture gradients, more seasonal fluctuation in longitudinal stress, tangential stress and longitudinal-tangential shear stress, and higher drying stress in tension compared to the smaller beam.
- Analysis of the material orientation contributes to an understanding of why bending tests are not a particularly suitable method of determining how reliable various material parameters are here. The results obtained showed spiral grain in particular to have a strong effect on the stress distribution and deflection that is characteristic of wooden beams generally, and is difficult to be eliminated from slender beams.
- The strongest effect that changes in the moisture content of the wooden beams that were studied had on the stress state the beams were subjected to in bending concerned the t-direction of the material orientation. For each beam configuration and each type of climatic condition that was involved, stress change between tension and compression was found to occur, this leading to an alternating of the stress states involved between the surface and the inner sections of the beams. This created an environment in which both surface and inner checks could develop and could result in splits or cracks, weakening the shear capacity of the beams.
- Calibration of the numerical model benefitted from the experimental methodology that was adopted, its providing a framework in which not only moisture content but also elastic, creep, hygro-expansive and mechano-sorptive behavior could be fitted to the experimental data. Although the experiment to validate the model was sufficient, it would have benefitted from constant recordings of changes in mass.
- A major challenge in regard to the three-dimensional models of relevance here is that of obtaining a sufficient amount of reliable experimental data for gaining an adequate understanding of the many material parameters needed to describe the moisture flow, and the hygro-mechanical and viscoelastic behaviour of Norway spruce, or of whatever type of wood is of interest.
- The model generally employed for describing creep trends towards an asymptote, making it difficult to predict creep outside of the time frame in which the model is calibrated.

6 Future studies

The adjustment of the material parameters of the wood that was studied to differing climatic conditions was used here to simulate moisture flow and material stress in the wood by use of linear or exponential mathematical expressions. Most of the expressions were calibrated on the basis of different sample sets that consisted of a variety of wood species, specimen sizes, test methods and climatic conditions. To overcome the limitations this represented, an experimental investigation could be conducted, aimed at identification of the moisture and temperature dependency of material parameters related to specific models of relevance that deal with elastic, hygro-expansive, creep and mechano-sorption behaviour. In work of our own with Norway spruce, we would be very much interested in investigating, at relevant levels of temperature and moisture content of the wood, loaded in primary material directions, small clear-wood specimens of Norway spruce. By means of matched specimens, the sample set or sets involved could be used to simulate and validate the long-term behaviour of both medium and large sized beams.

Declarations

Authors' contributions Conceptualisation: Sara Florisson (SF), Johan Vessby (JV), Sigurdur Ormarsson (SO); Methodology: SF, JV, SO; Software: SF; Validation: SF; Formal analysis: SF; Investigation: SF; Resources: SO; Data curation: SF; Writing – original draft: SF; Writing, review & editing: SF, JV, SO; Visualisation: SF; Supervision; SO, JV; Project administration: SF

Conflicts of interest/Competing interests On behalf of all authors, the corresponding author states that there is no conflict of interest.

Availability of data and material Not applicable

Code availability Not applicable

Funding Not applicable

7 References

EN 1995-1-1 (2004) Design of timber structures Part 1-1: General rules for buildings European Committee for Standardization (CEN), Brussels.

Aicher S, Dill-Langer G, Ranta-Maunus A (1998) Duration of load effect in tension perpendicular to the grain of glulam in different climates. Holz Roh Werkst, 56:295-305

Angst-Nicollier V (2012) Moisture induced stresses in glulam. Doctoral thesis, Norwegian University of Science and Technology (NUST), Trondheim

Armstrong LD, Christensen GN (1961) Influence of moisture changes on deformation of wood under stress. Nature, 4791:869-870

Armstrong LD, Kingston RST (1962) The effect of moisture content changes on the deformation of wood under stress. Aust J Appl Sci, 13:257-276

Avramidis S, Siau JF (1987) An investigation of the external and internal resistance to moisture diffusion in wood. Wood Sci Technol, 21:249-256 doi:https://doi.org/10.1007/BF00351396

Bengtsson C (2001) Variation of moisture induced movements in Norway spruce (*Picea abies*). Ann For Sci, 58:569-581 doi:https://doi.org/10.1051/forest:2001146

Bodig J, Jayne BA (1982) Mechanics of wood and wood composites. Van Nostrand Reinhold company, New York. ISBN 0894647776

Dahlblom O (1987) Constitutive modelling and finite element analysis of concrete structures with regards to environmental influence, 1004, Report TVSM-1004. Lund Institute of Technology, Lund

Dahlblom O, Persson K, Petersson H, Ormarsson S (1999) Inverstigation of variation of engineering properties of spruce. Paper presented at the IUFRO Wood Drying Conference: Wood Drying Research and Technology for Sustainable Forestry Beyond 2000, University of Stellenbosch, South Africa,

Dassault Systèmes (2017) Simulia User Assistance 2017. Abaqus User Subroutines Reference Guide. Vélizy-Villacoublay, France

Dodoo A (2011) Life cycle primary energy use and carbon emission of residential buildings. Doctoral thesis, Mid Sweden University, Sundsvall, Sweden

Engelund ET, Salmen L (2012) Tensile creep and recovery of Norway spruce influenced by temperature and moisture. Holzforsch, 66:959-965 doi:https://doi.org/10.1515/hf-2011-0172

Florisson S, Muszyński L, Vessby J (2021) Analysis of hygro-mechanical behaviour of wood in bending. Wood Fiber Sci, NOTE: accepted for publication

Florisson S, Ormarsson S, Vessby J (2019) A numerical study of the effect of green-state moisture content on stress development in timber boards during drying. Wood Fiber Sci, 51:41-57

Florisson S, Vessby J, Mmari W, Ormarsson S (2020) Three-dimensional orthotropic nonlinear transient moisture simulation for wood: analysis on the effect of scanning curves and nonlinearity. Wood Sci Technol:1197-1222 doi:https://doi.org/10.1007/s00226-020-01210-4

Fortino S, Hradil P, Genoese A, Genoese A, Pousette A (2019a) Numerical hygro-thermal analysis of coated wooden bridge members exposed to Northern European climates. Constr Build Mater, 208:492-505

Fortino S, Hradil P, Metelli G (2019b) Moisture-induced stresses in large glulam beams. Case study: Vihantasalmi bridge. Wood Mater Sci Eng, 14:366-380

Franke B, Franke S, Schiere M, Müller A (2019) Moisture content and moisture-induced stresses of large glulam members: laboratory tests, in-situ measurements and modelling. Wood Mater Sci Eng, 14:243-252 doi:https://doi.org/10.1080/17480272.2018.1551930

Gustafsson PJ (2003) Timber Engineering. John Wiley & Sons Ltd., West-Sussex, England. ISBN 0-470-48869-8

Gustafsson PJ, Hoffmeyer P, Valentin G (1998) DOL behaviour of end-notched beams. Eur J Wood Prod, 56:307-317 doi:https://doi.org/10.1007/s001070050325

Hanhijärvi A (1998) Deformation properties of Finnish spruce and pine wood in tangential and radial directions in association to high temperature drying. Eur J Wood Prod, 56:373-380 doi:https://doi.org/10.1007/s001070050415

Hayashi K, Felix B, Le Govic C (1993) Wood viscoelastic compliance determination with special attention to measurement problems. Mater Struc, 26:370-376

Hearmon RFS, Paton JM (1964) Moisture content changes and creep of wood. Forest Prod J, 8:357-359

Honfi D, Mårtensson A, Thelandersson S, Kliger R (2014) Modelling of bending creep of low- and high-temperature-dried spruce timber. Wood Sci Technol, 48:23-36

Hunt DG (1984) Creep trajectories for beech during moisture changes under load. J Mater Sci, 19:1456-1467

Johannesson B (2019) Thermodynamics of single phase continuous media: lecture notes with numerical examples. Lecture notes. Linnaeus University, Växjö.

Kangas J, Ranta-Maunus A (1989) Creep tests on the Finnish pine and spruce perpendicular to the grain Research Notes 969. Technical Research Centre of Finland, Espoo

Keunecke D, Sonderegger W, Pereteanu K, Lüthi T, Niemz P (2007) Determination of Young's and shear moduli of common yew and Norway spruce by means of ultrasonic waves. Wood Sci Technol, 41:309-327 doi:https://doi.org/10.1007/s00226-006-0107-4

Konopka D, Kaliske M (2018) Transient multi-Fickian hygro-mechanical analysis of wood. Comput Struct, 197:12-27 doi:https://doi.org/10.1016/j.compstruc.2017.11.012

Larsen F (2013) Thermal/moisture-related stresses and fracture behaviour in solid wood members during forced drying: modelling and experimental study. Doctoral thesis, Technical University of Denmark, Copenhagen

Malo KA, Abrahamsen RB, Bjertnæs MA (2016) Some structural design issues of the 14-storey timber framed building 'Treet' in Norway. Eur J Wood Prod, 74:407-424 doi:https://doi.org/10.1007/s00107-016-1022-5

McMillen JM (1958) Stresses in wood during drying, 1652, 1652. Forest Products Laboratory Madison S. Wisconsin, Wisconsin, United States

Müller A, Franke B, Schiere M, Franke S (2007) Advantages of moisture content monitoring in timber bridges. Paper presented at the 3rd International Conference on Timber Bridges, Skellefteå, Sweden,

Ormarsson S (1999) Numerical analysis of moisture related distortion in sawn timber. Doctoral thesis, Chalmers University of Technology, Gothenburg

Ormarsson S, Dahlblom O, Petersson H (1998) A numerical study of the shape stability of sawn timber subjected to moisture variation Part 1: Theory. Wood Sci Technol, 32:325-334 doi:https://doi.org/10.1007/BF00702789

Ormarsson S, Dahlblom O, Petersson H (1999) A numerical study of the shape stability of sawn timber subjected to moisture variation Part 2: Simulation of drying board. Wood Sci Technol, 33:407-423 doi:https://doi.org/10.1007/s002260050126

Ottosen N, Ristinmaa M (2005) The mechanics of constitutive modeling. Elsevier Science, Lund. doi:https://doi.org/10.1016/B978-0-08-044606-6.X5000-0

Ozyhar T, Hering S, Niemz P (2013) Viscoelastic characterization of wood: time dependence of the orthotropic compliance in tension and compression. J Rheol, 57:699-717

Ranta-Maunus A (1993) Rheological behaviour of wood in directions perpendicular to the grain. Mater Struct, 26:362-369

Ranta-Maunus A Moisture Gradient as Loading of Curved Timber Beams. In: International Association for Bridge and Structural Engineering, Seoul, South Korea, 2001.

Rosenkilde A (2002) Moisture content profiles and surface phenomena during drying of wood. Doctoral thesis, Royal Institute of Technology (KTH), Stockholm

Salin J-G (1992) Numerical prediction of checking during timber drying and a new mechano-sorptive creep model. Eur J Wood Prod, 50:195-200 doi:https://doi.org/10.1007/BF02663286

Schniewind AP, Barrett JD (1972) Wood as a linear orthotropic viscoelastic material. Wood Sci Technol, 6:43-57

Simpson WT (1971) Equilibrium moisture content prediction for wood. For Prod J, 21:48-49

Svensson S (1995) Strain and shrinkage force in wood under Kiln drying conditions Part I: Measuring strain and shrinkage under controlled climate conditions. Equipment and preliminary conditions. Holzforsch, 49:363-368

Svensson S (1996) Strain and shrinkage force in wood under Kiln drying conditions Part II: Strain, shrinkage and stress measurements under controlled climate conditions. Holzforsch, 50:463-469

Svensson S, Toratti T Mechano-sorption behaviour of wood perpendicular to grain. In: Hoffmeyer P (ed) Conference of COST Action E8 Mechanical Performance of Wood and Wood Products, Copenhagen, Denmark, 1997. pp 309-324

Säll H (2002) Spiral grain in Norway spruce. Doctoral thesis, Linnaeus University, Växjö

Toratti T (1992) Creep of timber beams in a variable environment. Doctoral thesis, Helsinki University of Technology, Helsinki

Toratti T, Svensson S (2000) Mechano-sorptive experiments perpendicular to grain under tensile and compressive loads. Wood Sci Technol, 34:317-326

Yeo H, Eom C-D, Han Y, Kang W, Smith WB (2008) Determination of internal moisture transport and surface emission coefficients for Eastern white pine. Wood Fiber Sci, 40:553-561

Yeo H, Smith WB (2005) Development of a convective mass transfer coefficient conversion method Wood Fiber Sci, 37:3–13

Yeo H, Smith WB, Hanna RB (2002) Mass transfer in wood evaluated with a colorimetric technique and numerical analysis. Wood Fiber Sci, 34:557-665